Compressible CFD simulations of aeroacoustics for automotive applications

Von der Fakultät für Maschinenbau
der Technischen Universität Carolo-Wilhelmina zu Braunschweig

zur Erlangung der Würde

eines Doktor-Ingenieurs (Dr.-Ing.)

genehmigte Dissertation

von:	Ali Dawi
aus (Geburtsort):	Hawally, Kuwait

eingereicht am:	23.01.2019
mündliche Prüfung am:	04.07.2019

Gutachter:	Prof. Dr. Ir. Rinie A. D. Akkermans
	Prof. Dr. Ir. Bernard J. Geurts

2019

Disclaimer

The results, opinions and conclusions expressed in this thesis are not necessarily those of Volkswagen Aktiengesellschaft.

Abstract

In this work, a direct noise computation method based on a low-Mach number flow solver is investigated. The new solver is implemented in the finite volume framework of the software OpenFOAM, accompanied with a new acoustic damping model based on the time derivative of the pressure. The new solver is utilised to calculate noise generation and propagation for automotive applications, while the damping model reduces spurious noise generated inside the computational domain.

In order to validate the applicability of the low-Mach flow solver, a benchmark consisting of two-struts is calculated. The simulated aerodynamic near field as well as aeroacoustic far field are compared to wind tunnel measurements. The acoustic far field is computed using the direct method as well as a hybrid method based on surface integral. Both methods are evaluated based on comparing far field spectra and directivity patterns with experimental results. Furthermore, the effect of the simulated span on the coherence function and correlation coefficient is presented. The direct noise computation using the new flow solver shows good agreement with wind tunnel measurements.

After validating the applicability of the low-Mach number solver, the topic of spurious noise generation in direct noise computation is addressed. Different spurious noise sources are presented and their generation mechanisms are investigated. Afterwards, two different strategies for spurious noise reduction, namely selective acoustic damping and numerical grid stretching, are discussed and validated. The acoustic damping model can substantially damp out spurious noise generated at grid interfaces without affecting the turbulence. It is also observed that the direction of grid refinement determines the direction of propagation of spurious noise. The strategies for spurious noise reduction are then applied on a side-mirror test case. For this, a new algorithm for automated and directional grid stretching is implemented. Spurious noise generation in the vicinity of the mirror's surface as well as in the mirror's wake could be substantially reduced and a quantitative analysis based on frequency-wavenumber spectra in the wake of the mirror is performed.

Finally, the proposed flow solver, along with the strategies for spurious noise reduction, are used to directly compute noise generation on a generic vehicle model. Two different variants, with and without side-mirror, are calculated and the effect of the A-pillar and the side-mirror regarding their contribution to the acoustic waves on the side-window is investigated. Aerodynamic as well as aero- and vibroacoustic spectra on the side-window are calculated and compared to wind-tunnel measurements. For both variants, the results calculated using the direct method show good agreement with experimental data.

Kurzfassung

In dieser Arbeit wird eine Methode zur direkten Berechnung von Aeroakustik basierend auf einen Strömungslöser für kleine Mach-Zahlen untersucht. Der Strömungslöser wird mit einem neuen Dämpfungsmodell, das auf der zeitlichen Ableitung des Druckes basiert, im finite Volumen Code OpenFOAM implementiert. Der neue Löser wird für die Berechnung der Entstehung und Ausbreitung von Schallwellen im Automobilbereich angewandt, während das Dämpfungsmodell für die Reduktion numerischer Schallwellen, die im Berechnungsgebiet entstehen können, eingesetzt wird.

Zur Validierung des neuen Strömungslösers, wird ein Benchmark, der aus zwei parallelen Streben besteht, berechnet. Das simulierte aerodynamische Nahfeld sowie das aeroakustische Fernfeld werden mit Windkanalmessungen verglichen. Das akustische Fernfeld wird mit der direkten sowie mit einer hybriden, auf der Berechnung eines Oberflächenintegrals basierenden Methode, berechnet. Beide Methoden werden anhand der Fernfeldspektren sowie der Richtcharakteristiken mit experimentellen Daten bewertet. Außerdem wird der Einfluss der simulierten Spannweite wird mithilfe der Kohärenzfunktion und des Korrelationskoeffizienten untersucht.

Nach der Validierung des Strömungslösers wird die Entstehung von numerischen Störungen in der direkten Methode analysiert. Es werden verschiedene Quellen numerischer Störungen sowie deren Entstehungsmechanismen dargestellt. Anschließend werden zwei verschiedene Strategien zur Reduktion von Störungen diskutiert und validiert. Das Dämpfungsmodell zeigt sein Potenzial bei der Reduktion von numerischen Schallwellen ohne Beeinflussung der Turbulenz. Es wird außerdem gezeigt, dass die Richtung einer Verfeinerung des numerischen Gitters die Richtung der Ausbreitung numerischer Schallwellen bestimmt. Die Strategien zur Reduktion numerischer Störungen werden weiterhin an einem einzelnen Seitenspiegel angewandt. Dafür wird ein neuer Algorithmus für eine automatisierte und richtungsdefinierte Gitterexpansion implementiert. Die Amplitude numerischer Störungen, die im Spiegelnachlauf entstehen, werden mit Hilfe einer Frequenz-Wellenzahl Analyse quantitativ untersucht. Es zeigt sich, dass das Dämpfungsmodell diese Störungen deutlich reduziert.

Abschließend wird der Strömungslöser zusammen mit den vorgeschlagenen Strategien in einer direkten Aeroakustikberechnung eines generischen Fahrzeugmodells angewandt. Es werden zwei unterschiedliche Varianten, mit und ohne Seitenspiegel, berechnet und der Einfluss der A-Säule und des Seitenspiegels bezüglich ihres akustischen Beitrags auf der Seitenscheibe untersucht. Sowohl aerodynamische als auch aero- und vibroakustische Spektren werden auf der Seitenscheibe berechnet und mit Windkanalmessungen verglichen. Für beide Varianten zeigen die Ergebnisse der direkten Methode gute Übereinstimmung mit den experimentellen Daten.

Contents

1 Introduction

1.1 Motivation

The sources of interior cabin noise in passenger vehicles are mainly divided into three categories: rolling noise generated through the interaction between tires and tarmac, noise generated by the engine and different drivetrain components, and thirdly aerodynamic noise generated by the air flowing past the vehicle. As both tire noise [78, 122] and engine noise [27] are continuously being reduced, aerodynamic noise is becoming increasingly important. For ICE (Internal Combustion Engine) driven vehicles, aerodynamic noise is the dominant noise source for cruising speeds exceeding 100 km/h. For BEV (Battery Electric Vehicle), engine noise is not present and aerodynamic noise becomes the dominating source at even lower speeds. Furthermore, customers comfort demands, including quieter rides, are constantly increasing. This particularly applies for future autonomous cars, in which the car itself is the actual driver and the passengers would rather want to have the feeling of sitting in their living room.

Apart from gaps, cavities, and open windows or sunroof, the main sources for aerodynamic noise are external mounted parts, such as side-mirrors, wind-shield wipers, and roof carrier systems. Besides, components that are a major part of a vehicles chassis, such as the A-pillar, could also be a dominant noise source. Not only the sources show a large disparity, but also their pathway into the cabin as well as the perception of the driver to different frequencies. For instance, a tonal noise at a certain frequency could be more annoying than constant broadband noise over a wide frequency range. Therefore, in order to efficiently reduce interior cabin noise, it is significant to study noise generated by the flow past different parts of the vehicle, the main pathway of acoustic waves generated by these sources into the cabin, and the distribution of their acoustic power and directivity among different frequencies. Such a study could be performed experimentally as well as numerically. Experimental studies of wind noise is usually performed in an aeroacoustic wind tunnel. Hereby, main noise sources can be identified using acoustic cameras, far field arrays, and artificial heads inside the cabin. Despite the high cost of such measurements, they can only deliver a limited amount of information regarding noise generation. On the other hand, numerical simulations can give a deeper insight into the noise generation mechanism and enables a more detailed analysis of the results. This is due to the availability of information at every point in the domain and the ability to measure various flow quantities at places that are difficult to access in the experiment. In addition, the overproportional increase of computational resources and the constantly decreasing costs of CPU hours make numerical simulations more attractive to be deployed in the product development process.

There exist different approaches for the computation of noise generation and sound propagation, which can be categorized into two main methods: direct noise computation (DNC) methods and the hybrid methods. In the direct method, the compressible Navier-Stokes (NS)

equations, which consist of the conservation equations of mass, momentum and energy, are directly solved. These equations describe the velocity, pressure, density, and temperature of each fluid particle. The solution of these equation includes the description of the fluid flow consisting of hydrodynamic pressure fluctuations as well as acoustic ones. Hence, the direct method delivers the hydrodynamic and acoustic solutions simultaneously. On the other hand, hybrid methods consist usually of two steps: the solution of the compressible or incompressible NS-equations as a first step, and the calculation of the acoustic solution using an acoustic solver, which is based on different equations than the NS-equations, as a second step. Such methods are usually utilised for the calculation of far-field acoustics, for which the direct method is too expensive to be used.

One major difference between direct and hybrid methods is the ability to capture the interaction between the flow field and acoustic waves propagating in the domain. Although the amplitude of acoustic pressure waves is orders of magnitude smaller than that of hydrodynamic ones, there are some situations in which acoustic waves interact with the fluid flow and cause a substantial change in the flow topology. This is the case for unstable shear layers that could be generated, for example, at the surface of a side-mirror. The instabilities in the shear layer could be triggered by small disturbances, such as acoustic waves, and the interaction between these disturbances and the onset of instability could grow into a feedback loop, causing the well-know whistling phenomenon. In order to capture this behaviour, the effect of acoustic waves on the flow and vice-versa has to be captured, which is only possible by solving the compressible NS-equations.

Apart from the interaction between acoustic and hydrodynamic waves, there are some applications for which the direct method is the preferable approach to compute noise generation. This is the case when computing noise generated by open-surface geometries, that cannot be considered as compact noise sources. One example of such geometries is the A-pillar of a vehicle.

1.2 State of research

Hybrid CAA-methods are currently wide spread for exterior noise computation in the automotive industry. These methods consist of calculating the flow field using a CFD solver and the acoustic field using a separate acoustic solver. Moreover, hybrid methods allow the calculation of the flow using an incompressible flow solver, which delivers surface pressure fluctuations on, for instance, the surface of a side-mirror. These fluctuations can then be used to calculate acoustic waves generation and propagation. An overview of surface integral methods was given by Lyrintzis [69]. These methods have already been utilised for automotive applications. For instance, Kabat vel Job et al. [48] showed that the side-mirror is the dominant acoustic source for a production vehicle and calculated the interior sound level based on sound waves emitted by the side-mirror. Unsteady surface pressure values resulting from an incompressible flow solver were also used by Kucukcoskun et al. [55] in order to calculated acoustic waves emitted by the surface of an exterior side-mirror.

Regarding the usage of direct methods for automotive applications, most studies were performed on simplified test cases (e.g. single side-mirror mounted on a flat plate). Van Herpe et al. [107] calculated acoustic waves generated by the flow past a side-mirror mounted on a table and performed a wavenumber-frequency analysis for the pressure fluctuations in the wake of the mirror. Their analysis allowed a detailed examination of hydrodynamic and acoustic contents of wall pressure fluctuations and showed spurious waves travelling upstream the flow direction, which was attributed to the effect of the outlet boundary of the computational domain. Such waves were also observed by Schell [91], who performed aeroacoustic computations on a generic vehicle model using a compressible solver. He showed that upstream travelling waves are in fact spurious waves generated by the interaction between the turbulent flow and refinement interfaces in the wake of the mirror. By extending the refinement zone downstream the surface of the mirror, he was able to reduce the amplitude of spurious noise impinging on the surface of the side-window. However, extending the refinement resulted in a dramatic increase of the overall number of grid cells. Apart from the calculation of noise generated by the side-mirror, few studies concerning the calculation of noise generated by the flow past the A-pillar were done. However, none of them show a detailed description of the utilised CFD-model.

1.3 Objective

Despite the relative simplicity of the concept of direct noise computation, namely solving the compressible NS-equations and inherently calculating noise generation and propagation simultaneously, there exist several challenges in general as well as regarding its utilisation to industrial applications and complex geometries specifically. Some of these challenges are:

- Dissipation and dispersion: computing acoustic propagation numerically is sensitive towards the characteristics of the utilised numerical schemes. Each scheme has its unique dissipation (amplitude) and dispersion (phase) characteristics. In order to preserve the amplitude and phase of acoustic waves during their propagation, the utilisation of high-order numerical schemes is typical for such applications. This is particularly the case when calculating far-field acoustics.
- Spurious noise: for flow configurations with high Reynolds number and low Mach number, there exist different sources of numerical spurious noise, that could mask out the physical noise and falsify the overall solution. The generation of spurious noise in direct noise computation is insufficiently researched, and understanding the mechanisms of spurious noise generation and developing different strategies for spurious noise reduction that are industrially applicable is inevitable.
- Other numerical artefacts: besides dissipation and dispersion of numerical schemes and different sources of spurious noise generation, there exist other artefacts that could affect the overall acoustic solution in the region of interest. Such artefacts are, for instance,

wave reflections at boundaries, numerical grid interfaces, or discontinuities in any flow variable.

The aim of this work is to develop a direct noise computation method for automotive applications. One particularity in automotive applications are the short propagation distances of acoustic waves, which provides a degree of simplicity regarding the order of utilised schemes. Since a new flow solver is implemented in this work, a validation based on an academic benchmark is required. Furthermore, automotive applications usually involve complex geometries with sophisticated grid topologies. Hence, one major objective in this work is to first investigate the effect of different numerical factors (e.g grid interfaces, numerical schemes) on the acoustic solution, and then develop suitable strategies for an accurate and yet stable simulation method. This simulation method can then be implemented in the product development process in order to predict the acoustic quality of different vehicle components during the design phase.

1.4 Outline of this thesis

This thesis is structured as follows:

- Chapter 2 consists of two parts: in the first part, the equations that describe the motion of a compressible fluid are discussed and the different approaches regarding turbulence modelling are presented. Furthermore, simplifications regarding low-Mach number flows are introduced. In the second part, the fundamental aeroacoustic equations are presented and a hybrid surface integral method for the calculation of acoustic propagation is introduced and discussed.
- The numerical method used to discretise the differential equations presented in chapter 2 is presented in chapter 3. Therein, approximation techniques of different terms are discussed, different numerical schemes and their advantages and disadvantages are presented, and the utilised iterative algorithm used in the course of this work is explained. Furthermore, an acoustic damping model is introduced and its characteristics regarding its effectiveness and stability are discussed.
- The proposed flow solver is then validated in chapter 4 based on an academic benchmark. Therein, the aerodynamic near field as well as the aeroacoustic far field are calculated and compared with wind tunnel measurements. The effects of the simulated span as well as the end-plates are illustrated, and the results quality of each CAA-method is discussed at the end of the chapter.
- Chapter 5 is dedicated to the investigation of spurious noise generation in direct noise computation. Two test cases are investigated: the first test case consists of a convected isotropic turbulence package, which is used to study the mechanisms and sources of spurious noise. Furthermore, different strategies for spurious noise reduction are discussed, and two of them are applied on the test case. In order to test the effectiveness of the proposed strategies, a second test case consisting of a single side-mirror mounted on a flat

plate is calculated. Different numerical aspects are studied and best practice parameters for the computation of noise generation and propagation on a side-mirror are derived.

- Finally, the flow solver, combined with the acoustic damping model and the grid stretching algorithm, is utilised to calculate noise generation on a generic vehicle model in chapter 6. Different noise sources are identified and their contribution to the acoustic power on the side-window is discussed. The simulated aerodynamic, aeroacoustic, and vibroacoustic results are compared to wind tunnel measurements and concluding remarks about the quality, applicability, and efficiency of the proposed method are given in chapter 7

2 Physical principles

In this chapter, the equations describing fluid motion as well as the generation and propagation of acoustic waves will be presented. Under the assumption of a small Knudsen number ($Kn = \lambda / l < 0.01$), where λ is the mean free path and l the characteristic physical length of the flow, the continuum mechanics formulation will be used to model the fluid motion. This assumption is considered valid for all automotive applications.

2.1 Fluid mechanics

Fluid mechanics is a sub-discipline of continuum mechanics which deals with motion of fluids. Such fluids can be categorised into Newtonian and non-Newtonian fluids, depending on the relation between strain rate of the fluid and shear stress applied on it. The fluid considered in this work will be air, which belongs to the category of Newtonian fluids. Hence, the following equations will be describing the motion of such fluids.

2.1.1 Conservation equations

The physical quantities that describe a fluid flow are the velocity vector $\vec{U}$, the pressure p, the density ρ, and the temperature T. These quantities are related by the conservation laws of fluid mechanics, namely the conservation of mass, momentum and energy (see e.g. [100], [24]). The conservation of a scalar quantity ϕ can be described by the differential form of the generic transport equation:

$$\underbrace{\frac{\partial(\rho\phi)}{\partial t}}_{\text{Transient term}} + \underbrace{\frac{\partial(\rho U_i \phi)}{\partial x_i}}_{\text{Advection term}} = \underbrace{\frac{\partial}{\partial x_i}\left(D\frac{\partial \phi}{\partial x_i}\right)}_{\text{Diffusion term}} + \underbrace{S}_{\text{Source term}} . \tag{2.1}$$

In Eq. (2.1), the Einstein summation convention is used. The first term on the left hand side describes the local acceleration of the scalar ϕ, where t denotes the time. The advection term describes the advective acceleration of ϕ due to fluid motion. Herein, U_i denotes the velocity component in each spatial direction x_i. The diffusion term describes the transport of ϕ due to its spatial gradient, in which D describes the diffusivity. All other effects that do not belong to the aforementioned terms can be put together into the source term S (e.g. mass sinks, heat sources, etc.). The conservation equations of mass, momentum and energy have the form of Eq. (2.1). The differential form of mass conservation equation, assuming no mass sources/sinks, is given by:

$$\frac{\partial \rho}{\partial t} + \frac{\partial(\rho U_i)}{\partial x_i} = 0. \tag{2.2}$$

Analogously, one can derive a differential equation for momentum conservation:

$$\frac{\partial(\rho U_i)}{\partial t} + \frac{\partial(\rho U_j U_i)}{\partial x_j} = \frac{\partial \sigma_{ij}}{\partial x_j} + b_i. \tag{2.3}$$

In Eq. (2.3), σ_{ij} denotes the stress tensor and b_i the sum of external body forces. For isotropic Newtonian fluids, the stress tensor can be written as:

$$\sigma_{ij} = -\left(p + \frac{2}{3}\mu\frac{\partial U_j}{\partial x_j}\right)\delta_{ij} + \mu\left(\frac{\partial U_i}{\partial x_j} + \frac{\partial U_j}{\partial x_i}\right), \tag{2.4}$$

where μ is the dynamic viscosity of the fluid and δ_{ij} is Kronercker-Delta:

$$\delta_{ij} = \begin{cases} 1 & \text{if } i = j \\ 0 & \text{if } i \neq j \end{cases}. \tag{2.5}$$

The stress tensor σ_{ij} is usually divided into the pressure part p and the viscous part τ_{ij}:

$$\begin{aligned} \sigma_{ij} &= -p\delta_{ij} + \tau_{ij}, \\ \tau_{ij} &= \mu\left(\frac{\partial U_i}{\partial x_j} + \frac{\partial U_j}{\partial x_i}\right) - \frac{2}{3}\mu\frac{\partial U_k}{\partial x_k}\delta_{ij}. \end{aligned} \tag{2.6}$$

Finally, the conservation of energy can be described by the following partial differential equation:

$$\frac{\partial(\rho e_t)}{\partial t} + \frac{\partial(\rho e_t U_i)}{\partial x_i} = -\frac{\partial(U_i p)}{\partial x_i} - \frac{\partial q_i}{\partial x_i} + \frac{\partial(\tau_{ij} U_j)}{\partial x_i}, \tag{2.7}$$

where the specific total energy $e_t = e + U_i U_i/2$ is equal to the sum of the specific internal energy e and the kinetic energy $U_i U_i/2$. In Eq. (2.7), momentum and energy source terms are neglected. The heat flux density q_i is given by Fourier's law for thermal conduction:

$$q_i = -k\frac{\partial T}{\partial x_i}, \tag{2.8}$$

where k denotes the thermal conductivity of the fluid. In this work, it is assumed that fluid (air) is a calorically perfect gas, for which the following relations apply:

$$p = \rho RT, \qquad de = c_v dT, \qquad dh = c_p dT, \qquad R = c_p - c_v, \qquad \gamma = \frac{c_p}{c_v} \tag{2.9}$$

In Eq. (2.9), R is the specific gas constant and is equal to 287.053 $\mathrm{Jkg^{-1}K^{-1}}$ for dry air. c_v and c_p are the heat capacities at constant volume and constant pressure, respectively. The

specific enthalpy is denoted by h and γ represents the heat capacity ratio. For diatomic gases, e.g. dry air, γ is equal to 1.4.

Using the relation between the specific internal energy e and the temperature T in Eq. (2.9), one can derive a conservation equation for the temperature:

$$\frac{\partial(\rho c_p T)}{\partial t} + \frac{\partial(\rho c_p T U_i)}{\partial x_i} = \frac{\partial p}{\partial t} + U_i \frac{\partial p}{\partial x_i} - \frac{\partial q_i}{\partial x_i} + \Phi, \tag{2.10}$$

where Φ denotes the total viscous dissipation.

For a calorically perfect gas, the dynamic viscosity μ and the thermal conductivity k can be expressed in terms of temperature T. For the dynamic viscosity, the Sutherland's law states [102]:

$$\mu(T) = \mu_{ref} \left(\frac{T}{T_{ref}} \right)^{3/2} \frac{T_{ref} + T_S}{T + T_S}, \tag{2.11}$$

where T_{ref} is a reference temperature, T_S the Sutherland temperature, and μ_{ref} the dynamic viscosity at T_{ref}. For dry air, these values are given by $\mu_{ref} = 1.7 \cdot 10^{-5}$ Pa·s, $T_{ref} = 273.15$ K, and $T_S = 110.4$ K.

The relation between the thermal conductivity k and dynamic viscosity μ can be expressed by the Prandtl number Pr, which is equal to the ratio of momentum diffusivity to thermal diffusivity:

$$\mathrm{Pr} = \frac{\mu c_p}{k} \tag{2.12}$$

For temperature ranges between 273.15 K and 773.15 K, Pr of dry air varies between 0.718 and 0.719, so that a constant value of Pr can be considered for automotive applications.

Eqs. (2.2), (2.3), (2.7) and (2.9) form a governing system of differential equations for fluid motion.

2.1.2 Turbulent flows

Fluid flows can be categorized into two main categories: laminar and turbulent flows. A laminar fluid flow is characterised by layers which do not mix with each other. Such flows are present, e.g., in small pipes with low fluid velocities. On the other hand, a turbulent flow is characterised by a stronger mixing behaviour due to vortical structures of different length scales present in the flow. Turbulent flows take place especially in systems with high velocities, where the ratio of inertial forces to viscous forces is large enough. This ratio is known as the Reynolds number Re:

$$\mathrm{Re} = \frac{UL}{\nu}, \tag{2.13}$$

where U and L are the characteristic velocity and length scale of the system, respectively, and $\nu = \mu/\rho$ the kinematic viscosity of the fluid. The Reynolds number was named after Osborne Reynolds, who for the first time experimentally observed the laminar-turbulent transition in a pipe flow. Figure 2.1 shows a laminar and a turbulent channel flow. Due to higher momentum exchange between fluid particles, the mean velocity profile in the turbulent flow is more uniform in the y-direction.

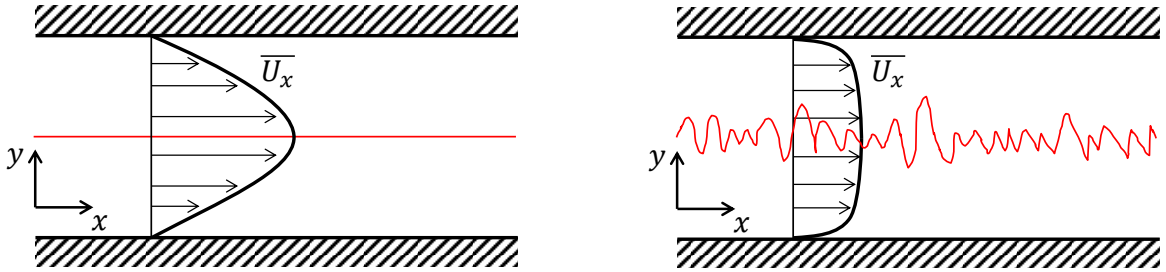

Figure 2.1: Schematic representation of (left) laminar and (right) turbulent channel flow. $\overline{U_x}$ denotes the temporal mean velocity profile and the red lines represent a dye visualisation of the flow.

In a turbulent flow field, there exist different characteristic length scales. Figure 2.2 shows an energy spectrum of a turbulent field as a function of wavenumber k. According to Pope [82], the energy spectrum can be divided into two main ranges: the energy-containing range and the universal equilibrium range. The first range, in which turbulence production takes place, contains eddies that are defined by the geometry and the boundary conditions of the flow. These eddies have an anisotropic nature. As large eddies decay, their energy passes down to smaller scales in the universal equilibrium range ($l < l_{EI}$). These scales are characterised by their isotropic nature and information regarding the geometry or boundary conditions gets lost. The smallest scales are present in the dissipation range and are known as the Kolmogorov scales. The relation between the Kolmogorov scales (subscript η) and the energy-containing scales (subscript 0) scale with Re as [82]:

$$\frac{l_\eta}{l_0} \sim \mathrm{Re}^{-3/4}, \qquad \frac{U_\eta}{U_0} \sim \mathrm{Re}^{-1/4}, \qquad \frac{t_\eta}{t_0} \sim \mathrm{Re}^{-1/2}, \tag{2.14}$$

where t corresponds to the characteristic time scale of an eddy.

2.1.3 Low Mach number flows

The speed of today's passenger cars on German highways ranges typically between 100 and 250 km/h. This corresponds to a Mach number range between $0.08 < Ma < 0.2$, which

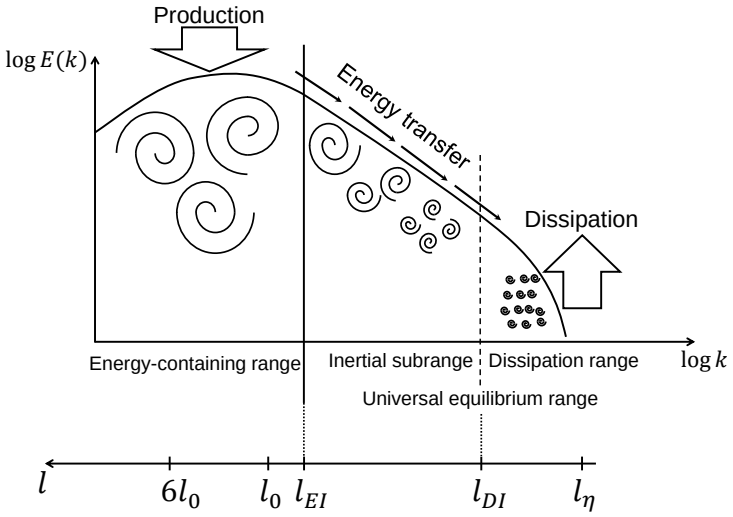

Figure 2.2: Energy spectrum of a turbulent field as a function of the wavenumber k. Different length scales are shown according to Pope [82].

belongs to the low Mach number regime $(Ma \ll 1)$. The density variation can be approximated by substituting the density-pressure relation for ideal gases in the momentum equation resulting in:

$$Ma^2 \frac{dU}{U} = -\frac{d\rho}{\rho}. \tag{2.15}$$

For $Ma \ll 1$ (subsonic flows), density variations are small (typically below 5%). Thus, compressibility effects can be ignored for this Mach number range. Furthermore, the heat transfer in the flow itself as well as energy loss due to viscous forces are negligibly small, so that the change of flow state can be considered reversible. Thus, one can assume that the change of flow variables past a vehicle as an isentropic process (adiabatic and reversible). This gives the possibility to calculate the temperature (and subsequently the internal energy) via the isentropic relation of ideal gases:

$$T = T_{ref} \left(\frac{p}{p_{ref}} \right)^{\frac{\gamma-1}{\gamma}}, \tag{2.16}$$

in which T_{ref} and p_{ref} correspond to the temperature and pressure in a reference state, respectively. These can be chosen to be the total variables:

$$T_t = T \left(1 + \frac{\gamma-1}{2} Ma^2 \right); \qquad p_t = p \left(1 + \frac{\gamma-1}{2} Ma^2 \right)^{\frac{\gamma}{\gamma-1}}. \tag{2.17}$$

Equation (2.16) enables the calculation of the temperature without solving the energy equation (2.10), which yields a substantial reduction of computational cost.

The isentropic assumption applies also for acoustic propagation due to the negligible heat transfer and viscous loss of acoustic waves. Thus, this assumption can be considered valid for aeroacoustic calculations of low Mach number flows.

2.2 Turbulence modelling

In the following paragraphs, different techniques for the calculation of turbulent flows are presented. These techniques range from resolving all length scales (e.g. no modelling), which could be challenging for high-Reynolds number flows, to statistical methods, which model the effect of turbulence without resolving any of the turbulent fluctuations (e.g. full modelling). Each technique has its advantages and disadvantages, which are discussed in the following sections.

2.2.1 Direct numerical simulation (DNS)

In a DNS, the fluid flow is calculated by directly solving the conservation equations presented in subsection 2.1.1. This includes resolving all length and time scales of the fluid flow without modelling any turbulent scales. However, according to Eq. (2.14), the relations of the dissipative to the energy containing length and time scales depend on the Reynolds number. Hence, if one wants to resolve all the dissipative scales, the number of computational nodes needed is $N \sim l_0/l_\eta \sim \mathrm{Re}^{3/4}$. Moreover, turbulent flows are three dimensional and thus, the overall number of nodes needed is equal to $N^3 \sim \mathrm{Re}^{9/4}$. Not only the number of spatial nodes, but also the number of time steps needed depends on the Reynolds number due to $t_0/t_\eta \sim \mathrm{Re}^{1/2}$. Moreover, according to [82], an accurate solution requires the CFL condition to be fulfilled, which further restricts the time step size and the number of time steps needed is then $T \sim \mathrm{Re}^{3/4}$. Combining the number of spatial nodes and the number of time steps required, the overall effort for a direct numerical simulation of a turbulent flow would be:

$$N^3 \cdot T \sim \mathrm{Re}^3. \tag{2.18}$$

Note that the above considerations apply for homogeneous turbulence, where the flow statistics are independent of space. For inhomogeneous turbulence, e.g. wall bounded flows, a higher computational effort has to be considered due to additional resolution requirements in boundary layers [82]. Therefore, DNS is currently used only in scientific research for simple geometries at low Reynolds numbers, e.g. flat-plate boundary layer [119], turbulent channel flow [4, 60, 77], and the flow past a backward-facing step [58]. The goal of such studies is usually to create a set of databases of flow features that are difficult to measure with experimental methods.

Besides the high computational effort required by DNS, highly accurate numerical methods are required in order to capture all length and time scales. Low-order numerical schemes

are often too dissipative to capture the dissipative length scales, so that high-order schemes or Fourier spectral methods are usually used for such simulations [121]. Furthermore, including the proper boundary conditions of complex geometries can be challenging for the utilisation of DNS [17].

2.2.2 Large eddy simulation (LES)

For industrial applications, engineers are usually interested in the main flow features of the simulated system, which mainly depend on the boundary conditions and the geometry of the simulated system. These flow features are mostly included in the energy containing scales and the small dissipative scales, which are rather universal (i.e. dependent of the fluid), are not of interest. Hence, modelling the effect of the dissipative scales would lead to a drastic reduction regarding computational effort and would be more suitable for industrial applications. One way to reduce this effort is to filter out these scales and model their effect on the energetic scales (see e.g. [29, 87, 114]). This is the idea behind a large eddy simulation.

In a LES, the conservation equations that describe the fluid flow are filtered and new equations for the filtered variables are obtained. The filtered variables describe the same fluid flow, but without the dissipative Kolmogorov scales. The smallest scales described by the filtered equations are then related to the cutoff wavenumber of the utilised filter and are larger than the Kolmogorov scales. However, in order to maintain energy equilibrium, the role of the dissipative scales has to be modelled and their effect on larger scales has to be accounted for. According to [114], the energetic part that has to be resolved by a LES is not strictly defined, but $80-90\%$ of the energy is deemed to be a typical minimum threshold for such simulations. The filter width, which determines the separation limit between resolved and unresolved scales, has to satisfy the physical criteria of a turbulent flow. This means, a LES has to resolve the main flow features, which include large scales that are defined by the geometry and boundary conditions, while dissipative scales, which have in general an isotropic behaviour and are independent of the flow topology, can be modelled. The unresolved part in a LES is usually referred to as subgrid-scales.

In an LES, a variable ϕ is decomposed into a filtered (resolved) part $\widehat{\phi}$ and a residual (subgrid scale) part ϕ':

$$\phi = \widehat{\phi} + \phi' \tag{2.19}$$

The filtered part $\widehat{\phi}$ is defined as [10]:

$$\widehat{\phi}(\mathbf{x},t) = \int_{-\infty}^{+\infty}\int_{-\infty}^{+\infty} G\left(\mathbf{x}-\mathbf{x}',t-t'\right)\phi\left(\mathbf{x}',t'\right)d\mathbf{x}'dt'. \tag{2.20}$$

In Eq. (2.20) $G(\mathbf{x},t)$ denotes the filter kernel in physical space. Examples of typical filter kernels and their transfer functions are presented in Table 2.1.

Table 2.1: Filter kernels of the different filters in physical and wavenumber spaces.

	Gaussian filter	Sharp cutoff filter	Box filter
$G(\mathbf{x})$	$\sqrt{\frac{6}{\pi\Delta^2}}e^{\frac{-6\mathbf{x}^2}{\Delta^2}}$	$\frac{\sin(\pi\mathbf{x}/\Delta)}{\pi\mathbf{x}}$	$\frac{1}{\Delta}H(\frac{1}{2}\Delta-\lvert\mathbf{x}\rvert)$
$\widehat{G}(k)$	$e^{\frac{-k^2\Delta^2}{24}}$	$H(\pi/\Delta-\lvert k\rvert)$	$\sin\left(\frac{1}{2}k\Delta\right)/\frac{1}{2}k\Delta$

According to [114], the filters presented in Table 2.1 fall into the category of theoretical explicit filters. In addition to explicit filtering, several implicit filtering processes are done in a practical LES. These processes are categorised in [114] as grid filter, numerical filter, and subgrid model filter. For detailed information about the nature and effect of each filter, the reader is referred to [114]. Furthermore, the filtering process introduced in Eq. (2.20) does not account for the presence of walls. Filtering the governing equations near boundaries requires the modification of the filtering procedure in order to minimise commutation errors [93].

Applying a filtering operation to Eq. (2.3) and assuming a constant density (incompressible flow) and viscosity results in:

$$\frac{\partial\widehat{U}_i}{\partial t}+\frac{\partial\widehat{U_iU_j}}{\partial x_j}=-\frac{1}{\rho}\frac{\partial\widehat{p}}{\partial x_i}+\nu\frac{\partial^2\widehat{U}_i}{\partial x_j\partial x_j}. \tag{2.21}$$

The difference between the second term on the left hand side of Eq. (2.21) and the product of the filtered velocity $\widehat{U}_i\widehat{U}_j$ is the residual stress tensor [82]:

$$\tau_{ij}^R=\widehat{U_iU_j}-\widehat{U}_i\widehat{U}_j. \tag{2.22}$$

The residual stress tensor is usually decomposed into an isotropic part $\tau_{kk}^R/3$ and an anisotropic part $\tau_{ij}^r=\tau_{ij}^R-\tau_{kk}^R/3\delta_{ij}$. The isotropic part is then added to the filtered pressure $\widehat{p}$, resulting in a pseudopressure in the filtered momentum equation:

$$\Pi=\widehat{p}+\frac{1}{3}\tau_{kk}^R. \tag{2.23}$$

The anisotropic part τ_{ij}^r contains the filtered non-linear term $\widehat{U_iU_j}$, which is unknown, and thus has to be modelled.

Extending the filtering operation to the compressible case requires the introduction of additional non-linearities due to the density inside the derivatives. Filtering the compressible

momentum equation, analogously to the incompressible one, would result in $\widehat{\rho U_i}$. This term is usually written as:

$$\widehat{\rho U_i} = \widehat{\rho}\tilde{U}_i; \qquad \tilde{U}_i = \frac{\widehat{\rho U_i}}{\widehat{\rho}}. \tag{2.24}$$

$\tilde{U}_i$ represents the density-weighted filtered velocity (also referred to as Favre-filtering). Further analysis of the filtered compressible momentum and energy equations reveals the complexity of the filtering procedure in the compressible case. This is due to the non-linearity of the basic variables [114], which makes a decomposition of the filtered variables inevitable. In [114], two different decomposition systems are presented. Each system results in different subgrid terms and as a result in different modelling strategies.

There are several approaches in order to model the residual stress tensor in Eq. (2.22). These approaches can be categorised into functional and structural modelling approaches [114]. While structural approaches aim at modelling the residual stress tensor τ_{ij}^R itself, regardless of the interaction between resolved and subgrid scales, functional models aim to account for the effects of the residual stress tensor on the resolved scales. These effects are the result of the gradient of τ_{ij}^R in Eq. (2.21).

Modelling the stress tensor is an active research area [124]. In this study, one of the simplest models to account for the energy dissipation of subgrid scales is utilised. The model introduces an additional dissipation term into the momentum equation:

$$\tau_{ij}^r = -2\nu_t \widehat{S}_{ij}, \tag{2.25}$$

where $\widehat{S}_{ij}$ is the filtered rate of strain:

$$\widehat{S}_{ij} = \frac{1}{2}\left(\frac{\partial \widehat{U}_i}{\partial x_j} + \frac{\partial \widehat{U}_j}{\partial x_i}\right). \tag{2.26}$$

This is the well-known model that was introduced by Smagorinsky [96]. The eddy viscosity ν_t can be written, using dimensional analysis [114], as:

$$\nu_t = \left(C_s\widehat{\Delta}\right)^2 \sqrt{2\widehat{S}_{ij}\widehat{S}_{ij}}, \tag{2.27}$$

where C_s is the Smagorinsky constant and $\widehat{\Delta}$ the length of the effective filter. The constant C_s can be analytically determined for decaying homogeneous isotropic turbulence. The Smagorinsky model assumes a continuous flow of energy across the energy spectrum. The production rate of energy is assumed to be equal to the energy transfer rate across the inertial subrange and the energy dissipation rate of the subgrid scales. This assumption of local equilibrium does not account for backscattering effects, i.e. inverse energy transfer from small scales to larger ones. However, these effects play a minor role for isotropic turbulence

due to the dominance of energy transfer from larger to small scales. Moreover, accounting for backscattering effects could introduce numerical instability due to the energy input into the resolved scales [114].

2.2.3 Reynolds-averaged Navier-Stokes equations (RANS)

Further saving of computational cost can be achieved by utilising the Reynolds-averaged Navier-Stokes equations (RANS). The method is based on Reynolds averaging, which was introduced by Osborne Reynolds. While LES is used to resolve the energetic part of the energy spectrum and model the dissipative scales, RANS based methods are utilised to model the whole energy spectrum without resolving any turbulent scales. Therefore, the complete energy spectrum has to be modelled. This sets higher demands on the turbulence model since it has to cover a large range of length scales. RANS methods can be used for flow configurations with statistical stationary flow behaviour in one or more spatial directions. They allow capturing main flow features without resolving any transient turbulent scales. This can be useful for applications where the user is only interested in the overall behaviour of the flow. The variation of the averaged flow field determines the spatial resolution required. Therefore, grids usually used for RANS simulations are coarser than those utilised for LES or DNS.

Similar to LES, RANS equations are based on splitting the flow variables into two parts. However, the splitted variables in RANS exhibit a major difference compared to those of LES. Consider a variable ϕ. In RANS, ϕ is splitted into:

$$\phi = \overline{\phi} + \phi', \tag{2.28}$$

where $\overline{\phi}$, assuming a statistically stationary flow, corresponds to the temporal mean of ϕ:

$$\overline{\phi}(\mathbf{x}) = \lim_{T\to\infty} \frac{1}{T} \int_0^\infty \phi(\mathbf{x},t)\,\mathrm{d}t. \tag{2.29}$$

The averaging in Eq. (2.29) corresponds to temporal averages. It is also possible to introduce spatial averages, in which the mean value $\overline{\phi}$ is a function of time. However, spatial averages are not often used for external aerodynamic applications.

It is worth mentioning that the variable splitting in Eq. (2.28) is rather suitable for statistically stationary processes. In some applications, e.g. periodic processes, the mean value of a variable is also time dependent. Mockett [76] proposes an alternative decomposition of ϕ for periodic processes. Further examples of processes, in which the mean value of a variable is time dependent, are the transient detachment of boundary layers on the rear spoiler of a vehicle. In some cases, such boundary layers are unstable and show detachment as well as reattachment in a random manner. This causes the time dependency of the mean flow variable in the wake of the vehicle. However, this time dependency cannot be classified as a

turbulent fluctuation. Hence, it is favourable to differentiate between turbulent fluctuations ϕ' and mean variable fluctuations. This can be done by suitably choosing the averaging time T to be large enough to filter out all turbulent fluctuations ($T > \tau_t$), but small enough to preserve transient, non turbulent flow features. This results in a so called unsteady RANS (URANS).

The mean value of the fluctuation ϕ' is equal to zero, which is a main difference between filtering and averaging. This means that multiple averaging of a variable ϕ is equivalent to single averaging of ϕ:

$$\overline{\overline{\phi}} = \overline{\phi}; \qquad \overline{\phi'} = 0. \tag{2.30}$$

Applying the averaging on the mass and momentum conservation equations (Eqs. (2.2)-(2.3)) and assuming a constant density (incompressible case) results in:

$$\frac{\partial \overline{U_i}}{\partial x_i} = 0, \tag{2.31}$$

$$\frac{\partial \overline{U_i}}{\partial t} + \frac{\partial \overline{U_j U_i}}{\partial x_j} = -\frac{1}{\rho}\frac{\partial \overline{p}}{\partial x_i} + \mu\left(\frac{\partial \overline{U_i}}{\partial x_j} + \frac{\partial \overline{U_j}}{\partial x_i}\right). \tag{2.32}$$

The continuity equation for the averaged variables is equivalent to the equation of the initial variable. Same applies to the momentum equation, except for the non-linear term $\overline{U_j U_i}$, since:

$$\overline{U_j U_i} = \overline{\left(\overline{U_j} + U_j'\right)\left(\overline{U_i} + U_i'\right)} = \overline{U_j}\,\overline{U_i} + \overline{U_j' U_i'}. \tag{2.33}$$

The last term in Eq. (2.33) can only be zero, if the two variables U_i' and U_j' are uncorrelated, which is rarely the case in turbulent flows. This term is called Reynolds stress tensor, which is unknown and has to be modelled or expressed in terms of the averaged variables. It is worth mentioning that the time derivative in Eq. (2.32) vanishes if the average of U_i is time independent. This is the case for statistical stationary flows. Similar to LES, Favre-averaging is usually utilised for compressible flows and the variable decomposition in Eq. (2.28) becomes:

$$\phi = \langle\phi\rangle + \phi''; \qquad \langle\phi\rangle = \frac{\overline{\rho\phi}}{\overline{\rho}}, \tag{2.34}$$

where $\langle\phi\rangle$ is the density-weighted average of ϕ.

A wide range of modelling techniques exists for modelling the unknown terms in RANS equations. Each model has its own mathematical and numerical complexity and provides a certain level of physical accuracy. An overview of these models is given in [76]. In this

work, a model based on the Boussinesq approximation [92] is used. It states that momentum exchange caused by turbulent fluctuation is analogous to the one caused by molecular viscosity. Thus, a new property scalar μ_t, called eddy viscosity, is introduced. The calculation of μ_t in this work is performed using the shear stress transport (SST) formulation of the $k-\omega$ two equations model. The model consists of solving two differential equations for the turbulent kinetic energy k and the specific dissipation rate ω, where the relation between these two variables and the eddy viscosity:

$$\mu_t = \rho \frac{k}{\omega}. \tag{2.35}$$

There exist several SST formulations for the $k-\omega$ model. In this work, the formulation of Menter [73] [1] is utilised. The models equations read:

$$\frac{\partial(\overline{\rho}k)}{\partial t} + \frac{\partial(\overline{\rho}\langle U_i\rangle k)}{\partial x_i} = P_k - \beta^\star \overline{\rho} k\omega + \frac{\partial}{\partial x_i}\left[(\mu + \sigma_k \mu_t)\frac{\partial k}{\partial x_i}\right], \tag{2.36}$$

$$\begin{aligned}\frac{\partial(\overline{\rho}\omega)}{\partial t} + \frac{\partial(\overline{\rho}\langle U_i\rangle \omega)}{\partial x_i} =& \alpha\overline{\rho}\frac{P_k}{\mu_t} - \beta\overline{\rho}\omega^2 + \frac{\partial}{\partial x_i}\left[(\mu + \sigma_\omega \mu_t)\frac{\partial \omega}{\partial x_i}\right] \\ &+ 2(1-F_1)\frac{\overline{\rho}\sigma_{\omega 2}}{\omega}\frac{\partial k}{\partial x_i}\frac{\partial \omega}{\partial x_i}.\end{aligned} \tag{2.37}$$

The production term P_k is defined as:

$$P_k = \min(P, 10\beta^\star \rho\omega k), \tag{2.38}$$

with

$$P = \mu_t\left(\frac{\partial\langle U_i\rangle}{\partial x_j} + \frac{\partial\langle U_j\rangle}{\partial x_i}\right)\frac{\partial\langle U_i\rangle}{\partial x_j} - \frac{2}{3}\frac{\partial\langle U_k\rangle}{\partial x_k}\left(\mu_t\frac{\partial\langle U_k\rangle}{\partial x_k} + \overline{\rho}k\right). \tag{2.39}$$

The blending function F_1 is defined as:

$$F_1 = \tanh\left\{\left[\min\left(\max\left(\frac{\sqrt{k}}{\beta^\star\omega d}, \frac{500\nu}{\omega d^2}\right), \frac{4\overline{\rho}\sigma_{\omega 2}k}{CD_{k\omega}d^2}\right)\right]^4\right\}, \tag{2.40}$$

in which d is the distance to the nearest wall. The function $CD_{k\omega}$ is defined as:

1 In [73], there was a typographical error which was subsequently corrected by the authors. More details about the error and its correction can be found on `https://turbmodels.larc.nasa.gov/sst.html`.

$$CD_{k\omega} = \max\left(\frac{2\overline{\rho}\sigma_{\omega 2}}{\omega}\frac{\partial k}{\partial x_i}\frac{\partial \omega}{\partial x_i}, 10^{-10}\right). \tag{2.41}$$

The model constants are calculated using the blending function F_1:

$$c = F_1 c_1 + (1 - F_1)\, c_2, \tag{2.42}$$

where c_1 represent the constant 1 and c_2 the constant 2. These constants are defined as:

$$\begin{gathered} \alpha_1 = 5/9; \qquad \alpha_2 = 0.44; \qquad \sigma_{\omega 1} = 0.5; \qquad \sigma_{\omega 2} = 0.856; \\ \sigma_{k1} = 0.85; \quad \sigma_{k2} = 1; \quad \beta_1 = 3/40; \quad \beta_2 = 0.0828; \quad \beta^\star = 0.09. \end{gathered} \tag{2.43}$$

The eddy viscosity is then calculated as:

$$\mu_t = \frac{\overline{\rho} a_1 k}{\max\left(a_1 \omega, \mathbf{S} F_2\right)}. \tag{2.44}$$

The blending function F_2 is defined as:

$$F_2 = \tanh\left\{\left[\max\left(\frac{2\sqrt{k}}{\beta^\star \omega d}, \frac{500\nu}{d^2\omega}\right)\right]^2\right\}. \tag{2.45}$$

The $\mathbf{S}$ term in Eq. (2.44) corresponds to the invariant measure of the strain rate $\mathbf{S} = \sqrt{2\left\langle S_{ij}\right\rangle\left\langle S_{ij}\right\rangle}$. Finally, the constant a_1 is equal to 0.31.

The SST model has originally been developed for aeronautics applications [73], but has made its way in almost every commercial CFD-code and is being used in several industrial disciplines.

2.2.4 Hybrid RANS-LES methods

In order to directly calculate aeroacoustic sources and acoustic wave propagation, transient numerical simulations are inevitable, as these are related to pressure fluctuations in time. For automotive applications, the side-mirror is one of the major noise sources and the computation of these sources requires the calculation of pressure fluctuations on the surface and in the wake of the mirror. While RANS based methods can be insufficient for resolving these sources, LES can be computationally expensive for resolving near wall turbulent structures. Hence, hybrid RANS-LES methods were introduced in order to circumvent the computational demands of LES near walls. Despite the differences between the filtering in LES and the averaging in RANS, both methods can be written in the same mathematical form, provided negligible commutation terms [16]. Chaouat [16] has done a spectral analysis to

develop a theoretical formalism to unify RANS and LES methods. His analysis showed the possibility to unify both methods from a physical point of view [16].

Several categorizations of hybrid RANS-LES methods can be found in the literature. In the following, these methods will be categorized according to [26], who categorized hybrid methods based on segregated and unified modelling. Methods based on segregated modelling are categorized by employing LES in a certain region of the computational domain, where high resolution of turbulence is required, while utilising RANS/URANS in regions where the statistical mean description of the flow field is sufficient. The interfaces between both regions are not continuous, which leads to a discontinuous solution at such interfaces. Since RANS does not deliver a resolved turbulent flow field, turbulence has to be reconstructed at RANS-LES interfaces [5, 26, 56, 83, 88] and coupling between both methods has to be performed.

The counterpart of segregated modelling is unified modelling [26]. Assuming negligible commutation terms, the equations involved in a LES approach have the same structure as the RANS equations. The main difference between both approaches lies in modelling the additional terms that emerge from filtering/averaging. However, as illustrated in the previous sections, modelling these additional terms in a LES is derived from RANS modelling. Hence, it is possible to solve the same system of equations with different modelling procedures in different regions of the computational domain. This allows a continuous transition between RANS and LES regions.

It is worth mentioning that there exists additional methods for resolving tubulence which are solely based on URANS, such as the scale adaptive simulation (SAS) which was proposed by Menter [71, 72, 74] and the partially averaged Navier-Stokes method (PANS) proposed by Girimaji [30,31]. These methods are not discussed in this work and the reader is referred to the aforementioned literature.

The method utilised in this work is based on a detached-eddy simulation (DES) method, which falls into the category of unified modelling. More details about its formulation is provided in the following paragraph.

Detached-eddy simulation (DES)

Detached-eddy simulation is a hybrid RANS-LES method which was initially developed for the Spalart-Allmaras RANS model [98]. The method is based on a modified RANS method, which switches between LES and RANS behaviour depending on the local grid size [94, 105]. The method was motivated by the fact that resolving turbulent eddies in near-wall regions using a LES is almost impossible in industrial applications due to the small size of such eddies. On the other hand, several RANS models have proven their capability in modelling boundary layer turbulence. Hence, one can utilise a method with RANS-like behaviour in boundary layers while resolving energetic turbulent structures in detached flow regions and, as a result, switching to a LES-like behaviour in such regions. The ”detached” eddies do have a wide spectral range. Hence, it is possible to resolve the energetic part of

these eddies with an affordable computational effort while modelling the small structures, which cannot be resolved using an eddy-viscosity approach.

Although DES was initially developed for the Spalart-Allmaras model, it is possible to extend any RANS model with an appropriately defined length scale in order to deliver a DES-behaviour [101]. An example of this length scale is the distance function present in the Spalart-Allmaras model or the turbulence length scale that can be obtained from the model's equations of Menter's SST-model. This length scale serves as an indicator whether RANS- or LES-behaviour should be performed by comparing the length scale with the local grid size.

Despite its popularity in industrial applications, the original formulation of DES does have imperfections. One of them is the existence of the so called "grey area", which corresponds to the transition area between RANS and LES modi [99]. The intention of a DES is to perform RANS in boundary layers and LES in regions with flow separation. However, the indicator for RANS-LES transition did cause an undesirable behaviour of the model. This behaviour is known as modelled stress depletion (MSD) [26, 99]. MSD denotes the undesired switching to an LES-behaviour inside the boundary layer, which is caused if the grid is fine enough to trigger the DES indicator but not fine enough to resolve local turbulent structures. Since the user cannot control the grid size near all walls of a complex geometry (e.g. flow past a vehicle), this problem occurs often in industrial applications and causes a high reduction of eddy viscosity in the boundary layer without any resolved stresses [99]. Furthermore, this behaviour could cause non-physical (grid induced) flow separation, which could have a large impact on the development of the flow, especially in aeroacoustic applications. Several suggestions were made in order to solve the MSD problem, one of them was to disable the DES limiter in pre-selected regions, where the boundary layer is expected to be attached. However, this transforms the DES method into a "zonal" method, which could be difficult to apply on complex geometries, especially if the user cannot predict the regions with attached boundary layers.

In order to preserve the "non-zonal" behaviour of DES and avoid undesired RANS-LES switching in the boundary layer at the same time, the so called Delayed Detached-Eddy Simulation (DDES) has been introduced by Spalart et al. [99]. The DDES method is based on redefining the indicator used for RANS-LES switching to be not only dependent on the local grid size, but also on flow variables, such as the eddy viscosity. This delivers a type of shielding in regions where the boundary layer is attached and the RANS-behaviour is preserved.

A more improved version of the DDES is the Improved Delayed Detached Eddy Simulation (IDDES) approach, which was first introduced by Shur et al. [95]. It consists of combining the DDES with the wall-modelled LES (WMLES) approach. Although both methods belong to the hybrid RANS-LES family, WMLES consists of modelling a thin region, which is much smaller than the boundary layer thickness, using RANS, while DES/DDES are designed to model the whole boundary layer using RANS. First attempts to utilise DES-models as a WMLES resulted in strong Logarithmic Layer Mismatch (LMM). This was

the motivation of improving DES/DDES in order to be applicable as a WMLES. Since numerical simulations in this work are all based on the IDDES approach, the detailes of the governing equations of the model are given in the next paragraph. For detailed information regarding the DES and DDES approaches, the reader is referred to [34, 73, 99, 101, 104].

Finally, regarding the applicability of DES/DDES/IDDES for aeroacoustic applications, it should be noted that the RANS-behaviour of DES in boundary layers suppresses the calculation of boundary layer noise sources. However, this work focuses on sound generation in automotive applications, in which sound waves are mainly generated by the interaction of turbulence with solid surfaces, such as a side-mirror. In such cases, boundary layer noise plays a subordinate role compared to the noise generated by the interaction of turbulence with solid surfaces. Hence, DES-based methods are considered appropriate for this type of aeroacoustic computation. This consideration has also already been addressed by different authors [75].

Improved Delayed DES (IDDES) formulation of Menter's SST model

In this work, an IDDES variant of Menter's SST $k-\omega$ model is utilised due to its superior behaviour regarding boundary layer separation [101, 104]. The SST variant of IDDES consists of modifying the length scale $l_{k-\omega}$ of the $k-\omega$ SST model to the IDDES length scale l_{IDDES}. According to [104], the only term that has to be modified is the dissipation term in Eq. (2.36):

$$D^k_{RANS} = \overline{\rho}\beta^\star k\omega = \overline{\rho}\frac{k^{3/2}}{l_{k-\omega}}, \tag{2.46}$$

by substituting $l_{k-\omega}$ with l_{IDDES}, which is defined as:

$$l_{IDDES} = \tilde{f}_d\,(1+f_e)\,l_{RANS} + \left(1-\tilde{f}_d\right) l_{LES}, \tag{2.47}$$

with

$$l_{RANS} = l_{k-\omega} = \frac{\sqrt{k}}{\beta^\star\omega}, \quad \text{and} \quad l_{LES} = C_{DES}\Delta. \tag{2.48}$$

C_{DES} corresponds to the DES constant. Since the SST model operates as a $k-\omega$ model near wall regions and as a $k-\varepsilon$ model far from the wall, the DES constant C_{DES} has to be calibrated for both modes. The overall DES constant is then constructed by blending both constants using Menter's blending function:

$$C_{DES} = (1-F_1)\,C^{k-\varepsilon}_{DES} + F_1 C^{k-\omega}_{DES}. \tag{2.49}$$

The calibration of the constants $C_{DES}^{k-\varepsilon}$ and $C_{DES}^{k-\omega}$ has been done by Gritskevich et al. [34] resulting in:

$$C_{DES}^{k-\varepsilon} = 0.61; \qquad C_{DES}^{k-\omega} = 0.78. \tag{2.50}$$

It is worth mentioning that the values presented in (2.50) can vary depending on the utilised discretisation schemes [101].

The Δ in Eq. (2.48) is the subgrid length scale and is defined for the IDDES approach as [34]:

$$\Delta = \min\left[C_w \max\left(d_w, h_{max}\right), h_{max}\right], \tag{2.51}$$

in which C_w is set equal to 0.15. Eq. (2.51) shows that the subgrid length scale does not only depend on the cell size (h_{max}), but also on the wall distance d_w. This is motivated by the fact that the optimal model constants of the underlying subgrid scale model (e.g. Smagorinsky model) for free turbulent flows differ from that of wall bounded flows [106]. The difference between the model constants for both flow regimes also depends on the choice of the subgrid length scale Δ. A more comprehensive description of Eq. (2.51) can be found in [106].

The delay function $\tilde{f}_d$ and the function f_e in Eq. (2.47) are defined as [106]:

$$\tilde{f}_d = \max\left(1 - f_d, f_b\right), \quad \text{and} \quad f_e = f_{e2} \max\left(\left(f_{e1} - 1\right), 0\right). \tag{2.52}$$

with

$$f_d = 1 - \tanh\left[\left(C_{d1}\tilde{r_d}\right)^{C_{d2}}\right], \qquad \tilde{r_d} = \frac{\nu_t}{\kappa^2 d_w^2 \sqrt{0.5\left(\mathbf{S}^2 + \Omega^2\right)}}, \tag{2.53}$$

where κ is the von Karman constant ($\kappa = 0.41$), $\mathbf{S}$ the strain rate invariant, and Ω the vorticity rate invariant. The constants in the delay function have been recalibrated by Gritskevich et al. [34] for the SST-IDDES formulation and are set to $C_{d1} = 20$ and $C_{d2} = 3$. Furthermore, the terms in the function f_e are defined as [34]:

$$f_{e1} = \begin{cases} 2e^{-11.09\alpha^2} & \text{if } \alpha \geq 0 \\ 2e^{-9\alpha^2} & \text{if } \alpha < 0 \end{cases}, \qquad \alpha = 0.25 - \frac{d_w}{h_{\max}}, \tag{2.54}$$

$$f_{e2} = 1 - \max\left(f_t, f_l\right); \qquad f_t = \tanh\left[\left(C_t^2 \tilde{r_d}\right)^3\right]; \qquad f_l = \tanh\left[\left(C_l^2 \tilde{r_l}\right)^{10}\right], \tag{2.55}$$

where $\tilde{r_l}$ is defined as:

$$\tilde{r}_l = \frac{\nu}{\kappa^2 d_w^2 \sqrt{0.5\left(\mathbf{S}^2 + \Omega^2\right)}}. \tag{2.56}$$

and the constants in Eq. (2.55) are set to [34]:

$$C_t = 1.87; \qquad C_l = 5. \tag{2.57}$$

2.2.5 Summarizing the system of equations

The equations presented below correspond to the ones utilised using the IDDES approach based on the $k-\omega$ SST model. The equations will be written in terms of Favre averaged variables. However, these same variables correspond to the filtered variables in the LES regime. This can be done when assuming commutation between filtering and derivation, which applies in this work.

The equation for mass conservation reads:

$$\frac{\partial \overline{\rho}}{\partial t} + \frac{\partial \left(\overline{\rho}\left\langle U_i \right\rangle\right)}{\partial x_i} = 0. \tag{2.58}$$

The equation for momentum conservation reads:

$$\frac{\partial \left(\overline{\rho}\langle U_i \rangle\right)}{\partial t} + \frac{\partial \left(\overline{\rho}\langle U_i \rangle \langle U_j \rangle\right)}{\partial x_j} = -\frac{\partial \Pi}{\partial x_i} + \frac{\partial \tau_{ij}^{\mathrm{tot}}}{\partial x_j}, \tag{2.59}$$

in which:

$$\Pi = \overline{p} + \frac{2}{3}\overline{\rho} k, \tag{2.60}$$

where k corresponds to the modelled turbulent kinetic energy. The total stress tensor is defined as:

$$\tau_{ij}^{\mathrm{tot}} = (\mu + \mu_t)\left[\frac{\partial \left\langle U_i \right\rangle}{\partial x_j} + \frac{\partial \left\langle U_j \right\rangle}{\partial x_i} - \frac{2}{3}\frac{\partial \left\langle U_k \right\rangle}{\partial x_k}\delta_{ij}\right]. \tag{2.61}$$

For the fully compressible approach, the energy equation reads:

$$\frac{\partial \left(\overline{\rho}\left\langle e_t \right\rangle\right)}{\partial t} + \frac{\partial \left(\overline{\rho}\left\langle U_j \right\rangle \left\langle e_t \right\rangle\right)}{\partial x_j} = -\frac{\partial}{\partial x_j}\left[\left\langle U_j \right\rangle \overline{\Pi} - k\frac{\partial \left\langle T \right\rangle}{\partial x_j} - c_p \frac{\mu_t}{\mathrm{Pr}_t}\frac{\left\langle T \right\rangle}{\partial x_j} + \tau_{ij}^{\mathrm{tot}}\right], \tag{2.62}$$

while for the isentropic approach the temperature is simply calculated using the isentropic relation in Eq. (2.16).

Using the $k-\omega$ SST-IDDES approach, two transport equations for k and ω are solved. These variables are then used to calculate the eddy viscosity μ_t, which closes the system of equations:

$$\frac{\partial\left(\overline{\rho}k\right)}{\partial t}+\frac{\partial\left(\overline{\rho}\left\langle U_i\right\rangle k\right)}{\partial x_i}=P_k-\beta^{\star}\overline{\rho}k\omega+\frac{\partial}{\partial x_i}\left[\left(\mu+\sigma_k\mu_t\right)\frac{\partial k}{\partial x_i}\right], \tag{2.63}$$

$$\begin{aligned}\frac{\partial\left(\overline{\rho}\omega\right)}{\partial t}+\frac{\partial\left(\overline{\rho}\left\langle U_i\right\rangle \omega\right)}{\partial x_i}=&\alpha\overline{\rho}\frac{P_k}{\mu_t}-\beta\overline{\rho}\omega^2+\frac{\partial}{\partial x_i}\left[\left(\mu+\sigma_\omega\mu_t\right)\frac{\partial\omega}{\partial x_i}\right]\\&+2\left(1-F_1\right)\frac{\overline{\rho}\sigma_{\omega 2}}{\omega}\frac{\partial k}{\partial x_i}\frac{\partial\omega}{\partial x_i},\end{aligned} \tag{2.64}$$

$$\mu_t=\overline{\rho}\frac{k}{\omega}. \tag{2.65}$$

Eqs. (2.58)-(2.65) have to be numerically solved. In this work, this is performed using a finite volume method, which is discussed in the next chapter.

2.3 Aeroacoustics

The system of differential equations presented in the previous section describes the dynamics of a fluid flow. This includes the hydrodynamic as well as acoustic pressure waves. Hence, the solution of the system of equation provides a description of noise generation and acoustic wave propagation along to the calculation of turbulence and hydrodynamic pressure fluctuations. However, solving the complete system of equations for both hydrodynamics and acoustics could be expensive for certain applications. This applies for the calculation of far-field noise due to the difference in the time and length scales between hydrodynamic and acoustic waves. Moreover, for applications in which the interaction between sound waves and fluid flow is weak, one can decouple acoustic computation from flow calculation. Methods based on calculating fluid flow and acoustic waves separately are known as hybrid methods. Since a hybrid method is utilised for comparison with DNC in parts of this study, a brief description of the corresponding equations is given in the following.

2.3.1 Lighthill equation

One of the earliest studies performed in order to understand the mechanism of sound generation and propagation was done by Sir James Lighthill [63, 64]. He derived an inhomogeneous wave equation for the density of the fluid. The derivation of the equation consists of rearranging the exact compressible mass and momentum conservation equations. The

results is an equation consisting of a typical wave operator on the left hand side and the sum of all non-linear and viscous terms on the right hand side, which can be interpreted as source terms in the wave equation:

$$\frac{\partial^2 \rho'}{\partial t^2} - c^2 \frac{\partial^2 \rho'}{\partial x_i^2} = \frac{\partial^2 T_{ij}}{\partial x_i x_j}, \text{ with } T_{ij} = \rho U_i U_j - \tau_{ij} + \delta_{ij}\left(p' - c^2 \rho'\right). \tag{2.66}$$

In Eq. (2.66), ρ' corresponds to density fluctuations and T_{ij} to the Lighthill stress tensor.

Since the inhomogeneous wave equation Eq. (2.66) corresponds to the exact Navier-Stokes equations, it is valid for the whole domain in which the mass and momentum conservation equations apply. It is worth mentioning that Eq. (2.66) does not include any approximation or linearisation, and is a solely rearrangement of the Navier-Stokes equations. An analytical solution for the inhomogeneous wave equation exists and can be written as:

$$\rho' = \frac{1}{4\pi c^2} \frac{\partial^2}{\partial x_i \partial x_j} \int_{-\infty}^{\infty} \frac{T_{ij}\left(\mathbf{y}, t - \frac{r}{c}\right)}{r} d^3\mathbf{y}, \tag{2.67}$$

where $\mathbf{y}$ corresponds to the position of the noise source and r to the distance between the source and the observer $\mathbf{x}$ and is defined as:

$$r = |\mathbf{x} - \mathbf{y}(\tau)|. \tag{2.68}$$

Note that the source position $y(\tau)$ is calculated at the time τ, which corresponds to the retarded time. The difference between the retarded time and observation time t corresponds to the time needed for a signal to travel between the source and the observer. Hence, the following relation applies:

$$t = \tau + \frac{r}{c}. \tag{2.69}$$

The solution in equation Eq. (2.67) is valid for unbounded domains and is invalid in the presence of solid bodies inside the domain. Hence, its usability is restricted to applications, in which noise is generated due to turbulence, such as jet noise. In the presence of solid boundaries, Eq. (2.66) is still valid in the fluid domain, provided appropriate boundary conditions are set on solid surfaces. Setting appropriate boundary conditions on solid walls results in the extended Lighthill formulation, which is discussed in the next section.

2.3.2 Ffowcs Williams-Hawkings (FWH) formulation

Since the Lighthill equation corresponds to the exact mass and momentum conservation equations, it is valid for the whole fluid domain. Even in the presence of solid boundaries, the Lighthill equation is still valid for every fluid particle if appropriate boundary conditions are set on the boundaries. Ffowcs-Williams and Hawkings [117] derived an equation that is valid for a domain in the presence of solid walls. By using the Heaviside function H, they were able to separate fluid from solid region. Thus, the derived equation is valid outside as well as inside solid boundaries. Moreover, their formulation is also valid for moving solid surfaces, for which H is a function of time and space. The derivation of the FWH-equation is similar to the derivation of the Lighthill equation. The mass and momentum conservation equations are multiplied by the Heaviside-function and the time-derivative of the former is subtracted from the divergence of the latter. This yields the FWH equation [12]:

$$\begin{aligned}\Box^2 p'(\mathbf{x},t) =& \frac{\overline{\partial}^2}{\partial x_i \partial x_j}\left[T_{ij} H(f)\right] \\ &- \frac{\partial}{\partial x_i}\left[\left(P_{ij} n_j + \rho u_i (u_n - v_n)\right)\delta(f)\right] \\ &+ \frac{\partial}{\partial t}\left[\left(\rho_\infty v_n + \rho (u_n - v_n)\right)\delta(f)\right].\end{aligned} \tag{2.70}$$

In Eq. (2.70), $\Box^2$ is the wave operator, p' the pressure perturbation, P_{ij} the compressive stress tensor, n_j the unit normal vector of the solid surface pointing into the fluid, u_n the velocity of the fluid in the direction normal to surface, v_n the velocity of the surface in the direction normal to the surface, and $\delta(f)$ the Dirac delta function. The function $f(\mathbf{x},t)$ describes the moving surface. Furthermore, the bar over the derivative operator on the right hand side of Eq. (2.70) corresponds to a generalized differentiation [12].

Based on Eq. (2.70), an integral FWH formulation was developed by Brentner et al. [12]. Using the notations of di Francescantonio [22]:

$$U_{i,\mathrm{FWH}} = \left(1 - \frac{\rho}{\rho_\infty}\right) v_i + \frac{\rho u_i}{\rho_\infty}, \tag{2.71}$$

$$L_{i,\mathrm{FWH}} = P_{ij} n_j + \rho u_i (u_n - v_n), \tag{2.72}$$

equation Eq. (2.70) can be rewritten as:

$$\Box^2 p'(\mathbf{x},t) = \frac{\partial^2}{\partial x_i \partial x_j}\left[T_{ij} H(f)\right] - \frac{\partial}{\partial x_i}\left[L_{i,\mathrm{FWH}}\delta(f)\right] + \frac{\partial}{\partial t}\left[\left(\rho_\infty U_{n,\mathrm{FWH}}\right)\delta(f)\right]. \tag{2.73}$$

The solution of Eq. (2.73) can be written as [11]:

$$p'(\mathbf{x},t) = p'_T(\mathbf{x},t) + p'_L(\mathbf{x},t) + p'_Q(\mathbf{x},t), \tag{2.74}$$

where

$$\begin{aligned} 4\pi p'_T(\mathbf{x},t) = &\oint_S \left[\frac{\rho_\infty \left(\dot{U}_{n,\mathrm{FWH}} + U_{\dot{n},\mathrm{FWH}} \right)}{r\left(1-M_r\right)^2} \right]_{\mathrm{ret}} dS \\ &+ \oint_S \left[\frac{\rho_\infty U_{n,\mathrm{FWH}} \left(r\dot{M}_r + c\left(M_r - M^2\right) \right)}{r^2\left(1-M_r\right)^3} \right]_{\mathrm{ret}} dS, \end{aligned} \tag{2.75}$$

and

$$\begin{aligned} 4\pi p'_L(\mathbf{x},t) = &\frac{1}{c} \oint_S \left[\frac{\dot{L}_{r,\mathrm{FWH}}}{r\left(1-M_r\right)^2} \right]_{\mathrm{ret}} dS + \oint_S \left[\frac{L_{r,\mathrm{FWH}} - L_{M,\mathrm{FWH}}}{r^2\left(1-M_r\right)^2} \right]_{\mathrm{ret}} dS \\ &+ \frac{1}{c} \oint_S \left[\frac{L_{r,\mathrm{FWH}} \left(r\dot{M}_r + c\left(M_r - M^2\right) \right)}{r^2\left(1-M_r\right)^3} \right]_{\mathrm{ret}} dS. \end{aligned} \tag{2.76}$$

The term $p'_Q(\mathbf{x},t)$ in Eq. (2.74) corresponds to the first term on the left hand side of Eq. (2.73) and can be written as a volume integral. In Eqs. (2.75) and (2.76), the dotted variables are the time derivatives of the corresponding variable. The subscripts r and n correspond to the dotted product of the vector with the unit normal in the radiation direction $\mathbf{r}/r$ or the surface normal $\mathbf{n}/n$ respectively [12]. Furthermore, M represents the Mach number calculated using the velocity $\mathbf{v}$ of the integration surface.

2.3.3 FWH formulation for stationary rigid surfaces

The solution in Eq. (2.74) is valid for every surface enclosing all sound sources. Furthermore, the surface can be permeable or impermeable, depending on its positioning. Besides, in case of moving solid bodies, the surface can move with the velocity $\mathbf{v}$. In this section, certain simplifications are made regarding the application of the FWH formulation for automotive applications.

The main noise source relative to a driver of a vehicle is the side-mirror. Considering the mirror as the emitter and the side-window as the receiver, the sound source is stationary relative to the receiver. Furthermore, wind noise is relevant for production cars travelling at Mach numbers ranging between 0.08 and and 0.2. Due to the low Mach number, the quadrupole term p'_Q in Eq. (2.74) can be neglected compared to the other two terms. Furthermore, the surface of the mirror can be taken as an integration surface, which delivers further simplifications regarding the thickness noise term p'_T and the loading noise term p'_L. Since the surface of the mirror is rigid, the fluid velocity on the mirrors surface is equal

to zero. Moreover, the velocity of the mirror relative to the receiver is also equal to zero. Finally, the normal pressure gradient on the surface of the mirror can be considered equal to zero, apart from Reynolds number effects in the boundary layer. Under these assumptions, Eq. (2.74) reduces to the following surface integral:

$$p'_r(t) = \frac{1}{4\pi} \oint_S \left[\left(\frac{1}{cr} \frac{\partial p'_s(t)}{\partial t} + \frac{p'_s(t)}{r^2} \right) \frac{\partial r}{\partial n} \right]_{\text{ret}} dS, \tag{2.77}$$

where p'_r corresponds to the pressure fluctuation at the receiver position and p'_s to the pressure fluctuation at the surface of the source, which is in this case the surface of the mirror.

3 Numerical methodology

The solution of the complete equations presented in section 2.1 can only be obtained numerically, due to their complexity. In this work, a finite volume method is utilised to solve these equations, which is integrated in the framework of the software package OpenFOAM. All the results presented in this work are calculated with the OpenFOAM version 2.3.1. The software package was initially developed by Henry Weller in the late 1980s and is based on C++ programming language. The source code of the software is freely accessible and partial differential equations (PDE) solvers can be modified and programmed by the user. A comprehensive description of the numerics as well as their implementation can be found in [45, 116]. A documentation of the physical modelling and numerics can be found in [1, 2].

In this chapter, the finite volume method is briefly presented. The fully compressible solver initially implemented by the developers of OpenFOAM is discussed and a comparison between the fully compressible and isentropic approaches regarding numerical noise is discussed. The pressure correction method utilised in this study is presented and an alternative Rhie-Chow interpolation is implemented and its effects on numerical noise generation is presented. Furthermore, a new acoustic damping model is integrated into the framework of the isentropic solver and its effect on acoustic as well as on hydrodynamic pressure waves is discussed. Finally, boundary conditions utilised in this work are presented.

3.1 Finite volume method

The conservation equation presented in the previous chapter offer a continuous description of the flow field variables. The finite volume method is a numerical method for the calculation of discrete distribution of variables. The computational domain is subdivided into a finite number of cells (finite volumes) using a numerical grid and each field variable is calculated in each numerical cell. The numerical grids can be categorized into structured and unstructured grid. While structured grids possess a regular connectivity and each cell in the computational domain is uniquely connected to all other cells, unstructured grids involves arbitrarily defined cells and each cell can only access the information of the cells in its immediate proximity. The discretization of complex geometries, such as a whole vehicle model, is almost impossible using structured grids. Hence, unstructured grids are utilised in this work.

The calculated values in each numerical cell correspond to the volume integral of the continuous variable distribution in each cell. Thus, the differential form of the conservation equations presented in the previous chapter have to be integrated across each volume. This results in the integral form of the conservation equations. The volume averaged values in each cell are then approximated using surface integrals on the surfaces of the cell. The surface integrals corresponds to fluxes that enter or leave each cell. Since each flux entering a

cell is equivalent to the flux leaving the neighbouring cell which shares the same face, the finite volume method is considered to be globally conservative, which is one of the main reasons of this method's success.

The following will demonstrate the integration of the generic transport equation [Eq. (2.1)] over a cell with the volume V as well as different discretisation techniques used for the approximation of different surface integrals.

3.1.1 Generic transport equation

The generic transport equation represents the general form of all conservation equations presented in the previous chapter. Each term in the equation describes a certain physical mechanism in a mathematical form, and has to be appropriately discretized. Eq. (2.1) represents the differential form of the transport equation. Integrating this equation over a cell of volume V results in

$$\int_V \underbrace{\frac{\partial(\rho\phi)}{\partial t}}_{\text{Transient term}} dV + \int_V \underbrace{\frac{\partial(\rho U_i\phi)}{\partial x_i}}_{\text{Advection term}} dV = \int_V \underbrace{\frac{\partial}{\partial x_i}\left(D\frac{\partial\phi}{\partial x_i}\right)}_{\text{Diffusion term}} dV + \int_V \underbrace{S_\phi}_{\text{Source term}} dV. \tag{3.1}$$

Using Gauss's theorem, the volume integral of the advection and diffusion terms can be written as surface integrals

$$\int_V \frac{\partial(\rho\phi)}{\partial t} dV + \oint_{\partial V} \rho U_i \phi dS_i = \oint_{\partial V} D\frac{\partial\phi}{\partial x_i} dS_i + \int_V S_\phi dV, \tag{3.2}$$

where S_i corresponds to the outward pointing unit normal vector of each cell face multiplied by the surface area of that face. Each volume and surface integral in Eq. (3.2) is then approximated separately. The approximations techniques are presented in the following sections.

3.1.2 Approximation of integrals

The following section will provide a brief description on how the integrals in Eq. (3.2) are approximated in a finite volume method.

Approximation of the transient term

The first volume integral on the left hand side of Eq. (3.2) is the integral of the volume transient term. Using the product rule and mass conservation equation (2.2), this integral can be written as

$$\int_V \frac{\partial(\rho\phi)}{\partial t} dV = \int_V \left(\rho \frac{\partial \phi}{\partial t} + \phi \frac{\partial \rho}{\partial t} \right) dV = \int_V \rho \frac{\partial \phi}{\partial t} dV - \int_V \phi \frac{\partial(\rho U_i)}{\partial x_i} dV \tag{3.3}$$

The first term on the right hand side of Eq. (3.3) can be approximated using the midpoint rule

$$\int_V \rho \frac{\partial \phi}{\partial t} dV = \rho \frac{\partial \phi}{\partial t} V_p \tag{3.4}$$

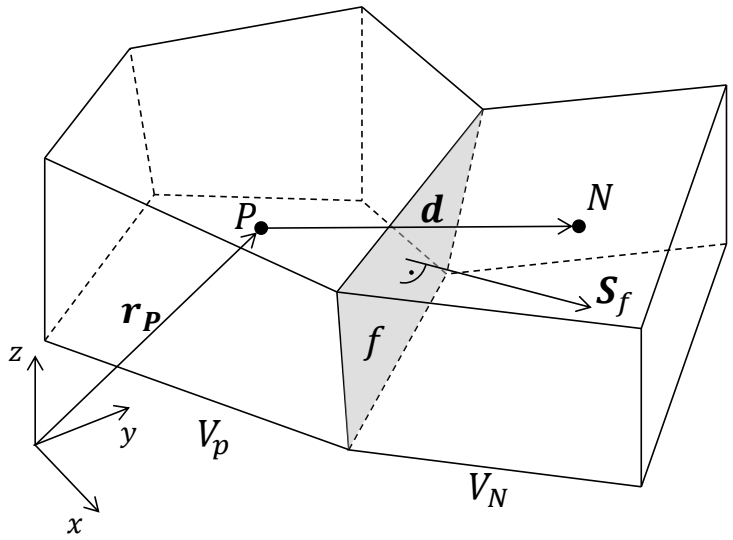

Figure 3.1: Schematic representation of two grid cells in a finite volume method. P represents the centroid of the cell, N the centroid of the neighbouring cell, f the face shared by both cells, d the vector connecting both cells centroids, and S_f the normal vector of the face f. V_p and V_N correspond to the volume of each cell.

Approximation of the advection term

The advection term in Eq. (3.2) consists of the surface integral

$$\oint_{\partial V} \rho U_i \phi dS_i \approx \sum_f [\rho U_i \phi]_f \delta S_{i,f}. \tag{3.5}$$

In Eq. (3.5), $\delta S_{i,f}$ corresponds to S_i of the face f and $[\cdot]_f$ denotes the value at the face center. The surface integral is approximated on each cell face via the midpoint rule, which corresponds to the value of the integrand at the face center multiplied by the face's surface area $|\delta S_{i,f}|$. The approximation of the surface integral using the midpoint rule is of second order [24].

Since the values at the face centres are known, they have to be approximated in terms of cell center values. Several schemes with different order of accuracy are available in OpenFOAM for approximating face values. The schemes utilised in this work will be presented in the next section.

Approximation of the diffusion term

The diffusion term in Eq. (3.2) involves the surface integral of the gradient of ϕ. This surface integral is approximated in a similar way as was done for the advection term, i.e. utilising the midpoint rule

$$\oint_{\partial V} D\frac{\partial \phi}{\partial x_i} dS_i \approx \sum_f \left[D\frac{\partial \phi}{\partial x_i}\right]_f \delta S_{i,f} = \sum_f [D]_f \left[\frac{\partial \phi}{\partial x_i}\right]_f \delta S_{i,f}. \tag{3.6}$$

The calculation of $[D]_f$ is done based on a linear interpolation in OpenFOAM

$$[D]_f = \delta_f [D]_P + \left(1-\delta_f\right)[D]_N, \tag{3.7}$$

where δ_f corresponds to the interpolation coefficient. For equidistant Cartesian cells, δ_f is equal to 0.5. $[D]_P$ and $[D]_N$ corresponds to the values of the diffusion coefficients at the centres of cells P and N. The approximation in Eq. (3.7) is of second order.

The gradients on the right hand side of Eq. (3.6) corresponds to the surface normal gradients of ϕ at the face centres. Since these gradients are unknown, they have to be approximated using values at cell centres. Similar to the approximation of the diffusion term D, surface normal gradients are approximated using linear interpolation:

$$\left[\frac{\partial \phi}{\partial x_i}\delta S_i\right]_f = \left[\frac{\partial \phi}{\partial x_i}\right]_f \delta S_{i,f} \approx \frac{([\phi]_N - [\phi]_P)}{|d|}|\delta S_{i,f}|. \tag{3.8}$$

This approximation is second order accurate for cells, whose non-orthogonality is equal to zero. The non-orthogonality corresponds to the angle between the vector connecting cell centres and the face normal vector. Although most of the cells involved in this work are orthogonal, non-orthogonalities emerge at, for example, refinement interfaces. This is illustrated in Figure 3.2, where α denotes the non-orthogonality between cells P and N. In this case, the calculation of the surface normal gradient in Eq. (3.8) is split into two parts [45]:

$$\left[\frac{\partial \phi}{\partial x_i}\right] \delta S_{i,f} = \underbrace{\left[\frac{\partial \phi}{\partial x_i}\right]_f n_{1i}}_{\text{implicit}} + \underbrace{\left[\frac{\partial \phi}{\partial x_i}\right]_f n_{2i}}_{\text{explicit}}, \tag{3.9}$$

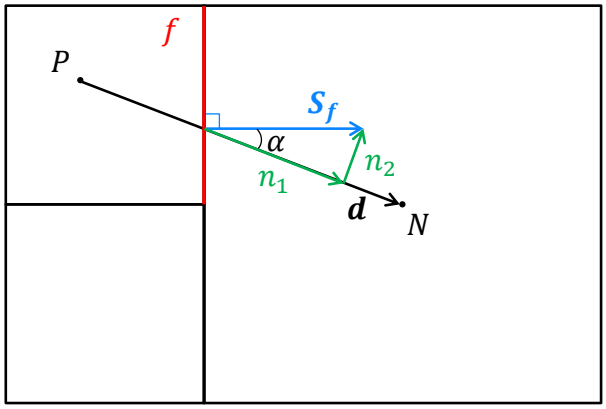

Figure 3.2: Two-dimensional refinement interface representing non-orthogonal cells. α represents the non-orthogonality.

where n_1 is the component of the surface normal vector S_f in the direction of the vector connecting the cell centers P and N, while n_2 is its complementary. The terms on the right hand side of Eq. (3.9) are then handled separately. The first term is calculated implicitly. Using linear interpolation for the face gradients, the implicit surface normal gradient is then equal to:

$$\left[\frac{\partial \phi}{\partial x_i}\right]_f n_{1i} \approx \frac{([\phi]_N - [\phi]_P)}{|d|} |n_{1i}|. \tag{3.10}$$

ϕ_P and ϕ_N in Eq. (3.10) corresponds to the unknown values in the cell centres (current time step). The explicit correction term in Eq. (3.9) is approximated using old values of ϕ at cell centres. Similar to the implicit term, the gradient in the explicit correction is approximated using linear interpolation of cell centre values:

$$\left[\frac{\partial \phi}{\partial x_i}\right]_f n_{2i} \approx \frac{([\phi]_N - [\phi]_P)}{|d|} |n_{2i}|. \tag{3.11}$$

For the sake of simplicity, the indices corresponding to the time steps are omitted.

Unlike the implicit part in Eq. (3.9), the explicit part is unbounded, which can lead to the divergence of the solution. For this reason, a limited version of the explicit correction is available in OpenFOAM. Hereby, the explicit part in Eq. (3.9) is clipped in order to ensure that its value stays smaller than the implicit part. More details regarding the limiter function can be found in [45].

Besides limiting the explicit part in the calculation of the surface normal gradient, a limiter can be introduced for the calculation of the face-gradients [e.g. Eqs. (3.10)-(3.11)]. Experience has shown that using a limiter for the calculation of the gradients in the transport equations of the turbulence quantities is beneficial. In this study, this corresponds to the gradients of k and ω. In this work, the gradients of the aforementioned quantities are limited using the cell-limited scheme. This scheme ensures that the face values of the quantity ϕ, which is extrapolated using the gradient at the cell centroid P, is limited between the values at the cell centroids P and N.

Approximation of source terms

The source term S_ϕ in Eq. (3.1) can be a function of space, time and the variable ϕ as well. Thus, the source term is first linearised:

$$S_\phi = S_p\phi + S_u. \tag{3.12}$$

The volume integral of S_ϕ can then be written as:

$$\int_V S_\phi dV = \int_V (S_p\phi + S_u)\, dV \approx [S_p\phi]_P V_P + [S_u]_P V_P. \tag{3.13}$$

The approximation in Eq. (3.13) is of second order accuracy. The decomposition in Eq. (3.12) should be done in such a way that S_p is negative. This strengthens the diagonal dominance of the coefficients matrix. In cases where S_p is positive, it is more practical to treat it explicitly and include it to the source S_u on the right hand side of the linear system of equations.

3.1.3 Linear system of equations

The approximations of volume and surface integrals in Eq. (3.1) leads to a linear system of equations of the form [45]:

$$a_P\phi_P^n + \sum_N a_N\phi_N^n = R_p, \tag{3.14}$$

where a_P represents the central coefficients of the matrix. The coefficients a_N correspond to the ones of the neighbouring control volumes surround the cell with the index P. Lastly, R_p corresponds to the source vector.

The system of equations (3.14) can be solved directly using a linear solver. However, the number of operations required by the solver in order to reach a certain tolerance increases

with the number of unknowns squared [45]. Moreover, the system of equations in industrial applications is usually so large, that the memory required by the direct solver is not affordable.

The second method for solving the system of equations (3.14) is using an iterative method. Herein, an initial guess of the solution is used and the solution vector ϕ is iteratively improved until the difference between the exact solution and the approximated one reaches a pre-defined tolerance. Iterative methods are substantially more efficient than direct ones when calculating large system of equations. However, they do have some restrictions regarding the properties of the coefficients matrix. One of these properties is the diagonal dominance, which is required in order to guarantee convergence. A matrix is said to be diagonal dominant when:

$$|a_{ii}| \geq \sum_{j \neq i} |a_{ij}| \qquad \text{for all } i. \tag{3.15}$$

The diagonal dominance of the coefficients matrix is influenced by the utilised discretisation schemes. It has been shown by [45] that the diagonal dominance can only be improved by the discretisation of the transient and the linear part of the source term in the transport equation. Further enhancement of the diagonal dominance can be achieved by using under-relaxation technique, which is discussed in the next section.

3.1.4 Under-relaxation

In order to increase the diagonal dominance of the coefficient matrix in Eq. (3.14), and hence improving stability and convergence rate of the solution, under-relaxation can be applied to the system of equation. The original system in (3.14) is then modified to:

$$a_P \phi_P^n + \alpha\phi \sum_N a_N \phi_N^n = \alpha_\phi R_p + \left(1 - \alpha_\phi\right) \phi_P^*, \tag{3.16}$$

where α_ϕ corresponds to the relaxation factor for the variable ϕ and takes a value between 0 and 1. ϕ^* corresponds to the solution of ϕ from the previous iteration. Although under-relaxation of primarily used for steady-state problems, it can improve convergence of transient problems. Depending on the pressure-correction algorithm utilised for the iterative solution, under-relaxation can be applied at different stages of the solution process. Analysing the system in (3.16) shows that under-relaxation causes the variable ϕ to change partially through the iteration process. The rate of change of ϕ is controlled by the relaxation factor α_ϕ. However, in order to maintain a physical plausible development of ϕ with time, the relaxation factor has to be set to 1 for the final calculation of ϕ for each time-step. Thus, under-relaxation can be utilised for the iterative calculation of ϕ inside one time-step, but has to be omitted $\left(\alpha_\phi = 1\right)$ for the final calculation of ϕ in the last iteration inside a time-step. The description of different iteration steps inside a time-step will be discussed in the next section.

The values of the relaxation factor α_ϕ depends on the variable ϕ. When solving a set of conservation equations, the relaxation factor of a variable can depend on the relaxation factors of other variables. For instance, the relaxation factor α_U for the velocity U depends on the amount of under-relaxation factor α_p of the pressure [90]. However, there are typical values for the under-relaxation factors for each variable. For the velocity U, typical values of α_U are between 0.6 and 0.8, while typical values for α_p are between 0.2 and 0.4 [90].

3.2 Discretisation schemes

In the previous section, different schemes for discretising the transient and diffusion terms have been presented. Due to its non-linear nature, the discretisation of the advection term can be challenging and the solution is highly dependent on the numerical scheme used for discretising it. The advection term is present in the conservation equations of momentum, energy, turbulent kinetic energy k and specific dissipation ω. As shown in Eq. (3.5), the discretised advection term can be written as a sum of face values. For simplicity, only one face f is considered in the following and the discretised advection term has the form:

$$[\rho U_i \phi \delta S_i]_f \,. \tag{3.17}$$

The term $\rho U_i \delta S_i$ corresponds to the mass flux $\dot{m}_f$ through the face f. This term is calculated explicitly using values from previous time steps. Thus, the only variable that has to be approximated is ϕ_f. The following illustrates different discretisation schemes used in this work in order to approximate ϕ_f.

Upwind differencing scheme (UDS)

The UDS is the simplest way to approximate the value ϕ_f. The face value ϕ_f is adopted from the upstream cell and is thus dependent on the flow direction. It can be written as:

$$\phi_{f,\mathrm{UDS}} = \begin{cases} \phi_p & \text{if } \dot{m}_f > 0 \\ \phi_N & \text{if } \dot{m}_f < 0 \end{cases}. \tag{3.18}$$

A schematic representation of UDS is shown in Figure 3.3. The UDS is highly stable due to its unconditional boundedness. The boundedness results from the positive coefficients of the discretised equation, which favours the diagonal dominance of the coefficients matrix. However, a Taylor expansion of the schemes shows first order accuracy in terms of the truncation error. Moreover, the scheme causes high diffusion of the solution, which increases with decreasing resolution (false diffusion). Thus, UDS is usually utilised when other, more accurate schemes, are unstable. This applies for example in cases where the Péclet number, which correponds to the ratio of advective to diffusive transport rate, is greater than 2. In such case, schemes with higher accuracy, such as central differencing schemes, can fail to converge. In this work, the UDS is utilised for discretising the advection term in the k and ω

transport equations. Experience have shown that using higher-order schemes to discretise these terms can cause high non-physical oscillations in the solution. Moreover, diffusion in the solution of k and ω has a minor effect on the diffusion of the velocity and pressure fields.

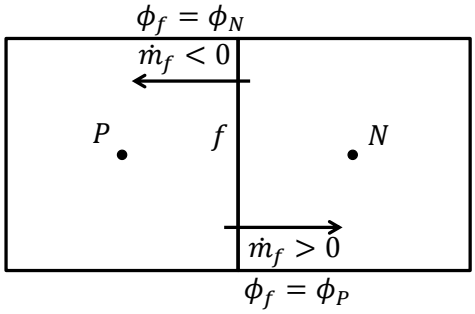

Figure 3.3: Approximation of face value ϕ_f using UDS.

Second order upwind differencing scheme (LUDS)

The second order upwind differencing scheme [115], also known as linear upwind differencing scheme (LUDS), is based on UDS with an additional correction based on the gradient at the upstream cell centre:

$$\phi_f = \begin{cases} \phi_P + \mathbf{Pf}\left[\dfrac{\partial \phi}{\partial x_i}\right]_P & \text{if } \dot{m}_f > 0 \\ \\ \phi_N + \mathbf{Nf}\left[\dfrac{\partial \phi}{\partial x_i}\right]_N & \text{if } \dot{m}_f < 0 \end{cases}, \tag{3.19}$$

where **Pf** and **Nf** are the vectors connecting P and N to the centre of face f respectively. The gradient-based correction terms in Eq. (3.19) are treated explicitly. The LUDS is second order accurate in terms of truncation error. However, the boundedness of UDS is lost when adding the gradient based explicit correction. The diffusive character of LUDS is lower than that of UDS and the accuracy of the solution is generally higher.

Central differencing scheme (CDS)

CDS is based on approximating the face value ϕ_f by linear interpolation using the values in centres of the cells sharing the face f. It can be expressed as:

$$\phi_f = \delta_f \phi_N + \left(1 - \delta_f\right) \phi_P; \qquad \delta_f = \frac{\overline{fP}}{\overline{fP} + \overline{fN}}. \tag{3.20}$$

Figure 3.4 shows a schematic representation of CDS.

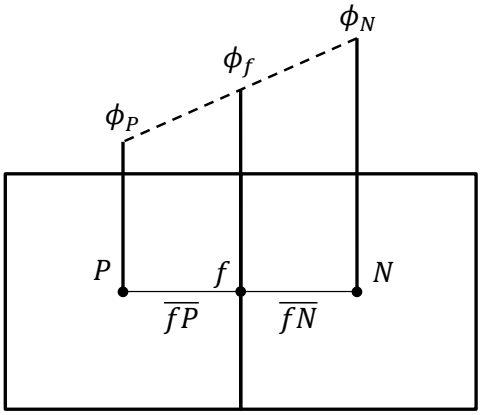

Figure 3.4: Approximation of face value ϕ_f using CDS.

The scheme is second order accurate in terms of truncation error. However, unlike UDS, CDS is unbounded and non-physical oscillations are typical when using the scheme for high Reynolds number flows. In general, CDS is known to be stable for Péclet numbers below 2, which is rarely the case in engineering applications. Hence, CDS is rarely used directly in such applications. However, there exists different stabilisation techniques that serve to make CDS applicable. One of them is the deferred correction procedure, which is presented below.

Deferred correction approach

The deferred correction approach was first introduced by Kholsa et al. [50] for a finite difference method. The aim of this approach is to combine the stability of upwind differencing with the accuracy of low dissipative schemes, which can be unstable for high Reynolds number flows. Herein, the face value ϕ_f is approximated using a low-order scheme (e.g UDS) and an explicit correction containing the approximation of ϕ_f using a high-order scheme (e.g. CDS) is added:

$$\phi_f^n = \phi_{f,\mathrm{UDS}}^n + \left(\phi_{f,\mathrm{CDS}}^{n-1} - \phi_{f,\mathrm{UDS}}^{n-1}\right), \tag{3.21}$$

where n and $n-1$ correspond to the current and previous time steps respectively. This way, the diagonal dominance is preserved since the matrix coefficients are determined by the implicit term approximated with UDS, while the explicit correction term is added to the source term and, hence, does not affect the matrix coefficients. The accuracy of the approximation in Eq. (3.21) is of second order and the iterative solution of ϕ leads to a result that approaches an approximation done by a pure CDS, but with considerable increased stability. Note that any two schemes can be combined using the deferred correction approach. In this work, a deferred correction scheme combining UDS as a low-order scheme and CDS as a high-order scheme is implemented and is therefore denoted by CDSdC.

Hybrid schemes

The deferred correction schemes does provide stability with acceptable accuracy. However, the stability of the CDSdC can deteriorate when approximating face values of cells with bad quality. Such cells are characterised by a non-orthogonality and high values of skewness. Such cell are inevitable when meshing complex geometries, such as a vehicle. In this case, the CDSdC scheme is not able to provide good convergence and spurious waves can be generated when applying this scheme on bad-quality cells.

Hybrid discretisation schemes provide a solution for this problem. They combine different schemes so that a high dissipative stable scheme is used to approximate values in bad-quality cells, while a low dissipative scheme is used in the domain where stability is not an issue. The following presents different blending strategies used in this study.

Fixed blending scheme The simplest blending technique is a linear combination between two different discretisation schemes. The face value of a variable ϕ is then approximated as:

$$\phi_f = \sigma_{\text{fix}} \phi_{HD} + (1 - \sigma_{\text{fix}})\, \phi_{LD}. \tag{3.22}$$

The blending factor σ_{fix} is a constant user-defined factor that determines the proportion of each scheme. In Eq. (3.22), *HD* denotes high dissipative and *LD* low dissipative schemes.

Local blending scheme Instead of choosing a constant blending factor, the user can define a field σ_{loc}, which can be a function of x_i. In regions of interest (e.g. wake of a side-mirror), a low dissipative scheme is required. Therein, σ_{loc} is set to zero. Outside the region of interest, a stable but more dissipative scheme can be utilised, as long as it does not affect the flow behaviour in the region of interest. Depending on the amount of numerical dissipation needed, σ_{loc} is set to a value between zero and one in this region. The approximation of face values is identical to the one in Eq. (3.22).

DES hybrid scheme Travin et al. [104] introduced a hybrid blending approach for DES, whose aim is to utilise a low dissipative scheme in LES-regions where the flow has a rotational nature, while a more dissipative stable scheme is utilised in the RANS-region, in which the flow has an irrotational nature and for which the numerical grid is usually coarse. The smooth transition between both schemes is achieved using a blending function σ_{Hyb}, which is a function of space and time. The blending function contains information about different flow quantities, so that it adapts to local flow. It is based on the turbulence length scale l_t, the integral length and velocity scales, and the strain and vorticity rate invariants $\mathbf{S}$ and Ω. The DES hybrid scheme implemented is this work is based on the blending function proposed by Spalart et al. [97]:

$$
\begin{aligned}
\sigma_{\text{Hyb}} &= \max\left[\sigma_{\max}\tanh\left(A^{C_{H1}}\right),\sigma_{\min}\right],\\
A &= C_{H2}\max\left[\frac{C_{DES}\Delta}{\max\left(l_t g, 10^{-15} l_{ref}\right)} - 0.5, 0\right], \quad l_t = \sqrt{\frac{\nu+\nu_t}{C_\mu^{3/2}K}},\\
K &= \max\left[\sqrt{\frac{\mathbf{S}^2+\Omega^2}{2}}, \frac{0.1}{\tau_0}\right], \quad g = \tanh\left(B^4\right),\\
B &= C_{H3}\Omega\frac{\max\left(\mathbf{S},\Omega\right)}{\max\left[\frac{\mathbf{S}^2+\Omega^2}{2}, \Omega_{\min}^2\right]}, \quad C_{H1}=3, \quad C_{H2}=1, \quad C_{H3}=2.
\end{aligned}
\tag{3.23}
$$

The face values are then approximated as:

$$
\phi_f = \sigma_{\text{Hyb}}\phi_{HD} + \left(1-\sigma_{\text{Hyb}}\right)\phi_{LD}. \tag{3.24}
$$

In this work, LUDS is chosen as a high dissipative and CDSdC as a low dissipative scheme.

The bending factor σ_{Hyb} is limited between $\sigma_{\min}$ and $\sigma_{\max}$. These values determine the amount of central differencing and the amount of dissipation in each of the LES- and RANS-regions. For instance, a $\sigma_{\max}=0.5$ and $\sigma_{\min}=0$ results in a pure low dissipative scheme in LES regions and a blended scheme in RANS regions containing 50% low dissipative scheme and 50% high dissipative scheme.

In the publication of Spalart et al. [97], the limiter $\Omega_{\min}=10^{-3}/\tau_0$, where $\tau_0 = l_{ref}/U_{ref}$. The reference length l_{ref} and the reference velocity U_{ref} are defined by the user and are application dependent. In this work, the implemented limiter $\Omega_{\min}$ can also be varied by the user. The value of 10^{-3} leads to undesired switching between $\sigma_{\min}$ and $\sigma_{\max}$, which results in the generation of spurious noise. The influence of different $\Omega_{\min}$ values on the resulting hybrid blending factor is presented in chapter 5.

In the rest of this work, the DES hybrid blending scheme is denoted by the acronym DESHyb.

3.3 Pressure-correction methods

The coupled conservation equations that describe flow variables can be solved either directly or using an iterative method. A direct solution of the system of equations is accompanied with high memory requirements related to the storage of the matrix a_{ij} [Eq. (3.14)], and high computational cost related to the inversion of the matrix, especially for the calculation of complex geometries with high number of grid cells. In this work, the system of equations is solved using an iterative method. The solver utilised in this study is a pressure-based solver. This family of solvers was originally developed for incompressible flows. Since the flow configurations in this study involve low Mach number flows ($Ma < 0.3$), pressure-based

solvers are considered to be suitable for this kind of problems. Furthermore, it is worth mentioning that the finite volume method implemented in OpenFOAM is based on collocated variable arrangement. This means that the velocity components as well as pressure values are calculated and stored at cell centres, unlike the staggered variable arrangement, in which velocity components and pressure values are calculated and stored at different locations (e.g. velocity components at cell faces and pressure values at cell centres). This importance of the variable arrangement will be discussed later in this section.

The conservation equations presented in chapter 2 have the form of the generic transport equation (Eq. (3.1)), except for some parts. For instance, the pressure gradient in the momentum equation does not have an analog in the generic transport equation. It can be categorized as a source term. However, there is a connection between the pressure and the continuity equation. Moreover, the conservation equations do not contain an explicit equation for the calculation of the pressure. The continuity equation serves as a kind of boundary condition rather than an explicit transport equation for the density or pressure. Hence, the calculation of the pressure does constitute a complication. There exist different methods for the calculation of the pressure, such as explicit and implicit time advance method, fractional step methods, artificial compressibility methods, and pressure-correction methods. The approach utilised in this work is based on the latter. The following presents a brief description of different pressure-corrections methods used in this work.

SIMPLE algorithm

The SIMPLE (**S**emi-**I**mplicit **M**ethod for **P**ressure-**L**inked **E**quations) was developed by Patankar and Spalding [81] in 1972 for incompressible and weak-compressible flows. The algorithm is based on solving a pressure equation in order to enforce mass conservation. It consists of an iterative solution algorithm, in which velocity and pressure values are successively corrected during multiple iterations, until the velocity field fulfils the continuity equation. In order to illustrate the iterative procedure, consider the semi-discretised momentum equation:

$$a_P U_{i,P} = H(U_i) - \frac{\partial p}{\partial x_i}. \tag{3.25}$$

Eq. (3.25) corresponds to a semi-discretised form of the momentum equation, since the pressure gradient is not yet discretised. It is assumed that an implicit time method is utilised for solving the equation. Hence, $a_P U_{i,P}$ and $\partial p/\partial x_i$ are unknown, since they corresponds to values of the current time-step (n). The term $H(U_i)$ is equal to the sum of the part corresponding to the matrix coefficients of neighbouring cells and the source term resulting from time discretisation of the transient term in the momentum equation:

$$H(U_i) = -\sum_N a_N U_{i,N} + \frac{U_i^{n-1}}{\Delta t}, \tag{3.26}$$

where $n-1$ corresponds to the previous time-step and Δt is the time-step size.

In order to illustrate the basic idea of the SIMPLE algorithm, the following is restricted to the incompressible case (constant density). The discretised incompressible continuity equation reads:

$$\sum_f [U_i]_f n_{i,f} \delta S_f = 0. \tag{3.27}$$

Reformulating Eq. (3.25) for $U_{i,P}$:

$$U_{i,P} = \frac{H(U_i)}{a_P} - \frac{1}{a_P}\frac{\partial p}{\partial x_i}, \tag{3.28}$$

and using Eq. (3.28) in order to express the face values $[U_i]_f$:

$$[U_i]_f = \left[\frac{H(U_i)}{a_P}\right]_f - \left[\frac{1}{a_P}\frac{\partial p}{\partial x_i}\right]_f, \tag{3.29}$$

and finally substituting Eq. (3.29) into the discretised continuity equation (3.27) results in the pressure equation:

$$\frac{\partial}{\partial x_i}\left(\frac{1}{a_P}\frac{\partial p}{\partial x_i}\right) = \frac{\partial}{\partial x_i}\left(\frac{H(U_i)}{a_P}\right). \tag{3.30}$$

The SIMPLE algorithm involves solving Eqs. (3.25) and (3.30) iteratively. The first step in the algorithm involves calculating an intermediate velocity using the values from the latest iteration. When solving the transient conservation equation, the iterative algorithm has to be performed in every time-step until convergence is reached. In the first iteration of a time step, the intermediate velocity is calculated using values from the last iteration of the preceding time-step. The intermediate velocity does not fulfil the continuity equation. Subsequently, the pressure is calculated using the pressure equation. Therein, the values of the intermediate velocity are substituted. The calculated pressure is then used to correct the mass fluxes across the faces of each cell and the velocity field is updated by solving Eq. (3.25) with the new pressure values. These step are repeated until convergence is reached. A converged solution represents the solution of one time-step in a transient simulation, or the final solution in a steady state simulation.

There exists different methods to include the calculation of the rest of independent variables, such as the temperature and turbulence quantities. In this study, the energy equation (or the isentropic relation in case of low-Mach number solver) is solved at the end of every SIMPLE iteration. Turbulence quantities can be updated every SIMPLE iteration or after the last SIMPLE iteration inside a time-step. The latter approach is used in this work in order to save computational time. Furthermore, the calculation of the test cases in this work exhibit

small time-steps, so that updating the turbulence quantities after every SIMPLE iteration does not result in a noticeable improvement of the accuracy in the turbulence fields.

It is worth mentioning that the SIMPLE algorithm is most suitable for steady-state calculations. The algorithm takes advantage of the under-relaxation of velocity and pressure in order to preserve stability. Furthermore, during the iterative procedure, there is no need to calculate the exact pressure field after each iteration. The main challenge in a SIMPLE algorithm is the treatment of the non-linearity in the momentum equation [45, 46].

PISO algorithm

The PISO (**P**ressure-**I**mplicit with **S**plitting of **O**perators) is a pressure correction approach which was developed by Issa [43] in 1986 for the calculation of transient flows. Similar to the SIMPLE algorithm, an iterative approach is used to calculate a velocity field that fulfils the continuity equation. However, the PISO algorithm calculates the momentum equation (3.25) only once at the beginning of each time-step. This is analogous to one SIMPLE iteration. However, unlike the SIMPLE approach, the pressure equation is calculated multiple times. This can be done due to the small time-step size required by the PISO algorithm, which results in the dominance of the linear pressure-velocity coupling over the non-linearity of the advection term in the momentum equation [45]. After each calculation of the pressure equation, the updated pressure is used to calculate a corrected velocity field using Eq. (3.28). Note that the difference between solving Eq. (3.25) and Eq. (3.28) is that the matrix coefficients in the latter are not updated after each iteration. After correcting the velocity field, the pressure equation is solved again with the updated velocity field. This loop is performed until the velocity-pressure coupling converges inside a time-step.

Unlike steady-state flows, the time-step size in transient flows is also limited by the physical behaviour of the flow. Under-relaxation is also limited within each time-step, since time accurate results are required at the end of each time-step. Moreover, the discretised momentum equation is solved only once within a time-step and the calculated values are used for a series of pressure correction steps. This leads to a limitation of the time-step size, which is related to the Courant number $Co = U\Delta t/\Delta x$.

PIMPLE algorithm

The PIMPLE algorithm is a combination of both SIMPLE and PISO algorithms. In each time-step, a series of SIMPLE iterations are performed. Inside each SIMPLE iteration, a the pressure equation is solved more than once and the pressure and mass fluxes are corrected according to the PISO algorithm. This way, the advantage of the PISO algorithm for transient simulations is combined with that of the SIMPLE algorithm regarding the ability to choose large time-step sizes. The Courant number stability limit is less pronounced in the PIMPLE algorithm and under-relaxation is possible (except for the last SIMPLE iteration within a time-step). Figure 3.5 shows the basic steps of the PIMPLE algorithm used for all simulations in this work.

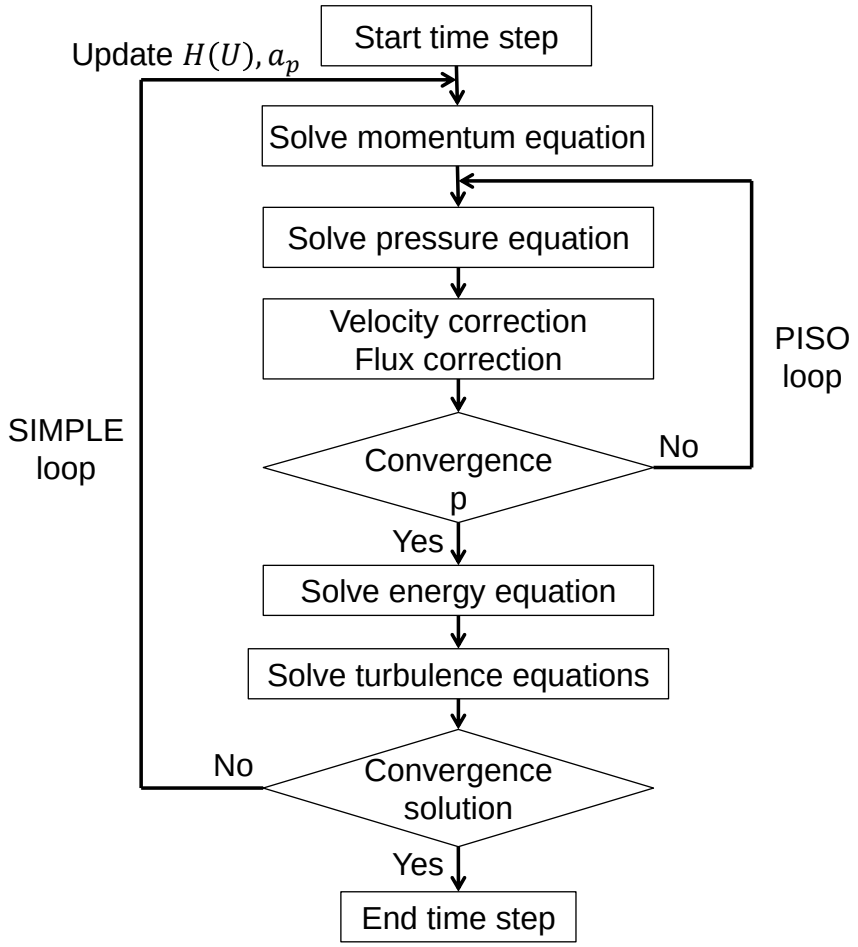

Figure 3.5: Basic steps performed during a time step using the PIMPLE algorithm.

The number of iterations inside a PISO/SIMPLE loop is pre-defined by the user. The loop ends either when a user-defined tolerance is reached or when the pre-defined number of iterations is reached before reaching convergence.

Pressure-velocity coupling

Solving the conservation equations using the above discussed algorithms based on collocated variable arrangement could cause the emergence of non-physical oscillations in the solution. This is the case when discretising the pressure term in the momentum equation as well as the velocity using central differencing schemes [86]. One possibility to avoid such oscillations is the use of methods based on staggered variable arrangement. However, a more effective method using collocated variable arrangement has been developed by Rhie & Chow [86], which is known as the ”Rhie & Chow interpolation”.

In this study, a generalised from of the Rhie & Chow interpolation, which was developed by Knacke [51], is utilised. The approximation of velocity face values is corrected using the following correction terms:

$$U_{i,f} \approx [U_i]_f + \Delta^{\alpha}_{i,f} + \Delta^{t}_{i,f} + \Delta^{p}_{i,f}, \tag{3.31}$$

with

$$\Delta^{\alpha}_{i,f} = (1-\alpha_U)\left(U^{*}_{i,f} - [U^{*}_i]_f\right), \tag{3.32}$$

$$\Delta^{p}_{i,f} = -\alpha_U \frac{1}{[a_p/\delta V]_f}\left\{\left(\frac{\partial p}{\partial x_i}\right)_f - \left[\frac{\partial p}{\partial x_i}\right]_f\right\}, \tag{3.33}$$

$$\Delta^{t}_{i,f} = \frac{\alpha_U}{\delta t}\frac{[\rho]_f}{[a_p/\delta V]_f}\left\{\gamma_1\left(U^{o}_{i,f} - [U^{o}_i]_f\right) + \gamma_2\left(U^{oo}_{i,f} - [U^{oo}_i]_f\right)\right\}. \tag{3.34}$$

A detailed derivation and description of the parameters in Eqs. (3.32)-(3.34) can be found in [51].

3.4 Acoustic damping model

The non-reflective pressure boundary conditions are usually applied in order to suppress reflections of acoustic waves at the boundaries of the computational domain. However, these boundary conditions work often in a certain frequency range, so that a complete suppression of wave reflection is hard to achieve. Acoustic waves could furthermore be generated at the domains boundaries due to the interaction between flow structures (e.g. vortices) and the domains boundaries. For this reason, different approaches were developed in order to suppress acoustic reflections and spurious waves generation at the boundaries of the domain. These techniques are often called absorbing-zone techniques [114]. Examples of such methods are the artificial dissipation [25, 42], explicit or implicit filtering [18, 112], and perfectly matched layers (PML) [8, 37–39].

The absorbing techniques mentioned are usually applied near the boundaries of the computational domain outside the region of interest, where the turbulence and acoustic waves have to be resolved. However, spurious noise can also be generated in the focus-region and applying the above mentioned techniques in such regions would result in modifying the characteristics of the flow field and altering the physics of the problem. For instance, spurious noise can be generated at grid interfaces in the wake of a side-mirror or in regions where the A-pillar vortex extends. Applying the above mentioned techniques in such regions would result in altering the flow past the mirror/A-pillar and falsifying the acoustic solution on the side-window. Therefore, it is desired to develop an acoustic damping model that selectively damps acoustic waves without affecting hydrodynamic pressure or velocity fluctuations. Based on this, one could then damp out spurious noise generated in regions where acoustic waves don't have to be resolved (e.g. at grid interfaces in the wake of a side-mirror), while maintaining turbulent structures.

In this study, an acoustic damping model based on the work done by Ramshaw et al. [84,85] is implemented. The model involves the introduction of an artificial pressure q into the momentum equation. The artificial pressure has the form:

$$q = -q_0 \rho c^2 \Delta t \left(\frac{\partial U_i}{\partial x_i} - \frac{\partial U_{i,0}}{\partial x_i} \right). \tag{3.35}$$

In Eq. (3.35), q_0 is a dimensionless coefficient and $\partial U_{i,0}/\partial x_i$ represents the target value of $\partial U_i/\partial x_i$ in the limit of zero Mach number. If the target value is equal to zero, the artificial pressure reduces to a simple bulk viscosity and every velocity gradient is damped out regardless of it nature (hydrodynamic or acoustic). Therefore, Ramshaw et al. [85] developed the artificial pressure in Eq. (3.35) in order to force the velocity gradient not necessarily to zero, but to a target value $\partial U_{i,0}/\partial x_i$ that would be obtained in the limit of zero Mach number.

Similar to the implementation done in [85], the artificial pressure q is implemented in this study by adding it to the thermodynamic pressure p on the right hand side of the momentum equation. This requires the calculation of the gradient of q. The only unknown in Eq. (3.35) is the target value $\partial U_{i,0}/\partial x_i$. This value has been approximated in [85] using a time-derivative of the pressure that is calculated using the internal energy and the density. In this study, the target value is calculated as:

$$\frac{\partial U_{i,0}}{\partial x_i} = \frac{1}{\rho c^2} \frac{\partial p}{\partial t}, \tag{3.36}$$

where $\partial p/\partial t$ is calculated explicitly at each time step. The resulting momentum equation is:

$$\frac{\partial}{\partial t}(\rho U_i) + \frac{\partial}{\partial x_j}(\rho U_i U_j + p\delta_{ij} - \tau_{ij}) = \frac{\partial}{\partial x_i}\left[q_0 \rho c^2 \Delta t \left(\frac{\partial U_i}{\partial x_i} - \frac{1}{\rho c^2} \frac{\partial p}{\partial t} \right) \right]. \tag{3.37}$$

The damping effect of the right hand side in Eq. (3.37) can be analytically derived, which was done in [20]. Therein, the frequency dependency of the damping effect has been shown. For a detailed derivation of the analytical expression, the reader is referred to [20].

It is worth mentioning that the explicit calculation of the time derivative of p on the right hand side of Eq. (3.37) requires the damping term to satisfy the stability limitation:

$$q_0 \leq \frac{\Delta x^2}{2c^2 \Delta t^2}. \tag{3.38}$$

This condition restricts the usage of the damping model in spatially high-resolved regions (small Δx) or for large time steps Δt. Throughout this work, the critical value of q_0 designates its maximum value at the stability limit ($\Delta x^2/2c^2\Delta t^2$).

4 Two-struts validation benchmark [1]

In order to ensure the usability of a CAA-method, a validation of its results quality and plausibility and the limits of its applicability is inevitable. The CAA-methods involved in this work are dedicated to the calculation of sound generation of a flow past a vehicle on one hand, and the calculation of sound propagation between the sound source and the receiver of interest on the other hand. For a driver, the main aeroacoustic sound source is the side-mirror. Moreover, the sound generated by the flow past a side-mirror propagates through the side-window to reach the driver's ear. These conditions provide two simplifications regarding the requirements to a CAA-method and the choice of a suitable benchmark for validation purposes:

- The flow configuration of interest falls into the category of high-Reynolds number and low-Mach number flows.
- The path of acoustic propagation is rather short, such that low-order numerical schemes (such as second-order CDS) can be utilised without any remarkable numerical dissipation of sound waves for the frequency range of interest.

The first item restricts the choice of the validation benchmark to configurations with low-Mach number flows. Consequently, assuming the absence of monopole-like sound sources, the dominant sources are the dipole-like ones. Hence, in a configuration, in which the flow interacts with some solid bodies, these bodies can be considered to be the main sound source. This fact enables the use of the previously mentioned hybrid method, which only takes sound sources on solid boundaries into consideration.

The second item motivates the validation of the available numerical schemes for near-field acoustic propagation. However, an analysis of sound waves in regions where turbulent pressure fluctuations are present can be difficult. The amplitude of turbulent fluctuations are order of magnitudes higher than those of acoustic waves. Hence, acoustic waves can be masked by the turbulent fluctuations. For this reason, a clear and definite validation of acoustic waves generation and propagation requires the analysis of acoustic waves far away from turbulent regions. Consequently, the validation benchmark has to involve far-field aeroacoustic analysis.

Besides the items listed above, the benchmark has to involve a turbulent flow, in order to validate the turbulence modelling approach, which is the IDDES in this investigation.

Several benchmarks that fulfil the above mentioned criteria were proposed by different authors for validation purposes of CAA-methods. Examples of such benchmarks are the rod-airfoil configuration [44], the tandem circular cylinder configuration [47], and the tandem

1 This chapter is an extended version of the results presented in A.H. Dawi, R.A.D. Akkermans, *Direct and Integral Noise Computation of Two Square Cylinders in Tandem Arrangement*, Journal of Sound and Vibration, Volume 436, p. 138-154, 2018

square cylinder configuration [79]. The latter is chosen for the validation of CAA methods in this work due to the simple geometry, which simplifies grid generation, but mainly the availability of detailed aeroacoustic and aerodynamic wind tunnel measurements.

The tandem square cylinder benchmark, also called two-struts benchmark, originates from flow and acoustic analysis for aerospace applications. The configuration represents the basic mechanisms of a flow past a landing gear of an aircraft and one of its objective was to provide an experimental database for validation purposes [79]. A cross section of the configurations geometry is shown in Figure 4.1. The benchmark was a part of the European project *Valiant* (**VAL**idation and **I**mprovement of **A**irframe **N**oise prediction **T**ools).

This chapter aims to validate DNC and FWH methods for aeroacoustic computations. A brief review of the work done by other authors regarding the tandem square cylinder configuration is given. After that, a description of the experimental setup is presented followed by a description of the numerical setup. Two numerical setups are discussed: the first one involves two square cylinders with a span smaller than the one measured in the wind tunnel. In the following, this setup is called "limited-span" case. The second setup involves the full span of both cylinders as measured in the wind tunnel. This setup is denoted as "full-span" case. Aerodynamic and aeroacoustic results are presented for both cases and a comparison to wind-tunnel measurements is done. Finally, a conclusion regarding the applicability of different CAA-methods is given.

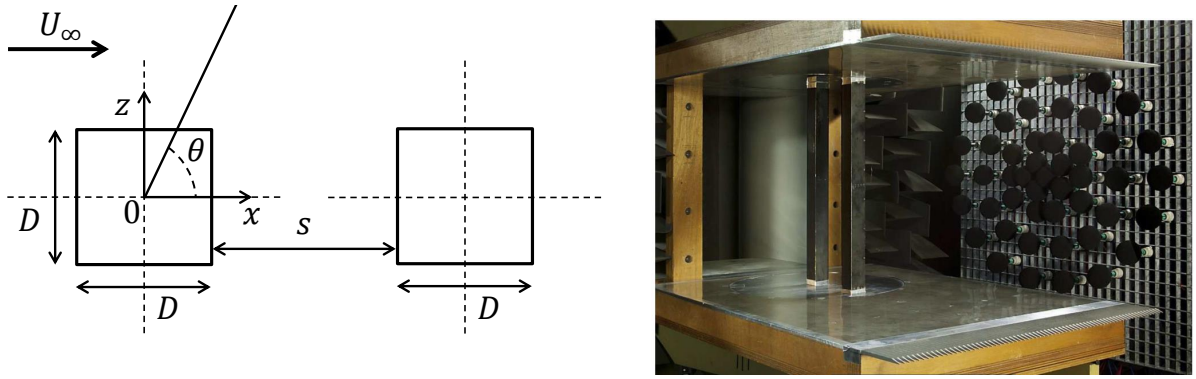

Figure 4.1: (Left) two dimensional representation of the tandem square cylinder configuration. U_∞ represents the freestream velocity, D the cylinders width, s the gap length between both cylinders, and θ the angle used for describing the location of far-field microphones. (Right) experimental setup of the two-struts benchmark in the NLR's anechoic wind tunnel. Picture is taken from [79].

4.1 Literature review

Several authors have already studied the flow past two square cylinders in tandem arrangements, both experimentally and numerically. One of the first studies was the experimental analysis done by Sakamoto et al. [89] in 1980. They studied the effect of the ratio between the gap s between the cylinders and the cylinders width D on the flow behaviour past the

cylinders for Reynolds numbers $\mathrm{Re} = U_\infty D/\nu$ between$2.67 \cdot 10^4$ and $5.52 \cdot 10^4$. They observed two different flow patterns. The first pattern takes place when $s/D < 3$. This pattern involves vortex shedding only in the wake of the downstream cylinder, whereas the shear layers separating from the leading edges of the upstream cylinder reattach on the surfaces of the downstream one. For $s/D > 3$, a second flow pattern involving vortex shedding in the wake of both cylinders was observed. The shear layers separating from the leading edges of the upstream cylinder flow intermittently into the gap between both cylinders forming von Karman like vortex shedding in the wake of the upstream cylinder. This pattern was furthermore split into two categories, depending on the synchronisation between the vortices shed from the up- and downstream cylinders [89]. The switch between flow behaviours at $s/D = 3$ causes an abrupt increase of the mean drag coefficient C_D. This behaviour was also observed in the experimental work of Luo et al. [68], who studied the flow past the configuration at $\mathrm{Re} = 5.67 \cdot 10^4$. By increasing and decreasing the gap s between both cylinders, Liu et al. [65] were able to observe a hysteresis of the drag coefficient with two discontinuous jumps. The limits of the hysteresis, corresponding to the ratios s/D where the jumps appear, were found to be dependent on the Reynolds number. Their study involved a range of $\mathrm{Re} = 0.2 - 1.6 \cdot 10^4$ and a gap to width ratio range of $s/D = 0.5 - 8$. They attributed the observed hysteresis to the two different flow patterns.

Besides experimental studies, computational analysis of the aforementioned tandem square cylinders has also been done by several authors. Inoue et al. [41] did a two dimensional study of the flow past tandem square cylinders for $\mathrm{Re} = 150$. They directly solved the two dimensional Navier-Stokes equations and observed a dependency of the level of aeolian tones produced by the cylinders on gap spacing between the cylinders. For $s/D < 3$, the sound level was two orders of magnitude lower than that of a single square. For large gap spacings $s/D > 3$, the flow pattern switched and a sudden increase in the sound level was observed. Similar to the Liu et al. [65], they suggested the presence of a hysteresis of the generated aeolian tones. Knacke et al. [51,52] analysed in the scope of *VALIANT* project the sound generated by tandem square cylinders for $s/D = 3$, $\mathrm{Re} = 1.82 \cdot 10^5$, and two different angles of attack. A DDES approach was utilised for the calculation of the turbulent flow past the cylinders and a FWH approach was used to calculate far-field acoustics. The same configuration was calculated by Abalakin et al. [3] using **E**dge-**B**ased **R**econstruction (EBR) schemes. The work was also done in the scope of *VALIANT* and the results were compared to wind tunnel measurements done by [79]. According to [51], all numerical approaches that were utilised in *VALIANT* showed one flow state, namely the one where vortices are shed in the wake of both cylinders.

4.2 Experimental setup

Wind tunnel measurements of the two-struts benchmark were done by Oerlemans [79] as a part of the *VALIANT* project. The measurements were carried out in **N**etherlands **A**erospace **C**entre (NLR) anechoic wind tunnel, which is an open jet wind tunnel and the test section is surrounded by 0.5 m foam wedges. The foam wedges yield 99% absorption for $f > 500$ Hz [79]. The outlet of the nozzle has a rectangular cross section and two horizontal plates

were placed on the upper and lower edges of the nozzle. In order to suppress reflections of acoustic waves, the plates were perforated and acoustically lined using 5.5 cm absorbing foam. The effect of plate's perforation on sound waves has been shown in [80]. Between both plates, two square struts of width D were placed vertically on rotatable disks, allowing measurements at different angles of attack. The distance between both plates, corresponding to the span of the cylinders, was set to 0.51 m. The distance between the leading surface of the upstream cylinder and the nozzle's outlet was set to 0.265 m. Different configurations regarding the position of the downstream strut relative to the upstream strut were performed. The experimental setup is shown in Figure 4.1 (right).

The wind tunnel experiment included aerodynamic as well as aeroacoustic measurements. For this work, surface pressure spectra on the surfaces of both cylinders were made available by the experimenter. Moreover, pressure coefficient distributions on both cylinders surfaces were provided. The positions of the surface pressure sensors are listed in [79]. The surface pressures were acquired at a measurement time of 20 s. The sampling frequency was $F_{s,\mathrm{exp}} = 102.4$ kHz. Subsequently, surface pressure spectra were calculated by splitting surface pressure measurements to different blocks with block size of 8192 samples and Fourier transforming them using a Hanning window with 50% overlap, resulting in a frequency resolution of $f_{\mathrm{exp}} = 12.5$ Hz.

Besides surface pressure measurements, PIV measurements including mean velocity fields and turbulence statistics in the wake of the upstream cylinder were provided. The measurements provided for this work are at a vertical plane at the mid-span between both cylinders. More measurement planes are presented in [79].

Regarding acoustic measurements, far-field pressure spectra were provided for this work. The microphones were placed in the mid-span plane at a 2 m radius from the centre of the upstream cylinder. The microphones used for this work were placed at $\theta = \{105°; 90°; 75°; 60°; 45°\}$. Note that these positions do not correspond to the ones used in the numerical setup due to installation effects. This will be discussed in the next section. Similar to surface pressure spectra, acoustic spectra were measured with a sampling frequency of 102.4 kHz and the provided data have a frequency resolution of 25 Hz. It is worth mentioning that all spectra provided represent power spectral density (PSD) with a reference pressure $p_{\mathrm{ref}} = 2 \cdot 10^{-5}$ Pa, which represents the threshold of hearing.

For a proper comparison between experimental and numerical results, background wind tunnel noise should be taken into account. For this, the level of background noise was determined from measurements of an empty test section. Consequently, the measured acoustic spectra were corrected by setting the spectral level equal to the background noise level if the signal-to-noise ratio is less than 3 dB. The frequencies for which the spectral level is clipped to the background noise level were also provided for this work. These data are used to determine the frequency range, for which a comparison between numerical and experimental data is valid.

In the rest of this chapter, only one configuration with the following parameters is considered: strut width $D = 0.04$ m, gap width $s = 3D = 0.12$ m, angle of attack $\alpha_{\mathrm{AoA}} = 0°$, transverse distance between the struts $T = 0$ m, freestream velocity $U_\infty = 70$ m/s, Mach

number $Ma = U_\infty/c \approx 0.2$, Reynolds number $\mathrm{Re} = U_\infty D/\nu \approx 1.82 \cdot 10^5$, and width of the struts in spanwise direction $L_{\mathrm{lim}} = 3D$ for the limited span case and $L_{\mathrm{full}} = L_{\mathrm{exp}} = 12.75D$ for the full span case.

For these parameters, two different flow patterns were observed in the wind tunnel: a pattern where vortices are only shed in the wake of the downstream cylinder (denoted as the "quiet" flow state), and a second pattern where vortices are shed in the wake of both cylinders (denoted as the "loud" flow state). Switching between both flow states could be accomplished by a simple "hand waving" in front the cylinders [79].

4.3 Limited-span case

In this section, numerical results for the limited span case are presented. This case serves as a validation for the IDDES approach utilised in this study based on aerodynamic quantities. Furthermore, acoustic results using the hybrid FWH method are compared to experimental ones. As presented in the following, the limited span case is not suitable for the aeroacoustic validation of the DNC approach. Nevertheless, acoustic results calculated with DNS are shown and compared to experimental ones, in order to show the effect of periodic boundary conditions on DNC calculations.

4.3.1 Numerical setup

The computational domain is chosen to have the dimensions of $250D$ in the x-direction, $40D$ in the y-direction and $3D$ in the z-direction. The center of the upstream cylinder shown in Figure 4.1 (left) coincides with the center of the computational domain in all three directions. At the inlet, a constant velocity boundary condition with a value $U_\infty = 70$ m/s is prescribed. The cylinders surfaces were set to no-slip walls and have zero gradient temperature and pressure boundary conditions. At all other boundaries, a non-reflective pressure boundary condition is imposed, except for the spanwise boundaries, for which periodic boundary conditions are applied. The low free stream turbulence intensity in the wind tunnel ($I = 5\%$) is accounted for by prescribing a viscosity ratio of $\nu_t/\nu = 0.1$ at the inlet.

The grid generated for the limited span case resembles the one utilised by Knacke in [51] regarding the spacial and temporal resolution. The generated grid consists of cubic Cartesian elements all over the domain, except in regions near the cylinders, where stretched boundary layer elements are generated. The resolution in the wake of the cylinders is set to $\Delta_x = \Delta_y = \Delta_z = D/32$, which fulfils LES requirements according to [51]. The grid is additionally refined to $D/64$ in the proximity of the cylinders. The extents of the regions resolved with $D/64$ are set for the first 20 wall-normal cells. The wall nearest cells have a constant wall-normal width of $\Delta_{\mathrm{wall}} \approx 2 \cdot 10^{-3} D$. Due to the geometrically defined separation points at the leading edges of the upstream cylinder, boundary layer effects on the flow development can be considered negligible. Furthermore, wall functions are utilised as boundary conditions for turbulence variables on the walls. Hence, the resolution of boundary layer

elements on the cylinders surfaces can be assumed to be sufficient. Outside the refinement box around the cylinders, the grid is coarsened using 2:1 grid refinement interfaces. In order to reduce numerical dissipation and dispersion in case of DNC, the resolution in the far-field region is set to $D/8$. A slice of the grid at the midspan of the cylinders is shown in Figure 4.2 and different refinement boxes are shown in Figure 4.3. The time step size is set to $\Delta t = 5 \cdot 10^{-6}$ s, which corresponds to an acoustic Courant number $Co_{ac} = c\Delta t/\Delta x \approx 0.35$ in the far-field. The spacial and temporal resolutions in the far-field are enough to resolve a $f = 3$ kHz wave with dissipation and dispersion errors less than 5%. This corresponds to a Strouhal number of $\mathrm{St} = fD/U = 0.71$. Due to the symmetry of the flow configuration in the z-direction, the far-field is only resolved on one side of the cylinders. The simulated physical time is equal to 0.6 s, of which the last 0.55 s are used for data sampling. The first 0.05 s are excluded from analysis and used to reach a statistical steady flow field. This transient corresponds to approximately 18 flow cycles past the configuration.

Turbulence is modelled using the SST-IDDES approach presented in chapter 2. All transient terms in the conservation equations are discretised using a second-order backward Euler method. Since the computational domain consists mainly of cubic cells, central differencing schemes can be utilised for discretising the advection term in the momentum equation. However, in order to ensure stability, the deferred-correction formulation of CDS is utilised and is additionally blended with a second-order upwind scheme. The blending factor is constant all over the domain and the resulting scheme consists of 95% CDSdC scheme and 5% LUDS scheme. Using this blending procedure, no stability issues were noticed and the solution did not show excessive dissipation or diffusion. Due to the small time-step size and as a result of the small Courant number, under-relaxation is not required and, consequently, the solver is able to reach lower residuals in a low number of iterations. The number of SIMPLE iterations in the PIMPLE algorithm is set to 3 and the number of PISO iterations inside each SIMPLE iteration is set to 4.

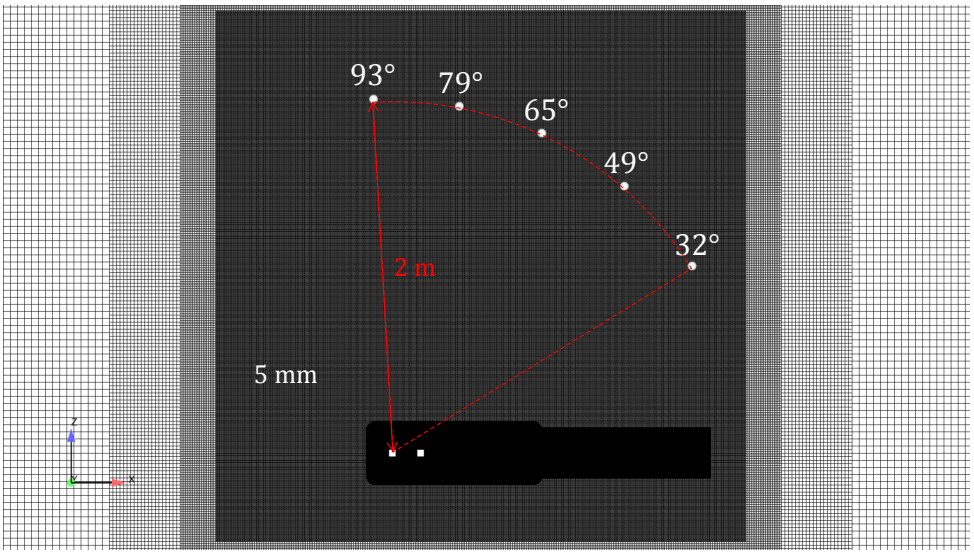

Figure 4.2: Slice of the numerical grid at the midspan showing the resolution of the far-field. White circles corresponds to microphone positions.

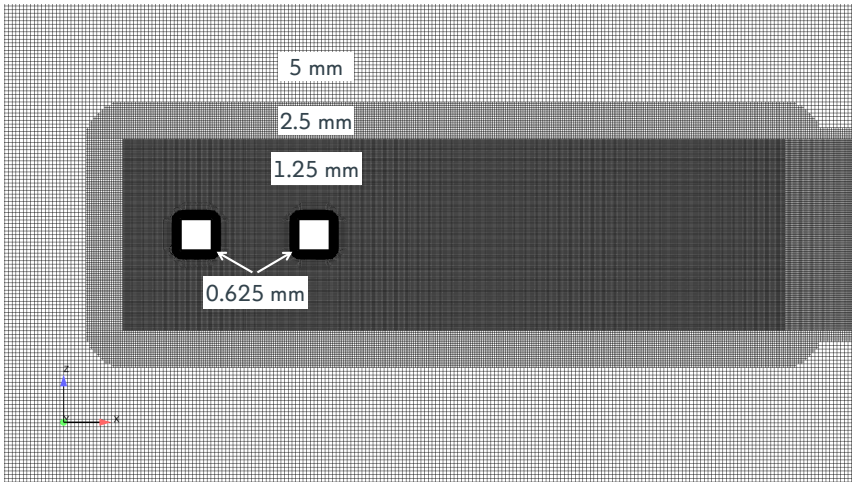

Figure 4.3: Numerical grid at the midspan showing different resolution regions near and in the wake of the cylinders (figure taken from [19]).

The sound pressure levels delivered in the experiment were corrected for shear layer effects (quiescent flow outside nozzle flow). Since the simulation does not include the shear layer produced by the wind-tunnel nozzle and the velocity in the simulation far-field is equal to U_∞, refraction effects are not included in the simulation. In order to account for these effects, far-field pressure spectra were corrected using the well-established Amiet method [6]. Moreover, the convection angles should be used for a valid comparison between simulation and experiment. For the angles presented in section 4.2 correspond to the convection angles $\{93°;79°;65°;49°;32°\}$, respectively. These angles are shown in Figure 4.2.

Similar to wind tunnel measurements, numerical results presented below showed two different flow patterns. The resulting flow patter highly depends on the initial velocity field U_0. First calculations were done using a homogeneous initial velocity field $U_0 = U_\infty$ all over the computational domain. This results in the quiet flow state. In order to ensure the stability of this state, simulations were done for over 1 s of physical time. The quite flow state proved to be stable and the flow pattern did not switch. In order to simulate the loud flow state, the vortex shedding in the wake of the upstream cylinder had to be triggered. For this purpose, the initial velocity field is perturbed upstream of the first cylinder. The velocity perturbation constitutes a vortex, which moves in the flow direction as the simulation starts. When the vortex impinges on the upstream cylinder, it causes an unbalance of the flow resulting in triggering of the vortex shedding between the two cylinders. This method resembles the "hand waving" technique used to switch the flow pattern in the wind tunnel experiments. The initial velocity field perturbations are defined as:

$$\begin{pmatrix} \delta U_x \\ \delta U_z \end{pmatrix} = \frac{U_\infty B}{R} \cdot e^{r^2/2} \begin{pmatrix} z_c - z \\ x - x_c \end{pmatrix} \quad \text{with} \quad r = \frac{\sqrt{(x-x_c)^2 + (z-z_c)^2}}{R}. \tag{4.1}$$

In Eq. (4.1), δU_x and δU_z correspond to the perturbations superimposed to $U_{0,x}$ and $U_{0,z}$, respectively, $R = D$ to the radius of the vortex and $B = 1/5$ to its strength. The initial center

position of the vortex (x_c, z_c) is taken equal to $(-3D, 0)$. Figure 4.4 shows the two different flow states at $t = 0.6$ s using two different initial velocity fields. In the quiet flow state, the shear layers separating from the leading edges of the upstream cylinder reattach on the surfaces of the downstream cylinder. In the loud flow state, the aforementioned shear layers flow intermittently into the gap between the cylinders causing vortex shedding in the wake of the upstream cylinder. It can also be observed that the wake in the loud flow state is generally wider than that of the quiet flow state. Moreover, large vortical structures can be observed in the wake of the downstream cylinder in the loud flow state. Such structures are not visible in the quiet flow state, although vortices do develop further downstream (this latter effect is not shown in Figure 4.4).

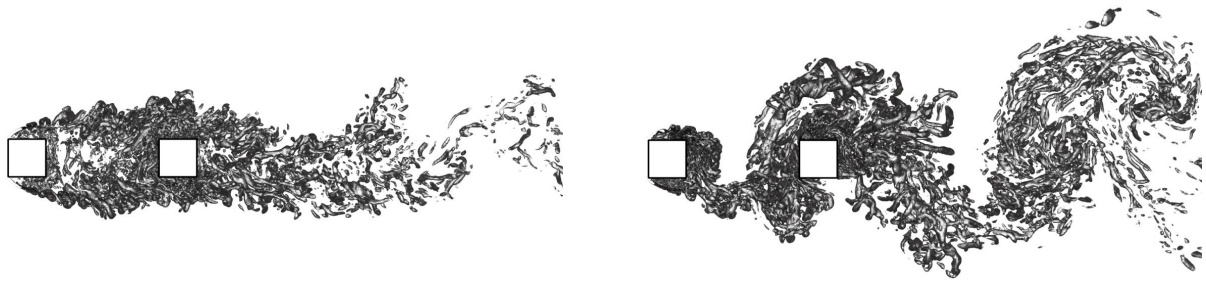

Figure 4.4: Snapshots of the (left) quiet and (right) loud flow states at the midspan at $t = 0.6$ s. The flow field is visualised by an isosurface of the Q criterion [35]. The isosurfaces are colored by the vorticity magnitude.

4.3.2 Aerodynamic results

A comparison of numerical and experimental acoustic spectra requires accurate calculation of the flow past the cylinders. The following presents an evaluation of the quality of the utilised numerical method based on comparing mean flow variables as well as spectral analysis on the surfaces of the cylinders. The following variables are compared between simulation and experiment: (i) mean flow field in the wake of the upstream cylinder, includeing mean streamlines, velocity fields, and different turbulence statistics, (ii) pressure coefficient distribution on the cylinders surfaces, and (iii) surface pressure spectra on different cylinders surface. Furthermore, spanwise correlation coefficients are presented and compared to numerical results given by Knacke in [51].

Mean flow field

The streamlines calculated using the mean velocity field are shown in Figure 4.5 for both flow states. Since only velocity components in the x- and z- directions were provided by the experiments, the y-component of the numerical mean velocity field $\langle U_{\text{streamlines}} \rangle$ is set to zero. For the loud flow state, numerical results show good agreement with PIV measurements. The vortex pair in the wake of the upstream cylinder is well predicted and the centres of vortices align well with the measured ones. However, one can observe the compression

of the streamlines far away from the cylinders. This goes back to blockage effects in the wind tunnel. The ambient pressure in the wind tunnel region, in which the fluid velocity is equal to zero, is higher than the pressure of the jet free stream. This causes the flow at the jet shear layers to be compressed towards the cylinders. This effect is absent in the simulation, since the freestream velocity is equal to 70 m/s in the far-field. Nevertheless, the simulated streamlines show good agreement with PIV measurements in the wake between the cylinders for the loud flow state.

In the quiet flow state, the differences between the simulation and experiment are rather larger than was seen for the loud state. The simulation shows two large symmetric vortices in the wake of the upstream cylinder. These can also be observed in the PIV measurements. However, the centres of the simulated vortices do not match perfectly with those in the experiment. The simulated streamlines far away from the cylinders show good agreement with wind tunnel measurements. Similar to the loud flow state, wind tunnel blockage effects can also be observed in the quiet flow state. The measured streamlines tend to be compressed towards the cylinders. This could be responsible for the deviation of the vortices positions between simulation and experiment. Furthermore, the periodic boundary conditions utilised in the simulation could also be the cause of the deviation between the simulation and experiment due to the modified spanwise correlation caused by the boundary conditions. This is further investigated in the next section, in which the results of the full span setup are discussed. A last reason for the differences between numerical and experimental results is the interaction between the potential core of the wind tunnel jet and the wake of the downstream cylinder. This has been analysed by Knacke [51], who approximated the length of an ideal planar jet and showed its possible interaction with large turbulent structures in the wake of the configuration. However, by comparing the extents of the structures in the z-direction in Figure 4.4, the interaction of the potential core with the flow past the cylinders should be more pronounced in the loud flow state than in the quiet one. Since the mean flow field in the loud flow state show good agreement with PIV measurements, it is rather unlikely that the potential core is responsible for the differences between simulation and experiment for the quiet flow state.

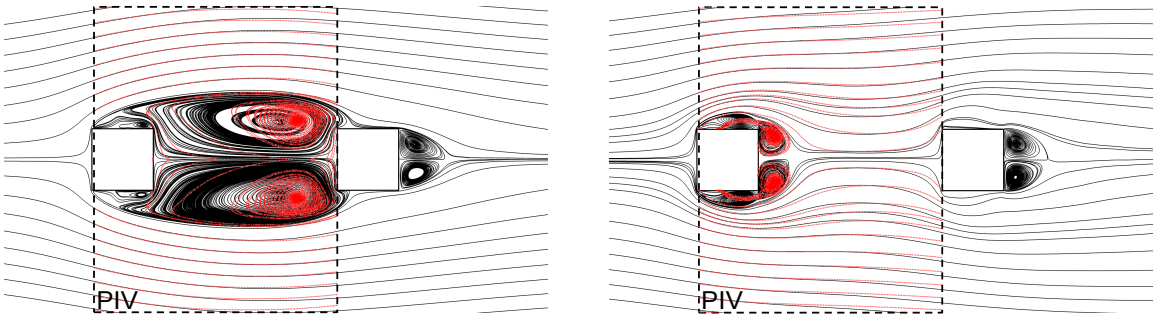

Figure 4.5: Streamlines using the mean velocity field for (left) the quiet flow state and (right) the loud flow state. (——) represent numerical results and (·····) PIV measurements. Numerical results correspond to the limited-span case.

Figure 4.6 shows simulated isolines of the mean streamwise velocity $\langle U_x \rangle / U_\infty$ compared to PIV measurements for both flow states. In the loud flow state, the isolines in the re-

gion between the cylinders show good agreement with experimental results. The lobe-shaped isoline at $\langle U_x \rangle / U_\infty = 1.2$ is well captured by the simulation. The same applies for $\langle U_x \rangle / U_\infty = 0$ in the wake of the upstream cylinder. Wind tunnel blockage effects can be observed for $\langle U_x \rangle / U_\infty = 1$. Similar to the mean streamlines, the measured isoline $\langle U_x \rangle / U_\infty = 1$ is compressed towards the cylinders.

The isolines in the quiet flow state show larger deviations to wind tunnel measurements than the loud flow state. The lobe-shaped isoline at $\langle U_x \rangle / U_\infty = 1.2$ is substantially larger than the one in the loud flow state and extends over the whole gap between the cylinders. The lines representing $\langle U_x \rangle / U_\infty = 0.8$ show good agreement between simulation and experiment, apart from deviations in the between the cylinders, which can be linked to wind tunnel blockage effects. The lines representing negative $\langle U_x \rangle / U_\infty$ in the wake of the upstream cylinder show large differences compared to experimental data. Possible reasons for these differences were already discussed previously while comparing the mean streamlines.

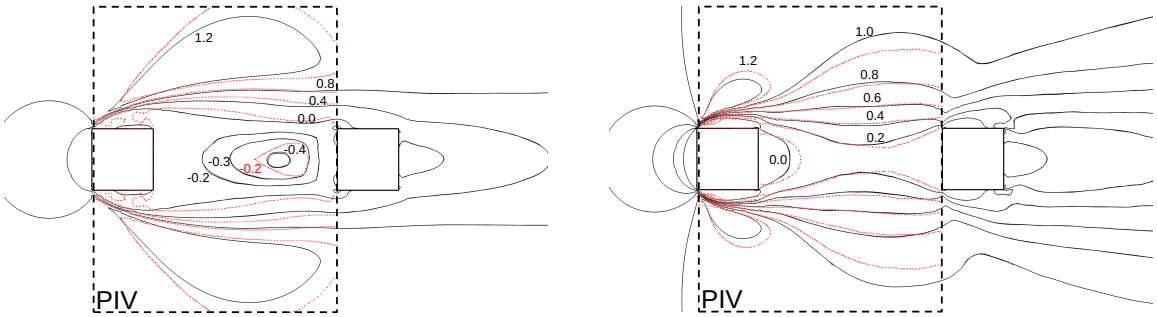

Figure 4.6: Isolines of the mean velocity field $\langle U_x \rangle / U_\infty$ for (left) the quiet flow state and (right) the loud flow state. (——) represent numerical results and (·····) PIV measurements.

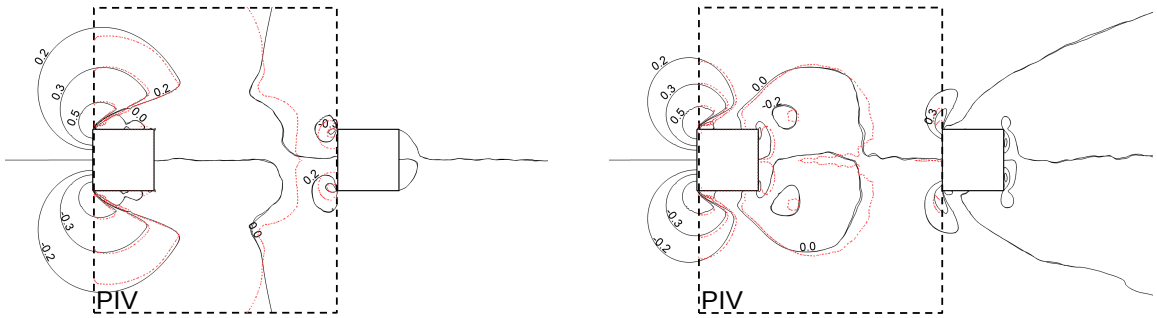

Figure 4.7: Isolines of the mean velocity field $\langle U_z \rangle / U_\infty$ for (left) the quiet flow state and (right) the loud flow state. (——) represent numerical results and (·····) PIV measurements.

Unlike the large differences between x-velocity fields of the quiet and loud flow states, the z-velocity isolines are rather similar in both flow states. This is shown in Figure 4.7. The bubble-shaped isolines on both sides of the upstream cylinder show good agreement with PIV measurements for both flow states. Differences between the flow states can be observed in the wake of the upstream cylinder as well as in the size of the bubble-shaped isolines, which are larger in the quiet flow state. This behaviour corresponds to the larger radius of

the separated shear layers on the upstream cylinders leading edges, which is also the reason for the larger bubble-shaped $\langle U_x \rangle$ isolines in Figure 4.6.

Mean pressure coefficient

Besides PIV measurements, time-averaged surface pressure coefficients C_p were measured on the surfaces of the cylinders. The time-averaged pressure coefficient is defined as:

$$C_p = \frac{\overline{p} - p_\infty}{\frac{1}{2}\rho_\infty U_\infty}, \tag{4.2}$$

where p_∞, ρ_∞, and U_∞ represent the pressure, density and velocity in the freestream, respectively, and $\overline{p}$ the time-averaged pressure value.

Figure 4.8 and Figure 4.9 show the distribution of C_p along the surfaces of the upstream and downstream cylinders at their midspan compared to wind tunnel measurements for both flow states. The distributions are represented as a function of the dimensionless length d, which represents the surface coordinate normalised with the cylinder width D. It runs from 0 at the center of the upstream surface of a cylinder, to 2 at the center of the downstream cylinder surface. The leading and trailing edges of a cylinder are hence at $d = 0.5$ and 1.5, respectively. Due to the symmetry of the mean flow about the x-axis, the pressure coefficient distributions on the upper and lower sides of each cylinder are the same. For convenience, these side are denoted by pressure side (PS) for the upper part and suction side (SS) for the lower part of each cylinder.

For the quiet flow state, numerical results show good agreement with wind tunnel measurements for the upstream cylinder. The pressure coefficient distributions on both sides of the cylinders are identical, which indicates the symmetry of the flow. The measured pressure coefficient at the center of the upstream surface of the upstream cylinder is not exactly equal to one, which goes back to the higher ambient pressure outside the free jet compared to the freestream pressure inside the jet. Despite the large differences in the mean flow between numerical and experimental results in the wake of the upstream cylinder in the quiet flow state, the simulated pressure coefficient distribution on the downstream cylinder show fairly good agreement to experimental results. The largest deviations can be observed for $0.5 < d < 1$, which corresponds to the upstream half of the surfaces on both pressure and suction sides of the downstream cylinders. These surfaces correspond to the ones on which the large vortex pair in the wake of the upstream cylinder impinges. Due to the differences in the position of the vortex pair centres shown in Figure 4.5 between simulation and experiment, deviations in the pressure coefficient distributions are expected.

Figure 4.9 (left) shows C_p curves in the loud flow state along the upstream cylinder. As for the quiet flow state, the simulated results show good agreement with experimental data. For reasons mentioned above, the measured pressure coefficient is not exactly unity at the stagnation point of the upstream cylinder. For $d > 0.5$, C_p is substantially smaller than in the quiet flow state. On the surface of the downstream cylinder (Figure 4.9 (right)), the

simulated pressure coefficient distribution shows good agreement with wind tunnel measurements for $d < 0.5$, while the C_p curves diverge on the PS, SS, and downstream surfaces of the downstream cylinder. This behaviour was also observed by Knacke in [51], as well as other contributers in the VALIANT project [3, 21]. In [51], it was assumed that installation effects and the interaction between the potential core with the wake of the downstream cylinder could be the reason for the differences between simulations and measurements. However, as will be shown in the next section, the limited span and the resulting modified spanwise correlation is main cause of these deviations.

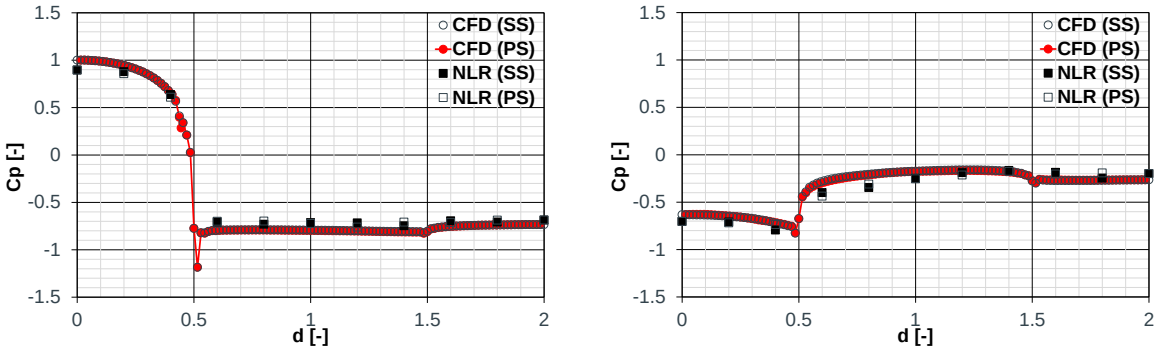

Figure 4.8: Time-averaged surface pressure coefficient C_p along (left) upstream and (right) downstream cylinders for the quiet flow state.

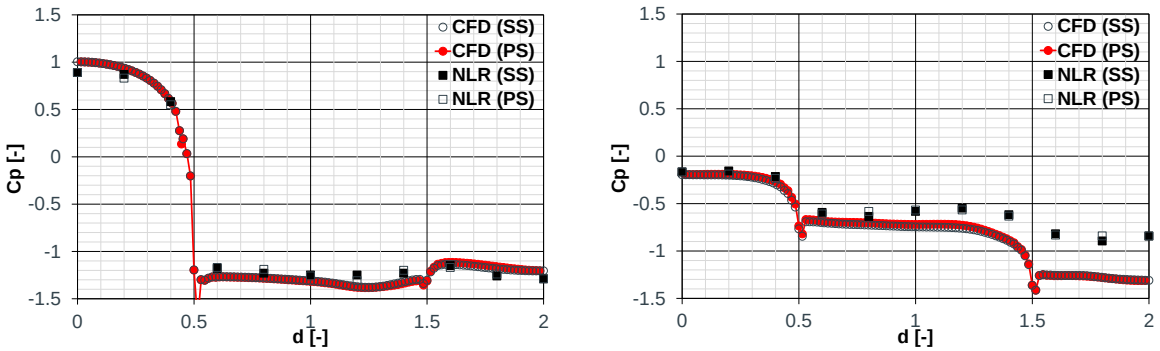

Figure 4.9: Time-averaged surface pressure coefficient C_p along (left) upstream and (right) downstream cylinders for the loud flow state.

Turbulence statistics

Figures 4.10 to 4.12 show simulated isolines of the Reynolds stresses for both flow states compared to wind tunnel measurements. For the quiet flow state, a large discrepancy between simulated isolines and PIV measurements can be observed. The simulated normal stresses are substantially higher in the wake between the cylinders. The isolines of the measured normal stresses extend to the region further downstream of the upstream cylinder. This behaviour applies also for the isolines of the shear stress $\langle U_x' U_z' \rangle$. These differences could be the result of the spanwise extent issues mentioned before.

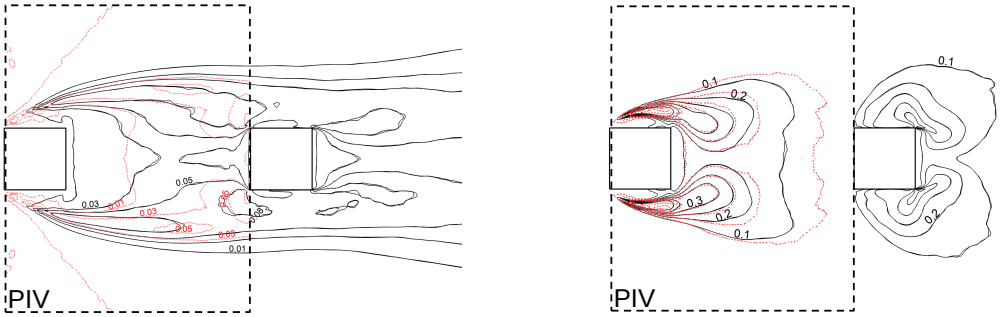

Figure 4.10: Isolines of the Reynolds stress $\langle U_x' U_x' \rangle / U_\infty^2$ for (left) the quiet flow state and (right) the loud flow state. (——) represent numerical results and (·····) PIV measurements.

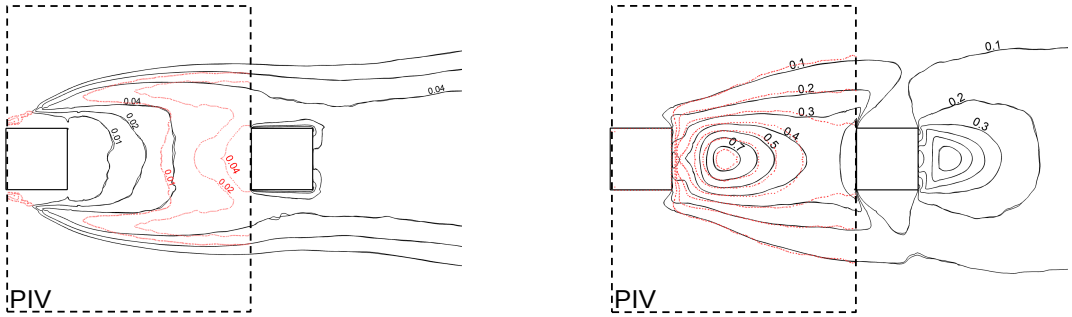

Figure 4.11: Isolines of the Reynolds stress $\langle U_z' U_z' \rangle / U_\infty^2$ for (left) the quiet flow state and (right) the loud flow state. (——) represent numerical results and (·····) PIV measurements.

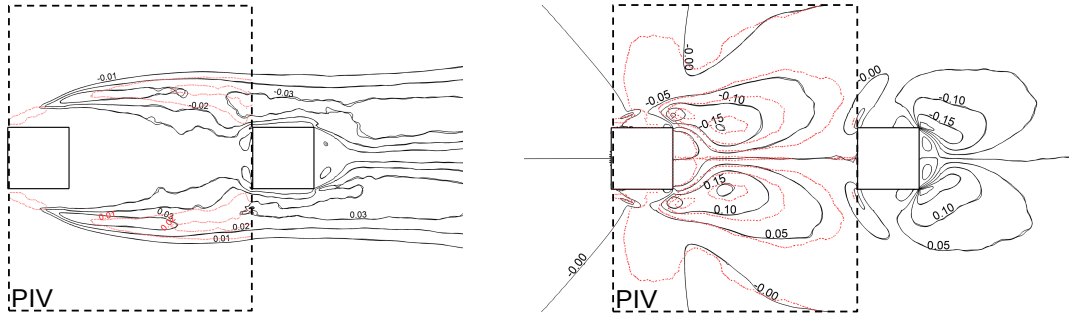

Figure 4.12: Isolines of the Reynolds stress $\langle U_x' U_z' \rangle / U_\infty^2$ for (left) the quiet flow state and (right) the loud flow state. (——) represent numerical results and (·····) PIV measurements.

The isolines of the Reynolds stresses in the loud flow state show better agreement with PIV measurements. In general, these stresses are approximately an order of magnitude higher than the ones in the quiet flow state. Some deviations in the wake of the upstream cylinder can be observed for the shear stresses $\langle U_x' U_z' \rangle$ and the normal stresses $\langle U_x' U_x' \rangle$, where the measured isolines extend further downstream of the upstream cylinder. These deviations were also observed in [51], who related the differences to the grid resolution in the wake of the cylinders. Since the spacial resolution of the grid utilised in this work corresponds to the ones used by Knacke in [51], the spacial resolution could indeed be the reason for the

differences between simulation and experiment. Furthermore, the interaction between the potential core of the free jet and the wake of the cylinders could also cause these differences. Nevertheless, a general good agreement can be observed between numerical results and wind tunnel measurements for the loud flow state.

The distributions of the Reynolds stresses in the wake of the upstream cylinder are shown in Figures 4.13 to 4.15 at $x = 1.25D$ for both flow states. For the quiet flow state, the peaks at $z/D \approx \pm 0.7$ in the numerical results are significantly larger than the measured ones. This applies for the normal stresses as well as the shear stress. However, the location of the peaks is well predicted by the simulation. On the other hand, numerical results show higher normal stresses than experimental ones at the center of the wake ($z/D = 0$), while the simulated shear stresses show good agreement with wind tunnel measurements. This is due to the symmetry of the flow which causes the shear stresses to vanish at $z/D = 0$.

Regarding the loud flow state, both normal stresses and the shear stresses are generally higher than those in the quiet flow state. furthermore, the distribution of the Reynolds stresses extend more into the center between the cylinders ($z/D = 0$). This could be the result of the vortex shedding in the wake of the upstream cylinder, which causes higher momentum exchange between both sides of the cylinders. The agreement between the numerical results in the loud flow state and wind tunnel measurement is rather good. The peaks in the Reynolds stresses are well predicted and the distributions along the z-axis corresponds to those in the experiment.

Surface pressure spectra

The surface of the cylinders are dominated by hydrodynamic pressure fluctuations due to turbulence. Since these pressure fluctuations are the input data for the integral aeroacoustic calculation method, it is important to ensure that these fluctuations correspond to the ones measured in the wind tunnel. The experiments done by [79] included unsteady surface pressure measurements at different locations on the surfaces of the cylinders. In this work, a comparison between the simulation and experiment is done for the sensors placed at the center of each surface of the cylinders. The parameters used for the calculation of surface pressure spectra are listed in Table 4.1.

Table 4.1: Parameters for the calculation of surface pressure spectra.

	T_{signal} [s]	F_s [kHz]	FFT block size	window / overlap	Resolution [Hz]
Sim.	0.55	100	8192	Hanning / 50%	12.21
Exp.	20	102.4	8192	Hanning / 50%	12.5

Figure 4.16 show the calculated surface pressure spectra compared to the measured ones on different surface of the cylinders for the quiet flow state. As previously discussed, the mean flow variables do show large discrepancies between simulation and experiment for the quiet flow state. For this reason, differences in the surface pressure spectra are to be expected.

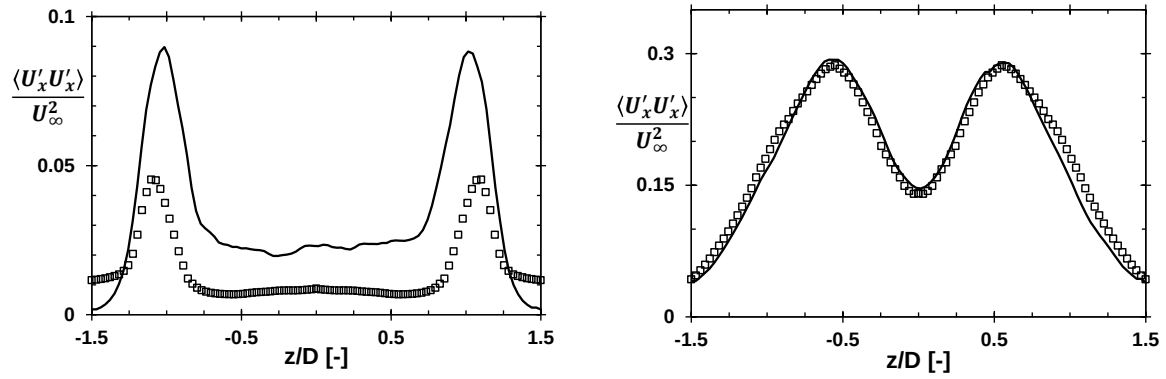

Figure 4.13: Normal stresses $\langle U'_x U'_x \rangle / U_\infty^2$ in the wake of the upstream cylinder at the midspan and $x = 1.25D$ for (left) the quiet flow state and (right) the loud flow state. Black solid lines represent numerical results and square symbols wind tunnel measurements.

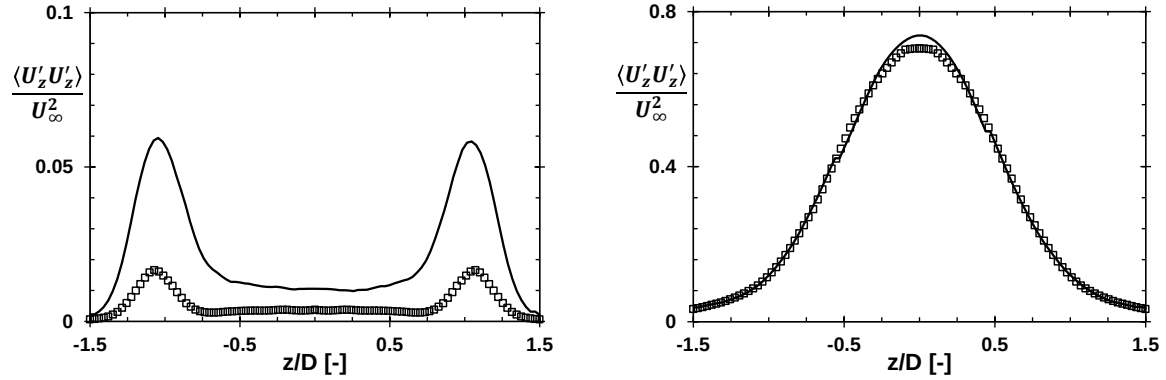

Figure 4.14: Normal stresses $\langle U'_z U'_z \rangle / U_\infty^2$ in the wake of the upstream cylinder at the midspan and $x = 1.25D$ for (left) the quiet flow state and (right) the loud flow state. Black solid lines represent numerical results and square symbols wind tunnel measurements.

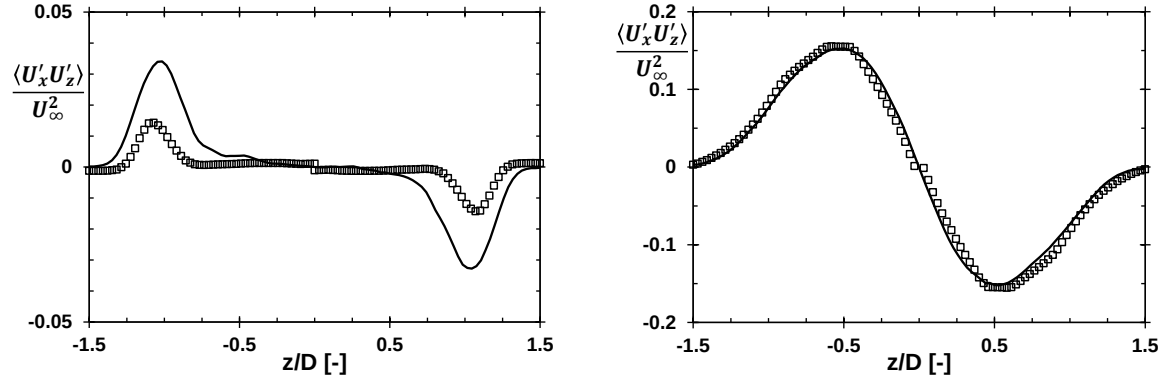

Figure 4.15: Shear stresses $\langle U'_x U'_z \rangle / U_\infty^2$ in the wake of the upstream cylinder at the midspan and $x = 1.25D$ for (left) the quiet flow state and (right) the loud flow state. Black solid lines represent numerical results and square symbols wind tunnel measurements.

Regarding the upstream cylinder, the spectrum on the upstream surface show a similar distribution to that measured in the wind tunnel. Higher spectral values can be observed for

$0.2 <\mathrm{St}< 0.8$. On the downstream surface of the upstream cylinder, the simulated spectrum resembles the measured one, apart from an offset of approximately 8 dB over a wide frequency range. This trend does not apply for the spectra on the pressure and suction sides of the upstream cylinders. These spectra exhibit peaks at $\mathrm{St}= 0.8, 1.55$, and 3. These peaks are not present in the experimental results. Moreover, the spectral level at the shedding frequency ($\mathrm{St}\approx 0.1$) is overpredicted in the simulation. The same applies for the broadband part (i.e., $0.1 <\mathrm{St}< 0.5$). A possible reason for the peak at high Strouhal numbers are the periodic boundary conditions and their effect on the spanwise correlation on the surfaces of the cylinders.

On the surfaces of the downstream cylinder, the calculated spectra show a slightly better agreement with experimental results for the quiet flow state. On the upstream surface of the downstream cylinder, the spectrum shows a distribution similar to the measured one. However, higher spectral levels can be observed. The streamlines presented in Figure 4.5 show that the vortex pair in the wake of the upstream cylinder does not perfectly match with the measured one. Hence, the shifted position of the reattachment points of the shear layers could be the reason for higher pressure fluctuations on the upstream surface of the downstream cylinder. On the pressure and suction sides of the cylinders, numerical data show good agreement with experimental ones. The shedding frequency is well predicted and the spectral level at this frequency corresponds to the measured ones. The broadband part exhibits a similar distribution to experimental data, but with slightly higher levels at $\mathrm{St}> 1$. On the downstream surface of the downstream cylinder, the spectral levels in the simulations are also higher than the measured ones. This is most likely due to the interaction between the wake of the cylinders and the potential core of the free jet, which is not accounted for in the simulation.

The simulated mean flow variables presented in the previous paragraphs showed good agreements with wind tunnel measurements for the loud flow state. Hence, surface pressure spectra are expected to show better agreements with experimental data for this flow state. This is indeed the case, as shown in Figure 4.17. The surface pressure spectra of the pressure, suction and downstream sides of the upstream cylinder show good agreement with experimental data. The spectral levels at the shedding frequency ($\mathrm{St}\approx 0.1$) are well predicted by the experiment. The same applies for the secondary frequency at $\mathrm{St}\approx 0.2$. Higher spectral levels can be observed for high Strouhal numbers ($\mathrm{St} \approx 2$) on the pressure and suction sides of the cylinders. These deviations were also observed in the results of Knacke [51]. As for the quiet flow state, a possible reason for these deviations could be the effects of the periodic boundary conditions on the spanwise correlation. The results of the full-span case in the next section show these effects. Regarding the upstream surface of the upstream cylinder, larger discrepancies between simulation and experiment can be observed. These deviations are equivalent to the ones observed by Knacke in [51], in which he discussed the reasons for these differences.

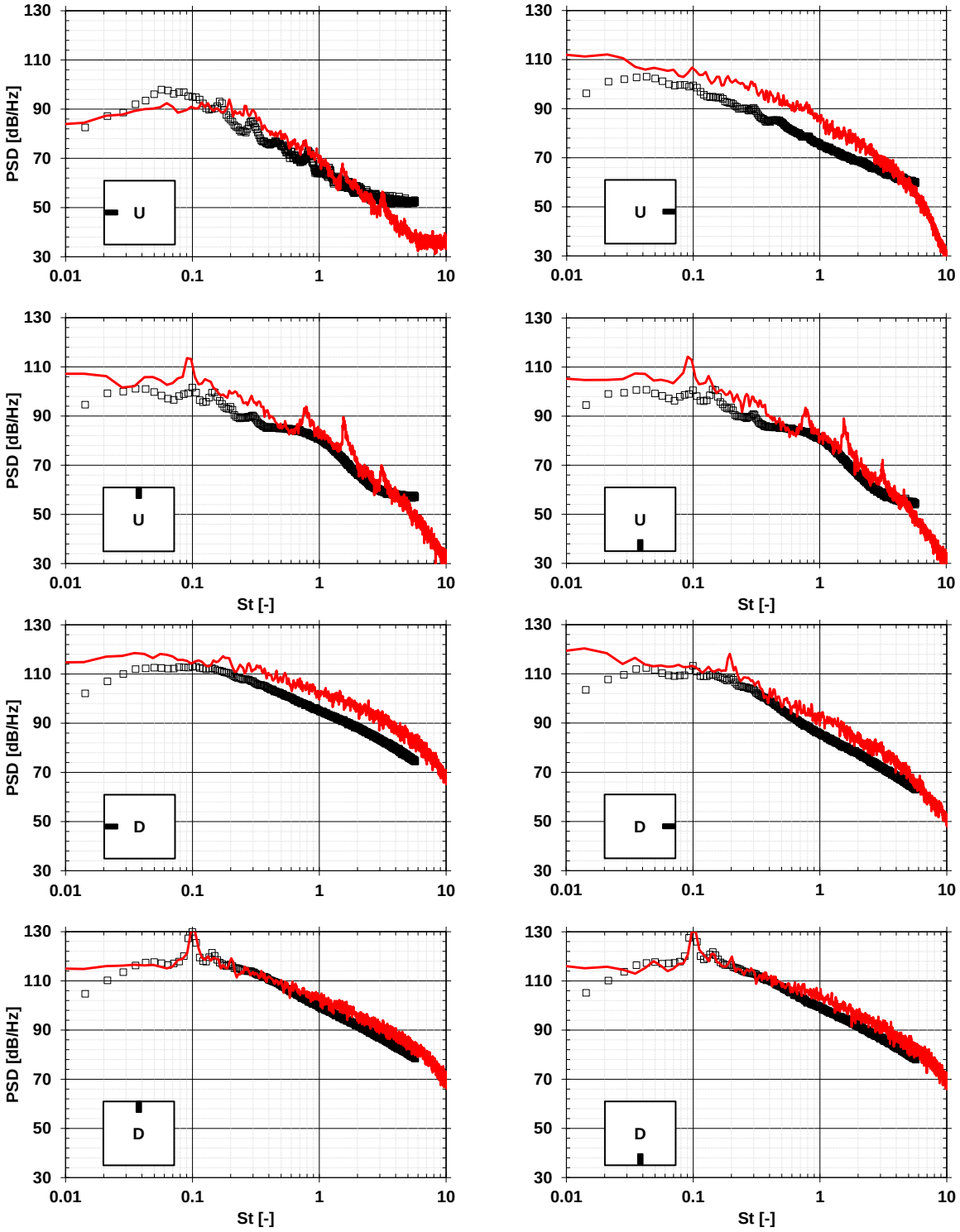

Figure 4.16: Surface pressure spectra on different surfaces of the upstream (U) and downstream (D) cylinders for the quiet flow state. Red lines correspond to numerical results and black square symbols to wind tunnel measurements.

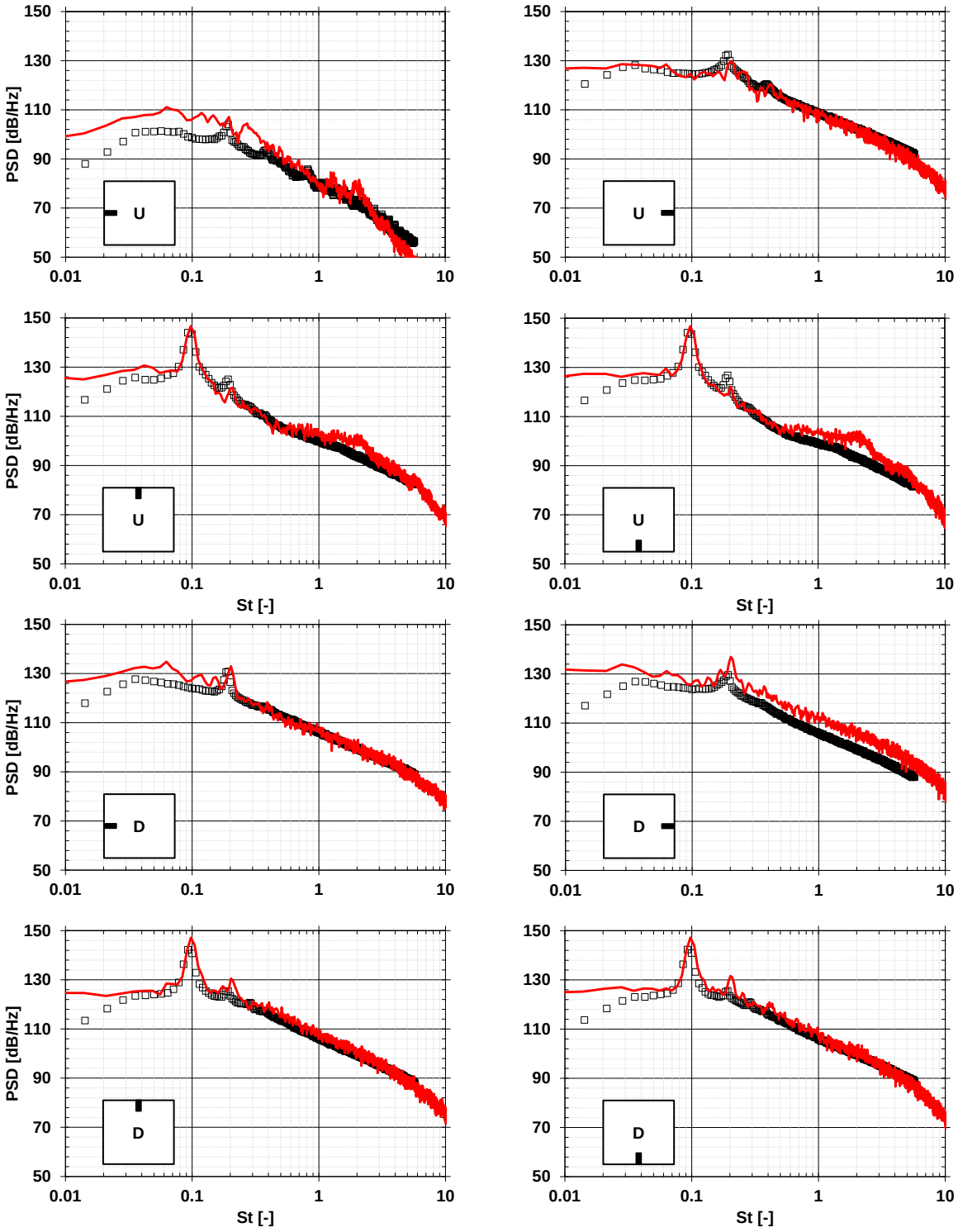

Figure 4.17: Surface pressure spectra on different surfaces of the upstream (U) and downstream (D) cylinders for the loud flow state. Red lines correspond to numerical results and black square symbols to wind tunnel measurements.

Regarding the downstream cylinder in the loud flow state, the simulated surface pressure spectra in Figure 4.17 show good agreement with wind tunnel measurements on all surfaces.

Both primary and secondary frequencies are well predicted as well as the broadband part of the spectra. Only deviations can be observed on the downstream surface, which were also observed in the numerical results in [51] and [3]. This is mainly attributed to the interaction between the free jet and the wake of the cylinders.

Spanwise coherence

Although no experimental data for the spanwise coherence were provided, this section shows the distributions of the correlation coefficient and coherence function along different surfaces of the cylinders and compares them with the numerical results presented in [51]. Moreover, the effects of the limited span and periodic boundary conditions become more apparent when comparing the distributions between the limited and the full span setups. It is worth mentioning that two different features can alter the distributions of correlation coefficient and coherence function along the cylinders: the periodic boundary conditions, which can increase the correlation between different points on a surface. This has already been studied on the tandem circular cylinders benchmark in [13]. On the other hand, the shorter span in the limited span case can itself cause an increase in the spanwise coherence due to the shorter distance between the boundaries in the spanwise direction. This has also been observed for the tandem circular cylinders benchmark [66]. In this work, the comparison between the coherence/correlation between the limited and full span test cases includes the superposition of the effects of both features.

Figure 4.18 shows the distribution of the magnitude-squared coherence as a function of the Strouhal number and the normalised distance $\Delta y/D$, which corresponds to the distance between two different points for which the coherence function is calculated. The magnitude-squared coherence function is defined as [70]:

$$\Upsilon_{ab}(f) = \frac{|G_{ab}(f)|^2}{G_{aa}(f)\,G_{bb}(f)}. \tag{4.3}$$

In Eq. (4.3), $a(t)$ and $b(t)$ correspond to two time signals, G_{ab} to the cross-spectral density between both signals, and G_{aa} and G_{bb} to the autospectral density of the signals $a(t)$ and $b(t)$, respectively. In this study, $a(t)$ and $b(t)$ corresponds to two transient pressure signals. Usually, the pressure exhibits a slower decay than the velocity components in the spanwise direction. Hence, the pressure is suitable for the assessment of the spanwise length of the cylinders. The spanwise coherence is calculated by setting the reference signal $a_{\mathrm{ref}}(t) = p_{\mathrm{ref}}(t)$ equal to the pressure signal at the center of a surface $y_{\mathrm{ref}} = 0$, and varying the second signal $b(t) = p(y_i,t)$ across the span of the corresponding surface. Hereby, y_i corresponds to the points on the mid-lines of the cylinders surfaces extending between $0 \leq y \leq L_{\mathrm{lim}}/2$.

Beside the spanwise coherence, the Pearson correlation coefficient $\Xi_{xy}(z)$ is calculated along the span of each cylinder surface according to [7]:

$$\Xi_{ab}(y) = \frac{\mathrm{cov}(a,b)}{\sigma_a \sigma_b}, \tag{4.4}$$

where $\mathrm{cov}(a,b)$ corresponds to the covariance of the signals $a(t)$ and $b(t)$, and σ_a and σ_b to the standard deviation of $a(t)$ and $b(t)$ respectively. The definitions of $a(t)$ and $b(t)$ are equivalent to the ones used for the calculation of the coherence function.

Since only the loud flow state was shown in [51], the distribution of the coherence function for this flow state is first discussed and the results are compared to those in [51].

Figure 4.18 shows the distribution of the coherence function along different surfaces of the up- and downstream cylinders for the loud flow state. Due to the symmetry of the flow, the distribution on the suction side of the cylinder is shown and the one on the pressure side is omitted. The distributions are equivalent to the ones presented in [51]. On the upstream surface of the upstream cylinder, the coherence function is equal to one for all Strouhal numbers along the complete span. This is due to the uniform flow impinging on that surface. The coherence function on the suction side of the upstream cylinder shows high values at $\mathrm{St} \approx 0.1$, which corresponds to the main shedding frequency. A peak can also be observed for $\mathrm{St} \approx 0.2$, corresponding to the first sub-harmonic. On the downstream surface of the upstream cylinder, high coherence values can be observed for $\mathrm{St} \approx 0.2$. This peak corresponds to the drag-oscillation frequency. Since the drag is not sensitive to the sign of the vortices shed in the wake of the cylinder, the drag-oscillation frequency is equal to the double of the lift-oscillation frequency, which is equivalent to the vortex shedding frequency. In this case, the drag-shedding frequency is equivalent to $\mathrm{St} \approx 0.2$. Furthermore, the coherence values are more pronounced at $\mathrm{St} \approx 0.4$ than in the results of Knacke [51].

On the surfaces of the downstream cylinder, the coherence distributions are almost identical to the results presented in [51]. As for the upstream cylinder, the downstream surface of the downstream cylinder show high coherence values at $\mathrm{St} \approx 0.2$, which corresponds to the drag oscillation frequency. This is also visible in the distribution of the coherence on the upstream surface of the downstream cylinder. On the suction side of the downstream cylinder, the coherence function shows the domination of the main vortex shedding frequency at $\mathrm{St} \approx 0.1$ as well as the first sub-harmonic at $\mathrm{St} \approx 0.2$.

The distribution of the correlation coefficient $\Xi(\Delta y)$ along different surfaces of the cylinders is illustrated in Figure 4.19 for the loud flow state. The pressure signals along the upstream as well as the pressure and suction sides of the upstream cylinder show a constant correlation coefficient of approximately one over the whole span of the cylinder. Only the downstream surface of the upstream cylinder show a descending correlation coefficient distribution in the spanwise direction. However, the minimum value of the coefficient is approximately 0.8 at $\Delta y = 1.5D$. These high values are attributed to the applied periodic boundary conditions in combination with the limited spanwise extent.

A qualitative similar behaviour can be observed for the downstream cylinder for the loud flow state, i.e., the distribution of the correlation coefficient is higher than 0.9 over the whole span except for the downstream surface, where the coefficient reaches a minimum value of $\Xi \approx 0.71$ at $\Delta y = 1.5D$. Moreover, for $\Delta y > D$, the correlation distribution on the downstream surface shows an almost constant value. This applies for the upstream as well as the downstream cylinders.

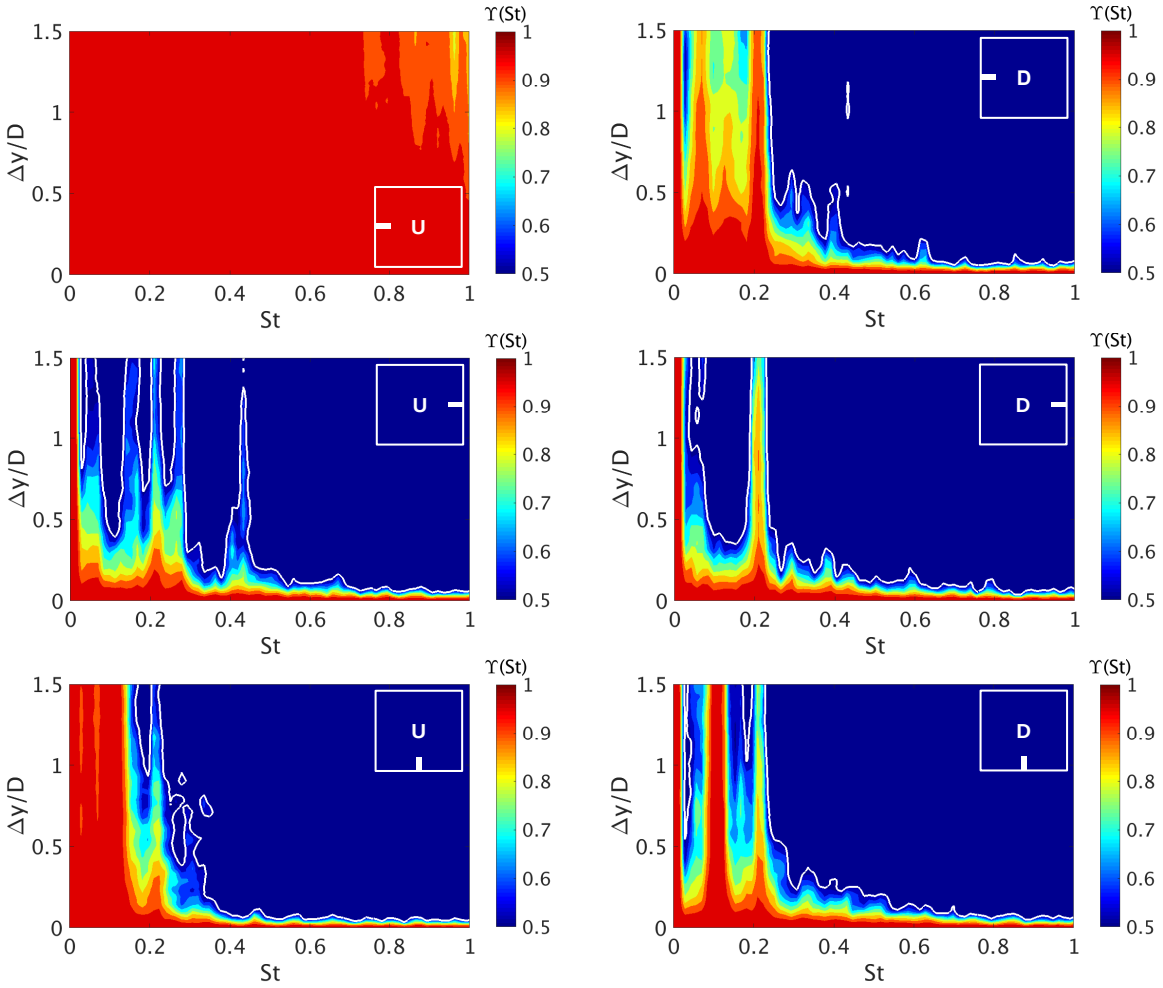

Figure 4.18: Magnitude-squared coherence function $\Upsilon\,(\mathrm{St}, \Delta y/D)$ along the surfaces of the up- (U) and downstream (D) cylinders for the loud flow state. The white solid line corresponds to the contour $\Upsilon = 0.5$.

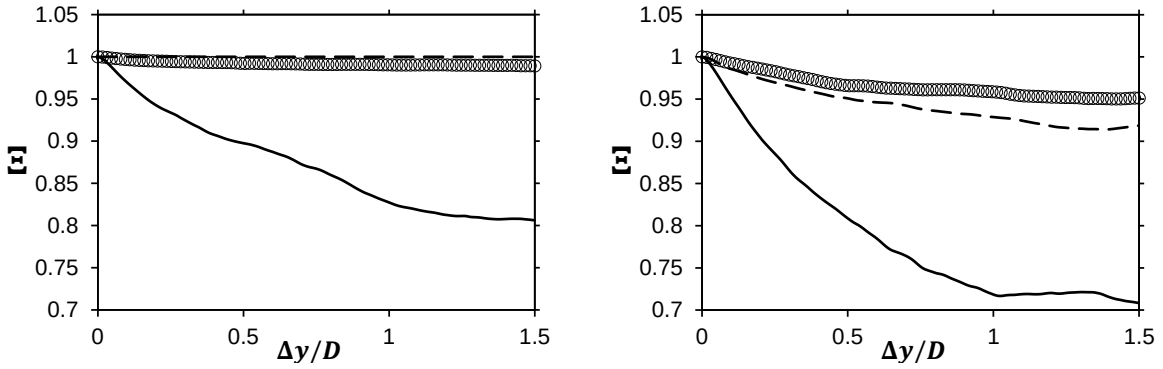

Figure 4.19: Correlation coefficient $\Xi(\Delta y/D)$ at different surfaces of (left) the upstream and (right) downstream cylinders for the loud flow state. (——) correspond to the downstream, (— —) the upstream surfaces, and (○) to the surfaces on the suction side of the cylinders.

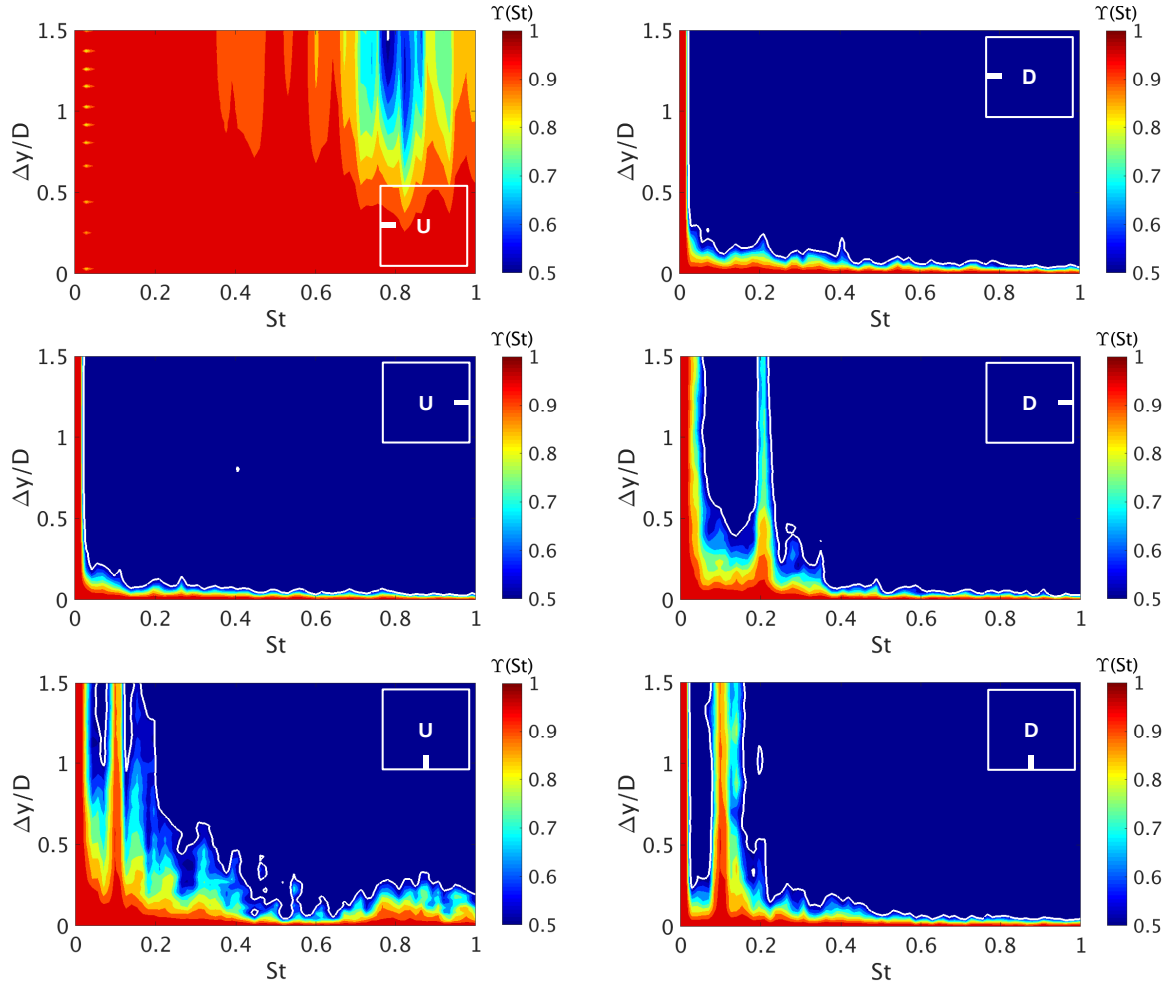

Figure 4.20: Magnitude-squared coherence function $\Upsilon\,(\mathrm{St}, \Delta y/D)$ along the surfaces of the up- (U) and downstream (D) cylinders for the quiet flow state. The white solid line corresponds to the contour $\Upsilon = 0.5$.

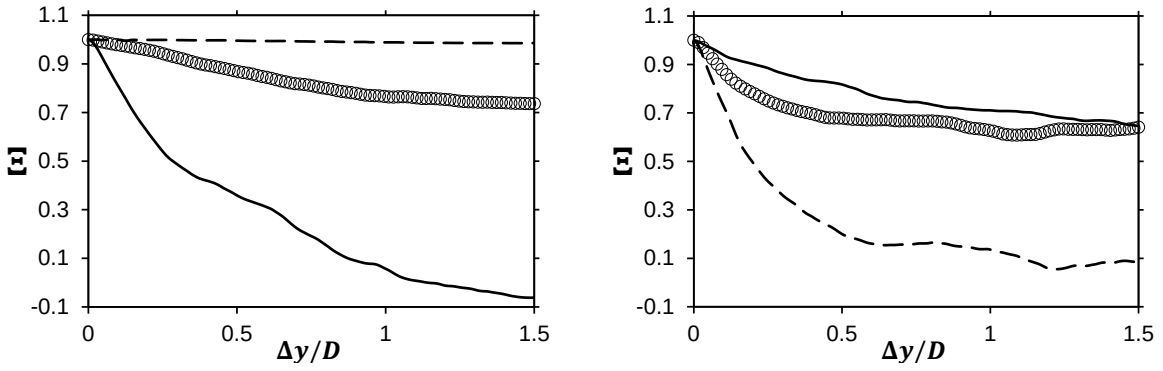

Figure 4.21: Correlation coefficient $\Xi(\Delta y/D)$ at different surfaces of (left) the upstream and (right) downstream cylinders for the quiet flow state. (——) correspond to the downstream, (— —) the upstream surfaces, and (○) to the surfaces on the suction side of the cylinders.

Figure 4.20 shows the coherence function distribution over different cylinder surfaces for the quiet flow state. In general, the coherence magnitude is lower than in the loud flow state. This could be related to the absence of the dominating vortex shedding in the wake of the upstream cylinder. The upstream surface of the upstream cylinder shows, similar to the loud flow state, high coherence values due to the uniform flow impinging on the surface of the upstream cylinder. The downstream surface of the upstream cylinder as well as the upstream surface of the downstream cylinder show low coherence values over the whole frequency range. This indicates uncorrelated pressure fluctuations, which could be attributed to the small turbulent length scales in the gap between the cylinders. The absence of vortex shedding between the cylinders results in the absence of large flow structures. This can be a reason for minimising the effect of the periodic boundary conditions and the limited span used in the simulation and, as a result, low coherence values along the surfaces facing the gap between the cylinders. The cylinders surface on the suction side show high coherence values at $\mathrm{St} \approx 0.1$. This corresponds to the vortex shedding frequency in the wake of the downstream cylinder. The oscillations in the drag force can be observed in the coherence distribution on the downstream surface of the downstream cylinder, where high coherence values are observed at $\mathrm{St} \approx 0.2$, which corresponds to the double of the vortex shedding frequency.

The distributions of the correlations coefficient $\Xi(\Delta y)$ are presented in Figure 4.21. As in the loud flow state, the upstream surface of the upstream cylinder show high correlation over the whole span. Other surfaces of the upstream cylinder in the quiet flow state show significantly lower correlation coefficients than in the loud state. On the downstream surface, the distribution of Ξ reaches negative values for $\Delta y/D > 1$. This behaviour is consistent with the distribution of the coherence function presented in Figure 4.20. The distributions of the correlation coefficient on the surfaces of the downstream cylinder in the quiet flow state also show lower values than in the loud flow state, which is also consistent with the coherence maps in Figure 4.20. Moreover, a remarkable behaviour of the distribution of Ξ on the upstream surface of the downstream cylinder can be observed. It shows a very similar distribution to that on the downstream surface of the upstream cylinder. Moreover, the correlation coefficient on the upstream surface is significantly lower than the distributions on the other surfaces of the downstream cylinder. These facts favour the assumption of smaller turbulent length scales in the flow between the cylinders in the quiet flow state.

4.3.3 Aeroacoustic results

In this section, aeroacoustic far-field spectra are compared between simulation and experiment. The far-field microphones are positioned at the points shown as Figure 4.2. These correspond to the corrected positions of the microphones utilised in the experiment. The calculation of acoustic waves in the far-field is performed using two different methods:

- Direct Noise Calculation (DNC): the flow solver used to calculate the turbulent flow field calculates density fluctuations based on the isentropic relation in Eq. (2.16). This relation can be considered valid for low-Mach number flows, which is the case for the two-struts

Benchmark. Hence, the solution of the equations contain the generation of acoustic waves. At the same time, the solver is able to propagate acoustic waves into the far-field. Due to low-order schemes utilised in this work, the spacial and temporal resolution in the far-field should be high enough to avoid significant wave dissipation and dispersion. This has already been discussed in subsection 4.3.1. It is worth mentioning that the capability of the low-Mach number solver to calculate acoustic waves generation and propagation is not known a priori. Hence, the goal of this study is to validate its capability and suitability for such flow problems, and, on the other hand, compare its performance to other CAA methods. Snapshots of acoustic waves in the computational domain at $t = 0.5$ s are shown for both flow states in Figure 4.22.

- The second method utilised in this study to calculate far-field spectra is an integral method based on the FWH-formulation for rigid stationary surfaces, as described in chapter 2. Due to the low-Mach number in the two-struts benchmark, one can neglect the effect of volume noise sources compared to surface sources. This fact has already been proved by Knacke in [51], who compared results of integral noise computation using permeable and solid integration surfaces. For a fair comparison between the integral method and DNC, the transient pressure values calculated by the flow solver are used as input data for the integral method. Hereby, the values are written out each second time-step, corresponding to a sampling frequency of 100 kHz. Since the integral method is not affected by the spacial resolution of the far-field, acoustic spectra are calculated on 360 microphones placed on a circle with a radius of $r = 50D$ and centred around the upstream cylinder. This can be used for a detailed description of the directivity pattern of sound waves emitted by the cylinders. A further advantage of the integral method is the ability to calculate sound waves emitted by each cylinder individually. This is not possible with the DNC method, since its solution consists of the superposition of all acoustic waves emitted by both cylinders.

The following section consists of two parts: first, far-field spectra are presented and compared to wind-tunnel measurements at certain microphone positions for both flow states. In the second part, directivity patterns are shown and compared to experimental data. Furthermore, directivity patterns of each cylinder calculated using the integral method at different frequencies are presented and compared to the results in [51] for the loud flow state.

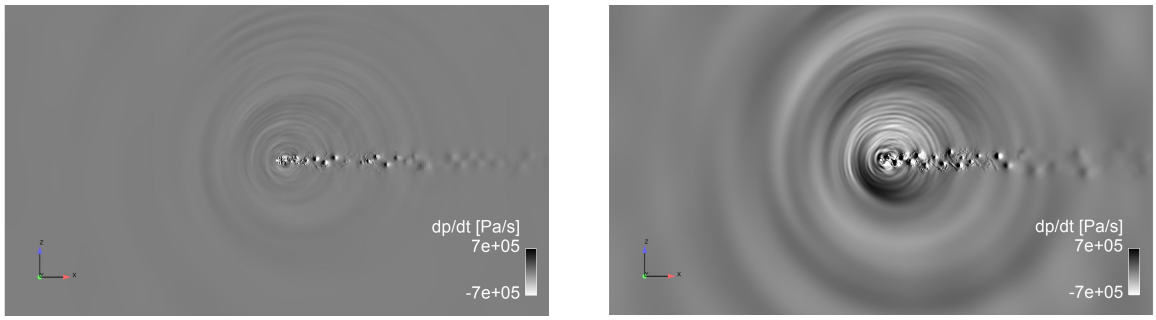

Figure 4.22: Snapshots of $\partial p/\partial t$ at $t = 0.5$ s for (left) the quiet flow state and (right) the loud flow state. The images show the whole computational domain. The upstream cylinder is positioned at the center of the domain.

Far-field spectra

A major difference between the limited-span simulation and the experiment is the spanwise length of the cylinders. The far-field microphones in the experiment measured acoustic waves emitted from two square cylinders, whose length is $L_{\text{exp}} = 12.5D$. When calculating far-field spectra using the integral method, the input data contain pressure fluctuations on the surfaces of the cylinders, whose spanwise length is $L_{\text{lim}} = 3D$. Therefore, the result of such calculations would be the noise generated by two square-cylinders with a span L_{lim}. The same applies when directly calculating acoustic waves using the compressible flow solver. In order to make numerical results comparable with experimental data, far-field spectra have to be corrected in order to account for the difference in the spanwise length. There exist several correction methods to compensate such difference. The method utilised in this work is the one proposed by Kato et al. [49], who proposed a correction of the PSD-spectra according to $\text{PSD}_{\text{corr}} = \text{PSD}_{\text{lim}} + \Delta_{\text{dB}}(f)$, where Δ_{dB} is a frequency dependent correction factor and is defined as:

$$\Delta_{\text{dB}}(f) = \begin{cases} 10\log_{10}\left(\dfrac{L_{\text{exp}}}{L_{\text{lim}}}\right) & \text{if } l(f) \leq L_{\text{lim}} \quad (4.5a) \\ 10\log_{10}\left(\dfrac{L_{\text{exp}}}{l(f)}\right) + 20\log_{10}\left(\dfrac{l(f)}{L_{\text{lim}}}\right) & \text{if } L_{\text{lim}} < l(f) < L_{\text{exp}} \quad (4.5b) \\ 20\log_{10}\left(\dfrac{L_{\text{exp}}}{L_{\text{lim}}}\right) & \text{if } L_{\text{exp}} \leq l(f) \quad (4.5c) \end{cases}$$

where $l(f)$ corresponds to the frequency dependent spanwise coherence length. According to Kato et al. [49], this length is equal to the length Δy, for which the coherence function $\Upsilon(f)$ reaches a values of 0.5. According to the coherence function distributions in Figure 4.18 and Figure 4.19, each surface could have a different coherence length at different frequencies. Hence, it is not trivial to determine a single coherence length for each cylinder. However, as the coherence distributions show that the coherence length on most cylinder surfaces can be considered greater than the experimental spanwise length of the cylinders in the region of vortex shedding frequency ($\text{St} \approx 0.1$). This applies for both flow states. Moreover, one can also observe that the distributions of the coherence function in Figures 4.20 and 4.22 show an abrupt decay in the broadband frequency region ($\text{St} > 0.3$). Consequently, one can assume that the coherence length $l(f)$ is smaller than the simulated spanwise length L_{lim}. Correspondingly, the PSD-spectra in the region of the vortex shedding frequency can be corrected using Eq. (4.5c) and the spectral levels in the broadband region can be corrected using Eq. (4.5a). These corrections corresponds to $\Delta_{\text{dB}} \approx +12.4$ dB and $\Delta_{\text{dB}} \approx +6.2$ dB, respectively.

Another major difference between the limited-span simulation and the experiment are the the spanwise boundary conditions. The periodic boundary conditions utilised in the experiment have two major effects on the numerical results. First, the spanwise coherence is generally increased by periodic boundary conditions. Knacke [51] used the data of one half of the spanwise length of the cylinders as an input for the integral method in order to decrease

the effect of periodic boundary conditions regarding the increased spanwise coherence. In this work, pressure fluctuations on the whole spanwise length ($L_{\text{lim}} = 3D$) are used as an input for the integral method, since the effect of periodic boundary conditions is not observed in the far-field spectra. The second effect of periodic boundary conditions is the reflection of acoustic waves calculated directly using the compressible solver. When an acoustic wave propagates through a periodic boundary, it re-enters the computational domain through the opposite corresponding boundary. Thus, acoustic waves stay trapped in the computational domain. Depending on the location of the microphones, these waves can cause constructive or destructive interference, that is not present in the experiment. Furthermore, the nature of wave interference is also frequency dependent. Thus, a direct comparison between far-field spectra calculated using DNC and experimental results is not straightforward, and it is expected that the directly calculated spectra would not show good agreement with experimental results.

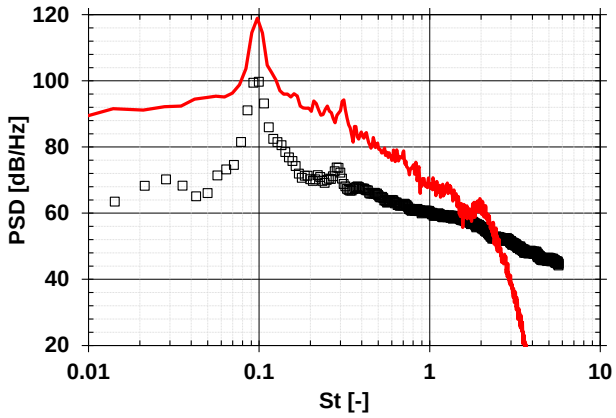

Figure 4.23: Far-field PSD spectra for the loud flow state at $\theta = 93°$. Red solid line corresponds to of DNC and square symbols to wind tunnel measurements.

Figure 4.23 shows calculated far-field spectra using DNC compared to wind tunnel measurements at $\theta = 93°$. The vortex shedding frequency at St ≈ 0.1 is well predicted by the simulation. The same applies for the sub-harmonic at St ≈ 0.3. However, the spectral levels calculated by DNC are substantially higher than those measured in the wind-tunnel. This is caused by the periodic boundary conditions, which prevent acoustic waves from leaving the computational domain. Moreover, the slope of the calculated PSD spectrum does not correspond to the experimental data. This is due to the frequency dependency of the effect of periodic boundary conditions. Therefore, DNC results are not further investigated for the limited-span case and the following results are restricted to those calculated using the integral method.

Figure 4.24 shows PSD-spectra calculated using the integral method at two different microphone positions compared to experimental results. The spectral levels at the vortex shedding frequency (St ≈ 0.1) are well predicted at both microphones. The first sub-harmonic at $\theta = 93°$ is also well predicted by the simulation. The same applies for the drag frequency at St ≈ 0.2 and $\theta = 32°$. The simulated broadband part show good agreement with wind tunnel measurements at $\theta = 93°$. At $\theta = 32°$, the simulation show slightly higher spectral

levels in the broadband part. This could be caused by the absence of acoustic-hydrodynamic interaction in the FWH-method. Furthermore, the corrections made in the experiments in order to account for shear-layer effects using the Amiet method could introduce some errors in the spectral levels, especially for small angles. Nevertheless, an overall good agreement between the simulated spectra and experimental data can be observed.

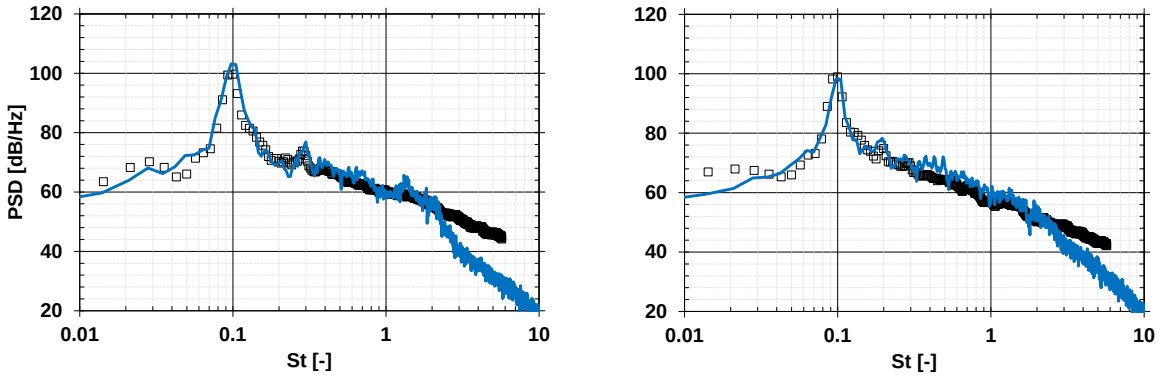

Figure 4.24: PSD-spectra of the loud flow state at (left) $\theta = 93°$ and (right) $\theta = 32°$. Blue solid lines correspond to FWH and black square symbols to wind tunnel measurements.

In the low-frequency region ($St < 0.08$), numerical results show some deviations from experimental ones. As already mentioned in section 4.2, background noise was determined by the experimenter using an empty wind-tunnel section and the spectral level was set to the background noise level if the signal-to-noise ratio is less than 3 dB. The frequencies, for which background noise dominates, depend on the flow state and on the microphone position. For the loud flow state, background noise dominated up to $St \approx 0.08$. Therefore, a comparison between numerical and experimental results for $St < 0.08$ would not be meaningful.

Although mean flow variables show large discrepancies between the simulation and experiment for the quiet flow state, far-field spectra were calculated for this flow state and compared to wind-tunnel measurements. Figure 4.25 shows a comparison between the integral method and experimental results at two different microphone positions. For low-frequencies ($St < 0.08$), numerical spectral levels are substantially lower than those in the experiment. Due to the dominance of background noise in this frequency range, these differences are not further discussed. The location of the peak at the vortex shedding frequency $St \approx 0.1$ is well predicted by the simulation. The simulated spectral level at this frequency shows good agreement with wind-tunnel measurements for $\theta = 93°$, while the simulated level at $\theta = 32°$ is lower than the experimental one. Despite the large deviations between the simulated surface pressure spectra and the measured ones in the broadband part, simulated far-field spectra show generally good agreement with wind-tunnel measurements. This applies especially for large angles ($\theta = 93°$). At $\theta = 32°$, the simulated broadband part shows higher levels than the measured ones. This could be the result of the interaction between the acoustic waves and the wake of the cylinders, which is not included in the calculation of far-field spectra using the integral method. The peaks that have been observed in the surface pressure spectra on the up- and downstream surfaces of the upstream cylinder in Figure 4.16

are not pronounced in the far-field spectra, which indicates their minor contribution in noise emission for the quiet flow state.

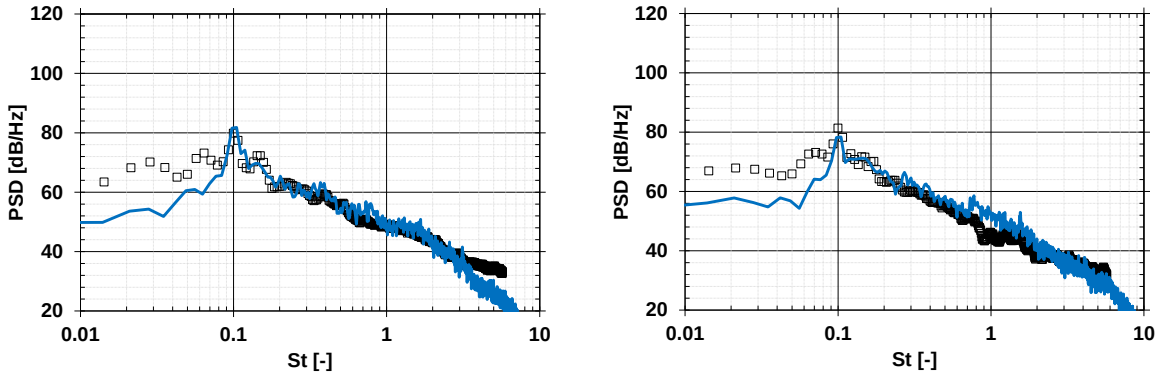

Figure 4.25: PSD-spectra of the quiet flow state at (left) $\theta = 93°$ and (right) $\theta = 32°$. Blue solid lines correspond to FWH and black square symbols to wind tunnel measurements.

Directivity patterns

Besides far-field acoustic spectra, directivity patterns based on the sound pressure level L_p are calculated using the integral method for both flow states. Similar to far-field spectra, the directivity patterns are corrected according to Eq. (4.5a) and (4.5c). The sound pressure level is calculated using the root mean square (rms) values of sound pressure at the same locations as for the far-field microphones:

$$L_p = 20\log_{10}\left(\frac{p_{\text{rms}}}{p_{\text{ref}}}\right). \tag{4.6}$$

Figure 4.26 shows the directivity patterns for both flow states at different frequencies. For the loud flow state, the directivity of the overall sound pressure shows a typical dipole characteristic, and it shows good agreement with wind-tunnel measurements. The dipole characteristic shows the dominance of acoustic waves caused by the oscillating lift-force at the main vortex shedding frequency $\text{St} \approx 0.1$. This dominance has already been observed in the far-field PSD-spectra. At $\text{St} \approx 0.6$, sound waves are emitted almost equally in all directions. The simulated directivity patterns are approximately 2 dB higher than wind tunnel measurements for $\theta \geq 49°$. For $\theta = 32°$, deviations up to 5 dB can be observed, which was also observed in the far-field PSD-spectra. Deviations between the simulation and experiment at low angles becomes more pronounced at $\text{St} \approx 1$, where the simulated patterns show good agreement with experimental data for $\theta \approx 95°$ but deviations up to 3 dB for $\theta = 32°$. As already mentioned, these deviations could be attributed to the absence of interaction effects between the wake of the cylinders and acoustic waves when calculating far-field acoustic using the integral method.

For the quiet flow state, the overall directivity pattern does not show a typical dipole characteristic as for the loud flow state. The far-field PSD-spectra showed that the spectral levels

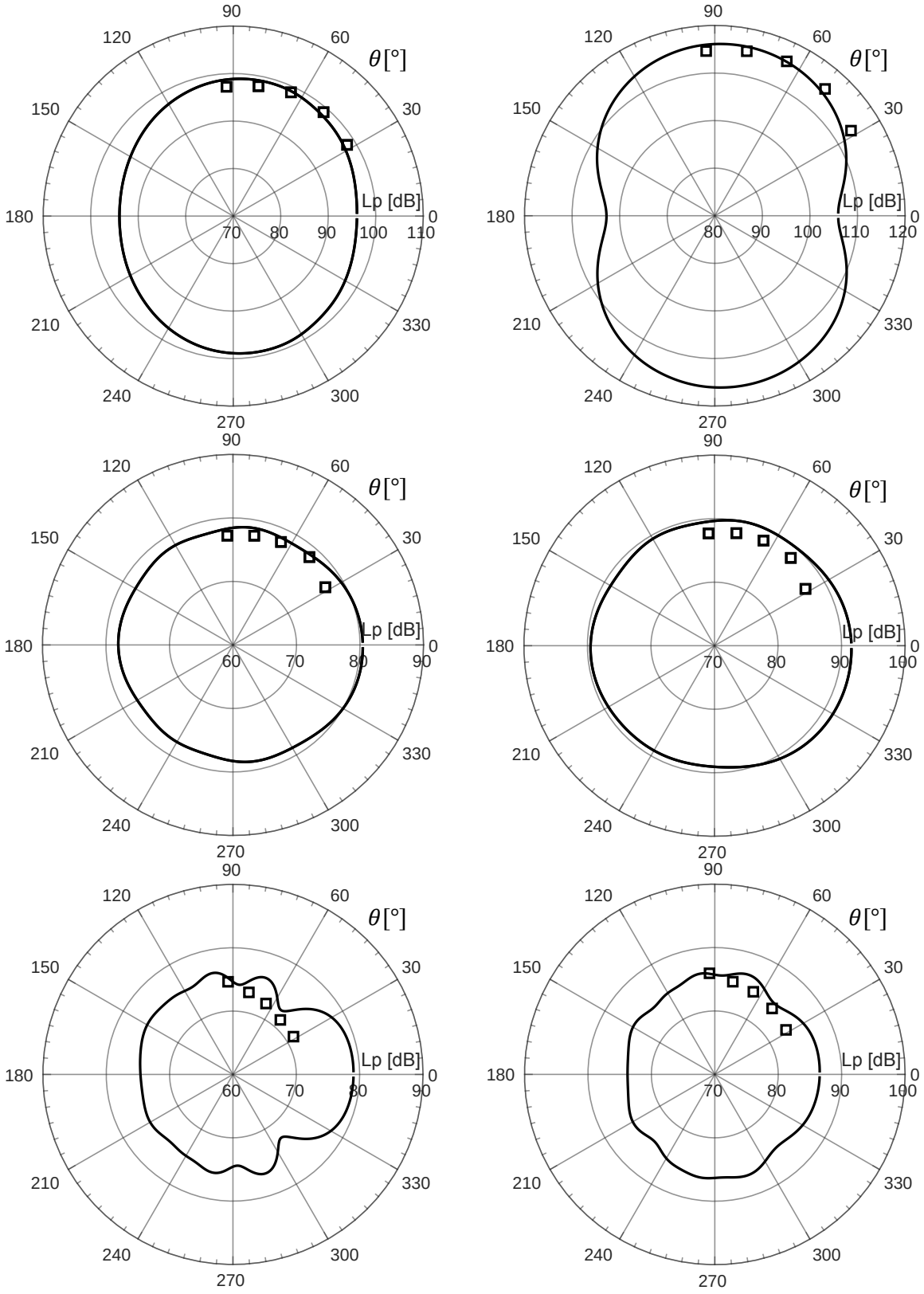

Figure 4.26: Directivity patterns of the tandem square cylinder configuration for (left) the quiet and (right) the loud flow states. The first row corresponds to the overall sound pressure level, the second to St ≈ 0.6, and the third to St ≈ 1. Black solid lines correspond to FWH results and square symbols to wind tunnel measurements.

at the main vortex-shedding frequency is not as dominating as the ones in the loud flow state. Moreover, the dominance of sound emission at $\theta = 32^\circ$ is lower than that at $\theta = 93^\circ$. Hence, in the direction of the axis connecting the centres of both cylinders, frequency components other than the vortex shedding frequency could be the dominant part in the overall sound pressure level, while the vortex shedding frequency dominates sound emission above and below the cylinders. The result is an oval shaped directivity pattern as shown in Figure 4.26. At $\mathrm{St} \approx 0.6$ and $\mathrm{St} \approx 1$, the simulated directivity patterns show good agreement with experimental results for high angles $\theta \geq 49^\circ$. At $\theta = 32^\circ$, simulated sound pressure levels are higher than measured ones. The reasons for this behaviour has already been discussed for the loud flow state.

4.4 Full-span case

The limited-span case was used in order to validate the integral method for aeroacoustic computation. Due to periodic boundary conditions, acoustic waves calculated directly using the compressible flow solver got reflected on the spanwise boundaries and a validation of DNC was omitted.

In order to validate the ability of the compressible solver to accurately calculate noise generation and waves propagation, a full-span case is calculated. The full-span case corresponds to the exact setup as in the experiment, except for the shear layers of the free-jet. The spanwise length of the setup corresponds to that of the experiment ($L_{\mathrm{full}} = 12.5D$). Additionally, the endplates, on which the cylinders were fixed, are included in the simulation and the effect of their perforation is analysed. In the following, a brief description of the numerical setup is given, and an analysis of the aerodynamic results based on mean flow variables and statistical analysis of surface pressure fluctuations is presented. Finally, far-field spectra and directivity patterns calculated using FWH and DNC are compared to experimental results.

4.4.1 Numerical setup

Figure 4.27 illustrates the geometry employed in the full-span case. The dimensions of the plates correspond to those utilised in the experiment. In the x- and z-directions, the dimensions of the computational domain are equivalent to those of the limited-span case. In the y-direction, the computational domain was extended to $40D$, resulting in a distance between each endplate and its corresponding spanwise boundary of approximately $13.6D$. This zone acts as buffer-layer, which allows acoustic waves to partially dissipate and leave the computational domain in the spanwise direction without being reflected back into the domain.

The grid topology in the x- and z- directions is equivalent to the ones utilised for the limited-span case. The only difference in the grid is its extension in the y-direction. Figure 4.27 (right) shows a slice of the computational grid at $z = 0$.

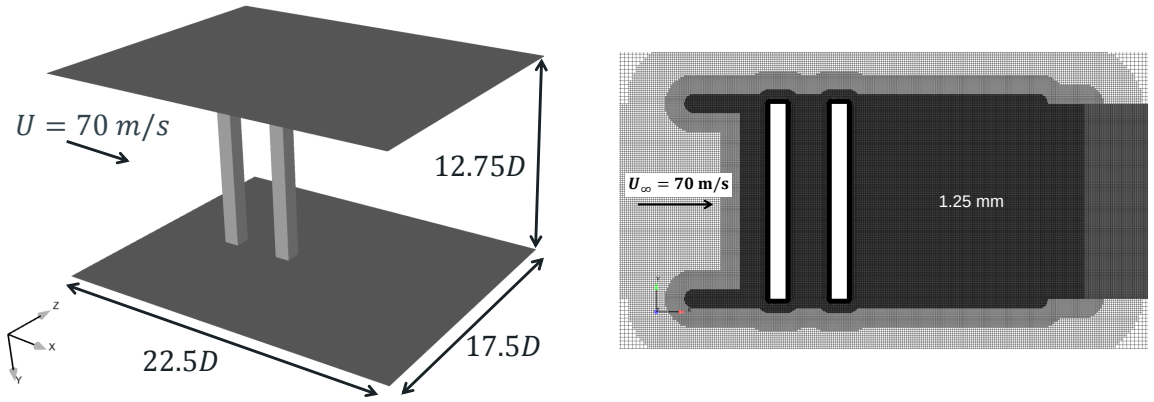

Figure 4.27: Geometry of the two-struts with the endplates used for the full-span case (left) and a slice of the grid at $z = 0$ (right). Left figure is take from [19].

The numerical parameters utilised for the full-span case are equivalent to the ones used for the limited-span case. This also applies for the microphone positions, the simulated physical time, and the sampling frequency of pressure fluctuations at the surfaces of the cylinders and in the far-field. Regarding the initialisation of the velocity field, the full-span case results in the same behaviour as the limited-span case: a uniform initial velocity fields leads to the quiet flow state and the loud flow state can only be achieved by triggering the vortex shedding using an initial vortex according to Eq. (4.1).

4.4.2 Aerodynamic results

Similar to the limited-span case, an analysis of the mean flow variables and surface pressure fluctuations is performed for the full-span case, and major differences between the results of both cases are presented.

Mean flow field

Figure 4.28 shows streamlines calculated using the mean velocity field of the full-span case for both flow states compared to PIV measurements. Comparing the results to the ones in Figure 4.5, no major differences can be observed. The locations of the vortex pairs in the wake of the upstream cylinder are almost identical between the limited- and the full-span cases, and the deviations compared to PIV measurements are similar. Hence, these deviations are not the result of periodic boundary conditions or the short spanwise length, and are rather related to the aforementioned installation effects. These effects are also responsible for the slight deviations between the streamlines in the simulation and PIV measurements in the free-stream, which are caused by the higher pressure outside the free-jet in the wind tunnel. These effects are observed in the limited- and full-span case. For the loud flow state, the good agreement between numerical and experimental results in Figure 4.5 for the limted-span case is also observed for the full-span case in Figure 4.28. A better agreement between the calculated and measured streamlines can be observed in the near-field of the

cylinders in the full-span case. However, this could be related to the limited simulated physical time. A longer averaging time would probably result in identical results between the full- and limited-span cases.

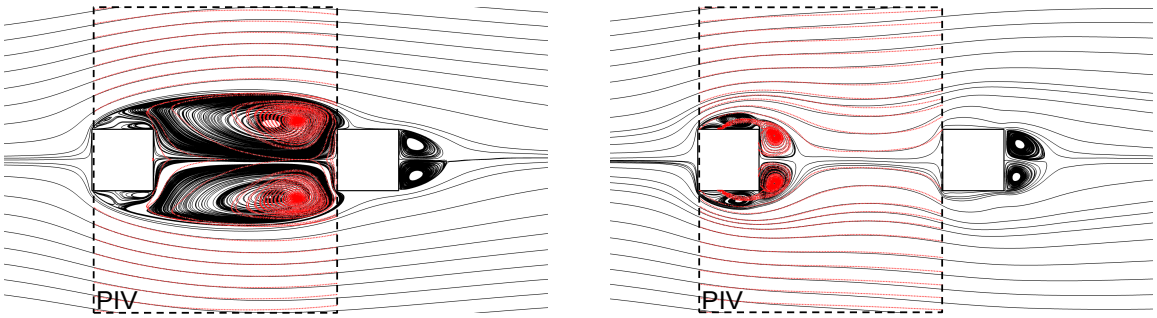

Figure 4.28: Streamlines using the mean velocity field for (left) the quiet flow state and (right) the loud flow state. (——) represent numerical results and (·····) PIV measurements. Numerical results correspond to the full-span case.

The isolines of the averaged velocity fields $\langle U_x \rangle$ and $\langle U_z \rangle$ resulting from the full-span case are almost identical to the ones showed in Figures 4.6 and 4.7 for the limited-span case. Therefore, a discussion of these fields is not presented in this section.

Mean pressure coefficient

As for the limited-span case, the mean pressure coefficient for the full-span case is calculated along the surfaces of both cylinders according to Eq. (4.2). Figures 4.29 and 4.30 show the distribution of the pressure coefficient C_p along the up- and downstream cylinders for both flow states. Compared to the results of the limited-span case, the results of the full-span case show better agreement with wind tunnel measurement on the upstream cylinder for the quiet flow state. This can be observed for the surfaces on the pressure and suction sides of the upstream cylinder ($0.5 < d < 1.5$). On the upstream surface of the downstream cylinder, the results of the limited-span case in Figure 4.8 show better agreement with wind-tunnel measurements. A slight displacement of the location of the vortex pair has already been observed in the mean streamlines, which could be related to the limited simulation time. This displacement could be the reason for the deviations in C_p on the upstream surface of the downstream cylinder. Moreover, the pressure coefficient is calculated on at the center of each cylinder. Hence, no averaging of C_p is done in the spanwise direction. A separate analysis of the pressure coefficient distribution at different locations in the spanwise directions did show some fluctuations in the pressure coefficient. Hence, an averaging of C_p in the spanwise direction could show better agreement with experimental results. Due to the small deviations observed for the quiet flow state, such averaging is not performed in this study.

Comparing the results of the full-span case for the loud flow state in Figure 4.30 to the results in Figure 4.9, a noticeable improvement in the calculation of the pressure coefficient distribution can be observed. This applies for the upstream cylinder at $0.5 < d < 1.5$ as well as the downstream cylinder at $d > 0.5$. Hence, low C_p values at the downstream surface

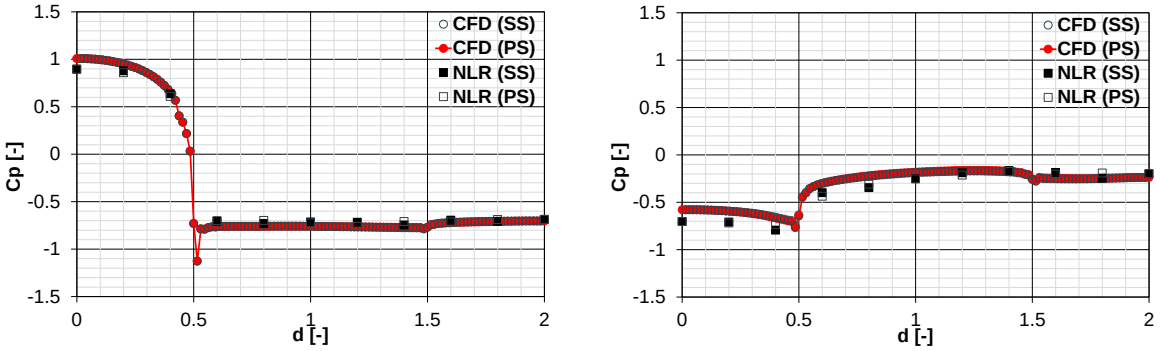

Figure 4.29: Time-averaged surface pressure coefficient C_p along (left) upstream and (right) downstream cylinders for the quiet flow state using the full-span setup.

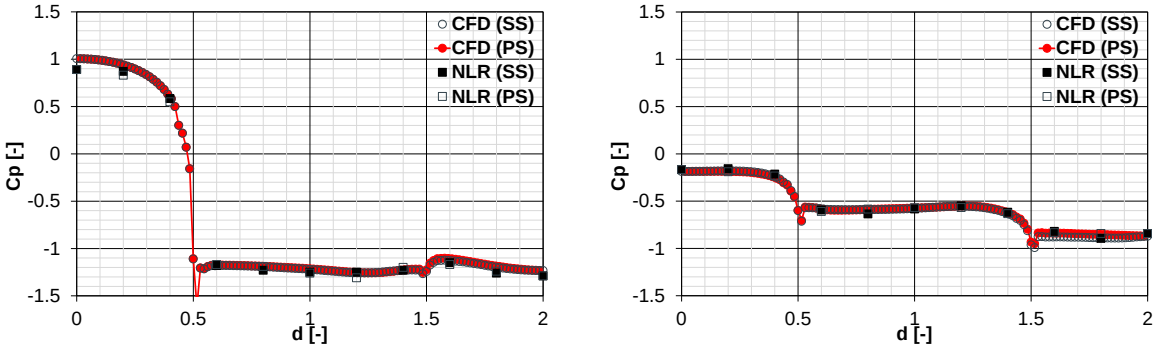

Figure 4.30: Time-averaged surface pressure coefficient C_p along (left) upstream and (right) downstream cylinders for the loud flow state using the full-span setup.

of the downstream cylinder in Figure 4.9 are indeed related to the limited spanwise length and not to the interaction between the wake of the cylinders and the potential core of the free-jet.

Turbulence statistics

The analysis of turbulence statistics for the full-span case showed the same results as was already seen for the limited span case (cf. Figures 4.13 to 4.15) and are thus not presented in this work.

Surface pressure spectra

The calculation of surface pressure spectra for the full-span case is performed with the same parameters as described in Table 4.1. The spectra on each surface of the both cylinders and for each flow state is calculated and compared to experimental results. Figure 4.31 shows the surface pressure spectra on the surfaces of both cylinders for the quiet flow state. Due to the symmetry of the flow, pressure spectra are only presented for one side of the cylinders (pressure side).

On the upstream surface of the upstream cylinder, numerical data show better agreement with experimental results compared to the limited-span case in Figure 4.16. This applies for the low-frequency region ($St < 0.1$) as well as the broadband region $St > 0.2$. On the downstream surface of the upstream cylinder, the simulated spectrum is almost identical to the one in the limited-span case in Figure 4.16. The spectral level of the simulated data is approximately 10 dB higher than the measured ones. This could be related to the difference in the location of the vortex pair in the wake of the upstream cylinder between the simulation and experiment (cf. Figure 4.28). On the upstream surface of the downstream cylinder, a continuous distribution of the simulated pressure spectrum can be observed and the agreement between numerical and experimental results is substantially better than in the limited-span case, especially in the broadband part.

The spectra on the surfaces of the downstream cylinder in the full-span case are almost identical to the ones in the limited-span case. The only remarkable difference is the absence of the peak at $St \approx 0.2$ on the downstream surface, which leads to a better agreement with wind-tunnel measurement. Hence, in general, the surface pressure spectra in the full-span case show better agreement with wind-tunnel measurements than the limited-span case. This could be the result of the absence of periodic boundary conditions as well as the extended spanwise length of the cylinders, which correspond to the exact length of the experimental setup.

For the loud flow state, surface spectra of the full-span case are shown in Figure 4.32. Compared to the simulated spectra of the limited-span case in Figure 4.17, the spectra of the full-span case show better agreement with wind-tunnel measurements in the flow frequency region ($St < 0.1$). This applies for the almost all surfaces of both cylinders. On the upstream surface of the upstream cylinder, the drag oscillation frequency ($St \approx 0.2$) is clearly captured by the simulation in the full-span case. On the pressure side of the upstream cylinder, the simulated spectrum show better agreement with wind-tunnel measurements than the ones in Figure 4.16 for $St > 0.6$. On the downstream surface of the downstream cylinder, deviations between the simulation and experiment are still present. As already mentioned, these deviations could be the result of the interaction between the potential core of the free-jet in the wind tunnel and the wake of the cylinders. Nevertheless, these deviations decrease in the full-span case compared to the limited-span case.

In summary, the surface pressure spectra calculated using the full-span case show better agreement with experimental results than the limited-span case. Remarkable improvement is observed in the low-frequency region. Pressure fluctuations in this frequency region correspond to large turbulent structures, which could have a larger spanwise extent. These structures could have a characteristic length larger than $3D$. A visualisation of the turbulent structures is presented in Figure 4.33 using the three-dimensional vorticity field. Particularly in the wake of both cylinders, flow structures that possess a spanwise length larger than $3D$ can be observed. Such structures cannot be resolved in the limited-span case and, as a result, pressure fluctuations in the low-frequency range are not captured by the simulation. Furthermore, the full-span setup show better agreement with experimental data in the broadband region. This could be the result of the improved calculation of the spanwise coherence and correlation on one side, and to the absence of periodic boundary conditions

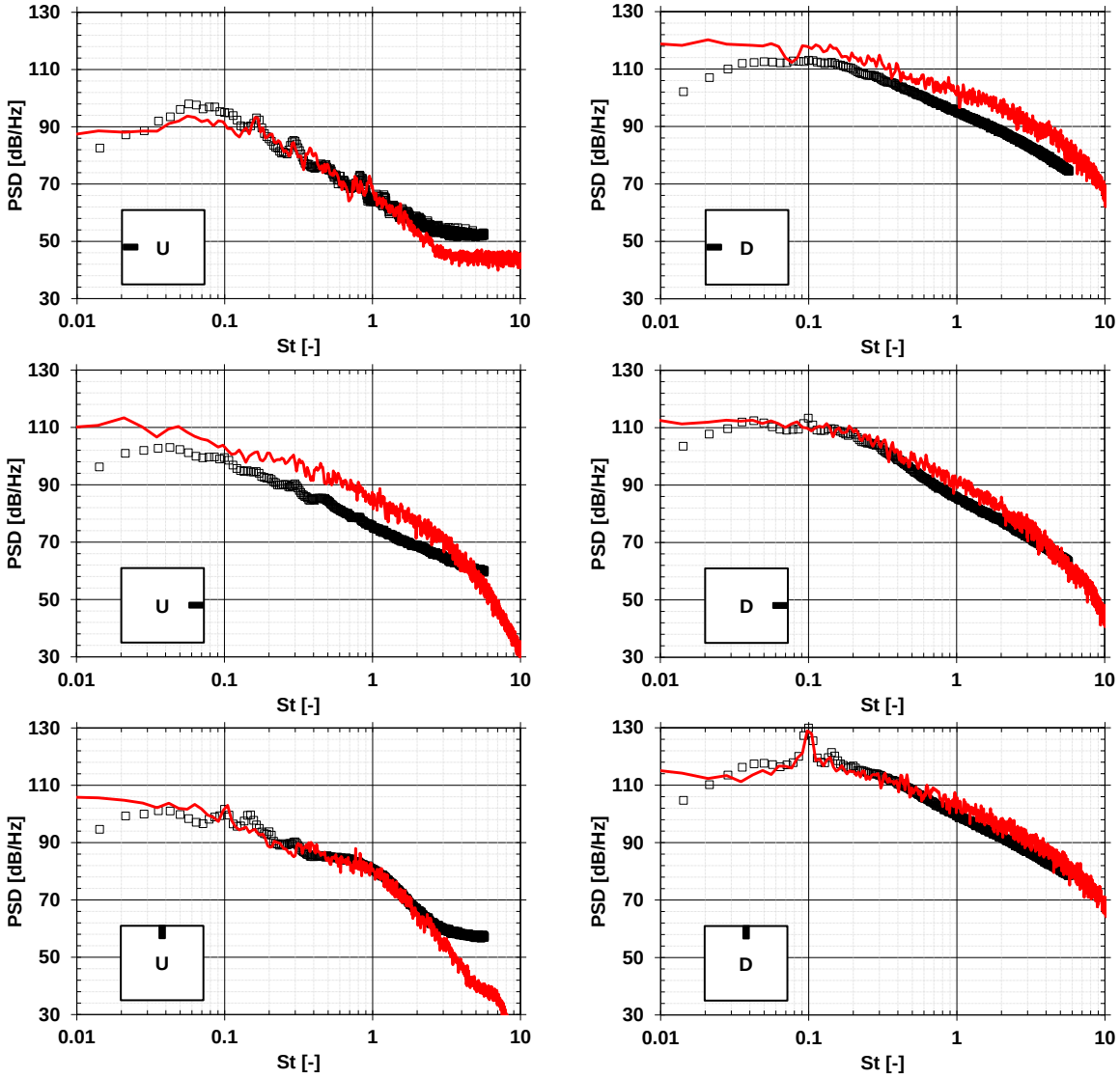

Figure 4.31: Surface pressure spectra on different surfaces of the upstream (U) and downstream (D) cylinders for the quiet flow state. Red lines correspond to numerical results of the full-span case and black square symbols to wind tunnel measurements.

and the inclusion of the endplates on the other side, resulting in fewer differences between the numerical and experimental setups.

Spanwise coherence

Due to periodic boundary conditions and the limited spanwise length of the cylinders in the limited-span case, high correlation coefficients were observed in Figures 4.19 and 4.21 along the span of both cylinders for both flow states. In order to analyse the effect of the periodic boundary conditions and the limited span of the cylinders, the distribution of the coherence function $\Upsilon(\mathrm{St})$ along different surfaces of the cylinders is calculated for the full-span case. The following analysis of the coherence function is restricted to the loud

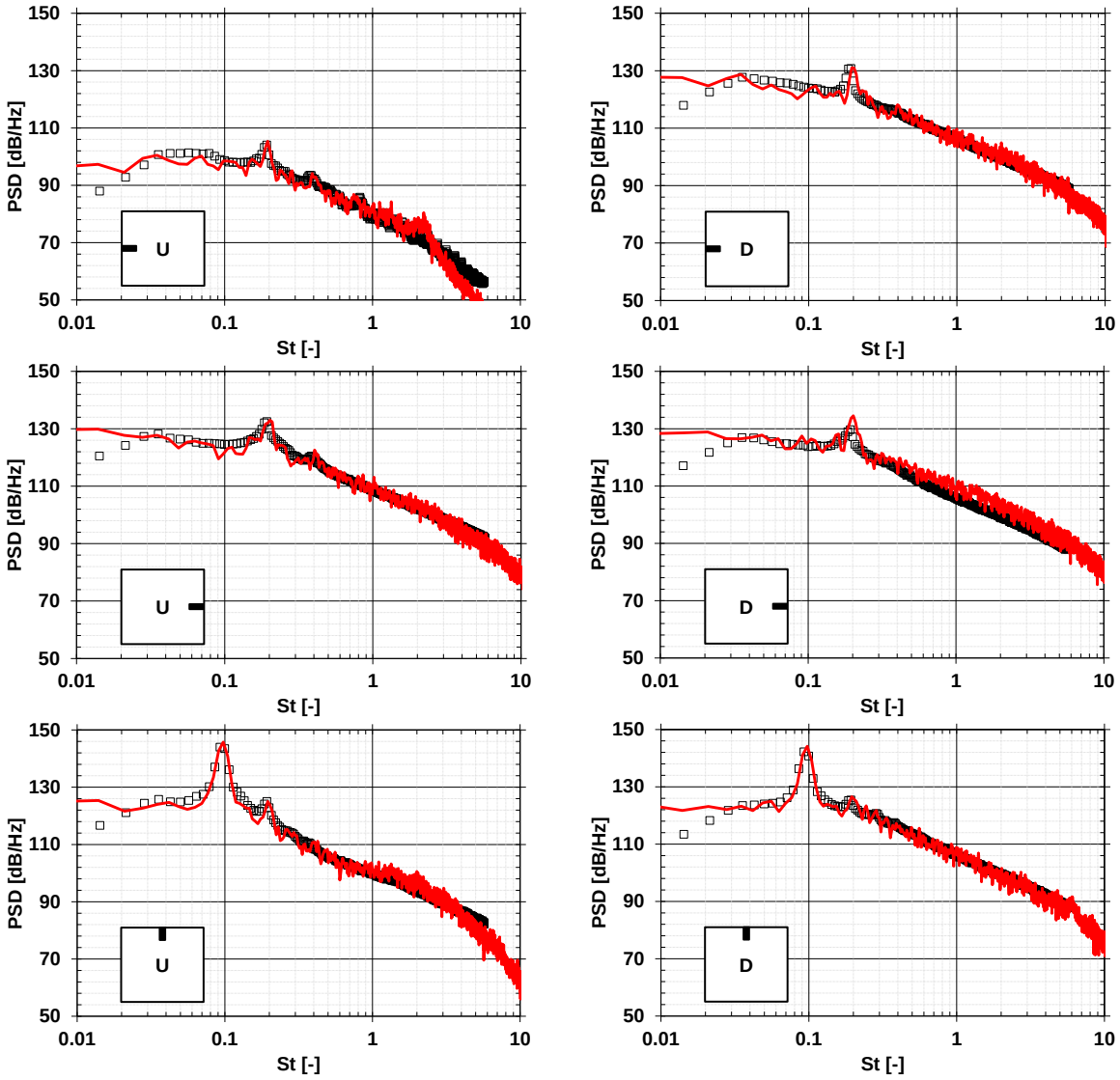

Figure 4.32: Surface pressure spectra on different surfaces of the upstream (U) and downstream (D) cylinders for the loud flow state. Red lines correspond to numerical results of the full-span case and black square symbols to wind tunnel measurements.

flow state, since similar behaviour was observed for both flow states. Furthermore, the distribution of the correlation coefficient $\Xi(\Delta y/D)$ is computed on different surfaces for the loud flow state using the data of the full-span setup.

Figure 4.34 shows the distribution of the coherence function for the loud flow state using the full-span case. Due to the longer span of the cylinders, the coherence function is calculated over half the span, which corresponds to $0 \leq \Delta y \leq L_{\text{full}}/2 = 6.25D$. On the upstream surface of the upstream cylinder, high values of $\Upsilon(\text{St})$ can be observed for all frequencies. However, the values of the coherence function at $\Delta y = 1.5D$ are lower than those in the limited-span case (cf. Figure 4.18). The same applies for all other surfaces. On the suction side surfaces of both cylinders, a unique peak can be observed at the vortex shedding frequency ($\text{St} \approx 0.1$). This was also observed in the limited-span case. However, the values of the coherence

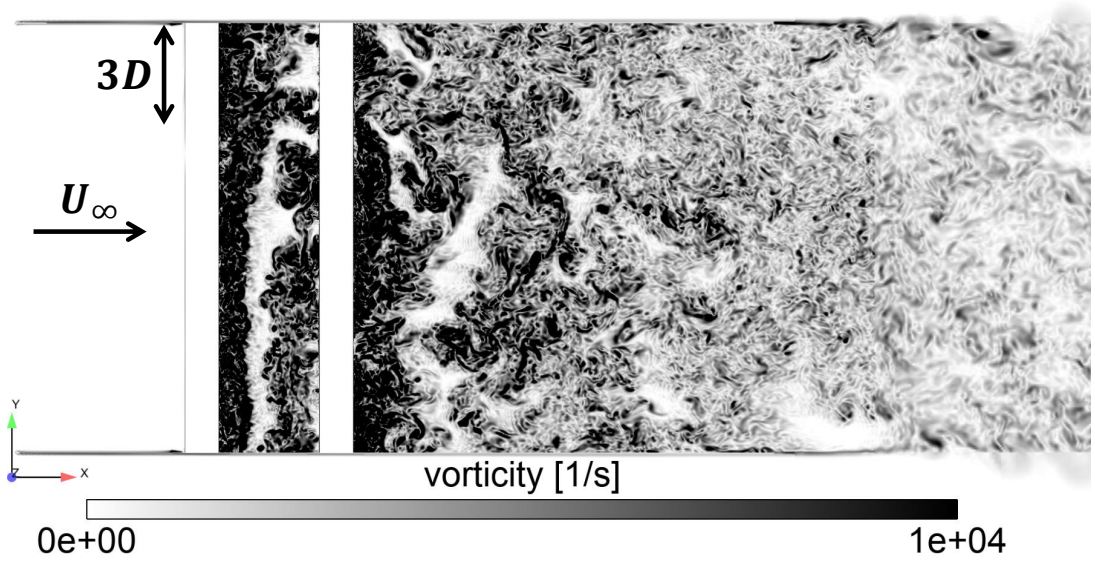

Figure 4.33: Instantaneous snapshot of the vorticity field at $z = 0$ and $t = 0.5$ s for the loud flow state using the full-span case.

function noticeably lower in the full-span case. This is particularly the case for St < 0.1 on the suction side surface of the upstream cylinder. The downstream surface of the upstream cylinder and the upstream surface of the downstream cylinder show similar distribution of the coherence function. A single peak at the drag oscillation frequency St ≈ 0.2 can be observed, at which the value of the coherence function Υ are similar to those in the limited-span case. However, the peaks distributed beside the main peak at St ≈ 0.2 in Figure 4.18 are not present in the full-span case. This behaviour is similar to the surface pressure spectra at the pressure and suction sides of the upstream cylinder. Finally, the coherence function distribution on the downstream surface of the downstream cylinder ion Figure 4.34 shows the same behaviour as in the limited-span case, which a slight lower magnitude for St $>$ 0.1.

The distributions of the correlation coefficient $\Xi(\Delta y)$ on different surfaces of the cylinders in the full-span case are presented in Figure 4.35. Similar to the coherence function distribution, the correlation coefficient is calculated for $0 \leq \Delta y \leq 6.25D$. Compared to the results of the limited-span case in Figure 4.19, pressure fluctuations on the upstream cylinder show higher decorrelation at $\Delta y = 1.5D$ in the full-span case. This applies for all surfaces of the cylinder. On the downstream surface of the upstream cylinder, the correlation coefficient reaches negative values at $\Delta y \approx 3D$ showing high decorrelation between pressure fluctuations. These fluctuations correspond to the ones on the upstream surface of the downstream cylinder, on which likewise high decorrelation of pressure signals can be observed. This behaviour was not observed in the limited-span case, in which the pressure fluctuations on the upstream surface of the downstream cylinder showed a correlation coefficient higher than 0.9 over the complete span. On the other surfaces of the downstream surface of the downstream cylinder, the correlation coefficient is higher in the full-span case at $\Delta y = 1.5D$ than in the limited-span case. However, it decreases to reach a value of approximately 0.4 at $\Delta y = 6.25D$. In general, the correlation coefficient of pressure fluctuations on both cyl-

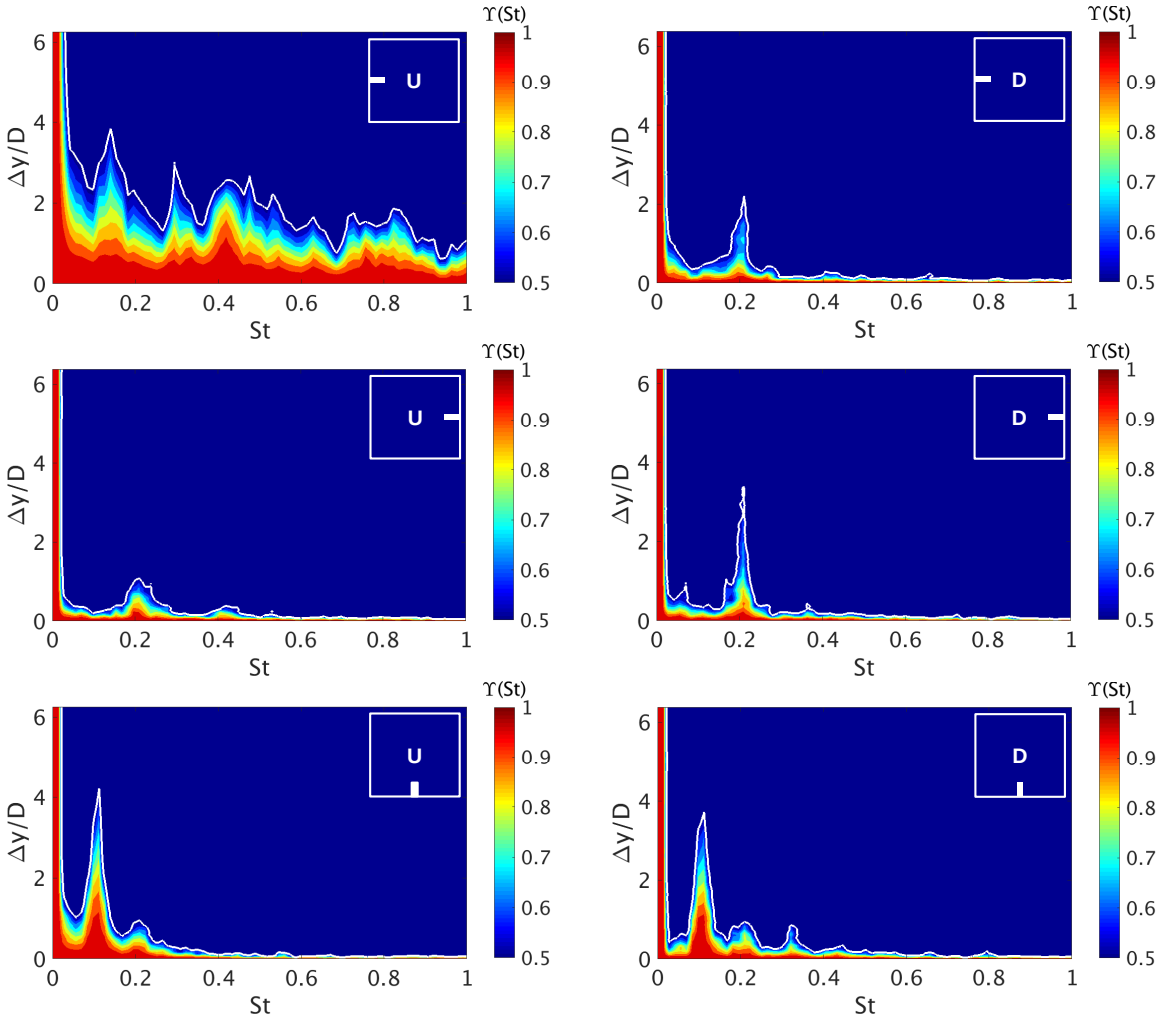

Figure 4.34: Magnitude-squared coherence function $\Upsilon\,(\mathrm{St}, \Delta y/D)$ along the surfaces of the up- (U) and downstream (D) cylinders for the loud flow state using the full-span case. The white solid line corresponds to the contour $\Upsilon = 0.5$.

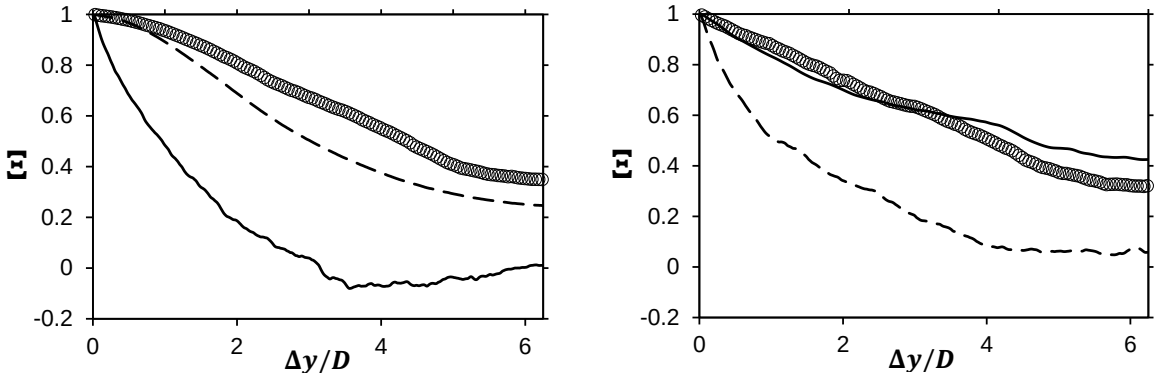

Figure 4.35: Correlation coefficient $\Xi(\Delta y/D)$ at different surfaces of (left) the upstream and (right) downstream cylinders for the loud flow state using the full-span case. (——) correspond to the downstream, (— —) the upstream surfaces, and (○) to the surfaces on the suction side of the cylinders.

inders surfaces in the full-span case is lower than the those in the limited-span case, which explains the effect of periodic boundary conditions as well as the limited simulated span on the flow topology.

4.4.3 Aeroacoustic results

The aim of the full-span case is to test the capability of the proposed compressible solver to directly calculate noise generation and propagation for low-Mach number flows. In the following, the results of the directly calculated acoustic waves are denoted by DNC. Additionally, the integral method is used to calculate acoustic waves in the far-field. Similar to the limited-span case, pressure fluctuations are stored over the whole span of both cylinders and used as an input for the integral method. The results of the integral method are denoted by FWH. Both methods are then compared to experimental results based on far-field spectra as well as directivity patterns.

Before discussing the results of both numerical methods, it is worth recapitulating the differences between the numerical and experimental setups. Similar to the limited-span case, the free-jet in the wind tunnel is not included in the full-span case. Hence, the corrections made by the experimenter in order to account for shear layer effects using the Amiet method are also valid in the following analysis. Since the whole span of the cylinders is calculated, there is no need to do any correction regarding the spectral level of the far-field acoustics as in the limited-span case. Hence, the results of both CAA-methods can be directly compared to wind-tunnel measurements. The third difference between the simulation and experiment are the perforated endplates. The plates included in the simulation have no-slip boundary conditions. Acoustically, these plates act like rigid walls and acoustic waves emitted from the cylinders in the direction of the endplates get reflected on these plates. The perforated plates in the wind tunnel are used in order to avoid wave reflections. These reflection affect the numerical results depending on the utilised CAA-method:

- The integral method uses pressure fluctuations on the cylinders surfaces in order to extrapolate acoustic waves into the far-field. This method does not account for acoustic volume sources, or any sound sources outside the surfaces of the cylinders. Acoustic waves impinging on the endplates are mostly reflected away from the cylinders surfaces. Hence, the integral method does not include the reflecting effect of the endplate and can be therefore compared directly with experimental data.
- The direct computation of far-field spectra does include the effect of wave reflections. The reflected acoustic waves propagate in the direction of the microphones in the far-field. Depending on the position of the acoustic sources on the cylinders surfaces, on the frequency of the emitted acoustic waves, and on the position of the microphones, acoustic waves, that are reflected by the endplates, can cause a deviation of the spectral level of far-field spectra compared to wind-tunnel measurements. Due to the complexity of the interference between these waves, a general correction method is not trivial.

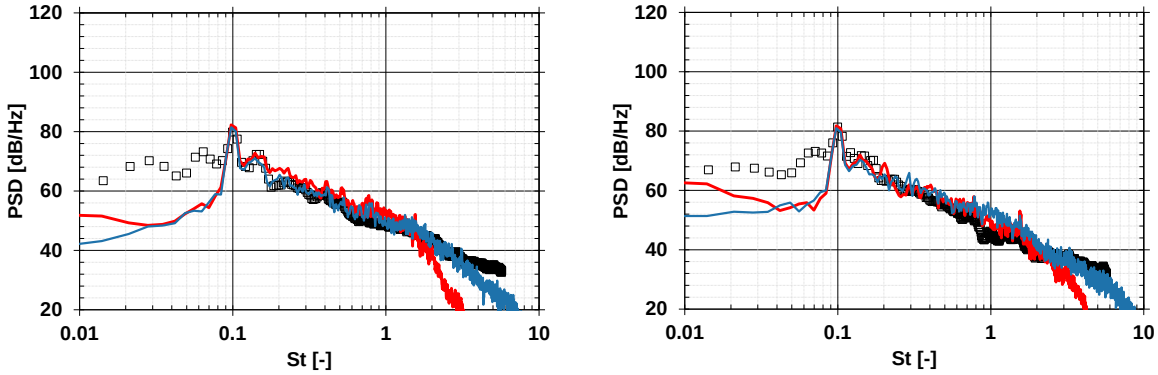

Figure 4.36: PSD-spectra of the quiet flow state at (left) $\theta = 93°$ and (right) $\theta = 32°$. Blue solid lines correspond to FWH, red solid lines to DNC, and black square symbols to wind tunnel measurements.

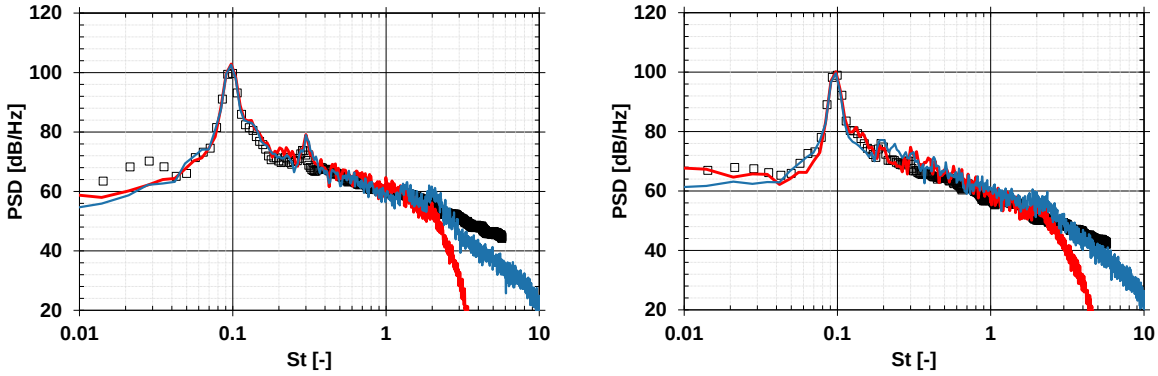

Figure 4.37: PSD-spectra of the loud flow state at (left) $\theta = 93°$ and (right) $\theta = 32°$. Blue solid lines correspond to FWH, red solid lines to DNC, and black square symbols to wind tunnel measurements.

Figure 4.36 shows numerical far-field spectra of the full-span setup calculated using both CAA-methods compared to wind-tunnel measurements at two different positions. In the low-frequency region ($St < 0.1$), large deviations between numerical and experimental results are present. This is most likely due to background noise in the wind tunnel. The main vortex shedding frequency is well captured by both methods. Moreover, the simulated broadband part shows a similar trend to the measured one. At $\theta = 93°$, DNC shows higher spectral levels over all frequencies. This is due to acoustic reflections caused by the endplates, which will be discussed later in this section. This behaviour is less pronounced at $\theta = 32°$, which is probably related to the direction of the emitted and reflected acoustic waves. The integral method shows good agreement with experimental results for $\theta = 93°$ and some deviations at $St \approx 1$ for $\theta = 32°$. The same deviations were observed and discussed in the limited-span case.

The calculated spectra for the loud flow state are presented in Figure 4.37. Both CAA-methods show good agreement with wind tunnel measurements over a wide-frequency range. The main vortex shedding frequency is well-captured, and the spectral levels in the broadband part match the measured ones. Similar to the quiet flow state, slightly higher

levels can be observed in the results of DNC at $\theta = 93°$, which is related to the reflection at the endplates. Moreover, these effects are not noticeable at $\theta = 32°$, which was also observed for the quiet flow state.

Effect of the endplates

In order to study the effect of the endplates on far-field spectra, the length of the width of the endplates in the z-direction is reduced from $17.5D$ to $3D$ with the aim of reducing wave reflections caused by the plates. For this setup, only the loud flow state is calculated. Figure 4.38 shows a comparison of the far-field spectra calculated using DNC and the original setup (wide endplates), the setup with short endplates, and wind tunnel measurements. At $\theta = 93°$, a slight decrease of the spectral level can be observed in the broadband part ($St > 0.3$). Moreover, the peak at $St \approx 0.3$ shows better agreement with wind-tunnel measurements when using the short endplates. The spectral level at the main vortex shedding frequency is almost identical between both cases. This is due to the quasi two-dimensional acoustic propagation at this frequency in the direction perpendicular to the main flow direction, which is not affected by the reflecting behaviour of the endplates. At $\theta = 32°$, the differences between both setups are barely visible. However, the differences between the results of both setups become clearer when observing the directivity patterns.

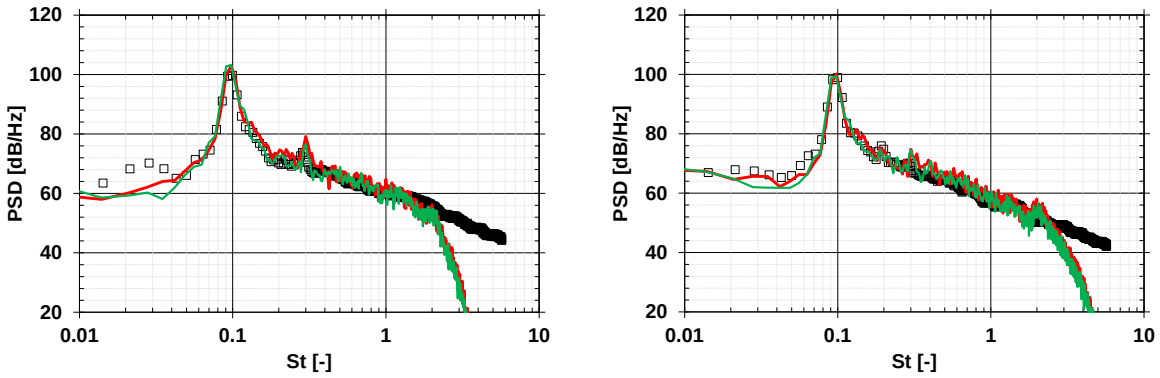

Figure 4.38: PSD-spectra of the loud flow state at (left) $\theta = 93°$ and (right) $\theta = 32°$. Red solid lines correspond to DNC results using wide endplates, green solid lines to DNC using short endplates, and black square symbols to wind tunnel measurements.

Directivity patterns

Directivity patterns of the loud flow state calculated using different CAA-methods are presented in Figures 4.39 and 4.40 at different frequencies. The directivity pattern of the overall radiated sound calculated using the integral method shows the typical dipole pattern. This is due to the dominance of the sound radiated at the vortex shedding frequency. The differences between the patterns calculated using DNC is negligible. As already mentioned, the propagation of sound radiated at $St \approx 0.1$ is quasi two dimensional in the z-direction. Hence, the effect of the endplates is not visible at this frequency and, therefore, not visible in the directivity pattern of the overall radiated sound. Nevertheless, results of both CAA-methods

show good agreement with experimental results. The largest deviations of approximately 2 dB are observed at $\theta = 93°$ and $\theta = 32°$, which is considered acceptable, baring in mind the differences between the experimental and numerical setups.

The effect of the endplates becomes visible when analysing the directivity patterns at higher frequencies, at which sound propagates in all directions and wave reflections at the endplates is no more negligible. Figure 4.40 shows the directivity patterns at St ≈ 0.6 and 0.9. The results of the setup with short endplates show lower spectral levels at these frequencies and better agreement with experimental results at all angles. This illustrates that acoustic waves generated by the cylinders are reflected by the endplates and cause a constructive interference at the microphones positions in the far-field.

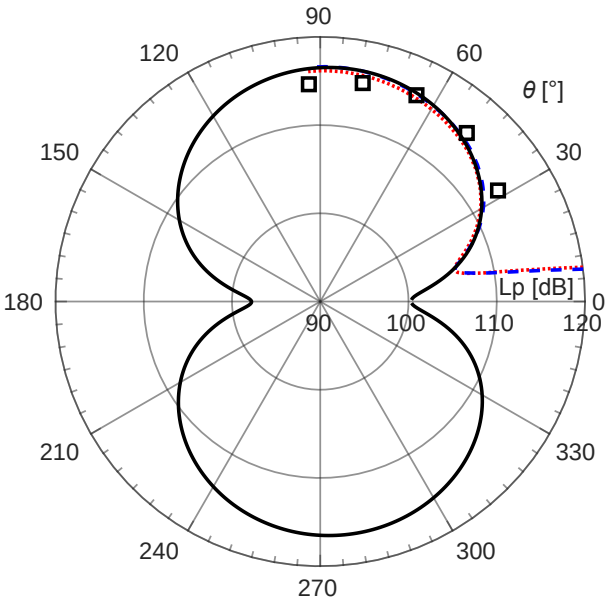

Figure 4.39: Directivity patterns of the overall radiated sound for the loud flow state using the full-span setup. Black solid line corresponds to FWH, blue dashed line to DNC with wide endplates, red dotted line to DNC with short endplates, and square symbols to wind tunnel measurements (figure taken from [19]).

The results of the integral method also show good agreement with experimental data. This applies for the microphones at $\theta \geq 49°$. At $\theta = 32°$, larger deviations can be observed. This could be due to the absence of flow-acoustic interaction in the integral method, in which the calculation of acoustic wave propagation assumes a uniform flow field with a velocity $U = U_\infty$. However, shear layers in the turbulent wake of the cylinders could cause sound waves to be diffracted. Since such effects are inherently included in the DNC, it does show better agreement with wind tunnel measurements at $\theta = 32°$.

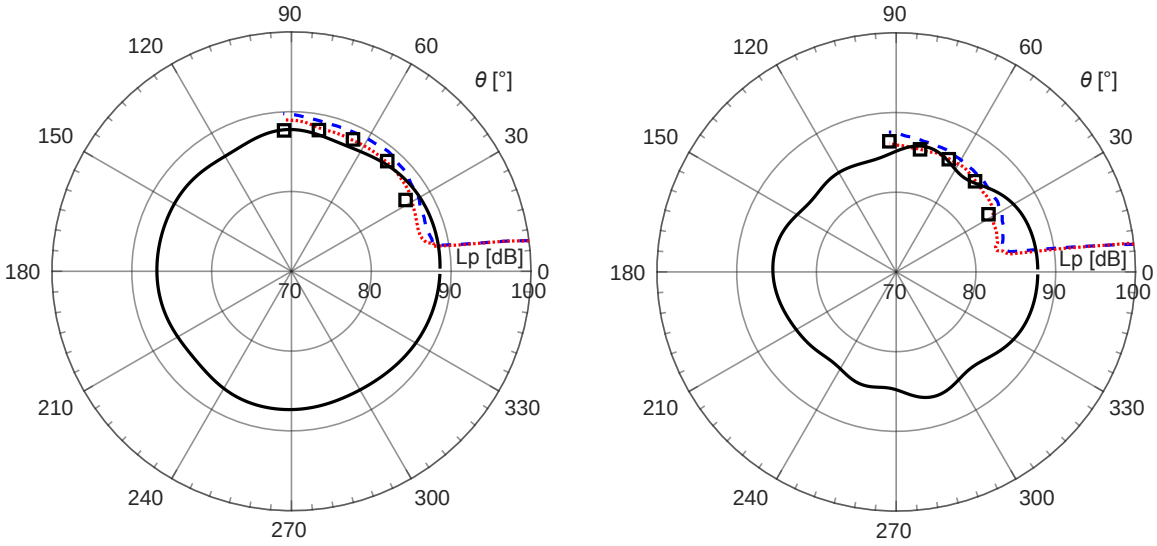

Figure 4.40: Directivity patterns of the radiated sound of the loud flow state at (left) St ≈ 0.6 and (right) St ≈ 0.9. Black solid lines correspond to FWH, blue dashed lines to DNC with wide endplates, red dotted lines to DNC with short endplates, and square symbols to wind tunnel measurements (figure taken from [19]).

5 Spurious noise generation in direct noise computation [1]

The analysis of the two-struts benchmark confirms the applicability of the compressible solver proposed in chapter 2 in combination with the IDDES approach for accurate aeroacoustic calculations. The simplicity of the geometry of the both cylinders facilitates the generation of the numerical grid, resulting in an almost uniform grid in the turbulent wake of the cylinders, consisting of purely cubic cells with a uniform resolution. This fact has two main advantages:

- A uniform spacial resolution is usually free of numerical artefacts. The IDDES approach introduced in chapter 2 depends highly on the local grid size. Hence, a uniform resolution supports a continuous transport of turbulent quantities across the numerical grid. Moreover, such a grid enables a continuous transport of the resolved turbulent kinetic energy without producing numerical artefacts.
- The second advantage is the cubic numerical cells in the previously analysed benchmark. Some characteristics of grid cells have already been introduced in chapter 3, such as skewness and non-orthogonality. In a finite-volume method, cubic cells have the best numerical characteristics, as such cells enable the usage of high-order schemes while maintaining the stability of the solution algorithm. For instance, it is possible to utilise a pure central differencing scheme in the majority of the computational domain without losing stability in the two-struts benchmark, which leads to a higher accuracy in the high-frequency region.

In industrial applications, e.g. aeroacoustic computation of a side-mirror on a vehicle, grid generation of complex geometries is inevitable. The surfaces of interest are usually highly resolved, while other parts of the computational domain, even in the vicinity of the vehicle, have a coarser spacial resolution. This variation in grid size facilitates a manageable number of cells and computational time. The result is a non-continuous grid spacing in critical domains around the vehicle, e.g. in the wake of the side-mirror. Furthermore, in order to accurately capture different surfaces of a vehicle, non-cubic cells are often required. Such cells deteriorate the quality of the grid and leads to certain restrictions regarding the usage of high-order schemes due to stability issues. The non-uniform grid spacing combined with non-cubic cells and special numerical schemes that guarantee the stability of the solution could result in the generation of spurious numerical noise that could deteriorate the acoustic solution. Since acoustic waves are orders of magnitude smaller than hydrodynamic ones, the level of numerical noise is of particular importance, especially in direct aeroacoustic computation. The level of spurious noise could be equal or even larger than the physical waves of interest. This results in a contaminated solution and sometimes to a misinterpretation of the results.

1 This chapter is an extended version of the results presented in A.H. Dawi, R.A.D. Akkermans, *Spurious noise in direct noise computation with a finite volume method for automotive applications*, International Journal of Heat and Fluid Flow, Volume 72, p. 243-256, 2018

After a brief literature review, this chapter illustrates the mechanism of spurious noise generation is analysed and its potential sources are identified, with a special emphasis on turbulent flows across grid interfaces. For this purpose, two different test cases are utilised:

- Convected isotropic turbulence (section 5.2): this test case exhibits a qualitative analysis of spurious noise sources. Therein, different grid structures as well as numerical schemes are applied and their effect on the direction and magnitude of spurious waves is evaluated.
- Side-mirror on a flat plate (section 5.3): this test case involves the calculation of the flow past a real side-mirror, with the aim of a quantitative evaluation of the level of spurious waves in industrial applications.

Additionally, a method based on the acoustic damping model proposed in chapter 3 is utilised in order to suppress spurious noise. The model is applied on both test cases and the results of acoustic waves generated by the surface of the side-mirror are compared to the results of the previously proposed integral method.

5.1 Literature review

One of the major spurious noise sources are grid interfaces that build up the transition between different refinement levels. Such a refinement interface was shown in Figure 3.2. Spurious errors generated at such interfaces can be classified into two categories: spurious reflections of acoustic waves propagating through the interfaces, and spurious noise generated while turbulence propagates across such interfaces.

Spurious reflections were already studied by several authors. One of the earliest studies was done by Vichnevetsky [109–111], who analysed spurious wave reflections on refinement interfaces, and derived an exact analytic expression for reflected waves in a standard finite-difference method. Additionally, he modified the treatment of refinement interfaces consisting of an overlapping region between the fine and coarse grid, and showed that wave reflection converge to zero with the third order of grid spacing. Besides such wave reflections, Vichnevetsky furthermore showed that spurious oscillations can occur at refinement interfaces. A study on wave propagation across refinement interfaces was also done by Berger et al. [9], who developed an adaptive mesh refinement algorithm along with a modified treatment of grid interfaces in order to maintain global conservation across such interfaces. For this purpose, they used ghost cells on the coarse side of the refinement interface. Such cell were also used by Huang in [40] in order to reduce oscillations generated at refinement interfaces while using high-order schemes. This technique was also combined with an artificial selective damping in order to damp out spurious oscillations. High-order schemes for finite-difference method were also developed by Visbal et al. [113] combined with high-order filtering scheme with the purpose of reducing high-frequency oscillations at grid interfaces. Similarly, Durbin et al. [23] developed discretisation schemes involving additional grid points on the coarse side of the grid. The larger numerical stencil delivers higher accuracy and minimises numerical errors at refinement interfaces. Numerical stencils involving grid points on both sides of refinement interfaces were also developed by Kok

et al. [53, 54] in a finite-volume framework using structured grid. Their method was combined with high-order schemes and a validation test case involving a convected isentropic vortex across different refinement interfaces showed a reduction of numerical error induces at the interfaces. Similarly, Zhang [123] utilised larger numerical stencils in combination with high-order conservative fine-coarse interpolation on refinement interfaces. Apart from the numerical solutions developed by the mentioned authors, physical solutions involving filtering of the flow field in the region of refinement interfaces were also elaborated. Goodfriend et al. [33] established an explicit filtering procedure combined with a reconstruction algorithm in order to reduce numerical errors at refinement interfaces, and validated their method using a large eddy simulation of isotropic turbulence advected across a refinement interface. A similar approach was developed by Vanella et al. [108], who smoothly increased the filter width in a large eddy simulation prior to a fine-coarse interface. They showed the advantages of this method in decreasing energy pileup at refinement interfaces, which helps avoid discontinuities in the solution across such interfaces. This behaviour was also analysed in [32].

The studies mentioned so far had the purpose of reducing numerical errors on refinement interfaces with the focus on the hydrodynamic field. Few studies were done regarding the generation of numerical errors in the context of spurious noise. Thiele [103] showed the presence of spurious noise by comparing aeroacoustic results of solid and permeable FWH surfaces on the tandem circular cylinders benchmark. Due to the low-Mach number ($Ma \approx 0.13$), the spectral level of high frequency spurious noise dominated the magnitude of physical acoustic waves. Refinement interfaces in the wake of the cylinders caused the generation of spurious waves. These numerical volume sources were included in the permeable FWH integration surface, which caused deviations between the results of permeable and solid surfaces in the high-frequency range. A method based on flux-reconstruction was developed by Le Bras et al. [59] in order reduced spurious noise on non-conforming grid interfaces. Lastly, spurious noise on refinement interfaces was also analysed for the Lattice Boltzmann method and new methods based on overlapping zones between coarse and fine regions were developed in order to reduce grid induced errors [14, 57].

5.2 Convected isotropic turbulence

In this section, a qualitative analysis of different spurious noise sources is performed. The considered flow situation is a cubic box representing isotropic turbulence which is convected by a uniform flow field. First, the effect of different discretisation schemes regarding spurious noise generation is analysed. For this purpose, a grid with a uniform grid spacing is utilised in order to exclude effects caused by refinement interfaces. Thereafter, the effect of refinement interfaces is analysed separately. Validation of the direction of refinement is studied as well as the directivity of spurious waves propagation. Finally, the effect of the acoustic damping model on turbulence and on acoustic waves is presented. Due to the low Mach-number of the flow, acoustic waves generated by the turbulence is negligible and an error-free solution would exhibit imperceptible generation of acoustic waves.

5.2.1 Numerical setup

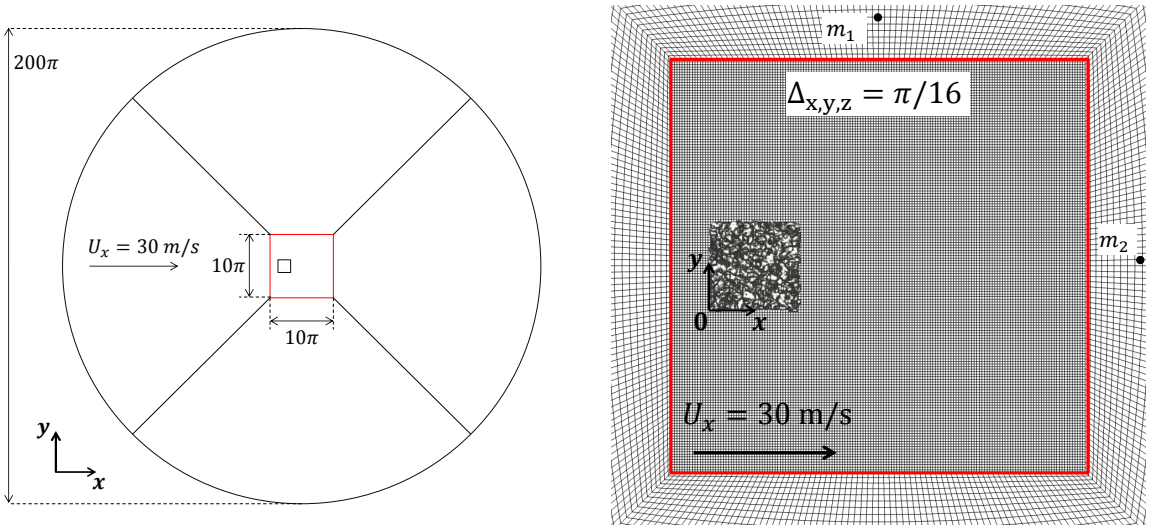

Figure 5.1: Geometry of the O-grid for the convected isotropic turbulence test case (left) and a slice through the grid at the midspan in the z-direction (right). The red solid lines represents the center-box of the O-grid. The turbulence box is visualised at $t = 0$ s using isosurfaces of $\lambda_2 = 10^{-1}$. Monitor points are denoted by m_1 and m_2 and have the coordinates $(4\pi, 7\pi, \pi)$ and $(10\pi, \pi, \pi)$, respectively.

The computational domain consists of a circular disk with a diameter of 200π and a spanwise thickness in the (z-direction) of 2π [cf. Figure 5.1 (left)]. The O-type grid has a square center box of width 10π which extends between the points $(-\pi, -4\pi, 0)$ and $(9\pi, 6\pi, 2\pi)$. The center box has a uniform spacial resolution and consists of cubic cells with a spacing of $\Delta_{x,y,z} = \pi/16$. The initial turbulence box shown in Figure 5.1 (right) represents a box of isotropic turbulence and has a width of 2π in all spatial directions. The initial velocity field of the isotropic turbulence is acquired from the John Hopkins Turbulence data base [62, 120]. The turbulence box is centred at the origin of the system of coordinates as shown in Figure 5.1 (right). The freestream velocity U_x is set to 30 m/s, corresponding to a Mach number of $Ma \approx 0.087$. An inlet boundary condition is prescribed at the boundary of the left half of the computational domain, and an outlet boundary condition on the right half. A non-reflective pressure boundary condition is applied on the complete outer circumference. In the spanwise direction, periodic boundary conditions are utilised. In order to monitor acoustic waves, two monitor points are positioned right outside the center box of the O-grid (cf. Figure 5.1). The time-step size is set to $\Delta t = 1.5 \cdot 10^{-4}$ s and 6667 time steps are calculated, which corresponds to 1 s physical time. Since the initial velocity field of the turbulence package originates from a DNS simulation of a box of homogeneous isotropic turbulence with periodic boundary conditions, the initial turbulence package has to adapt to its surrounding area consisting of a uniform velocity field. Therefore, acoustic waves of high amplitude are generated at $t = 0$ s as the turbulence package starts to move with the flow in the positive x-direction. These acoustic waves propagate outside the center box of the O-grid. At $t = 0.8$ s, the turbulence package reaches the right end of the center box and impinges on the refinement interface just before the monitor point m_2 causing spurious noise

generation. Therefore, the analysis of acoustic waves at the monitor points m_1 and m_2 is restricted to the time between 0.3 s and 0.8 s, so that initialisation effects and spurious noise generation at the right boundary of the center box are excluded from the analysis. During the simulation, the $\partial p/\partial t$ field is sampled every $3 \cdot 10^{-3}$ second. Similar to the two-struts benchmark, the time derivative of the pressure is used to visualise acoustic waves.

5.2.2 Effect of discretisation schemes

The discretisation of the divergence term in the momentum equation plays an important role in accurately resolving turbulence. For instance, central differencing is known to be accurate in resolving high-frequency fluctuations, while upwind-based schemes are rather dissipative in the high-frequency range. However, each scheme has its own pros and cons. Since high accurate scheme could cause spurious noise generation, it is sometimes necessary to use a certain amount of numerical dissipation in order to suppress spurious noise generation. In this section, different schemes are evaluated regarding the amount of spurious noise they produce. For this assessment, the uniform grid proposed in the previous section is employed in order to avoid any grid-induced noise due to refinement interfaces.

The most accurate scheme available in the course of this work is the second-order central differencing scheme (CDS). However, this scheme has stability limitations as described in section 3.2. The grid shown in Figure 5.1 exhibits some skewed cells at the corners of the center box. While simulating the case with a pure CDS, these cells were responsible for the instability in the solution. Small velocity fluctuations resulting from numerical errors increase in the course of the solution. Due to the unboundedness of CDS, immense velocity values are produced in these cells and the solution diverges.

One possibility for the stabilisation of the solution is the use of the deferred correction approach [Eq. (3.21)]. The CDSdC delivers an accurate solution and favours the stability of the algorithm at the same time. Figure 5.2 shows the convection of the turbulence package as well as the noise generated as the package moves downstream at different times. As the simulation starts ($t = 0.003$ s), high amplitude waves are produced as the turbulence package adapts to its surrounding field. At $t = 0.2$ s, the package reaches the center of the computational domain. Remarkably, the package leaves a tail-formed turbulent field behind. As previously mentioned, the CDSdC scheme is a low-dissipative scheme. Therefore, velocity fluctuations at the initial position of the turbulent package are not damped throughout the simulation. These fluctuations cause the excitation of further fluctuations upstream. This can be observed at the left boundary of the center box at $t = 0.2$ s. The last two snapshots show a further excitation of velocity fluctuations upstream of the center-box. As these fluctuations pass through the refinement interfaces at the left boundary of the box, spurious waves are generated. The source of these waves can clearly be observed at $t = 0.6$ s. The turbulence package itself does not produce visible acoustic waves. This is consistent with the assumption that volume sources caused by turbulence are negligible at low Mach numbers.

Due to the interaction between the excited velocity fluctuations and the refinement interface at the left boundary of the center-box, a pure CDSdC scheme is not suitable for further investigation of spurious noise generated by numerical schemes. Therefore, a certain amount of numerical dissipation has to be introduced in order to suppress the ”tail-building” behaviour of the turbulence package.

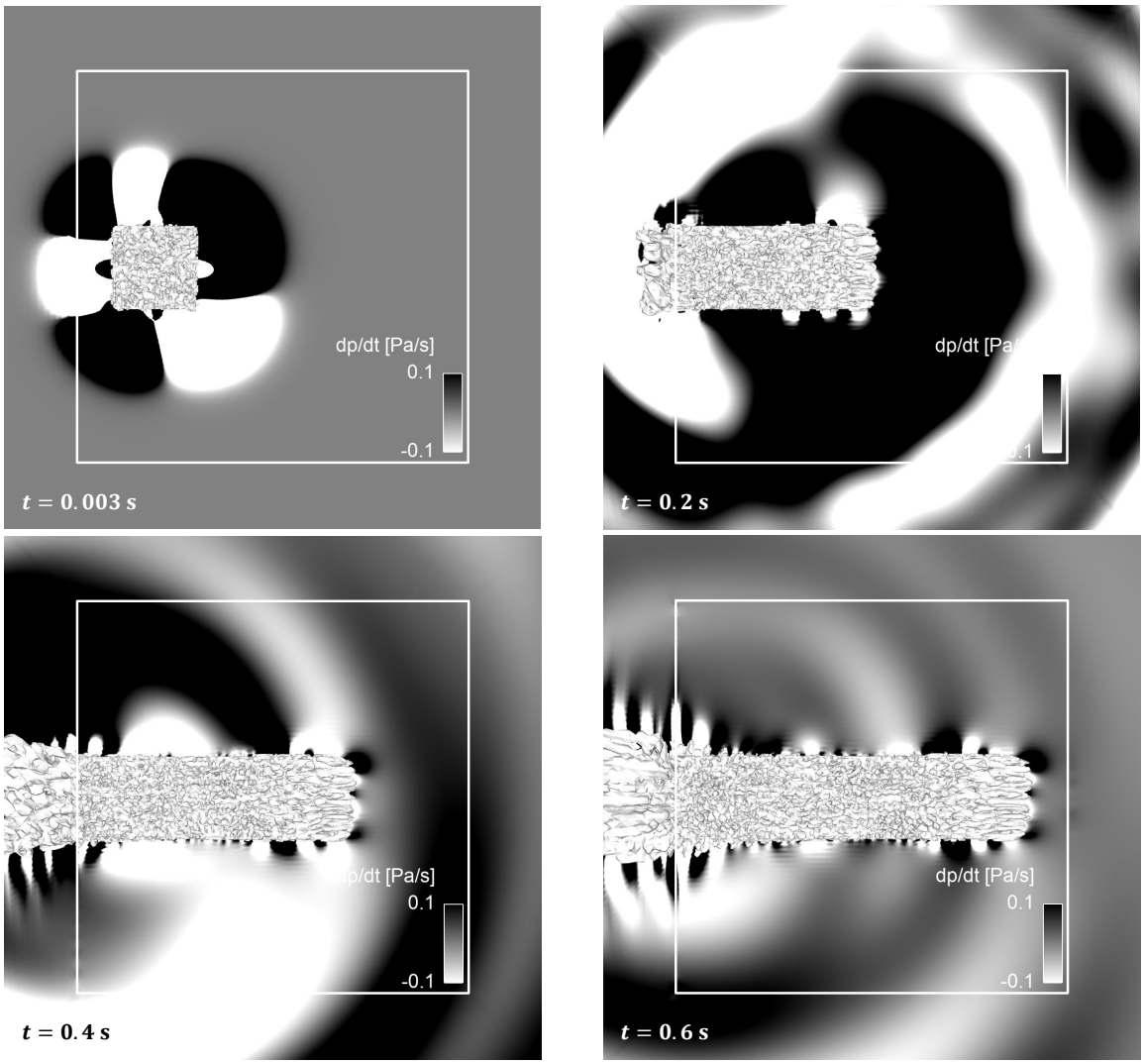

Figure 5.2: Snapshots of the convection of the turbulence package at different times using the CDSdC scheme. Turbulence is visualised using $\lambda_2 = 10^{-2}$ isosurfaces. The background represents a slice at the midspan of the computational domain and is coloured by $\partial p/\partial t$. The white box represents the boundaries of the center box of the O-grid.

One way to increase numerical dissipation is to use upwind-based schemes. However, such schemes cause high dissipation of fine turbulent structures. Resolving these structures is essential for an accurate aeroacoustic computation, since they could be responsible for the generation of physical acoustic waves. Therefore, a compromise between low dissipation and high accuracy has to be employed.

Blended discretisation scheme offer a good mixture between both numerical characteristics. The blending between two numerical schemes was defined in Eq. (3.22), and there exist several definitions of the blending coefficient σ. For the convected isotropic turbulence, two variants of blending are analysed: the fixed blending scheme with a constant value σ_{fix} all over the computational domain, and the DES hybrid scheme in which the blending coefficient is a function defined in Eq. (3.23).

Fixed blended scheme

A first attempt to damp out velocity fluctuations left by the turbulence package is to add 5% of the second order upwind scheme LUDS, i.e. $\sigma_{\text{fix}} = 0.05$ in Eq. (3.22). As an high-order scheme, the CDSdC scheme is utilised. Figure 5.3 shows the turbulence package as it gets convected through the computational domain. As for the CDSdC scheme, high amplitude pressure waves are produced at the beginning of the simulations. These waves propagate outside the center-box as shown in Figure 5.3 at $t = 0.2$ s. As these waves leave the center-box, the turbulence package keeps moving with the flow in the positive x-direction without producing any visible acoustic waves. This can be observed at $t = 0.4$ s and $t = 0.6$ s. Moreover, one can observe the traces left behind the turbulence package and how they are damped out with time. These traces can also be observed at the left boundary of the center-box. However, due to numerical dissipation of LUDS, spurious noise is not generated because of the low energetic content of such fluctuations.

Figure 5.4 shows the time history of the pressure fluctuation p' at the monitor points m_1 and m_2. Hereby, p' is defined as $p - p_\infty$, where p_∞ corresponds to the ambient pressure. Between $t = 0$ s and $t = 0.2$ s, spurious waves resulting from the initialisation can be monitored at m_1 as well as m_2. For $t > 0.8$, the turbulence package approaches m_2 and the pressure fluctuations increase. For $0.3 \text{ s} < t < 0.6$ s, pressure fluctuations are almost equal to zero at both monitor points [cf. Figure 5.3 (right)]. This indicates the absence of noise generation by the turbulence package. Due to the absence of spurious noise when using the fixed blended scheme, the corresponding results are used as a reference for comparison with results of other numerical schemes and in analysing spurious noise generation at refinement interfaces.

DES hybrid scheme

The second considered blending technique is the one proposed by Travin et al. [104]. As the blending coefficient σ_{Hyb} is a function in space and time, there is no need for the user to pre-define the regions in which high- and low-order schemes are employed. The coefficient is calculated in the course of the simulation and it adapts to the local flow topology.

The DESHyb scheme is applied to the convected isotropic turbulence case. The CDSdC scheme is used as a high-order scheme and the LUDS as a low-order scheme. First computations are done with $\sigma_{\max} = 1$ and $\sigma_{\min} = 0$. These values correspond to full central differencing for regions in which the hybrid blending factor is equal to 1 and a pure second order upwinding in regions where the blending factor is equal to 0.

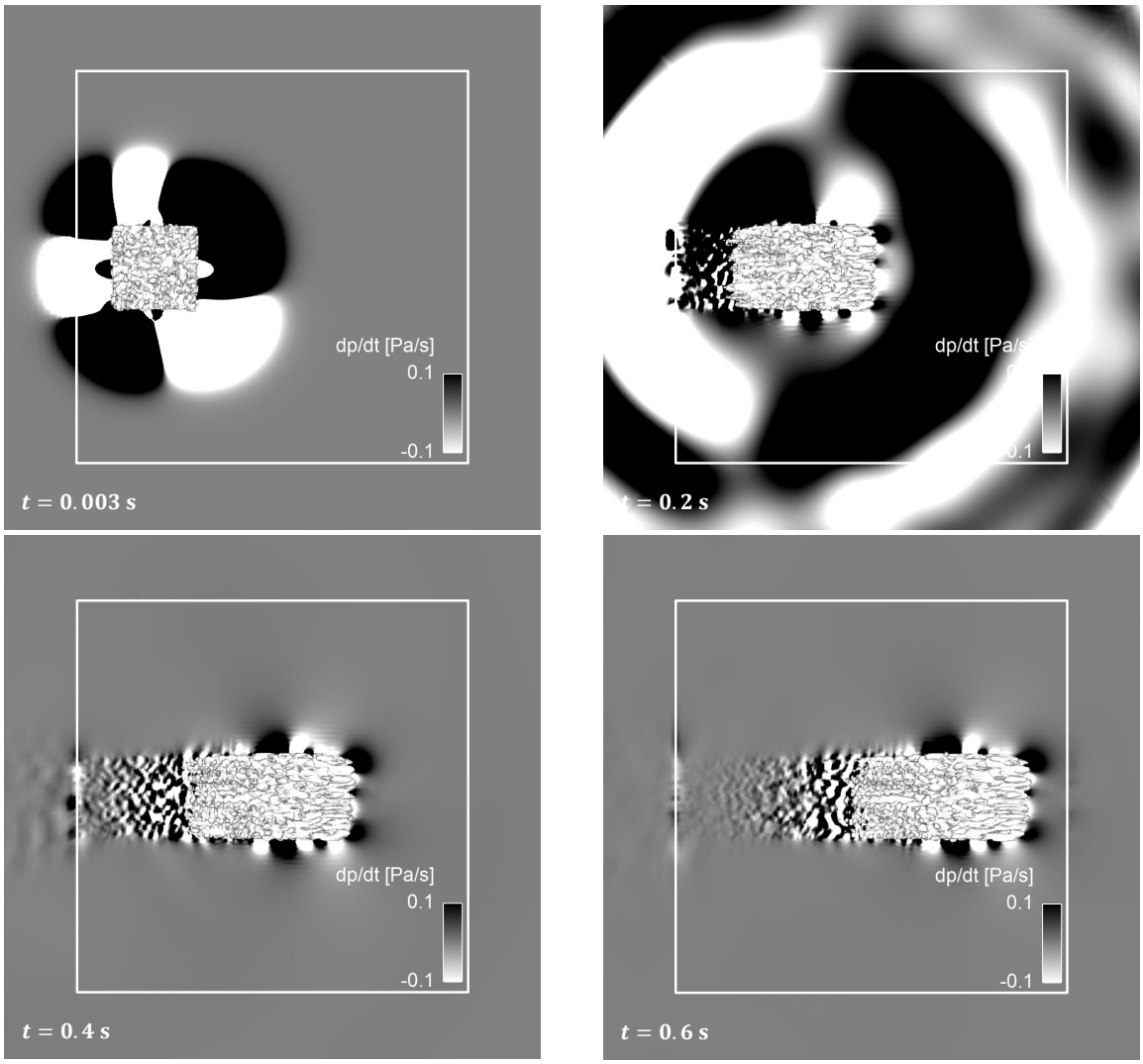

Figure 5.3: Snapshots of the convection of the turbulence package at different times using fixed blending between LUDS and CDSdC with $\sigma_{\text{fix}} = 0.05$. Turbulence is visualised using $\lambda_2 = 10^{-2}$ isosurfaces. The background represents a slice at the midspan of the computational domain and is coloured by $\partial p/\partial t$. The white box represents the boundaries of the center box of the O-grid.

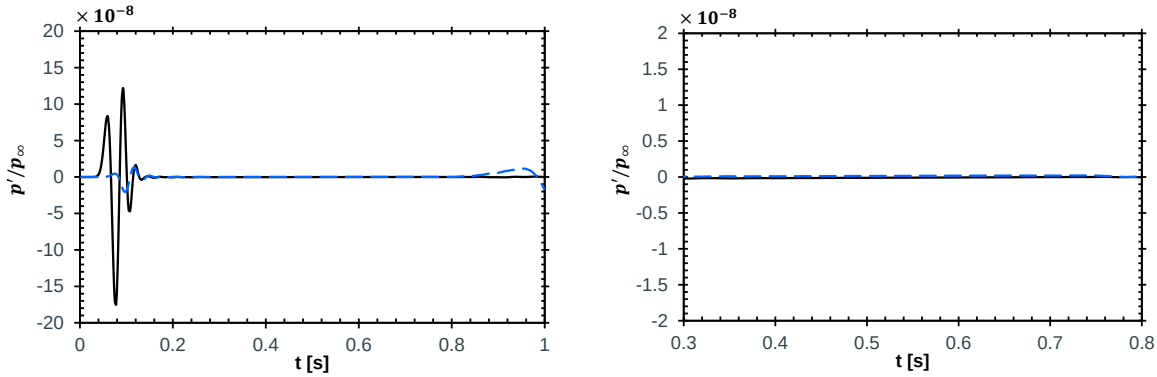

Figure 5.4: Time history of the pressure fluctuation p' using the fixed blended scheme with $\sigma_{\text{fix}} = 0.05$ at (——) m_1 and (– –) m_2. The right figure is a close-up of the left one.

Figure 5.5 (left) shows a snapshot of the distribution of the hybrid blending factor at $t = 0.4$ s. For this computation, the limiter $\Omega_{\min}$ is set to $10^{-3}/\tau_0$ as in the original formulation of Spalart et al. [97]. As expected, in regions where turbulent fluctuations are resolved, the blending factor is equal to 0. Outside the turbulent region, the blending factor switches to 1, corresponding to LUDS. The resolved turbulent structures are very similar to those calculated using the fixed blending scheme. However, by comparing the structures to those in Figure 5.3, one can observe that small turbulent fluctuations at at the tail of the turbulence package are not resolved when using the DESHyb scheme. A closer look at the distribution of the blending factor in Figure 5.5 explains this behaviour. In the center of the turbulence box, the blending factor is exactly equal to 0 (black color), apart from some cells in which the scheme switches to LUDS. At the tail of the box, the factor tends to take values between 0 and 1 (grey color) and continuously tend to 1 (white color). The calculation of the blending factor in Eq. (3.23) depends, amongst other variables, on ν_t, $\mathbf{S}$, and Ω. Hence, the blending factor is related to the size of the resolved turbulence. Since the turbulent structures at the tail of the turbulence package are smaller than the convected larger structures at the center of the package, the blending factor tends to take lower values and switches to 0 in region where small fluctuations would otherwise be resolved. The continuous region, in which the scheme goes from a pure central differencing to a pure upwind differencing is approximately 5 grid cells wide and this region moves with the turbulence package. Hence, small fluctuations in the tail of the package are transferred into an LUDS region, which is known to be more dissipative than CDSdC. The result is that these small scales are dissipated.

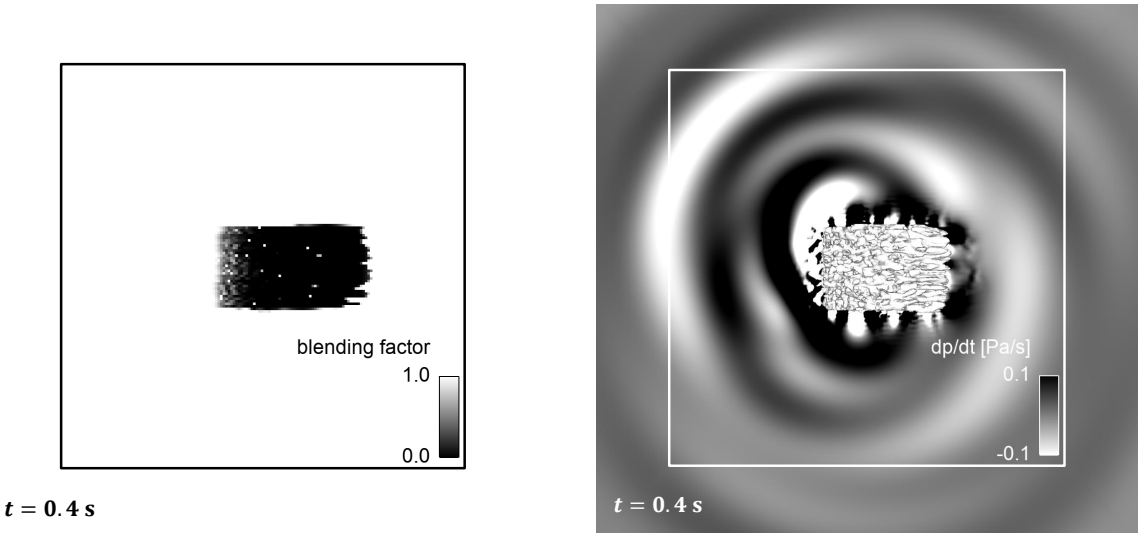

Figure 5.5: Distribution of the hybrid blending factor and $\partial p/\partial t$ at $t = 0.4$ s using the DESHyb scheme with $\sigma_{\min} = 0$, $\sigma_{\max} = 1$ and $\Omega_{\min} = 10^{-3}/\tau_0$.

Another phenomenon, which is related to the dissipation of small scales at the tail of the turbulence package, is the generation of spurious noise. In Figure 5.5 (right), one can observe that the spurious noise is generated almost exactly in the region where the blending factor increases from 0 to 1. As already mentioned, the region separating the CDSdC and LUDS schemes is approximately 5 cells wide. This transition causes a sudden dissipation of the turbulent scales at the tail of the package and energy contained in these scales is trans-

formed into spurious pressure waves. Figure 5.6 shows the recorded pressure signals at the positions m_1 and m_2. Comparing the pressure signals to those in Figure 5.4, it is clear that the DESHyb scheme generates spurious noise in both x- and y-directions. In order to study the behaviour of spurious noise generation caused by the DESHyb scheme, two scheme parameters are varied: the limited $\Omega_{\min}$ and factors $\sigma_{\min}$ and $\sigma_{\max}$.

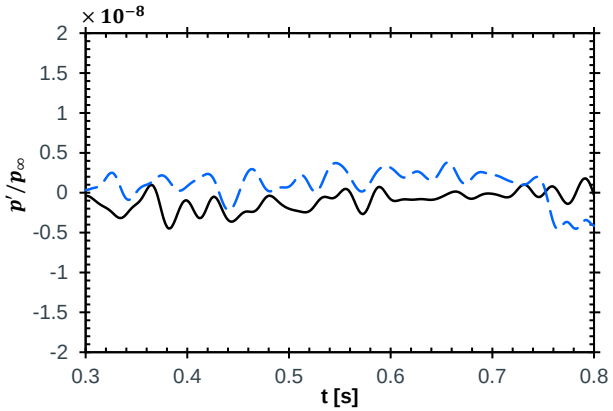

Figure 5.6: Time history of the pressure fluctuation p' using the DESHyb scheme with $\sigma_{\min} = 0$, $\sigma_{\max} = 1$ and $\Omega_{\min} = 10^{-3}/\tau_0$ at (——) m_1 and (— —) m_2.

Applying the DESHyb scheme on industrial cases showed that the switching behaviour between the blended schemes highly depends on the limiter $\Omega_{\min}$, especially on refinement interfaces. According to [97], the limiter $\Omega_{\min}$ is only active in the outer non-turbulent region. Hence, the limiter could have an effect on where the location of the continuous transition of the blending factor at the tail of the turbulence package. In this work, the limiter is varied between $10^{-3}/\tau_0$ and $1/\tau_0$.

Figure 5.7 shows the distribution of the hybrid blending factor for different $\Omega_{\min}$. For $\Omega_{\min} \leq 0.1/\tau_0$, the distribution of the blending factor does not show large variations with the limiter function. The only differences can be observed downstream of the turbulence package, where higher $\Omega_{\min}$ values cause delayed switching between high- and low-order schemes. Similarly, the region downstream the turbulence package shows slight differences as $\Omega_{\min}$ increases. The region, in a transition of the blending factor from 0 to 1 takes place is smaller for $\Omega_{\min} = 0.1/\tau_0$. For $\Omega_{\min} = 1/\tau_0$, the blending factor switches to 1 in the whole turbulent region. Hence, the whole domain is discretised with a low-order scheme, causing high dissipation of the hydrodynamic fluctuations.

The effect of the $\Omega_{\min}$ variation on spurious noise generation is illustrated in Figure 5.8. For $\Omega_{\min} \leq 10^{-2}/\tau_0$, spurious waves are almost identical at both m_1 and m_2. As already observed in Figure 5.7, the blending factor for these $\Omega_{\min}$ does not show remarkable variations upstream the turbulence package. The sharper transition when setting $\Omega_{\min}$ to $0.1/\tau_0$ is noticeable in larger spurious noise amplitudes at both m_1 and m_2. A further increase of the limiter results in a pure LUDS behaviour all over the computational domain for $\Omega_{\min} = 1/\tau_0$, resulting in the absence of the transition region at the tail of the turbulence package and, as a result, lower spurious noise amplitudes. However, comparing the amplitude of spurious waves to those in Figure 5.4, one can observe that the scheme still produces some amount of

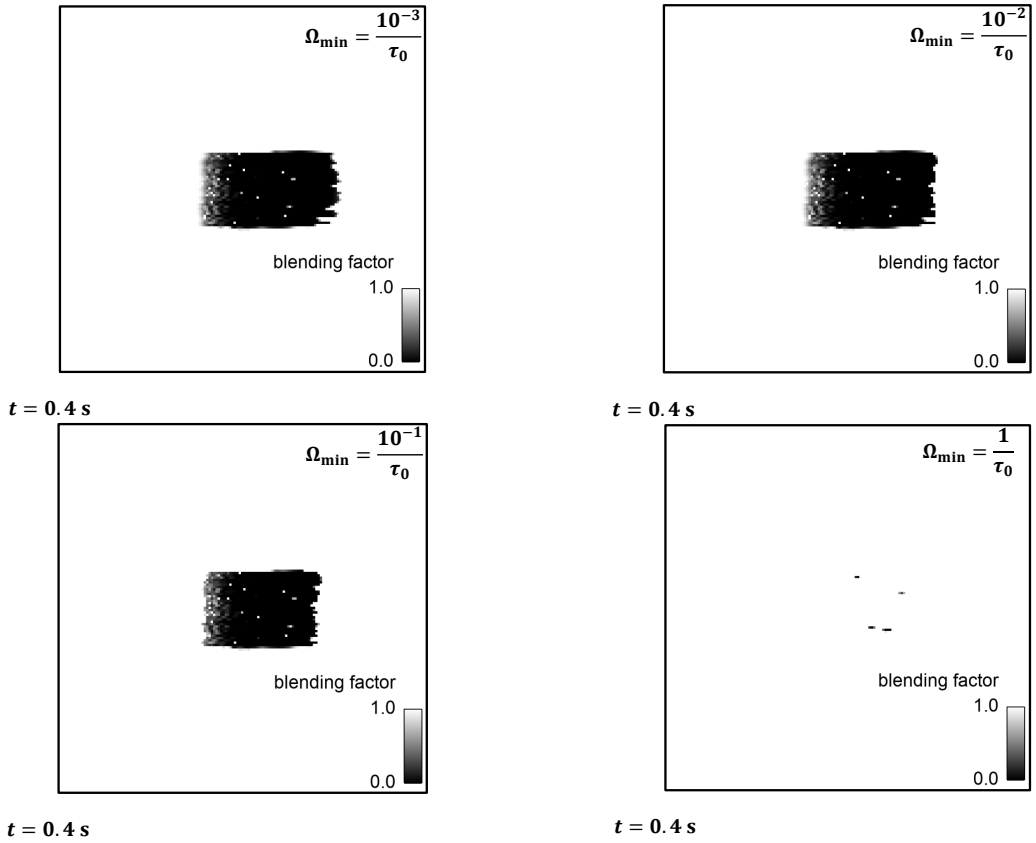

Figure 5.7: Distribution of the hybrid blending factor using the DESHyb scheme with $\sigma_{\text{min}} = 0$ and $\sigma_{\text{max}} = 1$ and different Ω_{min} values. All snapshots are taken at $t = 0.4$ s.

spurious noise at 0.3 s$< t <$ 0.5 s. This is probably caused by the alternating scheme switching at individual cells in the turbulent region. These cells are shown in black at $t = 0.4$ s in Figure 5.7.

The other parameter that could affect the amount of spurious noise generated by the DESHyb scheme is the amount of blending between the low- and high-order schemes, which is controlled by the parameters σ_{min} and σ_{max}. Ideally, one would choose to fix σ_{min} to zero, so that turbulent regions are discretised using a pure central scheme. On the other hand, the upwind-based scheme is chosen in order to stabilise the solution. One way to reduce the sudden transition from high- to low-order scheme is to decrease σ_{max} as much as possible while maintaining stability. In convected turbulence test case, a 5%-95% blending between LUDS and CDSdC did result in a stable solution using the fixed-blended scheme. Therefore, one could set σ_{min} to 0 and σ_{max} to 0.05, resulting in a pure CDSdC in the turbulent region and a 5%-95% blending in the outer region.

Figure 5.9 shows spurious noise generated at the tail of the turbulence package with two different σ_{max} values. For $\sigma_{\text{max}} = 0.5$, the directivity of spurious noise is equivalent to the one in Figure 5.5. However, the amplitude of $\partial p/\partial t$ is smaller. This means that a weaker blending results in the reduction of the amplitude of spurious noise. This can also be observed for $\sigma_{\text{max}} = 0.05$, which shows a further reduction in the amplitude of spurious waves

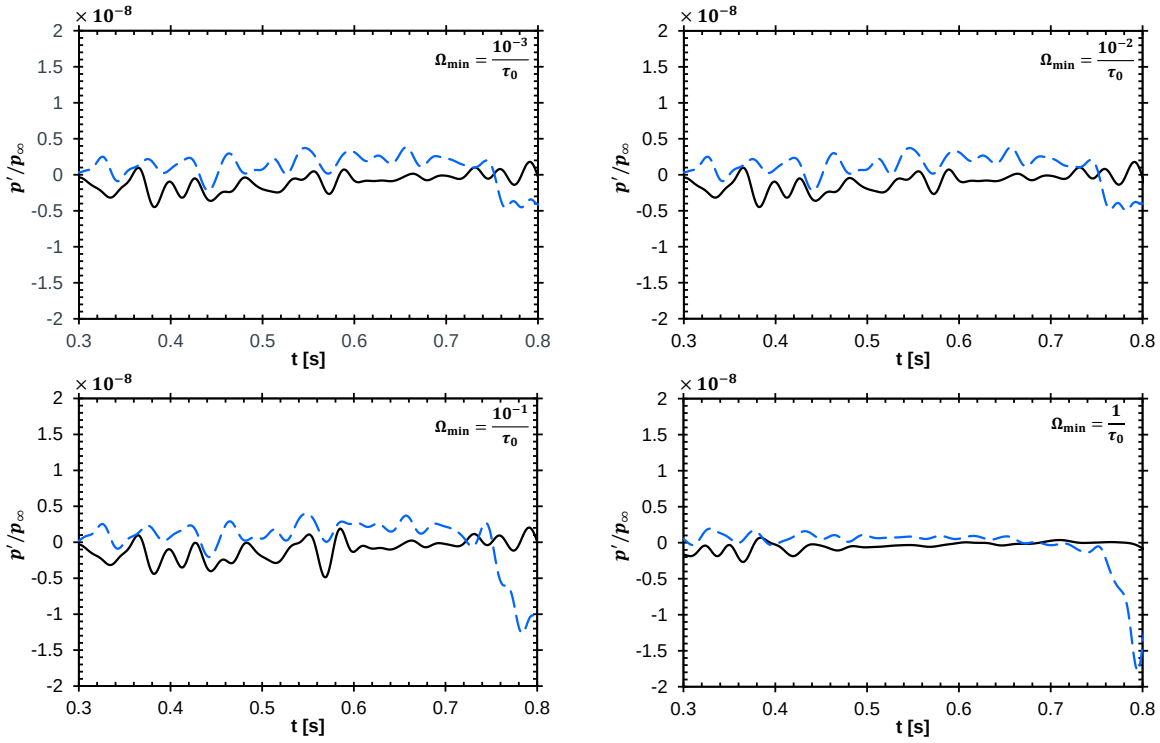

Figure 5.8: Time history of the pressure fluctuation p' using the DESHyb scheme with $\sigma_{\min} = 0$ and $\sigma_{\max} = 1$ for different $\Omega_{\min}$ values at (——) m_1 and (— —) m_2.

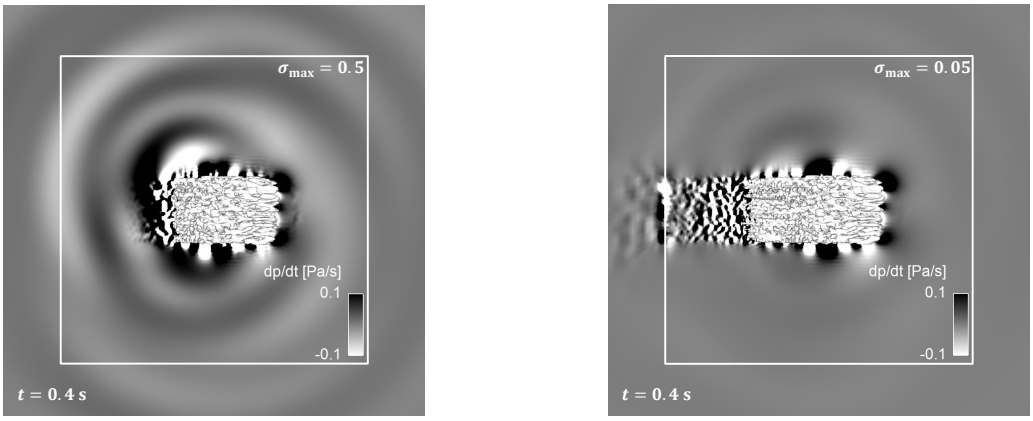

Figure 5.9: Snapshots of $\partial p/\partial t$ at $t = 0.4$ s using the DESHyb scheme with $\sigma_{\min} = 0$ and different $\sigma_{\max}$ values.

emitted at the tail of the package. Since $\Omega_{\min}$ is identical in both cases, the hybrid blending factor distribution is almost equivalent for both $\sigma_{\max}$. The only difference between both cases is the minimum value of the blending factor. This results in a less sudden transition between the schemes and, as a result, lower amplitude of spurious waves. Comparing the turbulence structures between Figure 5.9 (right) and Figure 5.5, one can observe that the resolved fluctuations are very similar. This is due to the similarity of the resulting scheme when using $\sigma_{\max} = 0.05$. Therefore, the small fluctuations at the tail of the package are also resolved, just like the result of the fixed blending scheme.

The amplitude of spurious waves for both $\sigma_{\max}$ values can be observed in Figure 5.10. Analogously to the snapshots of $\partial p/\partial t$, one can observe that weaker blending results in weaker spurious noise. For $\sigma_{\max} = 0.05$, spurious noise is almost equal to zero. Small fluctuations are, however, still visible. As already mentioned, this is caused by the scheme switching within individual cells in the turbulent region.

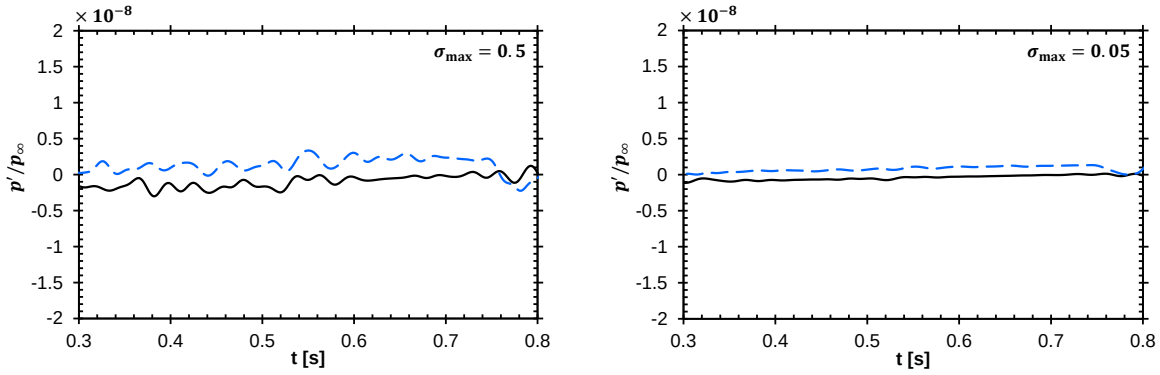

Figure 5.10: Time history of the pressure fluctuation p' using the DESHyb scheme with $\sigma_{\min} = 0$ and different $\sigma_{\max}$ values at (——) m_1 and (— —) m_2.

5.2.3 Effect of refinement interfaces

After analysing the role of different numerical schemes in spurious noise generation on a uniform grid, a second study on refinement interfaces and their effect on spurious noise generation is performed. In order to study spurious noise generated at refinement interfaces separately, the fixed blending scheme is mainly used for this analysis. As seen in the previous section, this scheme does not show any noise generation and, therefore, is appropriate to isolate numerical noise caused by refinement interfaces. Nevertheless, a comparison of the behaviour of different schemes on grid interfaces regarding spurious noise generation is also given.

The numerical setup is equivalent to the one used in the previous section. The grid is modified, so that a refinement interfaces is present at $x = 5\pi$. For this, all cells included in the center-box of the O-gird and are positioned at $x \geq 5\pi$ are coarsened in all three direction to have a resolution of $\Delta_{x,y,z} = \pi/8$. Figure 5.11 shows a close up of the numerical grid with the refinement interface.

Figure 5.12 shows snapshots of the turbulence package at two different time steps. At $t = 0.34$ s, the package reaches the refinement interface. Spurious noise is not visible due to the use of the fixed blended scheme. As the package passes the refinement interface, spurious waves are generated and propagate in different directions, which can be observed in Figure 5.12 at $t = 0.45$ s. The amplitude of spurious noise generated at the refinement interface can be appreciated in Figure 5.13. Compared to the case without refinement interface, strong spurious waves are present at both monitor points.

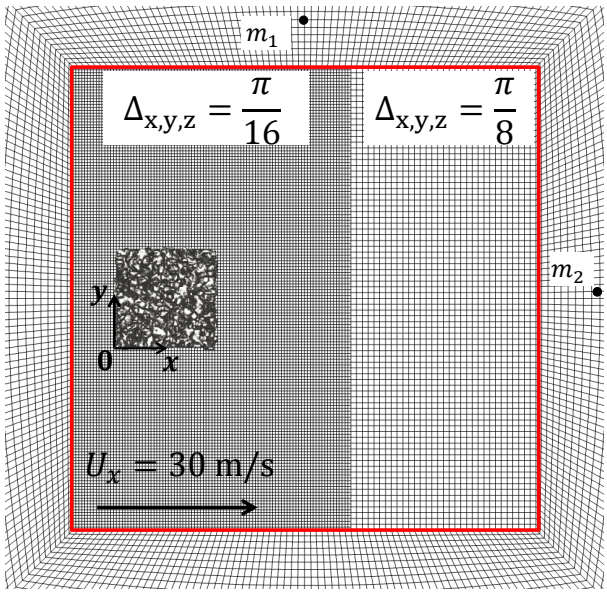

Figure 5.11: A slice through the numerical grid at $z = 0$ including the refinement interface at $x = 5\pi$.

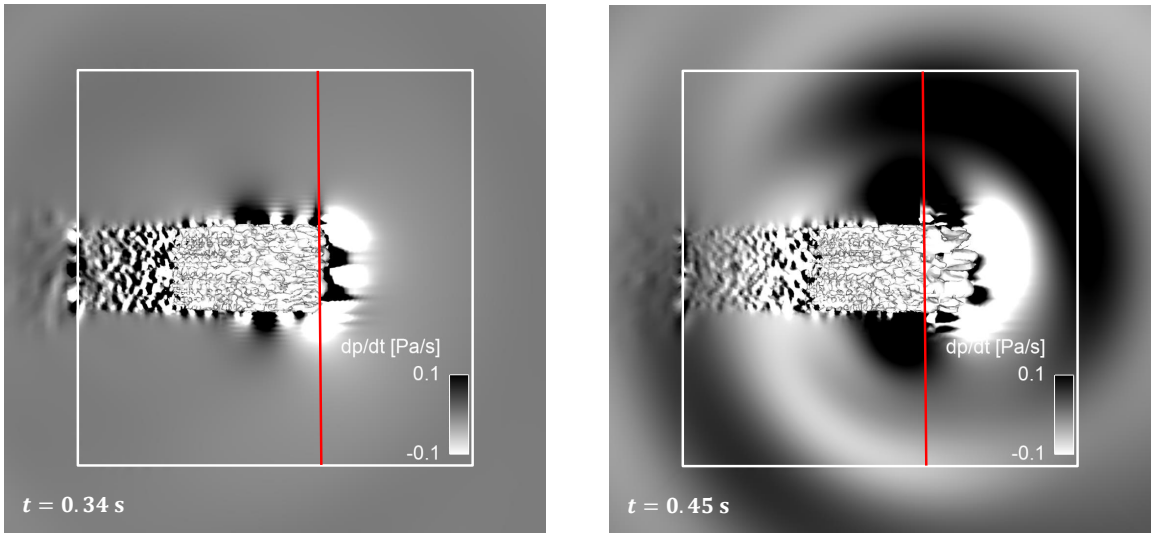

Figure 5.12: Snapshots of the turbulence package on the grid with refinement interface (red solid line) at two different times.

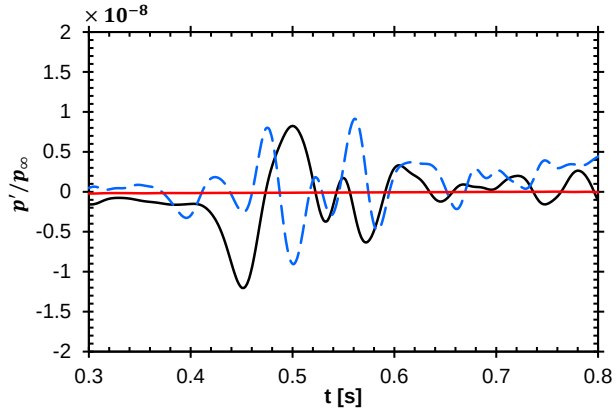

Figure 5.13: Time history of the pressure fluctuation p' using the fixed blending scheme with $\sigma_{\text{fixed}} = 0.05$ at (——) m_1 and (– –) m_2 on the grid with refinement interface. (——) corresponds to the pressure fluctuations at m_1 on the grid without refinement interface.

The reason for spurious noise generation can be explained as follows: on the fine side of the grid, the smallest fluctuation that can be resolved has a wavelength $\lambda_{\text{fine}} = 2\Delta_{x,y,z}$. Consequently, the cut-off wavenumber on the fine side of the grid is $k_{\text{fine}} = 2\pi/\lambda_{\text{fine}} = \pi/\Delta_{x,y,z}$. Since the grid is Cartesian, this wavenumber applies for all three directions. Similarly, the cut-off wavenumber on the coarse side of the grid is $k_{\text{coarse}} = k_{\text{fine}}/2$. The wavenumber components on the fine side cannot be fully resolved on the coarse side. Consequently, the energy contained in the components that cannot be resolved on the coarse side is transformed into spurious waves with equivalent energy content due to energy conservation.

Figure 5.14 shows a schematic representation of the energy spectrum of homogeneous isotropic turbulence. On the fine grid side, wavenumbers up to k_f can be resolved. However, due different numerical errors (numerical dissipation, diffusion, turbulence modelling,etc.), not all wavenumbers $k \leq k_f$ can be resolved, hence the green dashed line in Figure 5.14. The same applies for the coarse grid with a cut-off wavenumber of k_c. The shaded area represents the difference between the energy of the resolved parts on the fine and coarse grids. Since this energy cannot be resolved on the coarse grid, it propagates as spurious noise. The calculation of this amount of energy is not trivial, since it is related to the dependency of numerical error on the grid size. Furthermore, the filtering effects introduced in chapter 2 in a LES approach also depends on the grid spacing. As a result, an expression for the amount energy difference between the resolved parts on both grids is not straightforward.

Effect of the direction of refinement interfaces

The refinement interface in the aforementioned test case consists of cell-coarsening in all three spacial directions, which results in spurious noise propagation in different directions. In order to analyse the effect of the direction of refinement, additional test cases using refinement interfaces in each spacial direction are performed.

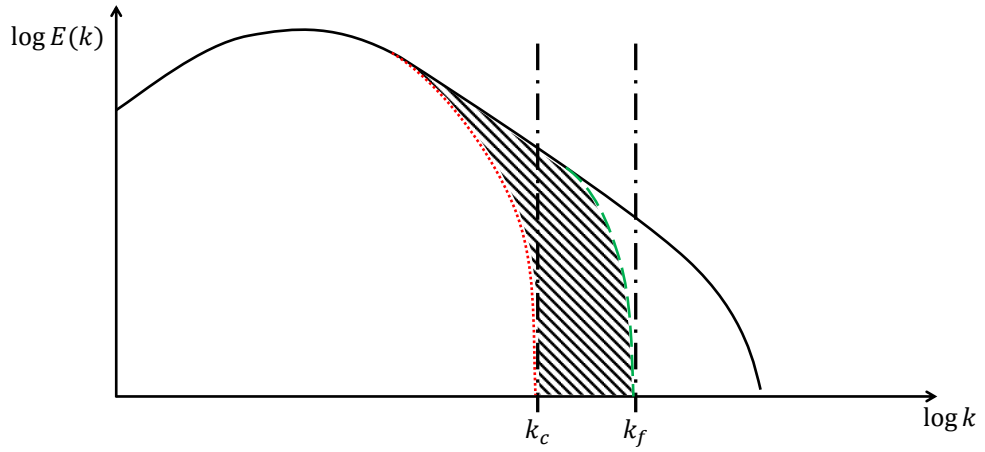

Figure 5.14: Schematic representation of the (——) complete energy spectrum of homogeneous isotropic turbulence, (·····) the spectrum resolved on a coarse grid with a cut-off wavenumber k_c, and (— —) the spectrum resolved on a fine grid with a cut-off wavenumber k_f. The shaded area represents the energy that is resolved by the fine grid but cannot be resolved on the coarse one.

Figure 5.15 shows two snapshots of $\partial p/\partial t$ as the turbulence package passes two refinement interfaces in different directions. A clear relation between the direction of spurious noise propagation and the direction of the refinement interface can be observed: coarsening the cells in the x-direction causes spurious wave propagation in the positive and negative x-directions. The same applies for spurious noise generated by a refinement interface in the y-direction.

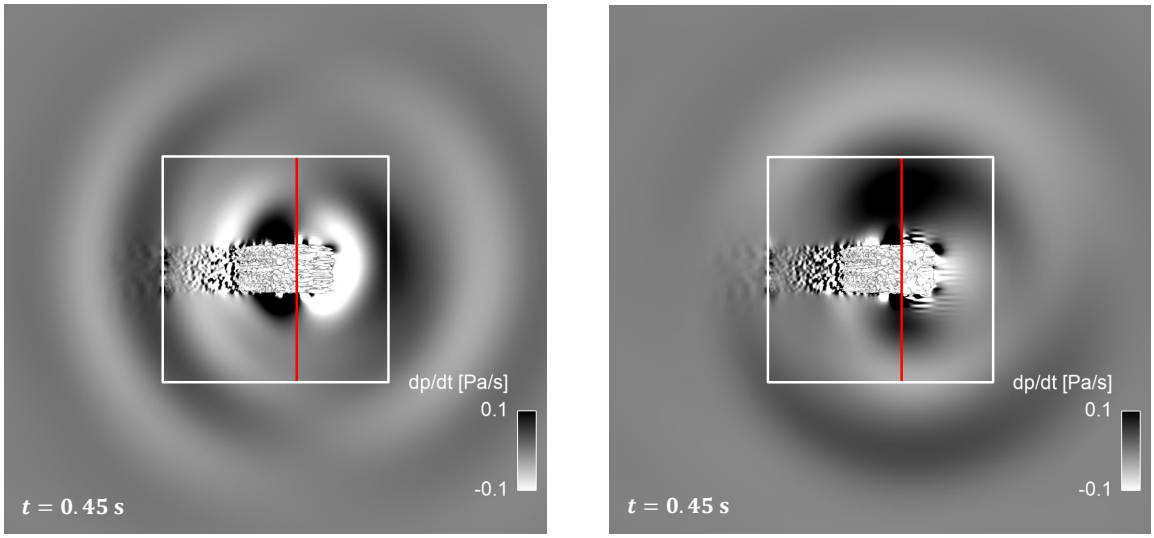

Figure 5.15: Snapshots of $\partial p/\partial t$ at $t = 0.45$ s as the turbulence package passes a refinement interface in the (left) x-direction and (right) y-direction. The red solid line corresponds to the refinement interface.

The direction of the generated spurious noise can also be deducted from the time history of the pressure fluctuation p' in Figure 5.16. For the refinement interface in the x-direction,

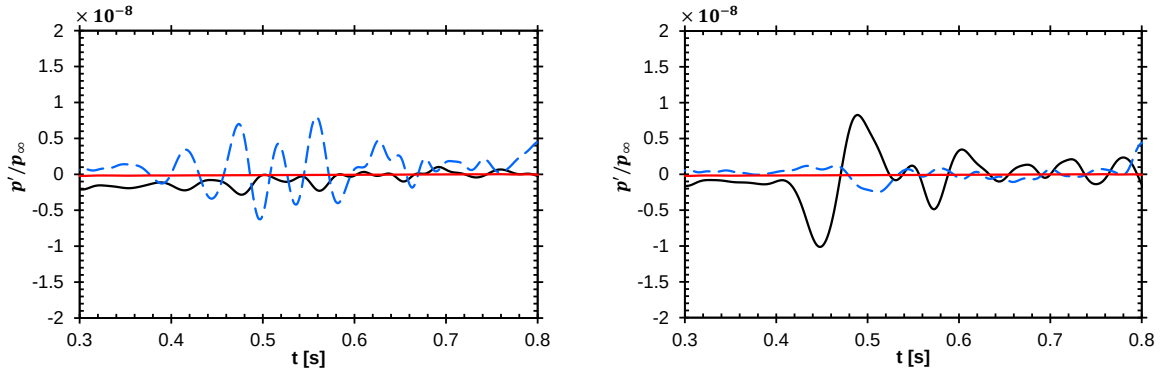

Figure 5.16: Time history of the pressure fluctuation p' on a grid with a refinement interface in the (left) x-direction and (right) y-direction at (——) m_1 and (– –) m_2. (——) corresponds to the pressure fluctuations at m_1 on the grid without refinement interface.

spurious noise detected at m_2 has a clearly higher amplitude than that detected at m_1 and the opposite applies to the refinement interface in the y-direction. Furthermore, an interesting phenomenon is that spurious noise detected at m_2 in the first case seems to have a higher frequency than the one detected at m_1 in the case of the interface in y-direction, although the turbulence package has an isotropic character. However, the convection direction could play a role in the frequency content of the generated spurious noise.

Effect of discretisation schemes on refinement interfaces

As illustrated in Figure 5.14, the energy content that cannot be resolved on the coarse side of the grid does not only consist of the energy contained in scales whose wavenumber components are larger than the cut-off wavenumber k_c. The behaviour of discretisation schemes on different grid as well as their dependency on the grid spacing could cause different energy distribution for different schemes. In this work, the behaviour of the fixed-blended scheme is compared to that of the DESHyb scheme on refinement interfaces. For this, $\Omega_{\min} = 10^{-3}/\tau_0$ is chosen, along with $\sigma_{\min} = 0$ and $\sigma_{\max} = 0.05$. These parameters have already shown low spurious noise generation (cf. Figure 5.10).

Figure 5.17 (left) shows the time history of p' at m_1 and m_2 using the DESHyb scheme on the grid with refinement interface in all three directions. The basic structure of the distribution of spurious noise is similar to that produced by the fixed blending scheme in Figure 5.13. However, one can observe that the noise produced at the refinement interfaces using the DESHyb scheme contains high frequency components. Therefore, the noise produced by the fixed blending scheme in Figure 5.13 is subtracted from that produced by the DESHyb scheme. This is shown in Figure 5.17 (right) at both monitor points. As expected, the differences between both signals are high-frequency signals whose mean value is approximately zero. Consequently, the spurious noise generated by the DESHyb scheme at the refinement interface can be considered as a superposition of the two parts: one part is caused by the refinement interface itself due to the lack of resolution on the coarse side of the grid. This part is equivalent to the spurious noise caused by the fixed blending scheme. The second

high-frequency part is related to the DESHyb scheme. The presumable cause for this kind of noise is the undesired switching between schemes on the refinement interface.

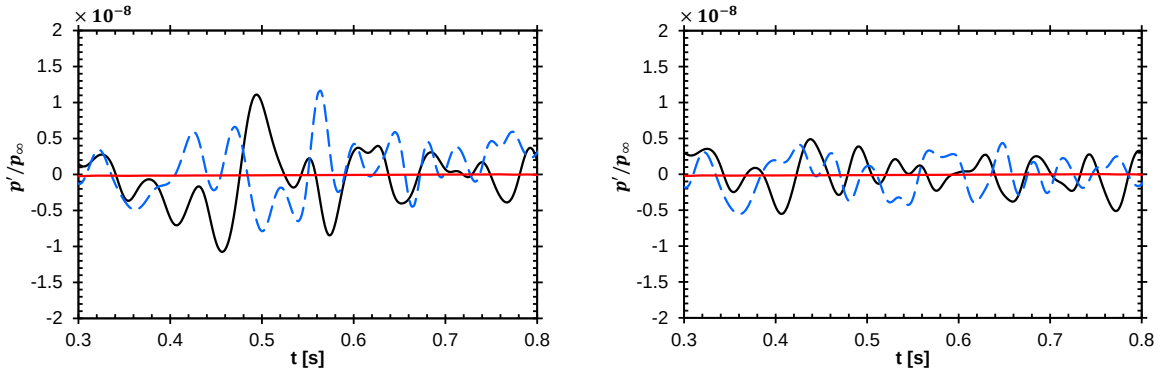

Figure 5.17: (Left) Time history of the pressure fluctuations p' using the DESHyb scheme on a grid with refinement interface at (——) m_1 and (– –) m_2. (Right): difference between the signals at (——) m_1 and (– –) m_2 using the fixed blending scheme and the DESHyb scheme on a grid with refinement interface.

5.2.4 Spurious noise reduction

The previous section shows two main sources of spurious noise: discretisation schemes and refinement interfaces. While spurious noise resulting from the discretisation scheme could be avoided by different blending techniques (e.g. fixed blending, weaker blending in DESHyb scheme), suppressing spurious noise generated at refinement interfaces is more challenging. As already discussed, the origin of spurious noise generated at refinement interfaces is mainly related to the energy contained in wavenumber components present on the fine side of the interface and which cannot be resolved on the coarse side of the grid. In order to avoid this issue, different approaches could be developed and employed:

- The first intuitive approach is to filter out the wavenumber components that cannot be resolved on the coarse side of the grid before the flow reaches a refinement interface. This way, the energy in the shaded region between k_c and k_f in Figure 5.14 is filtered out and the only source of spurious noise would be the shaded region for wavenumbers smaller than k_c. As previously explained, this region results from the dependency of discretisation scheme characteristics on the grid spacing and as a result on the cut-off wavenumber of the grid.

  Applying the filtering method is, however, not trivial. If certain wavenumber components have to be filtered, a spectral cut-off filter would be ideal for this job. This way, all components larger than k_c would be filtered out and the components smaller than k_c stay intact. However, the implementation of such a filter in a finite-volume framework based on unstructured grids is difficult. One way to filter the flow field would be to transform it every time-step into the wavenumber domain, apply a cut-off filter and transform it back to the time-domain. Such a method is prohibitively expensive and inconceivable for industrial applications.

An alternative method is to use of differential or discrete filters. Such filters were developed and utilised by, inter alia, Germano [28], Lele [61], and Visbal et al. [113]. However, in order to get the desired effect of a sharp boundary between the filtered and unfiltered wavenumber components, the differential or discrete filter has to be of high-order. Consequently, filtering a flow variable in one computational cell would require building up large numerical stencils. Building up such stencils could be challenging in a code based on unstructured meshes. Nevertheless, the discrete filters developed by Lele [61] were implemented in the course of this study by using multiple and consecutive differential operations. The filter did show good results regarding filtering high wavenumbers while leaving low wavenumber content unaffected. However, the computational effort needed for one filtering operation was so high, that its application to complex geometries with large number of cells was impractical. Lastly, filtering the flow field in the course of the PIMPLE algorithm in OpenFOAM is not straightforward. Applying an explicit filter on the momentum equation results in unknown terms, as shown in chapter 2. Apart from modelling these terms, Lund showed in [67] that the product of the filtered velocities in the convective term of the momentum equation could produce high frequency components. He proposed furthermore an alternative decomposition of the filtered non-linear term, which, however, does have negative side-effects if the utilised explicit filter is not of high-order. Such side-effects are, for instance, the absence of Galilean invariance.

- A second approach to avoid spurious noise generation is using unstructured grids with a low expansion ratio between fine and coarse regions. Continuious transition regions in a numerical grid provide a gradual transfer of the energy from high wavenumber components to low wavenumbers. This gradual transfer helps avoiding spurious noise generation caused by the numerical grid.

  In the course of this work, two different strategies for generating grids free of refinement interfaces are employed. The first method consists of generating unstructured grids with polyhedral cells. The advantage of such grids is their flexibility regarding refinement regions and the possibility of continuously coarsening cells for a smooth transition between fine and coarse regions of the computational domain. Furthermore, they are applicable for industrial applications and complex geometries. However, polyhedral cells are known to be more dissipative than Cartesian ones, which could be crucial for aeroacoustic applications. This does not only apply for the dissipation of acoustic waves, but also for pressure fluctuations on the surface of solid bodies, which are the main acoustic sources in this work. A first attempt to check the capability of polyhedral grids in accurately calculating noise generation and wave propagation is done on the two-struts benchmark. The results showed a noticeable dissipative behaviour in the far-field spectra compared to the grid employed in chapter 4. Furthermore, weak spurious noise was observed even in the domains where the spacial resolution is constant. This could be attributed to the slight difference in the spacial resolution between each polyhedral cell and its neighbouring one. A constant spacial resolution would be possible to achieve with hexagon-like polyhedral cells. However, the grid generator utilised for the generation of polyhedral cells was not able to produce such grids. For these reasons, this strategy was no longer pursued in this work.

The second strategy consists of using the Cartesian grids employed so far, and applying grid-stretching in the neighbourhood of refinement interfaces. A disadvantage of such a method is that the stretching can only be done in one direction at a time. However, the analysis performed in the last section did show a relation between the direction of refinement and the direction of spurious noise propagation, which can be exploited for specific applications. In order to explain how useful this technique could be, the following scenario considered. The main noise source regarding the sound heard by a driver of a vehicle is the exterior side-mirror. The sound generated by the mirror propagates to the window near the mirror which transmits the sound into the interior of the car. Therefore, pressure fluctuations on the surface of the mirror have to be accurately calculated. For this, a fine resolution of the mirrors surface is required. Furthermore, in order to accurately calculate the flow past the mirror, its wake has to be fine resolved. However, the fine resolution of the mirrors wake cannot be extended along the complete vehicle, otherwise the computational cost would be extremely high due to the high number of grid cells. At this point, the grid in the wake of the mirror has to be coarsened which introduces refinement interfaces. The interaction between the turbulent wake behind the mirror and the refinement interfaces produce spurious noise that propagates upstream to the surface of the window and falsify the calculated results. At this stage, one knows that spurious noise generated at refinement interfaces propagate in all three spacial directions. However, if the interfaces are downstream the surface of the window, one would only be interested in reducing spurious noise that propagate in the upstream direction. In the other directions, spurious noise can propagate through the computational domain till they get dissipated by the numerical grid or leave the domain boundaries. These waves do not affect the result on the surface of the side-window. As a result, a directional reduction of spurious noise could be practical for such applications. This is where directional refinement and directional stretching come into operation. In the next paragraph, the directional stretching is validated on the convected isotropic turbulence test case.

- The third approach to reduce spurious noise is to damp out acoustic waves generated at refinement interfaces. The damping effect should however not affect the turbulence. Taking the aforementioned scenario, spurious waves generated at refinement interfaces in the wake of the side-mirror could be damped out before they reach the side-window. On the other hand, the turbulent wake of the side-mirror as well as the turbulence in the wake of the vehicle has to remain intact. This could be achieved by applying the acoustic damping model introduced in chapter 3. This model can be activated wherever spurious waves are generated or even in region, where acoustic propagation is not needed. Only in regions, where physical noise generation and propagation has to be calculated, the damping model has to be deactivated. This approach results in two restrictions: the damping coefficient depends on the local spatial and temporal resolution due to stability issues, and refinement interfaces have to be avoided in regions where acoustic waves have to be resolved. The applicability of this model is illustrated in this section using the convected isotropic turbulence test case.

Grid stretching

In order to study the effectivity of grid stretching on reducing spurious noise, the uniform grid presented in Figure 5.1 is modified such that cells in the region $x > 4\pi$ are gradually streched in the positive x-direction. Three grids with different expansion ratios are considered. In order to isolate the effect of grid stretching in the x-direction, refinement interfaces in the y- and z-directions are omitted. Furthermore, to exclude the influence of varying numerical schemes, the fixed blending scheme is utilised for these studies. The above mentioned expansion ratio of the stretched cells is defined as:

$$\mathrm{ER}[\%] = \left(\frac{\Delta_{x,i+1}}{\Delta_{x,i}} - 1 \right) \cdot 100, \tag{5.1}$$

where Δ_x refers to the cell width and i and $i+1$ to two adjacent cells in the x-direction. For instance, a refinement interface where the grid size increases from Δ_x to $2\Delta_x$ corresponds to an ER of 100%. Three test cases with different ER values will be considered, i.e. with ER of 1%, 5% and 10%. The grids with ER = 1% and 10% are shown in Figure 5.18.

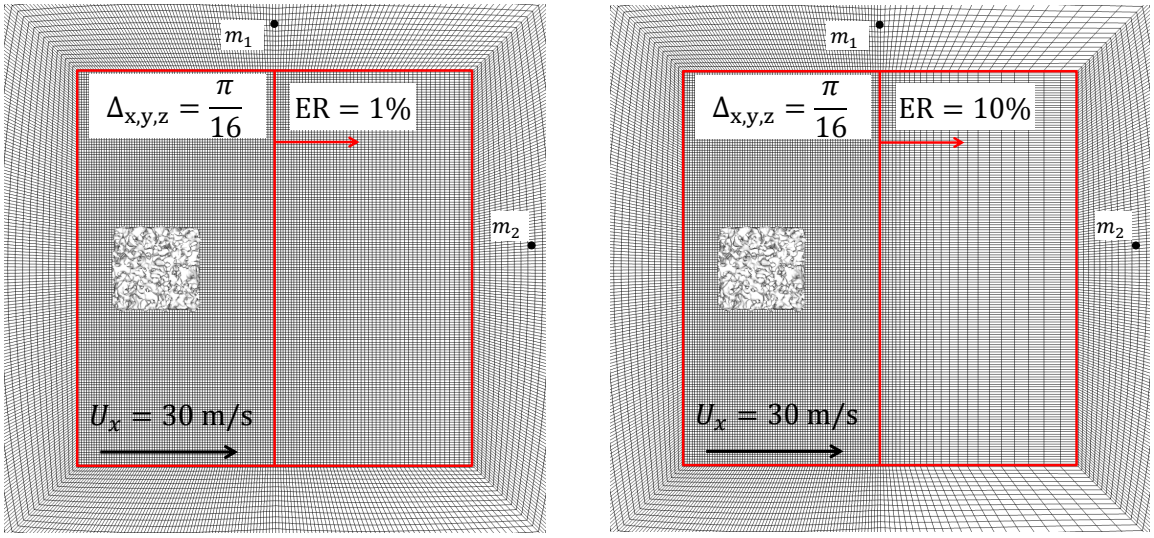

Figure 5.18: Vertical slice of the computational domain showing grids with (left) ER = 1% and (right) ER = 10%. The vertical red lines in the middle of the center box correspond to the begin of cell expansion.

Figures 5.19 to 5.21 show snapshots of the turbulence package as well as $\partial p/\partial t$ at $t = 0.6$ s for the grids with different expansion ratios. Furthermore, the time history of p' at m_1 and m_2 is plotted for each grid. For the grid with ER = 1%, no spurious noise is visible. The turbulence package as well as the distribution of $\partial p/\partial t$ are similar to those of the uniform grid, indicating minor to no effect of this ER. Moreover, the time history of p' does not show any spurious waves and resembles the distribution in Figure 5.4. As the expansion ratio increases, spurious noise is generated at the turbulence box passes the stretched grid. For ER = 5%, spurious waves can be observed in the $\partial p/\partial t$ distribution. However, these waves are so weak, that they can be barely noticed in the time history of p' at m_1 and m_2. For

larger expansion ratios (e.g. ER = 10%), the amplitude of spurious noise is distinctly higher at both monitor points. Moreover, the structure of their propagation is equivalent to that of the grid with ER = 5%. As the turbulence crosses the stretched grid, turbulent fluctuations get stretched in the x-direction. This "vortex-stretching"causes noise generation, which increases as the expansion ratio increases. The stretched structures can be observed in the $\lambda_2 = 10^{-2}$ isosurface.

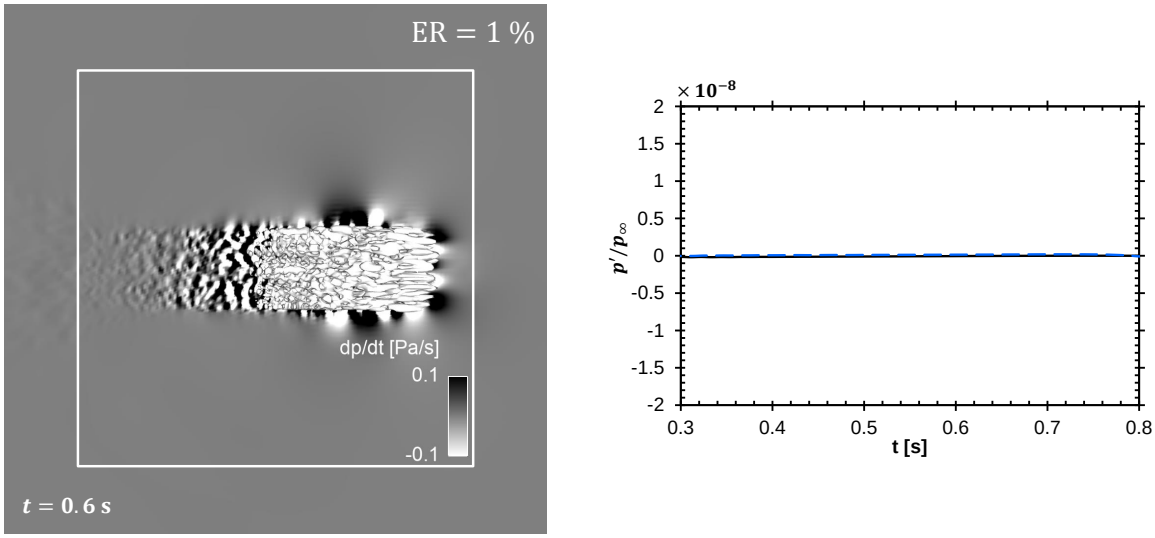

Figure 5.19: (Left) Snapshot of the turbulence package as well as $\partial p/\partial t$ at $t = 0.6$ s for the grid with ER = 1% and (right) time history of p' at (——) m_1 and (— —) m_2.

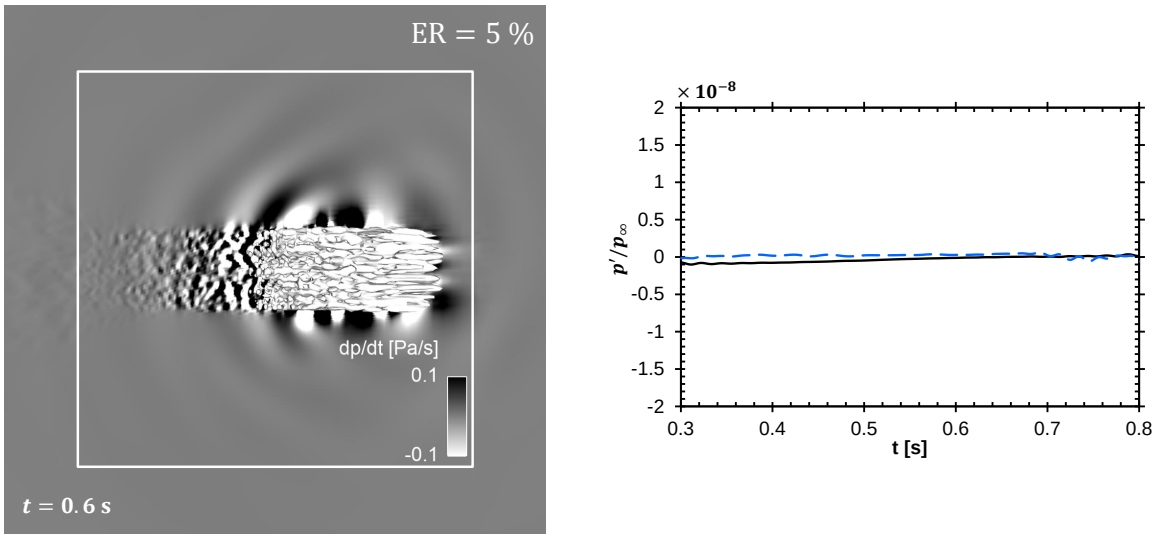

Figure 5.20: (Left) Snapshot of the turbulence package as well as $\partial p/\partial t$ at $t = 0.6$ s for the grid with ER = 5% and (right) time history of p' at (——) m_1 and (— —) m_2.

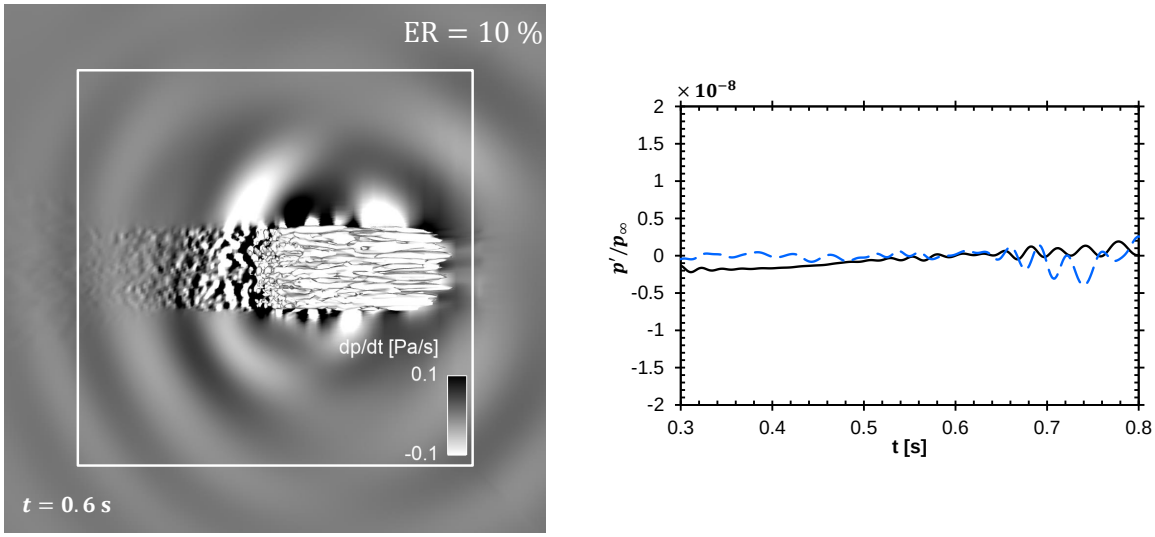

Figure 5.21: (Left) Snapshot of the turbulence package as well as $\partial p/\partial t$ at $t = 0.6$ s for the grid with ER = 10% and (right) time history of p' at (——) m_1 and (— —) m_2.

Acoustic damping

An alternative strategy for the reduction of spurious noise is damping out undesired spurious waves before they propagate into the region of interest. One important aspect that has to be considered is that the damping should only affect acoustic waves while maintaining the turbulence. The acoustic damping model proposed in chapter 3 is utilised for this purpose.

In order to test the effect of the damping model on turbulence, the damping coefficient is applied to the convected turbulence test case on a uniform grid. Hereby, the damping coefficient is applied all over the computational domain and the turbulence package is monitored at different time steps and compared to the case without damping model. The damping coefficient q_0 in Eq. (3.35) is chosen such that the stability criterion at the smallest cell of the domain is still fulfilled. In this case the smallest cells are present in the center box of the O-grid and correspond to a grid-spacing of $\Delta_{x,y,z} = \pi/16$ [cf. Figure 5.18]. Using a time-step size of $\Delta_t = 1.5 \cdot 10^{-4}$, the critical value of q is then:

$$q_c = \frac{\Delta_{x,y,z}^2}{2c^2\Delta_t^2} \approx 7.2. \tag{5.2}$$

Figure 5.22 shows two snapshots of the turbulence package at $t = 0.7$ s with and without damping model. The turbulent structures are almost equivalent in both cases. Even the small structures at the tail of the package are preserved when using the damping model. This indicates that the damping model does not affect hydrodynamic fluctuations and, therefore, preserves turbulence. Regarding spurious noise, Figure 5.23 shows the time history of p' on the uniform grid with activated damping model. As expected, the model does not produce any spurious noise and the distribution of p' is equivalent to the reference case in Figure 5.4

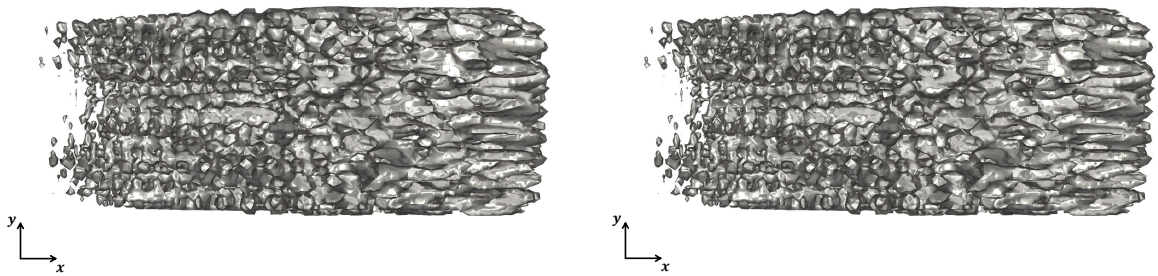

Figure 5.22: $\lambda_2 = 10^{-2}$ isosurfaces at $t = 0.7$ s on a uniform grid with (left) deactivated and (right) activated damping model.

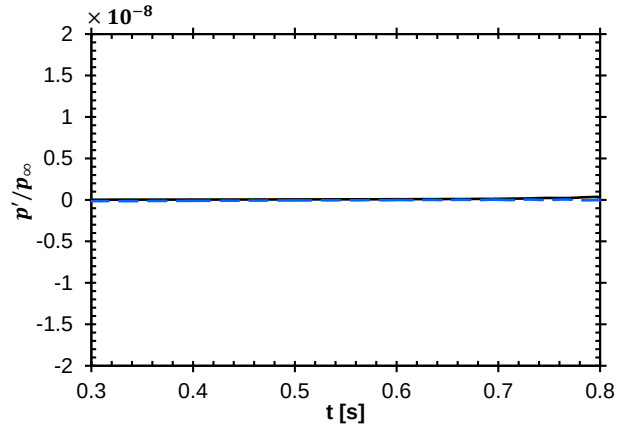

Figure 5.23: Time history of p' with the damping model activated in the whole computational domain at (——) m_1 and (— —) m_2.

After analysing the effect of the acoustic damping model on turbulence, a second test case consisting of the grid with refinement interface (cf. Figure 5.11) is calculated with the damping model activated in the whole computational domain. The purpose of this test is to check the capability of the damping model in damping out spurious noise generated at the refinement interface.

Snapshots of the λ_2-isosurfaces as the turbulence package passes the refinement interface are presented in Figure 5.24. Similar to the uniform grid, the damping model does not show any damping effect of the turbulent structures and the fluctuations are preserved across the refinement interface. Regarding spurious noise generated at the refinement interface, Figure 5.25 shows the time history of the pressure fluctuations p' with and without damping model at the two monitor points. Although spurious waves are not completely eliminated, a clear reduction of the amplitude of spurious noise can be observed at both points. Whether this reduction is enough for industrial applications depends on the specific application itself, as the damping coefficient depends on the local grid spacing and the time-step size. Hence, the next section shows a quantitative analysis of spurious noise on typical industrial grids with realistic time-step sizes as well as the applicability of the acoustic damping model for such applications.

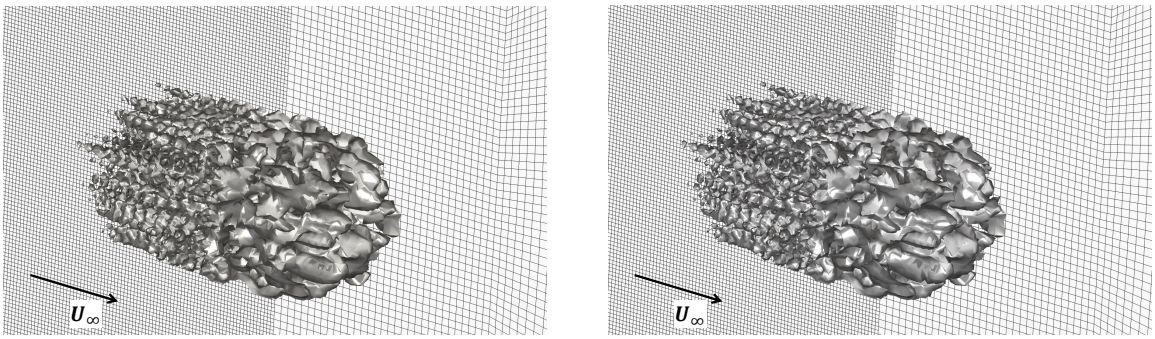

Figure 5.24: $\lambda_2 = 10^{-2}$ isosurfaces at $t = 0.55$ s on the grid shown in Figure 5.11 with (left) deactivated and (right) activated damping model. The background represents a periodic boundary of the computational domain.

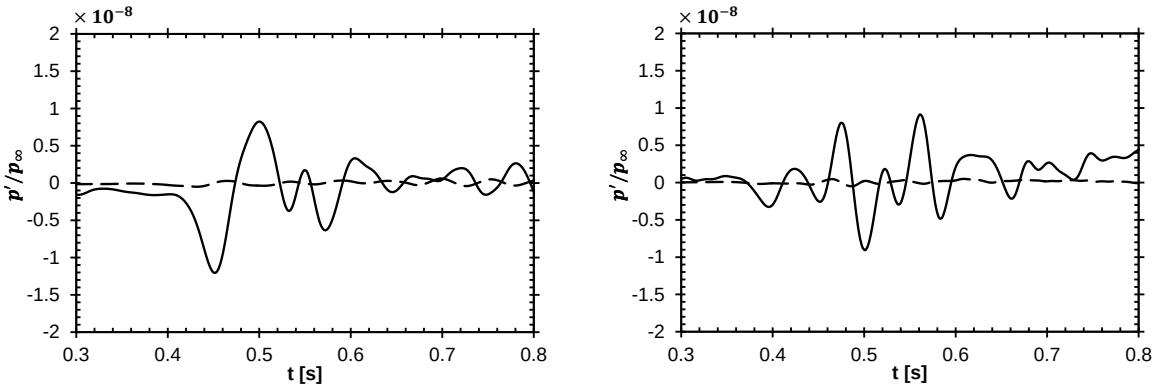

Figure 5.25: Time history of the pressure fluctuations p' at (left) m_2 and (right) m_2. Solid lines represent the reference case without damping model and dashed lines the case with activated damping model.

5.3 Flow past an exterior side-mirror

The analysis of the convected isotropic turbulence in the previous section helped in understanding the mechanism of spurious noise generation by discretisation schemes and grid interfaces. However, the assessment of spurious noise compared to physical noise was not possible, since the turbulence package did not produce sound waves due to the low Mach number of the flow. Furthermore, the critical value of the coefficient of the acoustic damping model was chosen based on the numerical setup of the convected turbulence, which does not necessarily correspond to the optimal choice for automotive applications.

In this section, a quantitative analysis of spurious noise is performed on a real side-mirror geometry. This enables the evaluation of the significance of spurious waves compared to physical waves generated by the side-mirror. Furthermore, an assessment of the applicability of the acoustic damping model is performed using the numerical parameters that are typical for flow calculation past a vehicle.

5.3.1 Numerical setup

The 3D geometry of the side-mirror is illustrated in Figure 5.26. It represents a side-mirror of a real production car. The mirror is mounted on a plate as shown in Figure 5.27, and is subjected to a uniform flow with a speed of $U_x = 39$ m/s. This corresponds to approximately 140 km/h, which is a typical speed for aeroacoustic analysis of passenger vehicles. It is worth mentioning that the flow upstream the side-mirror does not exhibit any turbulent fluctuations. No-slip boundary conditions are applied to the surface of the side-mirror and the plate on which it is mounted. Apart from the inlet and outlet boundaries, non-reflective boundary conditions are prescribed on the other boundaries of the computational domain.

In the course of this study, different grids were generated in order to examine and reduce spurious noise. At this point, the initial grid is presented and the modified versions of it are shown throughout the study. The computational domain has the dimensions of $90L$ in the direction (x-direction) of the flow and $45L$ in the other two directions (y- and z-directions), where L corresponds to the length of the side-mirror [cf. Figure 5.27]. The mirror is placed at the center of the plate and the origin of the coordinate system is at the center of the mirrors foot. The grid in the wake of the mirror consists of Cartesian cells with a grid spacing $\Delta_{x,y,z} = 2$ mm, and it extends 1.5 m downstream the mirrors foot. For $x > 1.5$ m, the grid is coarsened gradually to reach a resolution of approximately 0.5 m, resulting in successive refinement interfaces in the wake of the mirror. The same applies for the region upstream and above the mirror. A slice through the numerical grid is shown in Figure 5.27. Resolving the surface of the mirror with 2 mm cells was not enough to capture the main features of the mirrors geometry. Hence, the surface of the mirror is resolved using $\Delta_{x,y,z} = 0.5$ mm, resulting in two successive refinement interfaces in the vicinity of the mirrors surface as shown in Figure 5.28. The number of cells between refinement interfaces is set to 15 cells and is applies for all interfaces. The time step size is set to $\Delta t = 10^{-5}$ s and the simulated physical time is equal to 0.5 s. The drag coefficient calculated using the pressure on mirrors surface was monitored throughout the computation, and it showed a stationary behaviour after $t = 0.2$ s. Therefore, the flow between $t = 0.2$ and $t = 0.5$ s is assumed to be statistically stationary.

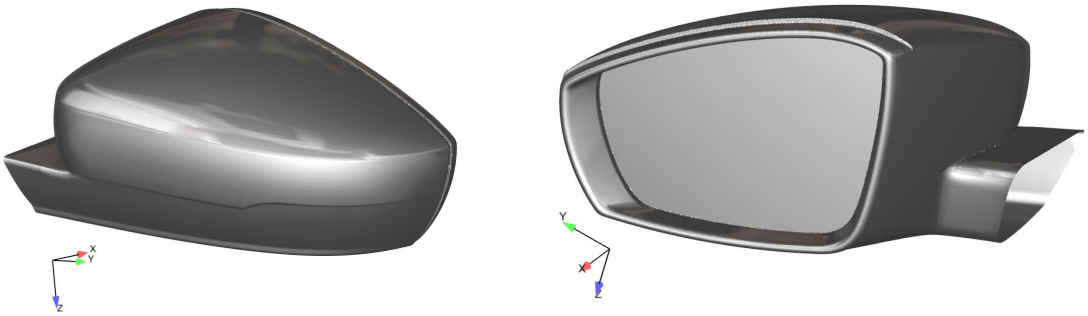

Figure 5.26: Geometry of the exterior side-mirror: (left) the mirrors cap and (right) its glass (figure taken from [20]).

Similar to the two-struts benchmark, acoustic waves are calculated directly using the compressible solver (DNC) as well as indirectly using the integral method (FWH). The aeroacous-

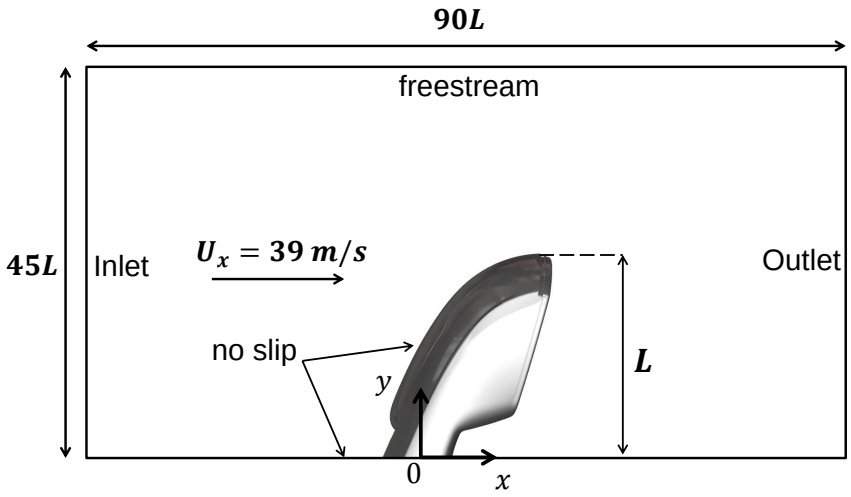

Figure 5.27: Schematic representation of the computational domain used for flow simulation past the side-mirror.

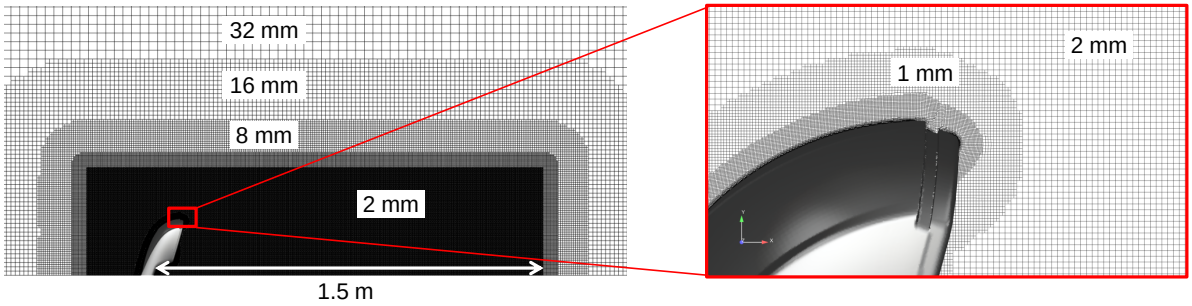

Figure 5.28: Slice through the numerical grid at $z = 0$ with the corresponding refinement regions and (right) a close up of the grid in the vicinity of the mirrors surface.

tic evaluation is done on the plate in the wake of the side-mirror. This corresponds to the side-window in a real production car. For the hybrid CAA computation, pressure fluctuations on the surface of the side-mirror are sampled every time step in the time $0.3 < t < 0.5$ s. This corresponds to a sampling frequency $F_s = 100$ kHz. Due to the low Mach number, it is assumed that the surface of the mirror is the major noise source. Hence, possible spurious noise generated outside the integration surface can be detected by comparing the directly calculated acoustic waves with the ones calculated using the FWH method. In the case of a spurious noise-free computation, both results should be equivalent.

5.3.2 Aeroacoustic evaluation in the wake of the mirror

The challenge in evaluating acoustic waves calculated using DNC in the wake of the mirror is the presence of hydrodynamic pressure fluctuations. The latter fluctuations are orders of magnitude larger than acoustic ones, which makes a separation between acoustic and hydrodynamic waves difficult. However, one major difference between both waves is their speed of propagation. In the wake of the mirror, hydrodynamic pressure waves propagate at

speeds equivalent to the convective velocity in the wake. These speeds are of the order of U_x. On the other hand, acoustic waves propagate at the speed of sound, which is significantly higher than the convective speed in this case. This fact can be exploited in order to separate acoustic from hydrodynamic pressure fluctuations in DNC. For this purpose, frequency-wavenumber analysis is performed on the plate in the wake of the mirror.

The frequency-wavenumber analysis consists of transforming the pressure signal from time and space into the frequency-wavenumber space. For this reason, pressure values are monitored on a two-dimensional array on the plate in the wake of the mirror. The array chosen in this study extends between the points with coordinates $(0.5;\ 0;\ -0.2)$ m and $(0.9;\ 0;\ 0.1)$ m. Considering the resolution of 2 mm in the wake, the array consists of 200 points in the x-direction and 150 points in the z-direction. Furthermore, pressure values are monitored at each time step between $t = 0.3$ and $t = 0.5$ s, resulting in 20,000 samples at each point of the array. The temporal dataset is split into different blocks with 4096 samples in each block and is Fourier transformed using a Hanning window with 50% overlap at each point of the array. For the spacial Fourier transformation, a single Hanning window is applied to the dataset in the x- and z-direction due to the limited number of points. Using the temporal and two-dimensional spacial Fourier transformations, the power spectral density (PSD) is calculated as a function of the frequency f and the wavenumbers k_x and k_z. The PSD-spectra shown in the following are calculated relative to a reference pressure $p_{\text{ref}} = 2 \cdot 10^{-5}$ Pa. For detailed information about the calculation procedure, the reader is referred to [15].

Figure 5.29 shows the frequency-wavenumber spectrum at $k_z = 0$. Therein, three major branches can be observed: the convective branch, which is characterised by its high amplitude and a slope of the order of the convective velocity U_x, an acoustic branch for $k_x > 0$, which correspond to acoustic waves propagating in the positive x-direction and exhibit a slope in the $k_x - f$ plane of $0.8U_x + c$, and branch in the $k_x < 0$ region characterising spurious noise. Note that the spurious noise branch exhibits a slope equal to $0.8U_x - c$, indicating that spurious waves propagate with the speed of sound. It is assumed that the average velocity in the x-direction in the wake of the mirror is approximately equal to $0.8U_x$. The dominance of the hydrodynamic pressure fluctuations can be observed in the high spectral levels of the convective branch in the $k_x - f$ plane. Figure 5.29 shows furthermore the frequency-wavenumber spectrum at a constant frequency $f = 3$ kHz. As for the $k_x - f$ plane, two acoustic components can be observed in the $k_x - k_z$: a component present in the $k_x > 0$ region indicating acoustic waves propagating in the positive x-direction, and another one in the $k_x < 0$ region indicating acoustic waves propagating in the negative x-direction.

Since no measurements are available for the side-mirror case, it is not possible to validate the spectral level of acoustic waves emitted from the surface of the mirror. However, due to the low Mach number of the flow, volume acoustic sources are negligible compared to surface sources, e.g. in this case the side-mirror. Hence, the surface of the mirror is the only acoustic source in the computational domain. Therefore, one would only expect an acoustic branch in the positive x-direction, since the plane, on which the frequency-wavenumber analysis is performed, is positioned in the wake of the mirror. Therefore, it is likely that the negative acoustic branch is the result of spurious noise generated at refinement interfaces in the wake of the mirror (cf. Figure 5.28). In order to prove this, a second test case

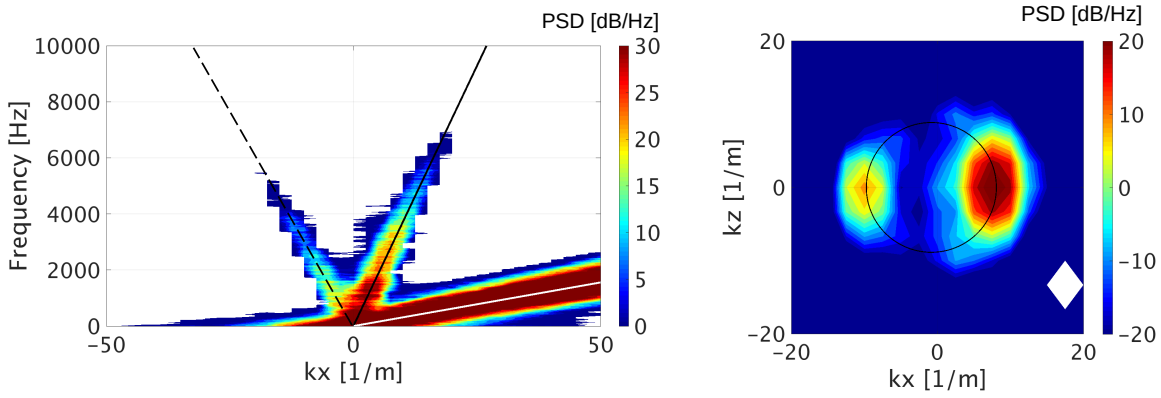

Figure 5.29: Frequency-wavenumber spectrum calculated on the plane in the wake of the side-mirror at (left) $k_z = 0$ and (right) $f = 3$ kHz. In the $k_x - f$ plane, the white solide line corresponds to $k_x = f/0.8U_x$, the black solid line to $k_x = f/(0.8U_x + c)$, and the black dashed line to $k_x = f/(0.8U_x - c)$. The black solid circle in the $k_x - k_z$ plane corresponds to the acoustic cone.

for which the 2 mm refinement region in the wake of the mirror is extended further downstream. The first refinement interface is then positioned 3 m instead of 1.5 m downstream the foot of the mirror. This way, the distance spurious noise has to cover in order to reach the frequency-wavenumber analysis plane increases. Furthermore, the energy contained in the turbulent wake decreases as the turbulence convects downstream the mirror. As a result, energy contained in high wavenumber components and, consequently, spurious noise generated at refinement interfaces significantly decrease.

Figure 5.30 shows the frequency-wavenumber spectrum at $k_z = 0$ and $f = 3$ kHz for the grid with extended refinement region in the wake. The positive acoustic branch is equivalent to the one in Figure 5.29, since the extended refinement region downstream has a minor influence on the flow past the side-mirror. On the other hand, the spectral level at the negative acoustic branch is remarkably lower than in the previous case. This indicates that the negative acoustic branch in the analysis of the original grid is the result of spurious noise generated at refinement interfaces in the wake of the mirror.

It is worth mentioning that the extended refinement region in the wake of the mirror results in an increase of the number of cells by approximately 45%. Consequently, reducing spurious noise just by extending the refinement region almost doubles the computational cost, which is critical in industrial applications. For this reason, alternative methods are needed for the reduction of spurious noise without significantly affecting the computational effort.

5.3.3 Reduction of spurious noise generated in the wake of the mirror

The grid shown in Figure 5.28 exhibits multiple refinement interfaces in the wake of the mirror. The frequency of spurious noise generated at each interface is related to the cut-off wavenumber of the grid on the coarse side of the interface. Hence, it is expected that the first

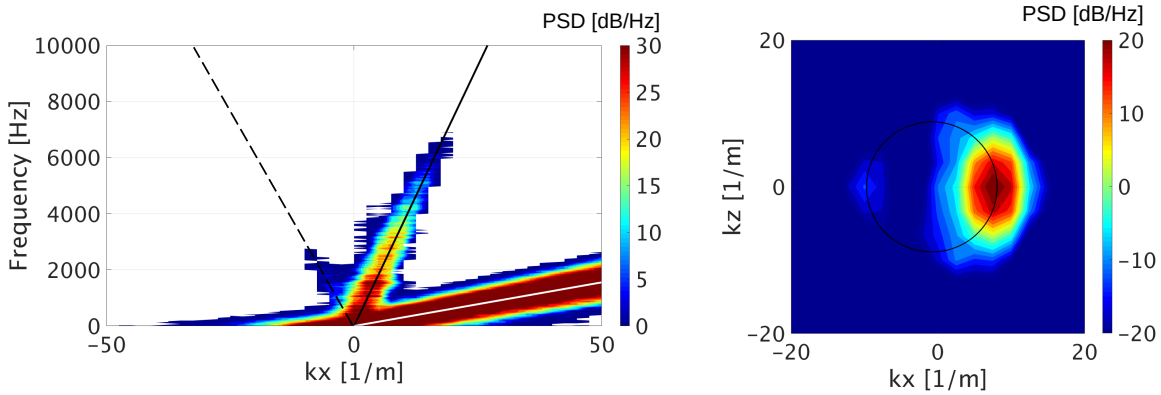

Figure 5.30: Frequency-wavenumber spectrum calculated in the wake of the side-mirror at (left) $k_z = 0$ and (right) $f = 3$ kHz. The results correspond to the grid with an extended 2 mm refinement region in the wake.

refinement interface connecting the 2 mm refinement region with the 4 mm region generates spurious noise of higher frequency than other interfaces. In order to prove this, the 4 mm refinement region is extended downstream of the mirror, so that spurious noise generated at the first refinement interface can be separately analysed. The increase in the number of cells due to the extension of the 4 mm region is significantly lower than the extension of the 2 mm region due to larger spacial resolution.

Figure 5.31 shows the frequency-wavenumber spectrum of the results obtained on the grid with extended 4 mm refinement region. At low frequencies ($f < 1$ kHz), the spectral level of spurious noise is lower than that in Figure 5.29. However, high-frequency spurious noise ($f \approx 2$ kHz) exhibits only a slight decrease compared to the original grid. This can also be observed in the $k_x - k_z$ plane at $f = 3$ kHz. This confirms that the first refinement interface is responsible for high-frequency spurious noise due the high cut-off wavenumber, whereas the subsequent interfaces are responsible for the low-frequency spurious noise.

In order to reduce high-frequency spurious noise, the acoustic damping model can be utilised. The analytical analysis of its damping effect presented in chapter 3 has shown its high effectiveness for high-frequency acoustic waves. In order to separately analyse the effect of the damping model, the following analysis is performed using the original grid shown in Figure 5.28. In the region, where acoustic waves have to be preserved, the damping model has to be deactivated. In the rest of the computational domain, the model is activated in order to damp out non-physical waves resulting either from spurious noise or wave reflections at refinement interfaces above and upstream of the surface of the mirror. Figure 5.32 shows the distribution of the damping coefficient at a slice of the grid at $z = 0$. The coefficient is set to the critical damping constant, which is equal to $\Delta^2_{x,y,z}/2c^2\Delta^2_t$. For the 2 mm resolution region, this corresponds to a critical value $q_c \approx 0.16$. In order to avoid spurious noise generation, the damping coefficient is linearly increased from 0 to 0.16 and correspondingly from 0.16 to 0.67 outside the 2 mm region.

Figure 5.33 shows the frequency-wavenumber spectrum calculated with the acoustic damping model. Compared to the spectrum in Figure 5.29, one can observe that high-frequency

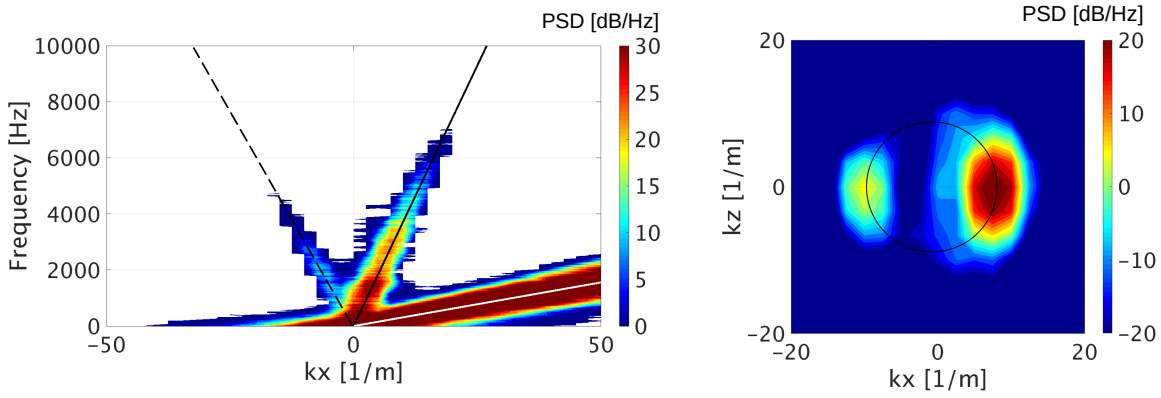

Figure 5.31: Frequency-wavenumber spectrum calculated in the wake of the side-mirror at (left) $k_z = 0$ and (right) $f = 3$ kHz. The results correspond to the grid with an extended 4 mm refinement region in the wake.

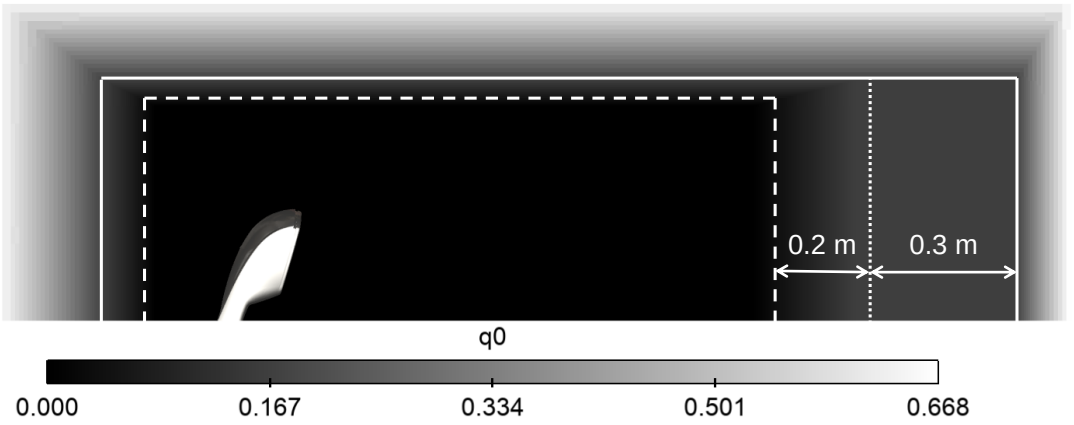

Figure 5.32: Distribution of the damping constant q_0 at $z = 0$. The solid white lines represent the 2 mm - 4 mm refinement interface. Between the vertical dashed line and the vertical dotted line, the damping constant increases linearly from 0 to 0.16 and stays constant until the refinement interface. The surface of the mirror is indicated in white for visual reasons, however, no damping is applied on it (figure taken from [20]).

acoustic waves propagating in the negative x-direction are clearly reduced. In the low-frequency region, spurious noise is still visible, due to the reduced effect of the acoustic damping model in the low-frequency region. Furthermore, acoustic waves propagating in the positive x-direction, which correspond to waves generated at the surface of the mirror, are preserved.

5.3.4 Comparison between different CAA-methods

The DNC and the FWH methods have already been validated in chapter 4 on the two-struts benchmark, and both methods show good agreement with experimental results. However, the Mach number in the side-mirror test case is lower than the one in the two-struts case. As already shown by Thiele [103], spurious noise could be present but not visible for $Ma \approx 0.2$.

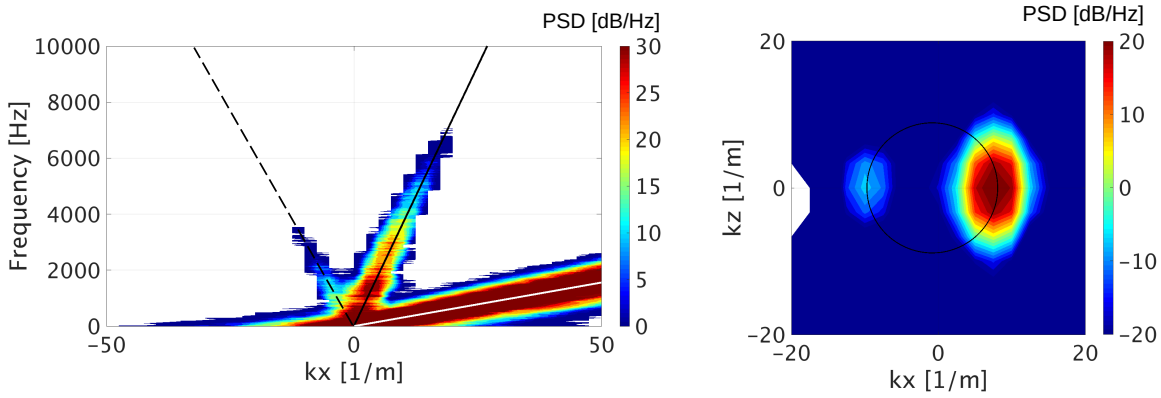

Figure 5.33: Frequency-wavenumber spectrum calculated in the wake of the side-mirror at (left) $k_z = 0$ and (right) $f = 3$ kHz after the activation of the acoustic damping model.

Furthermore, he showed the presence of spurious noise on the tandem circular cylinder benchmark, for which $Ma \approx 0.13$.

The Mach number in the side-mirror case is equal to 0.11. Therefore, the relevance of spurious noise compared to physical acoustic waves generated by the mirror is high. The previous sections have already shown that spurious noise is generated at refinement interfaces in the wake of the mirror and that their spectral level is comparable to that of physical noise propagating in the positive x-direction. However, the possibility of spurious noise propagating in the positive x-direction has not been checked yet. The presence of spurious noise in [103] has been observed by comparing the results of solid and permeable FWH integration surfaces. Similarly, one can compare the noise calculated by DNC to the results of the FWH method using the solid surface of the mirror as an integration surface. In case both results are equivalent, one can assume the absence of spurious noise generation outside the surface of the mirror.

For the comparison between both methods, the grid with an extended 2 mm refinement region is taken. This grid showed the lowest spectral level for spurious noise generated at refinement interfaces in the wake of the mirror. The compressible pressure fluctuations on the surface of the mirror are used as input for the FWH method, and acoustic waves calculated using FWH are propagated to the plane on which the frequency-wavenumber analysis is performed. Due to the wall boundary condition, pressure values calculated by the FWH method are doubled on the surface of the plate. Finally, a frequency-wavenumber spectrum is calculated using the pressure values obtained by the FWH method and is compared to the spectrum presented in Figure 5.30.

Figure 5.34 shows a comparison between the frequency-wavenumber spectra calculated using DNC and FWH at $k_z = 0$. Since the FWH calculates only acoustic wave resulting from the surface of the mirror, only the positive acoustic branch is visible. In the low-frequency region (up to 2 kHz), both spectra show similar spectral levels. However, for $f > 2$ kHz, the spectral level of acoustic waves calculated using DNC are substantially higher than those calculated using FWH, especially for the frequency range between 3 to 5 kHz. For a more detailed analysis of the differences between both results, the positive acoustic branch is

integrated over all wavenumber components k_x and k_z. This integration delivers the average PSD spectra of acoustic waves travelling across the frequency-wavenumber evaluation plane in the positive x-direction. These spectra are shown in Figure 5.35. For $f < 1.5$ kHz, the PSD-spectra of both methods show good agreement. For larger frequencies, the spectral level of the DNC result is substantially higher than that of FWH. This behaviour applies for the frequency range 1.5 kHz $< f <$ 6 kHz, in which acoustic waves calculated using DNC are up to 10 dB higher than those calculated using FWH. For $f >$ 6 kHz, the curve corresponding to DNC show an abrupt decrease due to numerical dissipation.

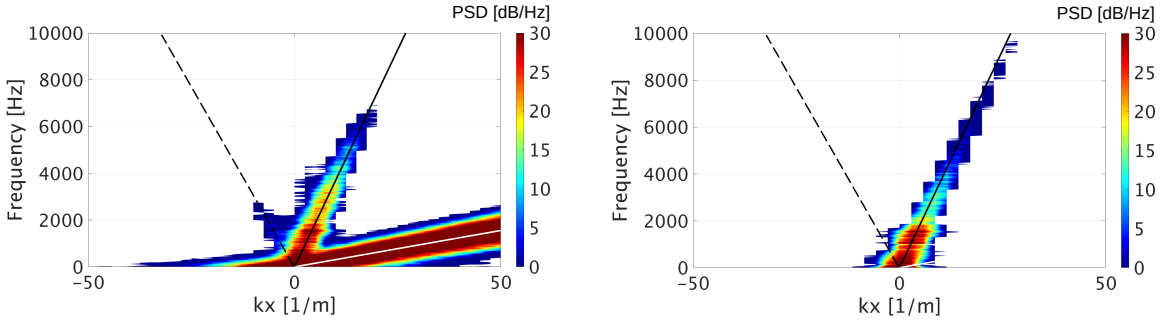

Figure 5.34: Frequency-wavenumber spectrum calculated in the wake of the side-mirror at $k_z = 0$ using (left) DNC and (right) FWH.

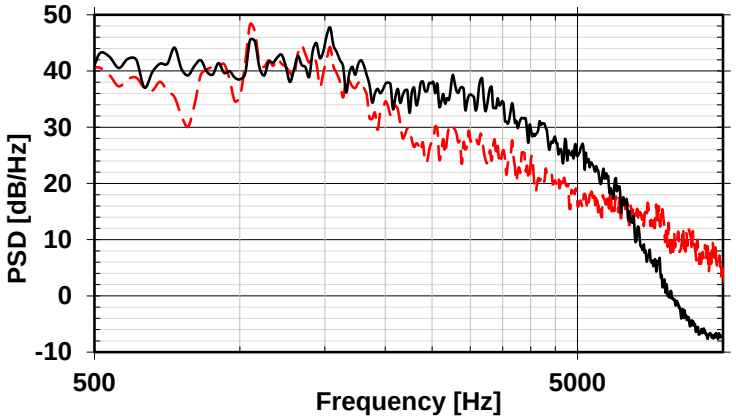

Figure 5.35: Integrated acoustic components for positive k_x. Black solid line corresponds to DNC and red dashed line to FWH.

The differences in the PSD-spectra between DNC and FWH could have different reasons. The first possible difference is the inclusion of volumetric acoustic sources in the DNC, which are not accounted for when using FWH on the surface of the mirror. However, as already shown in the two-struts benchmark, volume source at low Mach number are negligible compared to surface sources. The differences in the spectral levels in Figure 5.35 are up to 10 dB and it is unlikely that volume sources could cause such a high deviation between the two methods. The second possible source of this deviation is spurious noise generated at refinement interfaces in the vicinity of the mirrors surface. These refinement interfaces were shown in Figure 5.28. In order to prove this, refinement interfaces near the surface of the mirror have to be omitted. The deployment of the acoustic damping model near the surface

of the mirror is not possible for two reasons: first, the region, in which the acoustic model would have to be active, is narrow, which limits its effect on acoustic waves. Furthermore, even if the refinement regions could be expanded, the acoustic damping model would damp out both spurious noise as well as physical acoustic waves generated at the surface of the mirror. Therefore, the only possibility to reduce spurious noise generated at the refinement interfaces near the mirror is to avoid these interfaces.

A first attempt to avoid refinement interfaces near the surface of the mirror was to extend the 1 mm refinement region into the wake of the mirror. However, this resulted in over 200 million cells, which was impractical with the available computational resources. Therefore, the second attempt to reduce spurious noise at the 1 mm-2 mm interface was to omit the refinement in one direction at a time. Moreover, a deliberation regarding the relation between spurious noise and the direction of refinement suggests that the refinement in the x-directions, which corresponds to the direction of convection, produces more spurious noise than the other two directions. This has already been observed in the convected isotropic turbulence test case. Therefore, the first test case consists of extending the 1 mm-2 mm refinement interface in the x-direction up to 1.3 m downstream the foot of the side-mirror, producing a refinement interface in the x-direction at $x = 1.3$ m. As a result, the values of the damping coefficient are adapted to the new grid in order to maintain numerical stability.

Figure 5.36 shows the frequency-wavenumber spectrum in the wake of the mirror using both CAA-methods. Due to the grid resolution of 1 mm in the wake of the mirror, the damping coefficient had to be reduced to approximately 0.042 before the 1 mm-2 mm interface. This reduces the effect of the acoustic damping model and results in higher spurious noise levels in the frequency-wavenumber spectrum of the DNC results. On the other hand, the positive acoustic branches of both CAA-methods are almost equivalent. This is also observed in the integrated spectra of positive k_x components in Figure 5.37, in which the spectra show good agreement up to $f \approx 6$ kHz. For higher frequencies, the DNC method shows lower spectral levels due to numerical dissipation.

The good agreement between DNC and FWH using the above mentioned grid shows the importance of the refinement interface in the direction of convection near the surface of the side-mirror. Despite the good agreement between both results, additional test cases with extended 1 mm-2 mm refinement interfaces in the y- and z-directions were performed. The results matched the ones presented in Figures 5.36 and 5.37, which indicates the minor role of these interfaces in the generation of spurious noise. A probable cause for this behaviour are the wavenumber components contained in the shear layer separating at the trailing edge of the mirror. The absence of spurious noise at refinement interfaces normal to the convective direction indicates the low energy content at wavenumbers $k_y > k_{yc}$ and $k_z > k_{zc}$, where k_{yc} and k_{zc} correspond to the cut-off wavenumbers of the 2 mm grid in the y- and z-directions respectively. Consequently, spurious noise generated by the separating shear layer at the 1 mm-2 mm interface near the surface of the mirror is negligible compared to the physical noise generated by the mirror itself. A detailed analysis of the wavenumber components contained in the shear layer could be performed by calculating a wavenumber spectrum in the vicinity of the refinement interfaces. However, due to the narrow region of the 1 mm refinement region, this analysis is not performed in this work.

The good agreement between DNC and FWH also shows the minor role of the 0.5 mm-1 mm refinement interface near the surface of the mirror. Due to the higher cut-off wavenumber of the 0.5 mm refinement region, the energy contained in wavenumber components $k > k_{c,1\text{ mm}}$, where $k_{c,1\text{ mm}}$ corresponds to the cut-off wavenumber of the 1 mm grid, is low. Furthermore, the 0.5 mm refinement region is very close to the mirror, so that the separating shear layer does not have enough space to spread its energy among all wavenumber components.

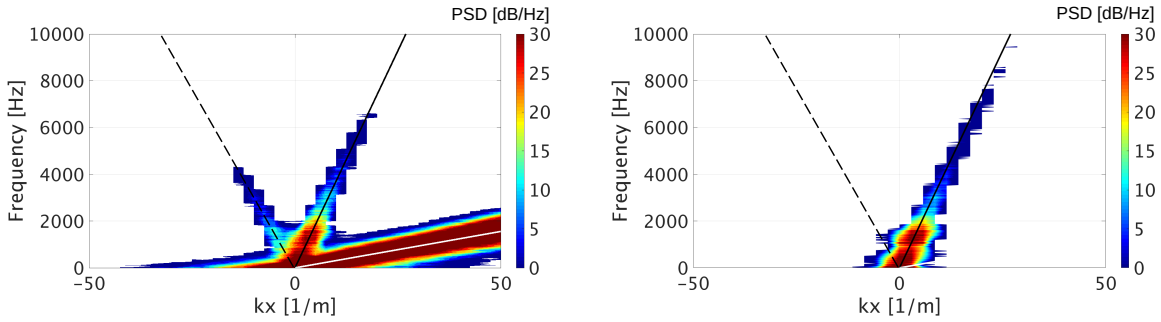

Figure 5.36: Frequency-wavenumber spectrum calculated in the wake of the side-mirror at $k_z = 0$ using (left) DNC and (right) FWH. The results correspond to the grid with an extended 1 mm-2 mm refinement interface in the x-direction.

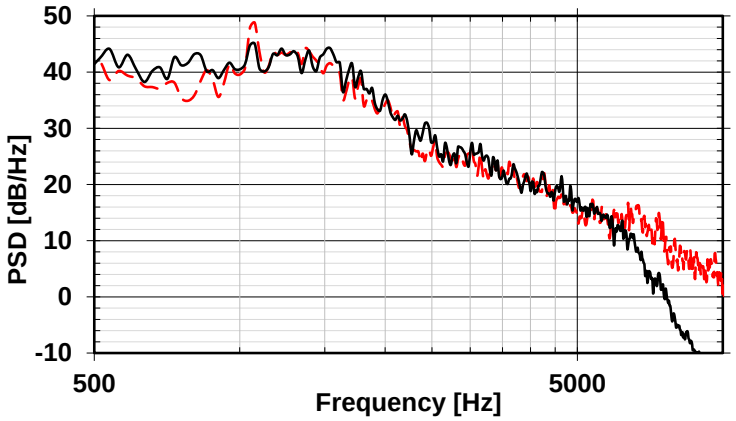

Figure 5.37: Integrated acoustic components for positive k_x. Black solid line corresponds to DNC and red dashed line to FWH. The results correspond to the grid with an extended 1 mm-2 mm refinement interface in the x-direction.

The effect of the 1 mm-2 mm refinement interface in the x-direction was tested on different side-mirrors with different geometries. All test cases have shown good agreement between DNC and FWH, as long as the aforementioned interface near the surface of the mirror is omitted. For this reason, it is assumed that this refinement interface is responsible for most of the spurious noise generated near the surface of the mirror and its omission results in a substantial reduction of spurious noise amplitude.

5.3.5 Grid stretching

One disadvantage of extending the 1 mm refinement interface in the x-direction is the limitation of the damping coefficient [Eq. (5.2)]. Furthermore, the increase in the number of cells is significant, especially when extending the refinement region in the wake of the mirror mounted on a production car. Therefore, an alternative method to bypass this refinement interface had to be developed.

The grid stretching technique did show its potential in reducing spurious noise generation. However, the grids shown in Figure 5.18 were generated manually and creating such grids in the wake of a mirror mounted on a production car would be time-consuming. Therefore, a new algorithm for an automated process for stretched grid generation is developed in cooperation with ESI-OpenCFD. Therein, the user defines the region and direction in which the grid has to be stretched. The final expansion ratio of the cells in the stretched region can be controlled by the size of the user-defined region and the number of iterations that are needed to reach a continuous grid spacing. Figure 5.38 shows a schematic representation of the refinement regions in the wake of the mirror as well as the smoothing region, in which the cells are stretched in the x-direction.

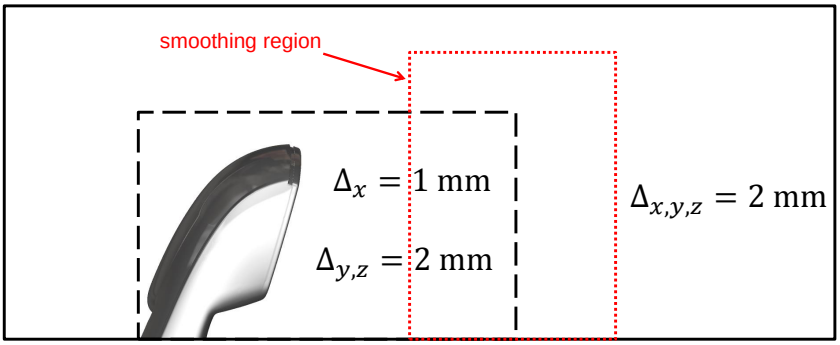

Figure 5.38: Schematic representation of different refinement regions in the wake of the mirror. The dashed black line represents the extended refinement region, in which $\Delta_x = 1$ mm and $\Delta_{y,z} = 2$ mm. The red dotted line represents the smoothing region, in which cells are stretched in the x-direction.

Figure 5.39 shows the grid after stretching at $z = 0$. The expansion ratio of the cells in the transition region is below 0.5% and the total number of cells increased by approximately 6% compared to the reference grid in Figure 5.28.

Due to the continuous transition between the 1 mm and 2 mm refinement regions in the x-direction, the first refinement interface in the direction of convection is the same as in the reference grid at $x = 1.5$ m. Hence, the distribution of the damping coefficient on the stretched grid is equivalent to the distribution in Figure 5.32.

Figure 5.40 shows the integrated acoustic components resulting from DNC and FWH using the grid shown in Figure 5.39. The integrated positive k_x acoustic components show good agreement between DNC and FWH. Furthermore, the results are equivalent to those shown in Figure 5.37 with the extended 1 mm refinement region in the convective direction. This

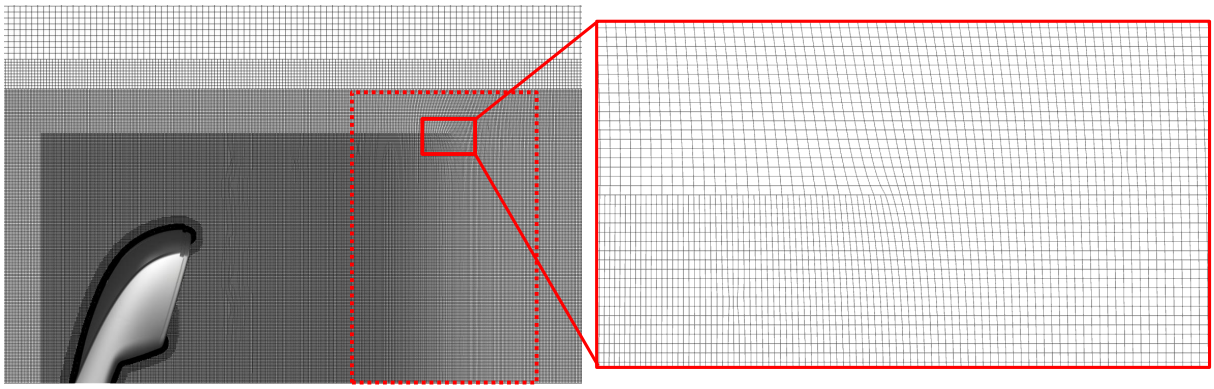

Figure 5.39: A slice through the grid at $z = 0$ after the stretching step. The red dotted line corresponds to the smoothing region.

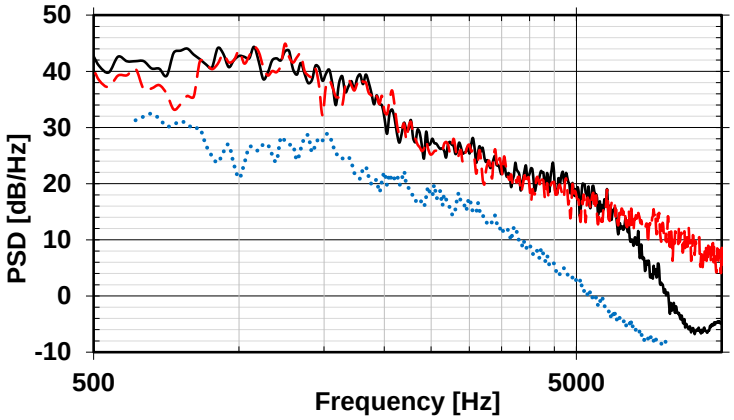

Figure 5.40: Integrated acoustic components. Black solid line corresponds to positive k_x components resulting from DNC, red dashed line to positive k_x components resulting from FWH, and blue dotted line to negative k_x components resulting from DNC The results correspond to the grid shown in Figure 5.39.

indicated the absence of spurious noise generation in the stretched grid region. Furthermore, Figure 5.40 shows the integrated negative k_x acoustic components, which exhibit remarkably lower spectral values than positive ones. This is due to the higher damping effect that could be utilised in the wake of the mirror due to the 2 mm refinement region and the higher critical damping constant. In sum, the test case shows the potential of grid stretching in reducing the number of cells and providing the possibility of increasing the damping effect in the wake of the mirror without producing spurious waves.

Note that the grid stretching algorithm could be also utilised in the wake of the side-mirror and the activation of the acoustic damping model in the wake of the mirror would not be necessary. However, this approach would have disadvantages. First, the time needed for grid generation and stretching would noticeably increase. Moreover, the number of grid cells would also increase in the stretching region. Apart from the increasing computational effort, the stretching algorithm would not work in regions with step-like surfaces (e.g. B-pillar in the wake of a side-mirror). Therefore, the stretching algorithm could only be utilised in the

vicinity of the mirrors surface and spurious waves generated further downstream could only be reduced by activating the acoustic damping model.

5.3.6 Vibroacoustic

The pressure fluctuations on a side-window of a vehicle consist of two parts: turbulent pressure fluctuations, which propagate at the convective speed, and acoustic pressure fluctuations propagating at the speed of sound. Assuming the side-window is a thin plate, these fluctuations cause the vibration of the plate and these vibrations cause the transmission of sound from outside the vehicle into the passengers cabin. In order to calculate the plates vibration, the bending wave equation is calculated:

$$\rho h \frac{\partial^2 \omega}{\partial t^2} + EI\Delta^2(\omega) = p(\mathbf{x},t), \tag{5.3}$$

where ω is the displacement of the plate, h the plates thickness, E its Young's-Modulus, and $p(\mathbf{x},t)$ the pressure distribution resulting from the CFD-simulation. I is the moment of inertia of the cross-section of the plate given by [48]:

$$I = \frac{h^3}{12(1-\nu_p)}, \tag{5.4}$$

where ν_p corresponds to the Poisson's ratio of the plate, which describes the ratio of the relative contraction strain normal to the applied force to the relative extension strain in the direction of the applied force.

Equation (5.3) was implemented by Kabat vel Job [48] in the OpenFOAM framework and his implementation is used in this work to calculate the plates vibration. Since the bending wave equation is solved explicitly in the time-domain, the time-step size is restricted by the acoustic Courant number $Co_{ac} = \Delta_t c/\Delta_x$. For a realistic and practical computational effort, the bending wave equation is solved on a grid with $\Delta_x = 5$ mm, regardless of the shape of the plate.

The computation of the acoustic propagation using the FWH approach is performed on a grid different than the one used for the flow computation. The grid is chosen to have a grid spacing of 5 mm, so that the calculated pressure values can be directly mapped on the vibroacoustic grid. The situation is different when calculating pressure fluctuations (i.e., including both acoustic and hydrodynamic pressure fluctuations) using the DNC approach, which are calculated directly on the numerical grid used for flow simulation. This grid has typically a higher spacial resolution than the vibroacoustic grid in order to resolve high wavenumber turbulent fluctuations. Consequently, a direct mapping between the CFD-grid and the vibroacoustic grid could cause aliasing effects due to the hydrodynamic pressure fluctuations that are resolved on the CFD-grid but cannot be resolved on the vibroacoustic grid.

In order to circumvent errors emerging from aliasing effects, the pressure field resulting from the DNC is filtered for all time steps. The spacial filter should filter out all wavenumber components that cannot be resolved on the 5 mm grid. For this, an area weighted filter is utilised, which corresponds to a triangular filter (also known as Bartlett filter). More information about the filter equation can be found in [48].

In order to validate the filtering and mapping process, the vibrations of a virtual plate in the wake of the side-mirror are calculated. The plate extends between $(0.3;\ 0;\ -0.2)$ m and $(0.6;\ 0;\ 0.1)$ m and is shown in Figure 5.41. At the boundaries of this plate, clamped boundary conditions are enforced. For more details regarding this boundary condition, the reader is referred to [48]. The calculation of the plate vibration in the wake of the side-mirror is just a numerical experiment and its purpose is to ensure the equivalence of vibration values resulting from pressure fluctuations of DNC and FWH. Hence, boundary conditions are irrelevant for the purpose of this test as long as the calculation of vibrations resulting from both CAA methods exhibits the same material properties and boundary conditions.

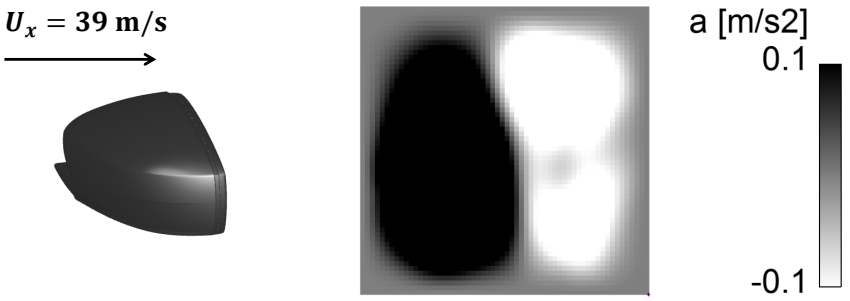

Figure 5.41: Geometry of the side-mirror as well as the plate for which the vibrations are calculated. The plate is colored by the normal acceleration values a at $t = 0.4$ s calculated using DNC.

Before discussing the vibroacoustic results, it is worth analysing the effect of the filter on hydrodynamic as well as acoustic waves. Ideally, acoustic waves should not be filtered out due to their importance to the vibration of the plate. On the other hand, filtering high wavenumber turbulent fluctuations plays a minor role in the vibration of the plate due to their short wavelength. As already shown in [48], hydrodynamic pressure fluctuations cause the vibration of a side-window in the low frequency region (i.e., $f < 1$ kHz) and acoustic fluctuations cause the vibration for frequencies above 1 kHz. Furthermore, the excitation of the plates vibration in the low-frequency region is mainly caused by low wavenumber turbulent fluctuations of high amplitude. Therefore, filtering out high wavenumber turbulent fluctuations is assumed to be of minor importance for the plates vibration.

In order to analyse the effect of the filter, the frequency-wavenumber spectrum is calculated using the CFD-data before and after filtering. Hereby, the spectrum is calculated using pressure values on the plate shown in Figure 5.41. In Figure 5.42, the frequency-wavenumber spectrum is shown at $k_z = 0$ before and after filtering. Before filtering, the convective branch extends beyond the cut-off wavenumber of the 5 mm grid, which is equal to 100 m^{-1}. After filtering, all wavenumber components beyond $k_x = 100\ \mathrm{m}^{-1}$ are filtered out and the convective branch representing hydrodynamic fluctuations is substantially smaller. It is

worth noting that both spectra are calculated before the mapping process, meaning on the original CFD-grid. In order to assure the absence of aliasing, the frequency-wavenumber spectrum is calculated on the same plane after mapping the pressure values on the 5 mm grid. This frequency-wavenumber spectra calculated on the 5 mm grid are shown in Figure 5.43 with and without filtering. Mapping the results on the coarser grid without filtering high wavenumber components results in aliasing effects that can be observed at negative wavenumbers in Figure 5.43. Filtering the results before the mapping process results in the same frequency-wavenumber spectrum as on the 2 mm grid without any appreciable aliasing.

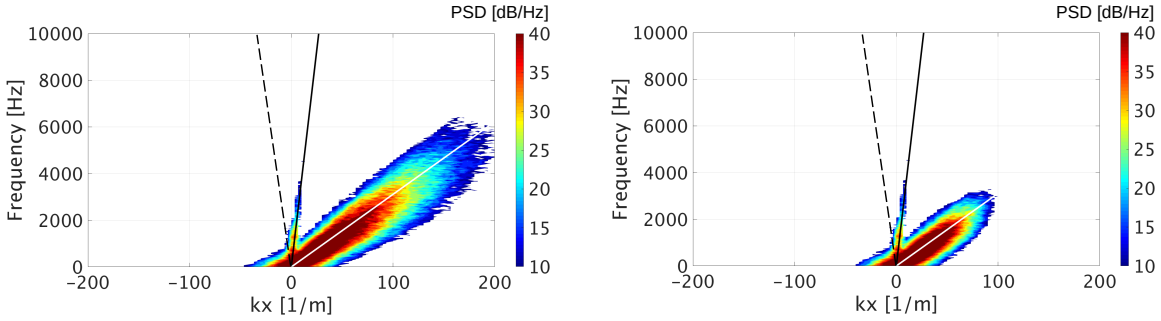

Figure 5.42: Frequency-wavenumber spectrum calculated in the wake of the side-mirror at $k_z = 0$ for the 2 mm grid (left) before and (right) after filtering.

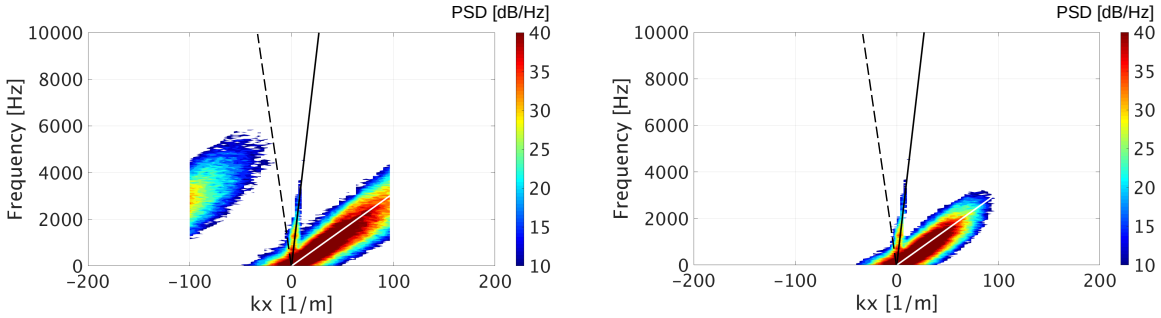

Figure 5.43: Frequency-wavenumber spectrum calculated in the wake of the side-mirror at $k_z = 0$ after mapping the results on the 5 mm vibroacoustic grid (left) without and (right) with filtering.

Besides analysing the effect of mapping and filtering on the convective branch in the frequency-wavenumber spectrum, an analysis of the acoustic branch is also performed in order to assure that acoustic waves are unaffected by filtering and mapping. For this, the average acoustic spectra are calculated using the integration process described in the previous section (cf. Figures 5.35 and 5.37). Figure 5.44 shows a comparison between the acoustic spectra on the original CFD-grid and on the vibroacoustic grid after filtering and mapping. Both spectra are equivalent for all frequencies, apart from slight differences for frequencies above 5 kHz. However, these differences are below 1 dB and the frequency range is out of interest for the current study due to numerical dissipation.

After filtering and mapping the pressure fluctuations calculated by the compressible solver, the bending wave equation is solved on the vibroacoustic grid. Furthermore, the plates vi-

bration is also calculated using the acoustic waves calculated by FWH. For a comparison between both results, the values of the plates acceleration are compared at different locations on the plate. For this, the acceleration values are Fourier transformed and PSD-spectra are calculated in the frequency domain relative to a reference acceleration $a_{\text{ref}} = 5 \cdot 10^{-8} \text{m/s}^2$. A comparison between the results of both methods is shown in Figure 5.45 at two different locations on the plate. In the frequency domain 0.3 kHz $< f <$ 6 kHz, both CAA-methods deliver equivalent values of acceleration at both locations on the plate. This agrees with the equivalence of the integrated acoustic spectra performed in the previous section in the wake of the mirror. For higher frequencies, the FWH method shows higher spectral levels, which is attributed to numerical dissipation in the DNC approach. The effect of the excitation of the plate through hydrodynamic pressure fluctuations can be observed at $f <$ 0.3 kHz. As shown in Figure 5.42, the filtered pressure field still contain a hydrodynamic branch that can be resolved on the vibroacoustic grid. This branch is absent in the pressure values calculated using FWH. Therefore, the excitation of the plate through hydrodynamic pressure fluctuations at low frequencies is responsible for the higher spectral levels of DNC in Figure 5.45.

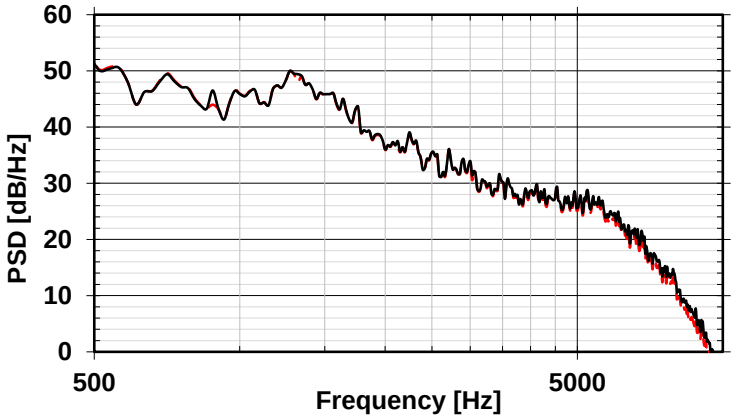

Figure 5.44: Integrated acoustic components for positive k_x. Black solid line corresponds to the original DNC results on the CFD-grid and red dashed line to the filtered and consequently mapped results on the vibroacoustic grid.

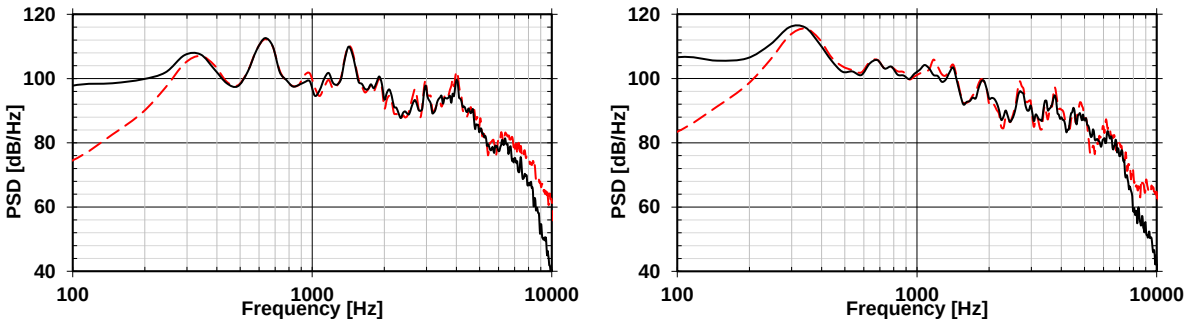

Figure 5.45: PSD-spectra of the plates acceleration at (left) $(0.45;\ 0;\ -0.05)$ m and (right) $(0.35;\ 0;\ -0.15)$ m. The black solid lines correspond to DNC and red dashed line to FWH results.

5.3.7 Grid study

The results shown so far are based on a resolution equal to 0.5 mm on the surface of the mirror and 1 or 2 mm in its wake. This is sufficient to do numerical experiments and compare different CAA-methods, since the input data of the hybrid method are equivalent to those calculated using the compressible solver. Since no experimental data is available for the side-mirror test case, it is not possible to determine the sufficiency of the aforementioned resolutions. However, the next section exhibits a comparison between numerical and experimental results. Therefore, a grid study is needed before calculating a whole vehicle model.

As already mentioned, the spacial resolution utilised in the side-mirror case can be divided into two parts: the surface resolution of the mirror and the volume resolution in its wake. Due to the low Mach number of the flow, the surface of the mirror is the main noise source. Hence, pressure fluctuations on the surface of the mirror have to be sufficiently resolved and the surface resolution of the mirror is the critical factor for a correct calculation of acoustic waves generation. On the other hand, volume sources play a minor role regarding noise generation. The main effect of the resolution in the wake of the mirror is numerical dissipation of acoustic waves. However, the previous sections have shown good agreement between DNC and FWH for frequencies up to approximately 6 kHz. Since the FWH approach is non-dissipative, this means that the volume resolution in the wake of the mirror is enough to transport acoustic waves up to 6 kHz without considerable dissipation. Therefore, the following study focuses on refining the surface resolution of the mirror while keeping the volume resolution in the wake equivalent to the previously discussed test cases.

Two additional cases are calculated in order to study the effect of surface resolution: the first case exhibits a resolution of 0.25 mm and the second a resolution of 0.125 mm on the surface of the mirror. The time-step size for the first case is equivalent to the one chosen so far $\left(\Delta t = 10^{-5}\text{s}\right)$. For the second case, the time-step size is decreased to $\Delta t = 5 \cdot 10^{-6}$ s in order to maintain numerical stability of the solution. The distribution of the damping coefficient is equivalent to the one shown in Figure 5.33 for both cases.

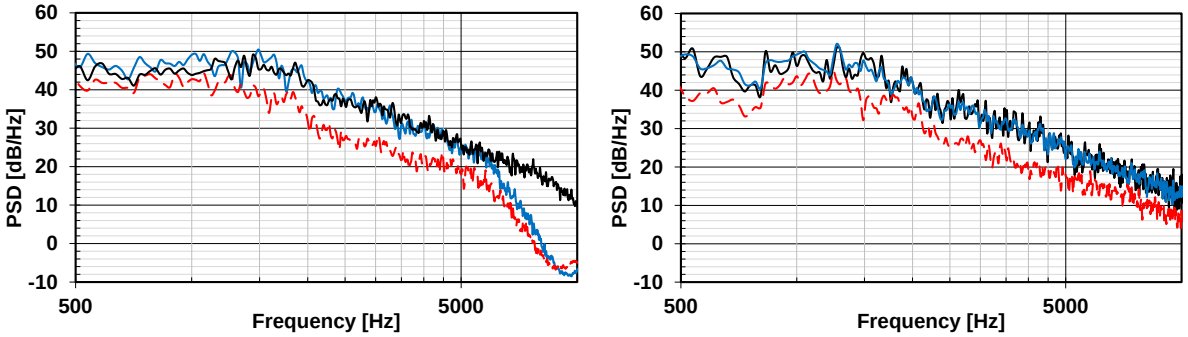

Figure 5.46: Integrated acoustic components for positive k_x in the wake of the mirror calculated using (left) DNC and (right) FWH. Black solid lines correspond to a resolution of 0.125 mm, blue solid lines to 0.25 mm and red dashed lines to 0.5 mm on the surface of the mirror.

Figure 5.46 shows the acoustic spectra in the wake of the mirror for three different surface resolutions calculated using DNC and FWH. A remarkable difference can be observed between the 0.5 mm and 0.25 mm resolutions for a wide frequency range. This could be due to different flow prediction on the surface of the mirror (e.g. different separation points, etc.). Figure 5.47 shows the mean velocity distribution at the lower side of the mirror for both resolutions. A major difference between both cases is the flow separation at the leading edge at the bottom of the mirror. Discretising the surface of the mirror with 0.5 mm cells causes the flow to remain attached to the surface, while a finer resolution (0.25 mm) shows a flow separation at the bottom of the mirror. This flow separation could be the reason for higher surface pressure fluctuations and as a result higher acoustic spectral levels in the wake of the mirror. Between the 0.25 and 0.125 mm surface resolution cases, the hybrid method does not show any differences in the acoustic spectra. This indicates a converged acoustic solution regarding the surface resolution of the mirror. The spectra calculated using DNC show good agreement upto $f \approx 6$ kHz. For higher frequency, the case with 0.125 mm surface resolution shows a spectrum equivalent to the one calculated using FWH. This indicates lower dissipation of acoustic waves, which is related to the smaller time-step used in the 0.125 mm case. This additionally approves the solution convergence regarding the surface resolution of the mirror.

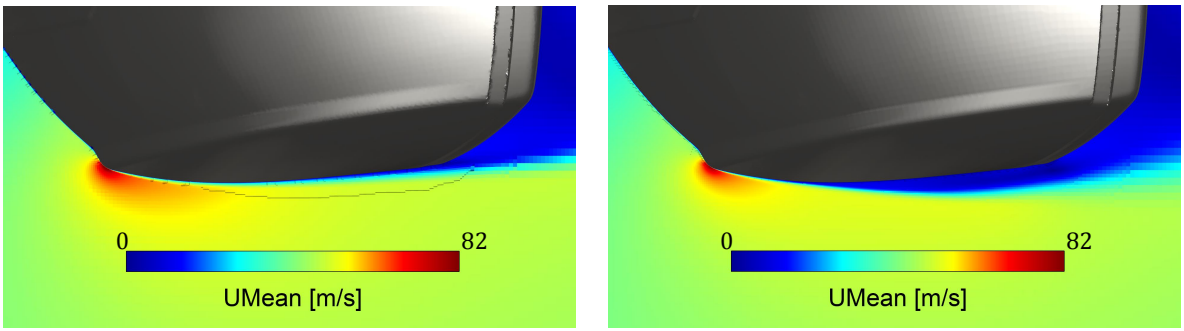

Figure 5.47: Mean velocity field at the bottom of the mirror calculated with a surface resolution of (left) 0.5 mm and (right) 0.25 mm.

6 Noise computation of a generic vehicle model [1]

In chapter 5, the challenges in direct noise simulation regarding spurious noise generation and their effect on the overall acoustic spectra has been shown. The simulation of a single side-mirror on a flat plate showed the potential generation of high amplitude spurious noise due to the interaction between the turbulent wake with refinement interfaces, as well as the generation of spurious noise at refinement interfaces in the vicinity of the mirrors surface. Two different solution strategies were proposed in order to reduce spurious noise generation and its propagation: acoustic damping and grid stretching. Is has been shown that each strategy is applicable in certain regions of the domain. For instance, it was not possible to apply acoustic damping on refinement interfaces near the surface of the mirror. Hence, grid stretching was the only solution to reduce spurious noise generated at such interfaces. On the other hand, in order to reduce the computational effort, acoustic damping was applied in the wake of the mirror without adversely affecting the flow topology. Moreover, acoustic damping allowed the presence of refinement interfaces in the wake and avoided extensive grid stretching strategies.

The above mentioned strategies did show good results for noise computation of a single side-mirror. However, the evaluation of the acoustic quality of a side-mirror requires the simulation of the complete vehicle model in order to ensure the correct calculation of the incident flow upstream of the mirrors surface. Consequently, the complexity of the geometry increases rapidly and the corresponding numerical grid exhibits multiple regions, in which spurious noise could be generated and contaminate the final acoustic solution. Therefore, a validation of the introduced methods on a vehicle model that possesses the major features of a production car is necessary in order to assure its industrial applicability.

In this chapter, the aforementioned CAA-methods are validated based on the flow past a generic vehicle model. This model is a modified variant of the SAE (Society of Automotive Engineers) reference notchback model [118]. The main modifications of the original model is filling up the rear notch to create a full-back, similar to an estate vehicle. Furthermore, a side-mirror is installed and a glass window is mounted within the side panel of the body. Moreover, a realistic A-pillar geometry is mounted on the front slant in order to simulate a realistic A-pillar vortex, similar to a production car. The geometry of the modified SAE-body is shown in Figure 6.1.

This chapter is structured as follows: first, the experimental setup is briefly described and different measured quantities are discussed. Afterwards, the numerical model is presented including the numerical grid, the utilised schemes, and boundary conditions. In section 6.3, numerical results are presented and compared to experimental data. Similar to the two-struts benchmark, the results are divided into two parts: aerodynamic and aeroacoustic results. In

1 This chapter is an extended version of the results presented in A.H. Dawi, R.A.D. Akkermans, *Direct noise computation of a generic vehicle model using a finite volume method*, Computers and Fluids, Volume 191, Article 104243, 2019.

section 6.4, the results of the CFD-simulation are used to compute the vibration of the side-window. Hereby, the results of the direct and hybrid CAA-methods are compared to wind-tunnel measurements.

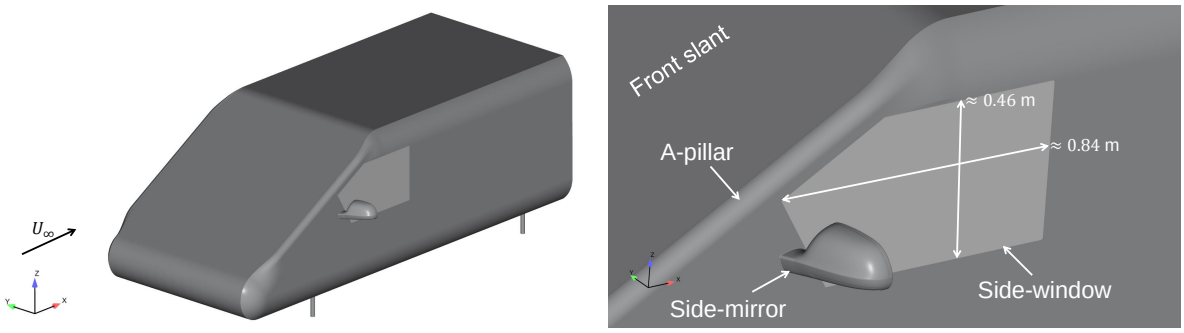

Figure 6.1: Geometry of the full-back SAE reference body.

6.1 Experimental setup

The SAE-body was the main test object within the scope of the working group of German automobile manufacturers for aeroacoustic simulation [36]. Several measurements were performed on the test body with different parameters including different A-pillar variants, side-mirror geometries, and inflow velocities, in order to understand the mechanism of noise generation and its propagation into the passenger cabin. The measurements were mainly performed at the aeroacoustic wind tunnel of Audi AG. Figure 6.2 shows the SAE-body in this wind tunnel.

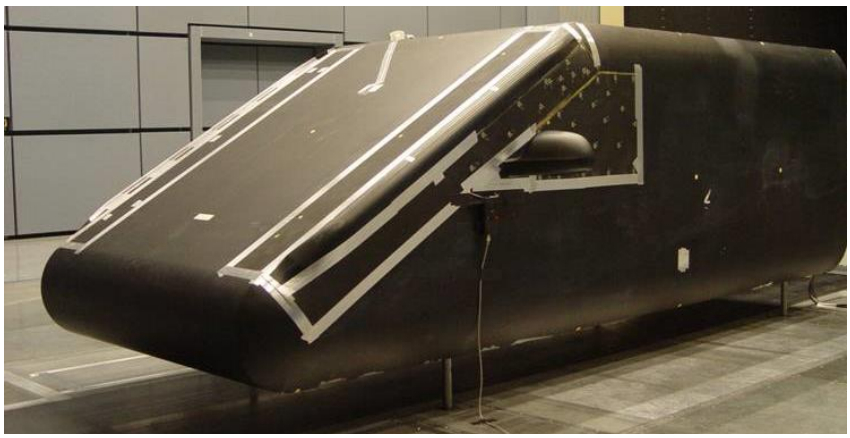

Figure 6.2: Fullback SAE-body in the aeroacoustic wind tunnel of Audi AG with a side-mirror mounted on the side-panel. The picture shows the model before installing a glass window.

For the study of the aerodynamic behaviour in the region of the glass window, 96 surface microphones were installed in order to measure pressure fluctuation in the region of the win-

dow. Three different distributions of the microphone positions were installed. Figure 6.3 (left) shows an example of such a distribution of the microphones, while Figure 6.3 (right) shows the distribution used for the comparison between simulation and experiment in this work. Due to the turbulent wake of the mirror and the A-pillar vortex, the surface microphones measure mainly the hydrodynamic pressure fluctuations on the side-window due to its dominance over the acoustic ones. However, a distribution of the sensors is also chosen in such a manner that a wavenumber-frequency spectrum of experimental data could be calculated. This was then used to separate the acoustic from the hydrodynamic components.

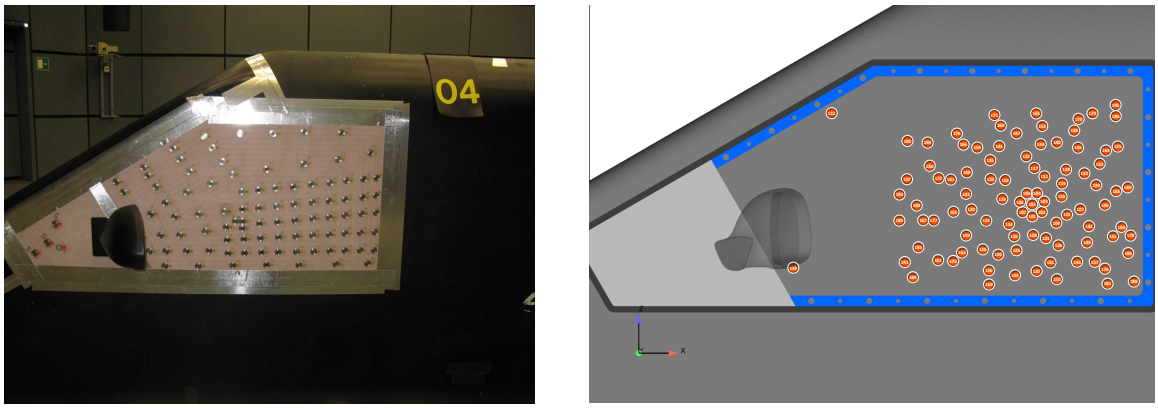

Figure 6.3: (Left) surface pressure microphones mounted on the side of the SAE-body in the wind tunnel and (right) the distribution of the microphones used in this study.

For the validation of the side-window vibration, acceleration sensors were installed on the side-window at different positions as shown in Figure 6.4. Different side-windows were measured in the wind tunnel. In this work, results for a tempered glass type window are studied and compared to experimental results. The material properties of the glass are listed in Table 6.1. Further measurements of acoustic waves were performed using microphones inside the cabin. However, these data are not calculated in the course of this work and, thus, won't be illustrated at this stage. For more details regarding different measurements done on the SAE-body, the reader is referred to [36].

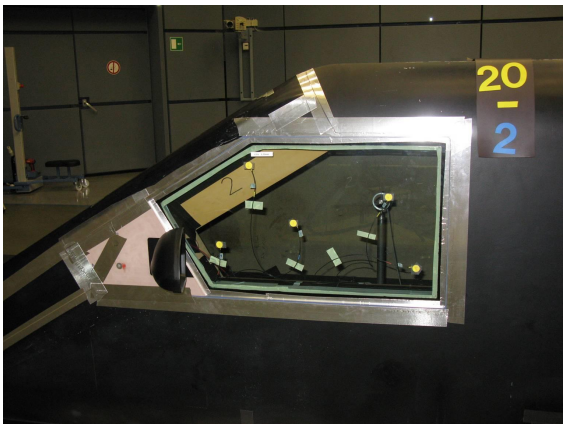

Figure 6.4: Acceleration sensors (yellow circles) on the side-window.

Table 6.1: Material properties of the side-window (taken from [48]).

Material	Young's Modulus [Pa]	Poisson's ratio [-]	Density [kg/m^3]	Thickness [mm]
Tempered glass	$7 \cdot 10^{10}$	0.3298	2700	3.15

For each measurement, the length of the signal was 30 s. In this work, the focus is on two basic variants: SAE-body with and without side-mirror. For both variants, the angle of attack of the free-stream flow is equal to 0 degrees and the free-stream velocity is $U_\infty =$ 140 km/h $\approx$ 38.89 m/s.

6.2 Numerical setup

The computational setup consists of a virtual wind tunnel in which the SAE-body is placed at its center. The body intersects the floor of the tunnel at its circular struts and the distance between the floor and the lower panel of the body is equal to 0.2 m. The computational domain is chosen to have the dimensions of 100 m in the x- and y-directions, and 50 m in the z-direction, and extends symmetrically in the x- and y-directions with respected to the origin. Since the mirror is mounted only on one side of the body, the vehicle model is asymmetric in the y-direction. Hence, the whole model is simulated. The origin of the system of coordinates coincides with the lower panel of the body and is placed at the level of the front struts in the x-direction. The direction of the flow coincides with the positive x-direction and the free-stream velocity is set to 38.89 m/s for all simulations. At the inlet, a constant velocity boundary condition is applied, while a no-slip boundary condition is prescribed to the lower patch (floor) of the computational domain. At all remaining boundaries, a non-reflective pressure boundary condition is applied.

The numerical grid exhibits multiple refinement boxes in the region of the SAE-body. The spacial resolution on the surface of the SAE-body is 4 mm. The surface of the side-window as well as the surface of the A-pillar have a resolution of 1 mm. Figure 6.5 (left) shows a slice of the grid at $y = 0$ m and at the floor of the wind tunnel in the case without side-mirror. One can observe the refinement region in the wake of the SAE-body, which has a resolution of 8 mm. Furthermore, Figure 6.5 (right) shows a slice of the grid at $z = 0.7$ m, where the refinement zone near the A-pillar is shown. Regarding the case with side-mirror, the surface of the mirror has a resolution equal to 0.25 mm. The grid study performed in the last chapter have shown the sufficiency of this resolution to resolve acoustic waves upto 6 kHz. The wake of the side mirror is resolved using 2 mm cells and the refinement box is extended 1.3 m downstream the surface of the mirror. In order to avoid spurious noise generation at grid interfaces in the vicinity of the mirrors surface, the stretching strategy is applied in the wake of the mirror in order to create a smooth transition between the 1 mm and 2 mm resolution regions in the convective direction. Figure 6.6 shows the numerical grid in the region of the side-mirror and in its wake.

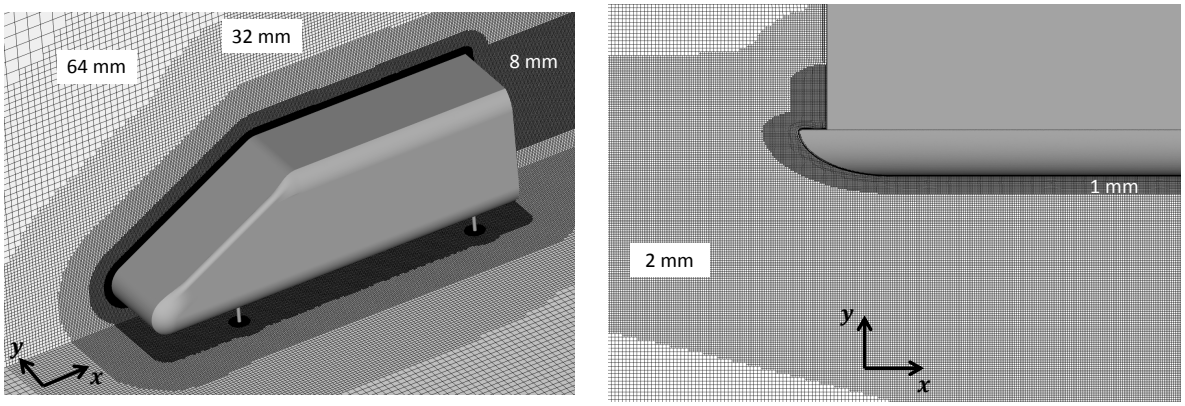

Figure 6.5: The numerical grid used for the calculation of the flow past the SAE-body: (left) slice at $y = 0$ m and at the floor of the wind tunnel, and (right) the grid at $z = 0.7$ m.

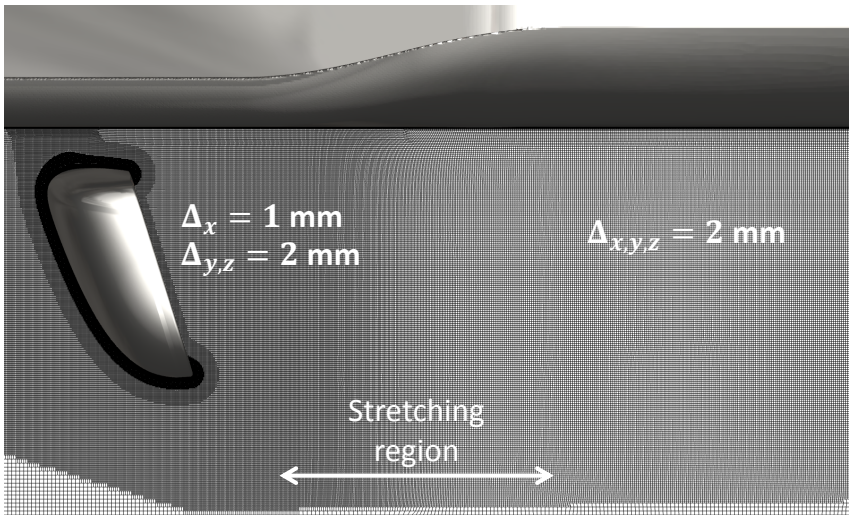

Figure 6.6: Numerical grid at $z = 0.7$ m in the region of the side-mirror.

In order to reduce spurious noise generated at refinement interfaces downstream the side-window, the acoustic damping model is utilised to damp out numerical noise before it reaches the surface of the window. Similar to the side-mirror test case in chapter 5, the damping constant is linearly increased in the wake of the mirror. Furthermore, in order to reduce acoustic waves reflections caused by refinement interfaces in front and on the sides of the SAE-body, the damping zone is extended to all regions, in which no acoustic sources are present. Experimental results have shown that the side-mirror and the top edge of the A-pillar are the main noise sources on the SAE-body [91]. Hence, the damping zone is activated in the whole computational domain except for the main noise sources and their transfer paths. Furthermore, the damping model is deactivated in the region below the side-mirror and the SAE-body, so that acoustic reflections at the floor of the wind tunnel are not damped. Besides, the noise generated at the struts below the SAE-body is also included in the simulation. The values of the damping constant is set to its critical value $q_c = \Delta_{x,y,z}^2 / 2c^2\Delta_t^2$. Figure 6.7 shows the distribution of the damping coefficient at $z = 0.7$ m and $x = 0.7$ m. The values of the damping coefficient are based on a time step size $\Delta t = 10^{-5}$ s.

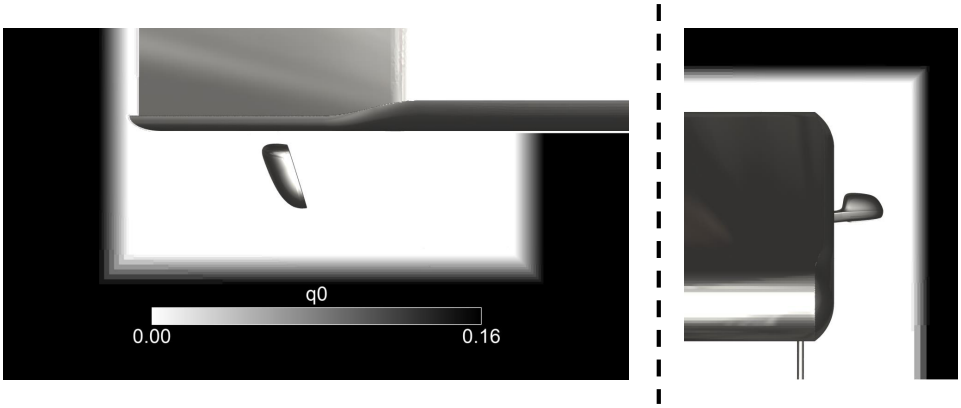

Figure 6.7: Distribution of the damping coefficient at (left) $z = 0.7$ m and (right) $x = 0.7$ m.

All simulations are done using the k-ω-SST IDDES approach. The time step size is set to 10^{-5} s and the simulated physical time is equal to 1.2 s. For the case with side-mirror, the time step size is decreased to $5 \cdot 10^{-6}$ s in order to reduce numerical dissipation of acoustic waves. The first second of the simulated time is used to reach a statistically stationary flow state. This was verified using the drag coefficient of the SAE-body. At $t = 1$ s, data sampling starts and surface pressure values are written for the side-mirror and the side-window every time step (every second time step for the case with side mirror). This results in a sampling frequency $F_s = 100$ kHz. These values are further used to evaluate surface pressure spectra as well as the vibration of the window.

In order to reduce numerical dissipation and maintain numerical stability, a blended scheme is utilised for the discretisation of the convective term in the momentum equation. Different numerical experiments with different numerical schemes were performed. The different schemes were assessed according to the range of resolved surface pressure fluctuations. The surface pressure spectra were compared to experimental results, and it was realised that schemes based on central differencing play an important role in resolving high frequency ($f > 4$ kHz) pressure fluctuations. However, as discussed in the previous chapters, CD-based schemes are numerically unstable for the given flow conditions. Hence, a blending technique that maintains numerical stability and provides high accuracy is needed.

Numerical stability is mainly critical in geometrical bad cells. Such cells are only present near solid boundaries due to the snapping process of the grid generator. The rest of the cells in the domain are Cartesian and are insensitive towards central differencing. Therefore, a blending technique consisting of a mixture of the CDSdC and LU schemes in cells near solid boundaries and a pure CDSdC scheme in the rest of the domain is utilised. In order to avoid sudden jumps between different numerical schemes, a blending coefficient is defined in order to control the level of blending near walls. Figure 6.8 shows the distribution of the blending factor near the lower trailing edge of the side-mirror. In the cells adjacent to the wall, the blending factor is equal to 0. This corresponds to a discretization scheme consisting of 90% CDSdC and 10% LU. The blending factor increases linearly to the value of one along a distance equal to 7 mm from solid walls. At this value, the discretisation scheme

corresponds to 99% CDSdC and 1% LU. In the transition region ($0 <$ blending factor < 1), the schemes at both extrema of the blending factor are linearly blended.

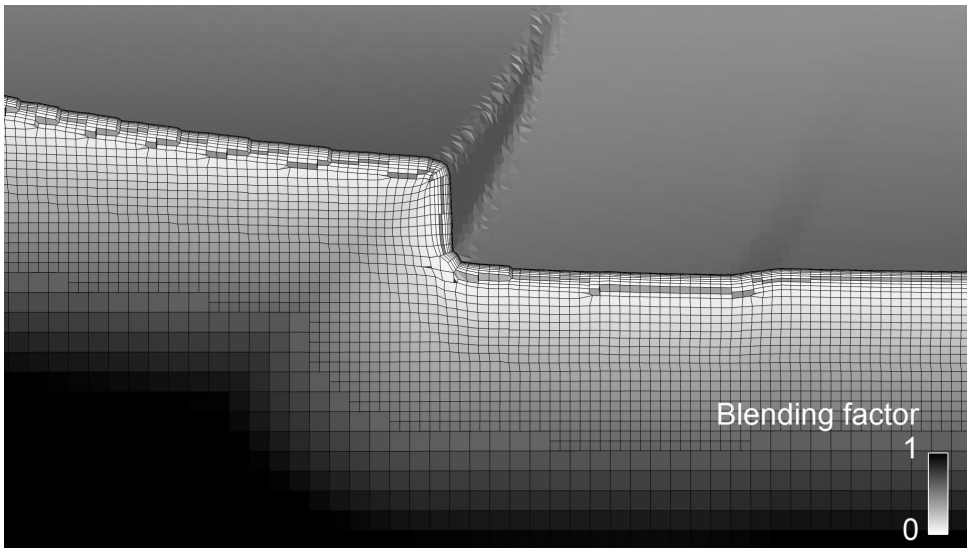

Figure 6.8: Distribution of the blending factor in a vertical slice at $y = -1.037$ m near the lower trailing edge of the side-mirror.

6.3 Aerodynamic results

In order to ensure the correct calculation of the flow past the SAE-body, surface streamlines on the surface of the A-pillar and side-window as well as surface pressure spectra on the side-window are compared to wind tunnel measurements. In the following, the results of the two variants, with and without side-mirror, are compared with experimental results.

6.3.1 Surface streamlines

Prior to the measurements performed at the aeroacoustic wind tunnel of Audi AG, some aerodynamic measurements were performed at the wind tunnel of BMW AG. These measurements include flow visualisation at the surface of the A-pillar, the side-window, and the side-mirror. The visualisation of the streamlines was performed using flow visualisation paint applied on the surface of the body. The visualisation was performed for different variants, with and without side-mirror.

The main challenge in simulating the flow past the SAE-body is the correct prediction of flow separation at the A-pillar. Different numerical experiments have shown the necessity of high spatial resolution at the surface of the A-pillar as well as low-dissipative numerical schemes in order to capture the correct flow behaviour over the A-pillar. Figure 6.9 shows the simulated streamlines compared to the flow visualisation in the wind tunnel for the case without side-mirror. In the wind tunnel, one could differentiate two major lines: a line that

runs along the A-pillar and another one that makes an angle of approximately 10 degrees with the A-pillar. In the simulation, the first line can be clearly observed. The second line that was observed in the wind tunnel cannot be clearly observed in the simulation. The patches of the SAE-body in the simulation are separated exactly at the position of the second line. Hence, the post-processing tool trims the streamlines at the patches boundaries. On the other hand, the second line in the wind tunnel constitutes of the separated flow that runs over the A-pillar and the boundary layer that flows in the positive z-direction upwards the side-panel. Due to the separated flow over the A-pillar, the streamlines in the simulation could not be clearly mapped on the surface of the body. Finally, the simulation shows a clear line that makes an angle of approximately 20 degrees with the A-pillar. This line separates the boundary layer that flows in the convective direction along the side-panel of the body from the one that flows upward in the positive z-direction. This line can also be observed in the wind-tunnel visualisation under the same angle as in the simulation.

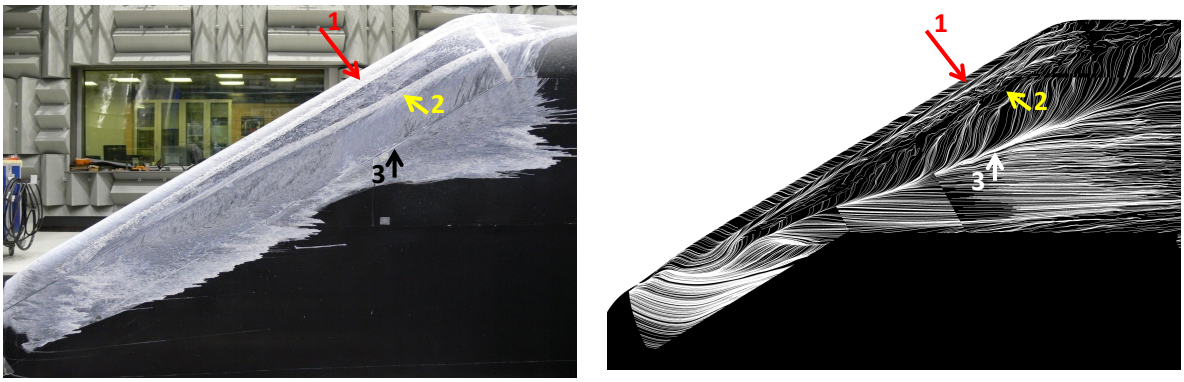

Figure 6.9: Surface streamlines in (left) the wind tunnel and (right) simulation for the case without side-mirror.

For the case with side-mirror, the flow was also visualised on the surface of the mirror in the wind tunnel using oil paint. Figure 6.10 shows a comparison between experimental and numerical results at the front surface of the mirror. The simulated location of the stagnation point shows good agreement with experimental results. The same applies for the location of the stagnation line that runs along the front surface of the mirrors foot.

A similar comparison is done in Figure 6.11, in which the simulated location of the separation line at the bottom of the side-mirror shows good agreement with experimental results.

6.3.2 Surface pressure spectra

For a more quantitative validation of the numerical results, surface pressure spectra on the surface of the side-window are compared to wind-tunnel measurements for the cases with and without side-mirror. Figure 6.12 shows the calculated surface pressure spectra on the surface of the side-window compared to wind-tunnel measurements at four different positions. Two positions are chosen to lay in the region of the A-pillar vortex (left column),

Figure 6.10: Surface streamlines at the front cap of the side-mirror in (left) the wind tunnel and (right) simulation.

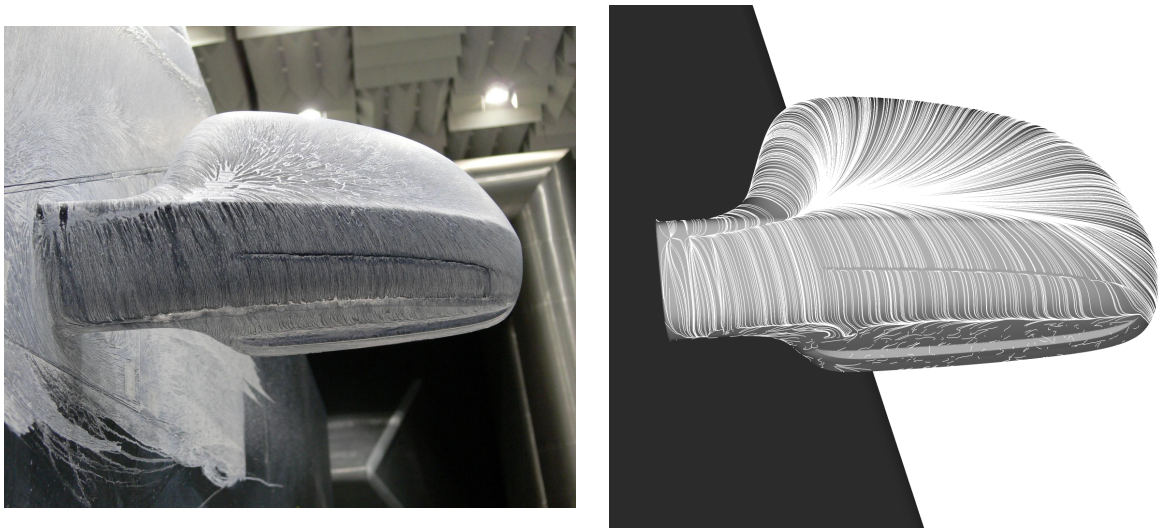

Figure 6.11: Surface streamlines at the bottom of the side-mirror in (left) the wind tunnel and (right) simulation.

while the other two are in the region below the A-pillar vortex. Generally, numerical results show good agreements with experimental data for the whole frequency domain upto $f = 8$ kHz. For higher frequencies, a higher spatial or temporal resolution might be required. The microphones positioned in the region of the A-pillar vortex indicate the accurate prediction of the A-pillar vortex position on one hand, and the correct calculation of the amplitude of pressure fluctuations on the other hand. The other two microphones indicate the accurate calculation of the turbulent boundary layer on the side panel of the SAE-body. The effect of the A-pillar vortex can be observed in the low-frequency domain: both microphones positioned in the A-pillar vortex region show high spectral amplitudes for $f < 2$ kHz, while the other two show a constant spectral amplitude of approximately 70 dB upto a frequency of approximately 2 kHz. The nature of the pressure fluctuations for the microphones positioned outside the A-pillar vortex can be determined by observing the flow on the side-window below the A-pillar vortex. Figure 6.13 shows the isosurface of the vorticity field at

5000 s^{-}1. Therein, the turbulent structures separating from the A-pillar and forming the A-pillar vortex can be observed. Below the A-pillar vortex, coherent turbulent structures can be observed. These structures are stretched in the flow direction and enter the side-window region. Hence, the spectra presented in Figure 6.12 represent hydrodynamic (turbulent) pressure fluctuations rather than acoustic ones. Nevertheless, in the high-frequency region $(f > 6)$ kHz, a turning point in the spectra can be observed. This could be an indication of the domination of acoustic waves over turbulent pressure fluctuations. A more detailed separation can be performed using the frequency-wavenumber spectrum on the surface of the side-window, which is shown in the next section.

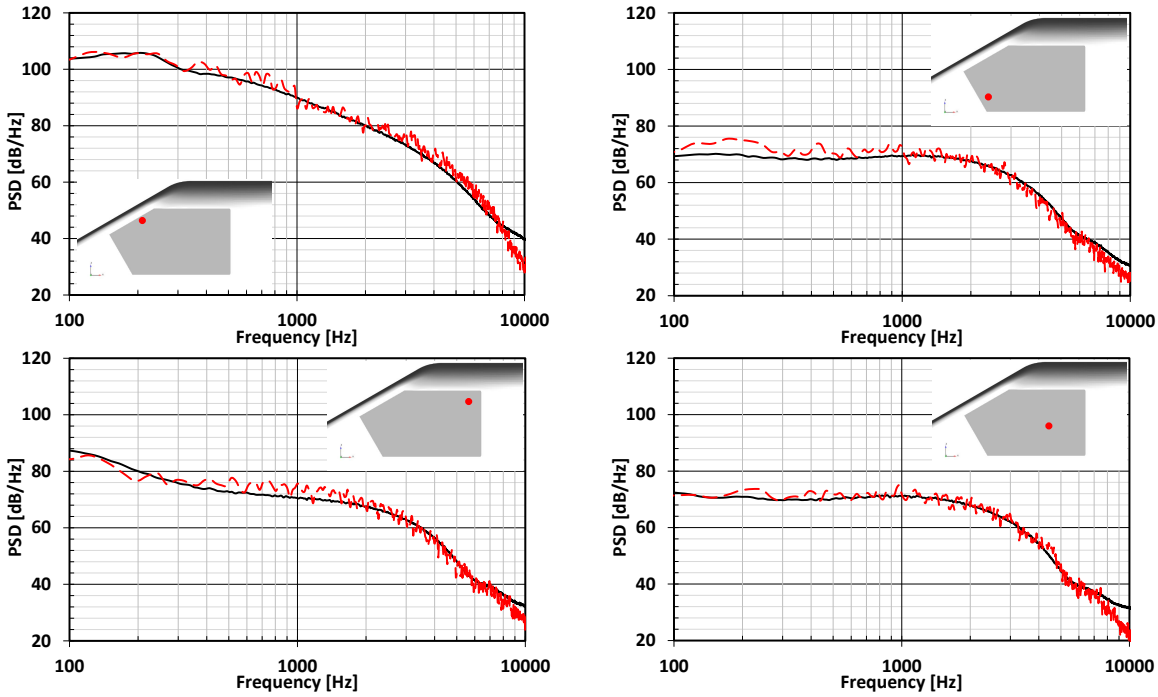

Figure 6.12: Surface pressure spectra at different positions (red dots in the insets) on the side-window in the case without side-mirror. Black solid lines corresponds to wind-tunnel measurements and red dashed lines to numerical results.

The analysis of surface spectra is also performed for the case with side-mirror. Figure 6.14 shows the calculated spectra at the same locations as in Figure 6.12 compared to wind-tunnel measurements. Similar to the case without side-mirror, the calculated surface pressure spectra show good agreement with wind-tunnel measurements at all locations. This indicates the accurate calculation of the A-pillar vortex as well as the wake of the side-mirror. Furthermore, the good agreement between the calculated pressure spectrum at the trailing edge of the side mirror (top of the right column in Figure 6.14) indicates the accurate calculation of the flow separation at the lower surface of the mirror. Comparing the spectral levels and their distributions along different frequencies in the region of the A-pillar vortex between the cases with and without side-mirror shows slight differences at some frequencies. This is due to the effect of the side-mirror on the location and size of the A-pillar vortex. Figure 6.15 shows the isosurface of the vorticity at 5000 1/s for the case with side-mirror. Comparing the flow topology to the case without mirror (cf. Figure 6.13), one can observe the side-

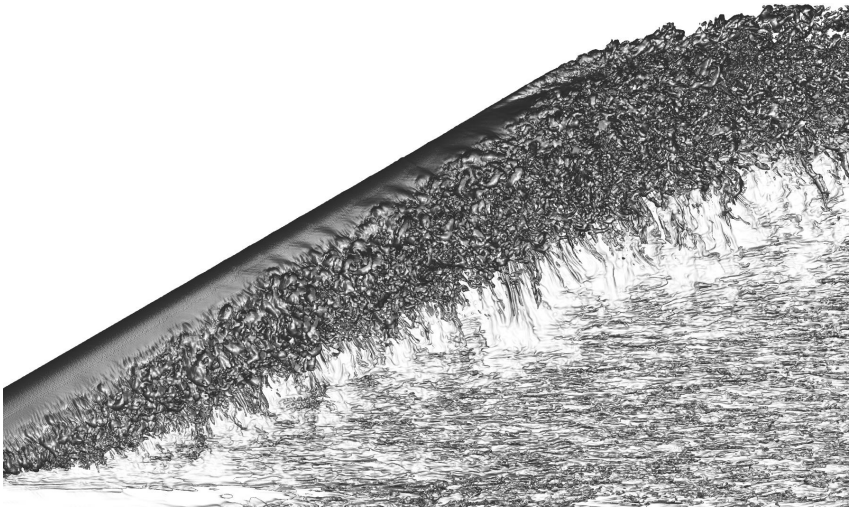

Figure 6.13: Isosurfaces of the vorticity field at 5000 1/s in the region of the A-pillar and side-window.

mirror ”pushing” the A-pillar vortex upwards, and an arc-shaped A-pillar vortex is formed above the mirrors surface. Furthermore, the presence of the side-mirror seems to affect the location of the onset of the A-pillar vortex, which in turn leads to a modification of both the vortex size its and location.

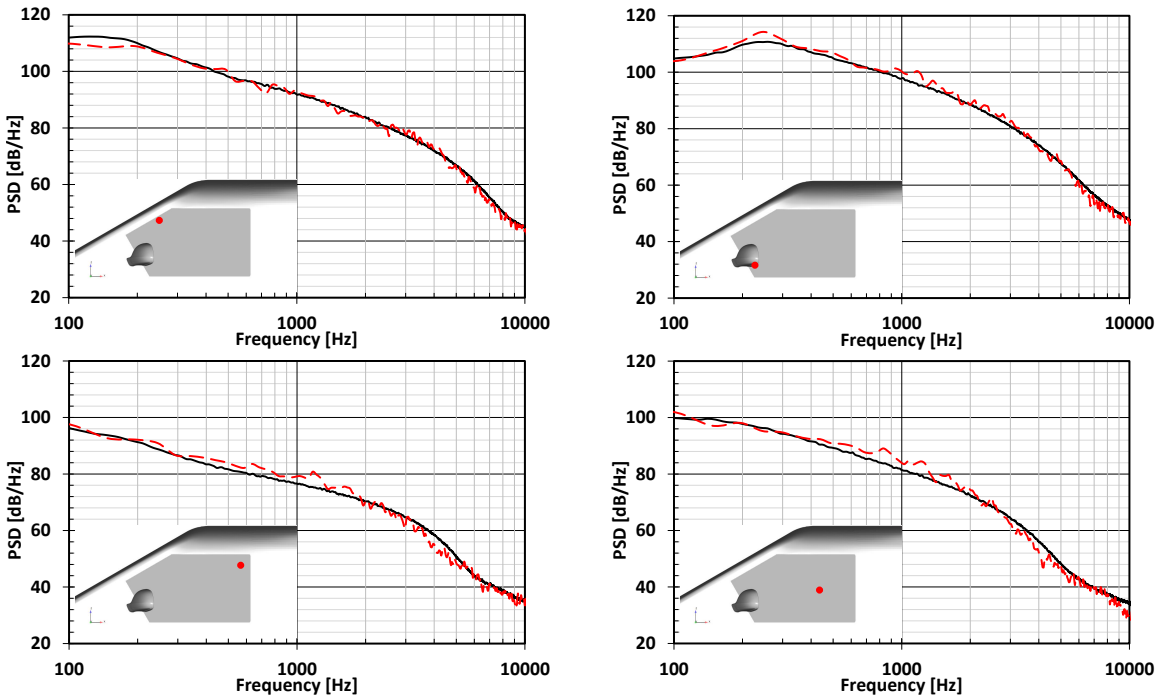

Figure 6.14: Surface pressure spectra at different positions (red dots in the insets) on the side-window in the case with side-mirror. Black solid lines corresponds to wind-tunnel measurements and red dashed lines to numerical results.

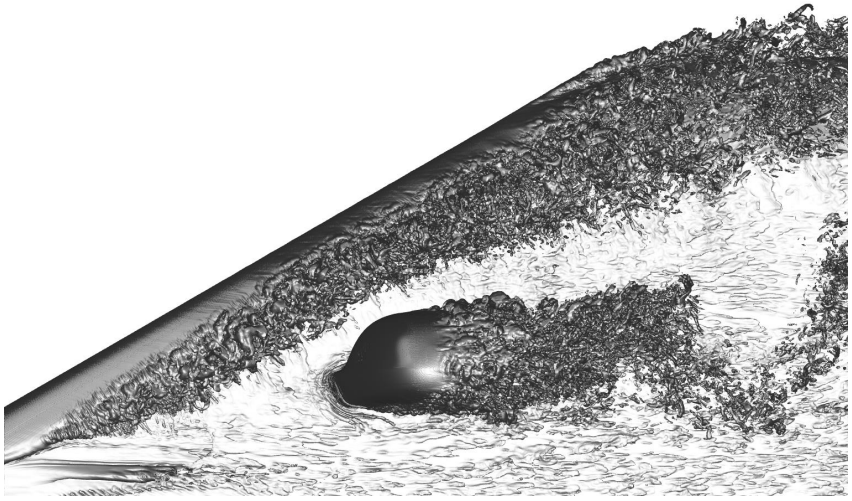

Figure 6.15: Isosurfaces of the vorticity field at 5000 1/s in the region of the A-pillar and side-window in the case with side-mirror.

6.4 Aero- and vibroacoustic results

The surface pressure spectra in the previous section showed good agreement between simulation and experiment. However, the spectra represent mainly hydrodynamic pressure fluctuations on the surface of the window due to their dominance over the acoustic ones. In order to validate the acoustic solution, the frequency-wavenumber spectrum can be used to separate different scales. However, the limited number of microphones used in the wind-tunnel measurements delivers only a coarse frequency-wavenumber spectrum and could only be used for a qualitative comparison. On the other hand, the vibration of the side-window can also be used for the validation of the acoustic solution. According to [48], the window's vibration is the result of hydrodynamic excitation in the frequency region $f < 800$ Hz. For higher frequencies, acoustic pressure fluctuations are mainly responsible for the excitation of the side-window. Hence, a comparison between the numerical and measured windows vibration can deliver a quantitative statement about the quality of the acoustic solution for $f > 800$ Hz.

Similar to the side-mirror test case, the acoustic solution is calculated using the direct and the hybrid methods for the case with side-mirror. For the calculation of acoustic waves using FWH, pressure fluctuations on the surface of the mirror are saved every time-step and used as an input for the solution of the FWH equation. It is worth mentioning that at this point, it is being assumed that the side-mirror is the main and dominant acoustic source with respect to the side-window. Although there exist other acoustic sources, such as the A-pillar and the lower struts of the SAE-body, these surfaces are not regarded in the hybrid calculation. This dominance of sound waves generated at the surface of the side-mirror has already been verified in [48]. This is also verified in the following by comparing the acoustic solution calculated using DNC and FWH. Since the DNC contains acoustic waves generated at all sources on the SAE-body, its solution should be equivalent to the result of the hybrid method in case of the dominance of acoustic waves generated at the side-mirror.

Regarding the case without side-mirror, acoustic waves are only calculated using DNC. In this case, the main noise source is the A-pillar. Since the A-pillars surface cannot be regarded as a closed surface, it is not trivial to calculate acoustic waves generated at the A-pillar using the hybrid method. Therefore, the hybrid acoustic computation for the case without side-mirror is omitted in this study.

6.4.1 Acoustic waves on the side-window

In the following, the frequency-wavenumber spectra are presented for both cases and an analysis of the hydrodynamic and acoustic parts is performed. For the case without side-mirror, the spectra are calculated using pressure values resulting from the CFD-simulation. On the other hand, for the case with side-mirror, the spectra are calculated using the results of the CFD-simulation as well as the ones calculated using FWH. Consequently, the acoustic solution of DNC and FWH are compared and the dominance of the sound generated at the side-mirror is discussed.

Figure 6.16 shows the domain, in which the frequency-wavenumber spectrum is calculated on the side-window. This domain is chosen in such a way, that different acoustic sources can be separated in the frequency-wavenumber spectrum. For instance, acoustic waves generated at the surface of the side-mirror align with the positive k_x axis in the spectrum. On the other hand, acoustic waves generated at the upper edge of the A-pillar would represent an acoustic branch aligning with the negative k_z axis in the spectrum.

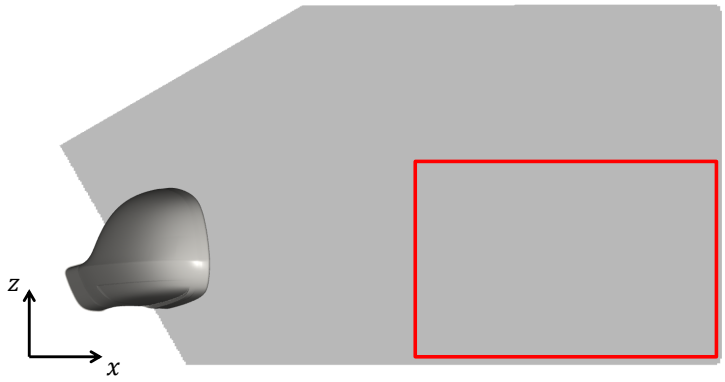

Figure 6.16: The domain, in which the frequency-wavenumber spectrum is calculated (red box).

Figure 6.17 (left) shows the frequency-wavenumber spectrum for the case without side-mirror. At $k_z = 0$, the acoustic branches show much lower spectral levels than the hydrodynamic ones and decrease rapidly for high frequencies ($f > 2$ kHz). This indicates the absence of acoustic waves propagating in the positive x-direction, which is intuitive due to the absence of the side-mirror. The main acoustic source in this case is the upper edge of the A-pillar, which is located exactly above the frequency-wavenumber calculation plane. Therefore, acoustic waves mainly propagate in the negative z-direction for this case. These waves are not visible in the $k_z = 0$ plane. Figure 6.17 (right) also shows the frequency-wavenumber spectrum at $f = 4$ kHz. As expected, the main acoustic branch is aligned on

the negative k_z axis indicating an acoustic source above the red box in Figure 6.16, which is the upper edge of the A-pillar.

It is worth mentioning the absence of acoustic waves propagating in the negative x-direction. The side-panel of the SAE-body is planar and does not exhibit any geometrical steps, like the b-pillar in a real production car. Therefore, the only sound sources downstream the side-window would be the back-end of the SAE-body, which is approximately 2 m downstream the side-window. Hence, acoustic waves generated at the back-end will dissipate rapidly before reaching the side-window and their contribution to the frequency-wavenumber spectrum is therefore negligible. This provides the opportunity to verify the absence of spurious noise generated at refinement interfaces downstream the A-pillar and the side-window. In the case without side-mirror, the frequency-wavenumber spectrum in Figure 6.17 does not show any remarkable acoustic components in the negative k_x region, indicating the absence of spurious noise that could be generated by the interaction between the A-pillar vortex and the refinement interfaces downstream the side-window. This illustrates the successful functionality of the utilised acoustic damping model.

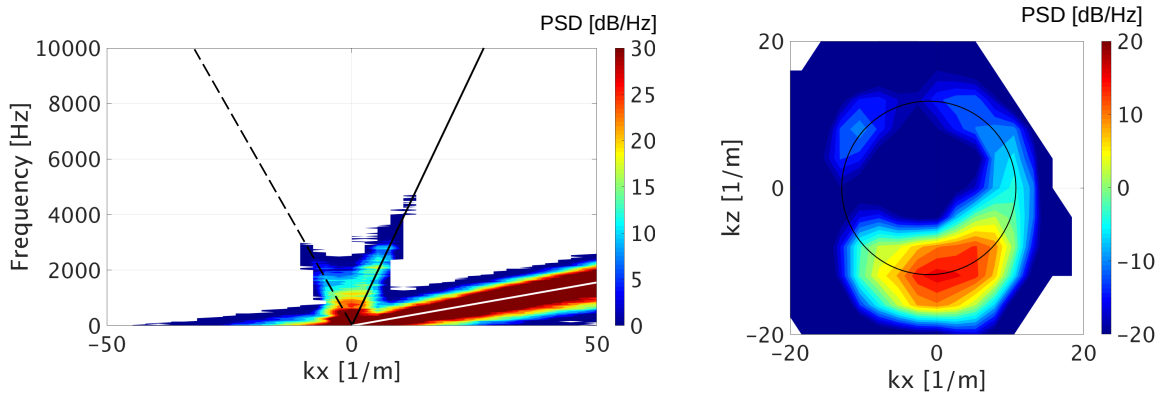

Figure 6.17: Frequency-wavenumber spectrum calculated on the surface of the side-window for the case without side-mirror at (left) $k_z = 0$ and (right) $f = 4$ kHz.

A quantitative assessment of the the acoustic and hydrodynamic branches is performed by integrating the frequency-wavenumber spectrum. Figure 6.18 shows the integrated spectrum over all wavenumbers k_x and k_z compared to the integrated acoustic branch. The integration of the acoustic branch is performed analogous to the method used in the side-mirror test case. Furthermore, the integrated acoustic branch forming an angle of ± 45 degrees with the negative k_z-axis is shown. This branch corresponds to the acoustic waves generated at the edge of the A-pillar. The integrated spectra show the dominance of the hydrodynamic pressure fluctuations compared to the acoustic ones. Furthermore, the integrated acoustic branch is equivalent to the integrated branch corresponding to sound waves generated at the tip of the A-pillar above the side-window. This indicates the dominance of the A-pillar as a sound source in the absence of the side-mirror. In the low frequency region ($f < 1$ kHz), the acoustic branch increases as the frequency decreases. This goes back to the contribution of hydrodynamic pressure fluctuations in the integration domain. The frequency-wavenumber spectrum at $k_z = 0$ (cf. Figure 6.17) shows how the acoustic and hydrodynamic branches merge for $f < 1$ kHz. Therefore, an accurate separation of both branches is not possible

for low frequencies. For frequencies $f > 5$ kHz, a rapid drop in the acoustic spectra can be observed. This is likely related to the coarse surface resolution of the A-pillar. Consequently, the rest of the analysis related to the case without side-mirror (e.g. vibration of the side-window) is restricted to the frequency region below 5 kHz.

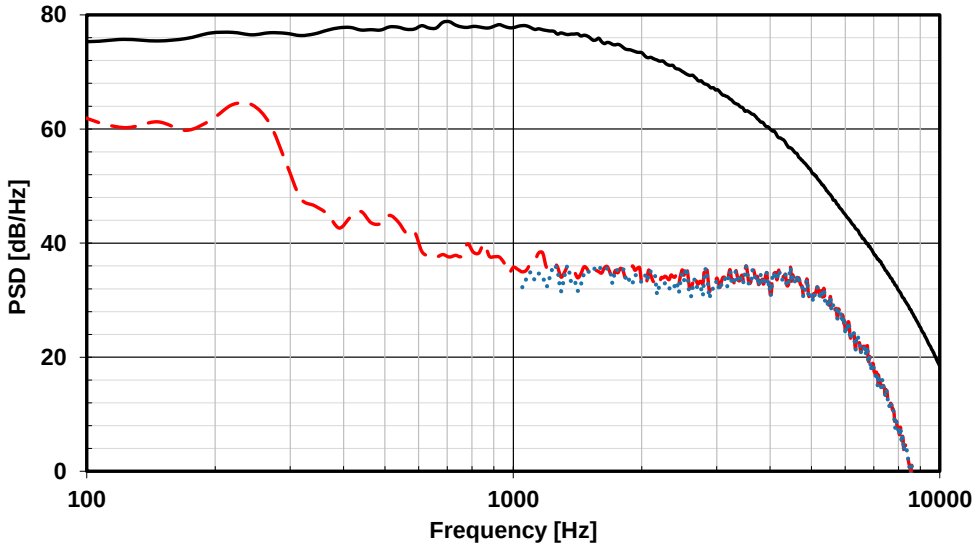

Figure 6.18: Integrated frequency-wavenumber spectrum: black solid line corresponds to the integration of the whole spectrum, red dashed line to the integrated acoustic branch, and blue dotted line to the integrated acoustic branch making an angle of ± 45 degrees with the negative k_z-axis.

Analogously, the frequency-wavenumber spectrum is also calculated for the case with side mirror. Figure 6.19 shows the spectrum at $k_z = 0$ in the left plot and $f = 4$ kHz in the right plot. Acoustic waves propagating in the positive x-direction are significantly higher than those in the case without side-mirror (cf. Figure 6.17). These waves are generated by the side-mirror, which aligns with the k_x axis. Furthermore, the hydrodynamic branch is more pronounced, which is caused by the turbulent wake of the mirror propagating into the frequency-wavenumber analysis plane. Spurious noise can also be observed propagating in the negative x-direction, which is the result of the interaction between the wake of the mirror and grid interfaces further downstream. However, the spectral level of spurious noise is significantly lower than that of physical noise, so that their contribution to the total acoustic level on the side-window is negligible.

In the $f = 4$ kHz plane [cf. Figure 6.19 (right)], one can also observe two main acoustic components: one in the positive x-direction, resulting from the side-mirror, and the other one in the negative z-direction resulting from the A-pillar. Similar to the $k_z = 0$ plane, the level of spurious noise in the $f = 4$ kHz plane is much lower than the level of sound generated by the mirror. Moreover, one can observe that acoustic waves generated by the mirror dominate the ones generated at the A-pillar at $f = 4$ kHz.

In order to analyse the contribution of the side-mirror, A-pillar and spurious noise, each branch is integrated separately in the frequency-wavenumber spectrum. For the side-mirror,

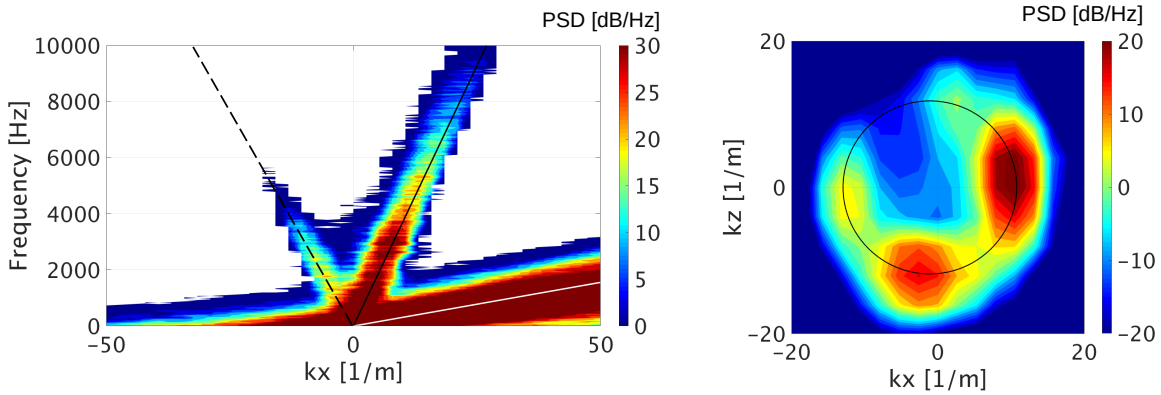

Figure 6.19: Frequency-wavenumber spectrum calculated on the surface of the side-window for the case with side-mirror at (left) $k_z = 0$ and (right) $f = 4$ kHz.

the region extending between ± 45 degrees around the positive k_x axis is integrated. Similarly, the contribution of the A-pillar and spurious noise are determined by integrating the regions extending ± 45 degrees around the negative k_z axis and ± 45 degrees around the negative k_x axis respectively. Figure 6.20 shows the integrated spectra compared to the overall acoustic level on the side-window. The spectra are compared between $f = 1$ and 10 kHz in order to exclude any effect of the hydrodynamic branch.

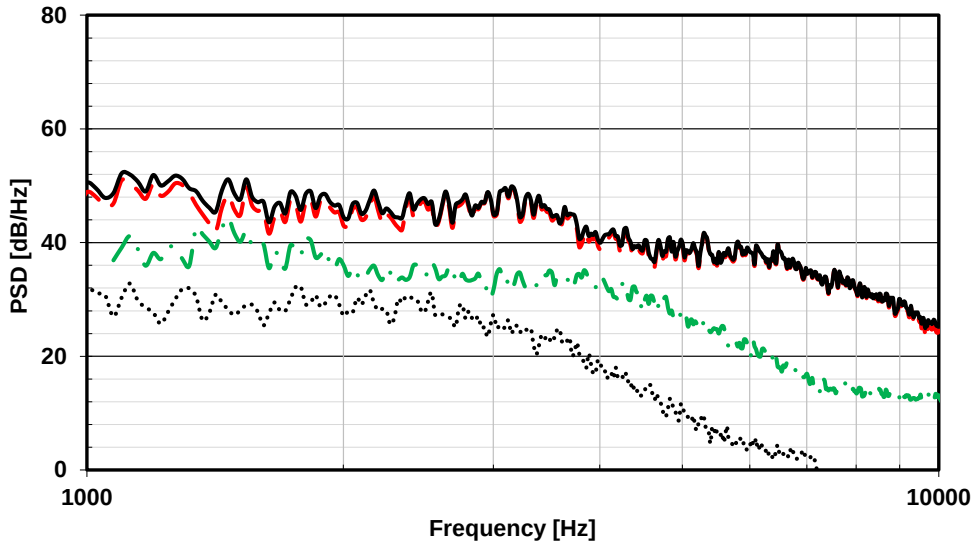

Figure 6.20: Integrated frequency-wavenumber spectrum: black solid line corresponds to the whole acoustic cone, the red dashed line to the region making an angle of ± 45 degrees with the positive k_x-axis, the green dash-dotted line to the region making an angle of ± 45 degrees with the negative k_z-axis, and the black dotted line to spurious noise.

In Figure 6.20, it is clear that acoustic waves generated by the side-mirror dominate the overall spectrum. The spectral level of the waves coincide with the overall spectral level of the whole acoustic cone. The spectral level of waves generated at the A-pillar are considerably lower than those generated at the mirror. The same applies for spurious noise, whose level

is at least 10 dB lower than that of waves generated at the mirror for all frequencies. This comparison confirms the minor role of the generated spurious noise.

Additional computation of sound waves generated at the surface of the mirror are performed using the hybrid method. The integrated acoustic branches corresponding to waves generated by the side-mirror are shown in Figure 6.21 for DNC and FWH. Both methods deliver the same spectral levels along the whole frequency range.

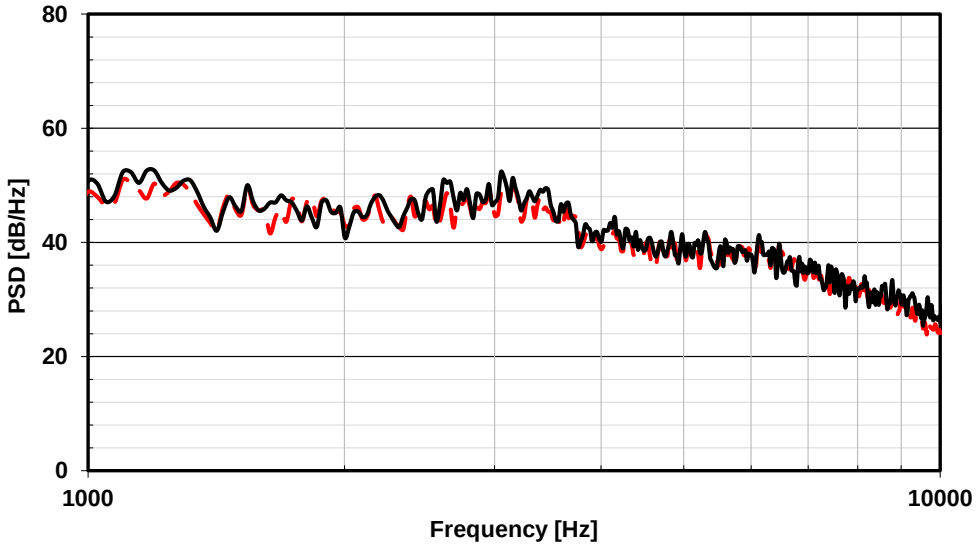

Figure 6.21: Integrated frequency-wavenumber spectrum in the region making ±45 degrees with the positive k_x-axis. Black solid line corresponds to FWH and red dashed line to DNC results.

6.4.2 Vibration of the side-window

For the validation of the acoustic solution, the vibration of the side-window is calculated. For this purpose, the method described in the previous chapter is utilised and the parameters listed in Table 6.1 are used. For the case without side-mirror, transient pressure values resulting from the compressible CFD simulation are used as an input for the bending wave equation, while the results of both CAA-methods are used to calculate the windows vibration for the case with side-mirror.

The acceleration values on the side-window are compared between simulation and experiment. For this, PSD spectra of these values are calculated relative to a reference acceleration $a_{\text{ref}} = 5 \cdot 10^{-8}$ m/s^2.

Variant without side-mirror

Figure 6.22 shows the PSD spectra of the acceleration values on the side-window at different positions. Furthermore, it shows the average of the spectra at all positions compared to wind tunnel measurements. The numerical results show good agreement with experimental

ones up to $f \approx 5$ kHz. At higher frequencies, the numerical results exhibit a rapid drop. This goes back to the high damping loss factor implemented in the vibroacoustic model. As described in [48], the damping loss factor of the side-window on the SAE-body was modeled using a polynomial fit, which was only valid for frequencies up to $f = 5$ kHz. For higher frequencies, the polynomial expression delivers higher damping values. Therefore, the following comparisons between numerical and wind tunnel measurements are restricted to frequencies up to 5 kHz. At frequencies below 300 Hz, numerical results show lower spectral levels than experimental ones. Although the hydrodynamic part of the pressure fluctuations was not filtered out at low frequencies, the difference between the simulated (0.2 s) and measured (30 s) physical time could be the reason for these differences. Hence, a comparison between between numerical and experimental data for $f < 300$ Hz is excluded in the rest of the analysis. Further differences between the simulated spectra and wind tunnel measurements can be observed in the region of the windows coincidence frequency $f_{\mathrm{co}} \approx 4$ kHz. First, it was presumed that spurious noise, which could be generated at the refinement interface directly above the upper edge of the A-pillar, could be the reason for higher acoustic levels. Consequently, a simulation with a 2 mm surface resolution of the A-pillar without refinement interfaces was performed. The total acoustic level was lower than the ones in Figure 6.22 due to the coarser surface resolution. However, the hump in the PSD spectra at the coincidence frequency was almost identical to the ones observed in Figure 6.22. Therefore, it is unlikely that spurious noise is generated at the aforementioned interface and the differences in the coincidence region could be related to inaccurate modelling of the damping behaviour of the side-windows vibration. It is worth mentioning that the hump shaped distribution of the PSD spectra at the coincidence frequency was also observed in some of the vibroacoustic results in [48], in which acoustic waves were calculated using a hybrid method.

Variant with side-mirror

For the case with side-mirror, acoustic waves are calculated using both CAA methods. Figure 6.23 shows the results of both methods compared to wind tunnel measurements at different positions. As mentioned before, the modelled damping loss factor of the window is valid for frequencies upto 5 kHz. Hence, the analysis is restricted to frequencies $f < 5$ kHz. One major difference between the results of DNC and FWH are the spectral levels for frequencies below 1 kHz. In this region, hydrodynamic pressure fluctuations are mainly responsible for the vibration of the window. Since the pressure fluctuations calculated using FWH do not contain the hydrodynamic part, the spectral levels for $f > 1$ kHz are substantially lower than the measured ones. On the other hand, the results of the DNC show good agreement with experimental results for $f < 1$ kHz, since the pressure fluctuations of the compressible CFD solution contain both hydrodynamic and acoustic parts. For $f > 1$ kHz, acoustic pressure fluctuations are mainly responsible for the windows excitation and the results of both CAA methods show good agreement with wind tunnel measurements. For the FWH approach, pressure fluctuations on the surface of the side-mirror were used to calculate acoustic waves on the side-window. On the other hand, the DNC approach contains all acoustic sources, including the side-mirror, A-pillar, and possible reflections from the wind

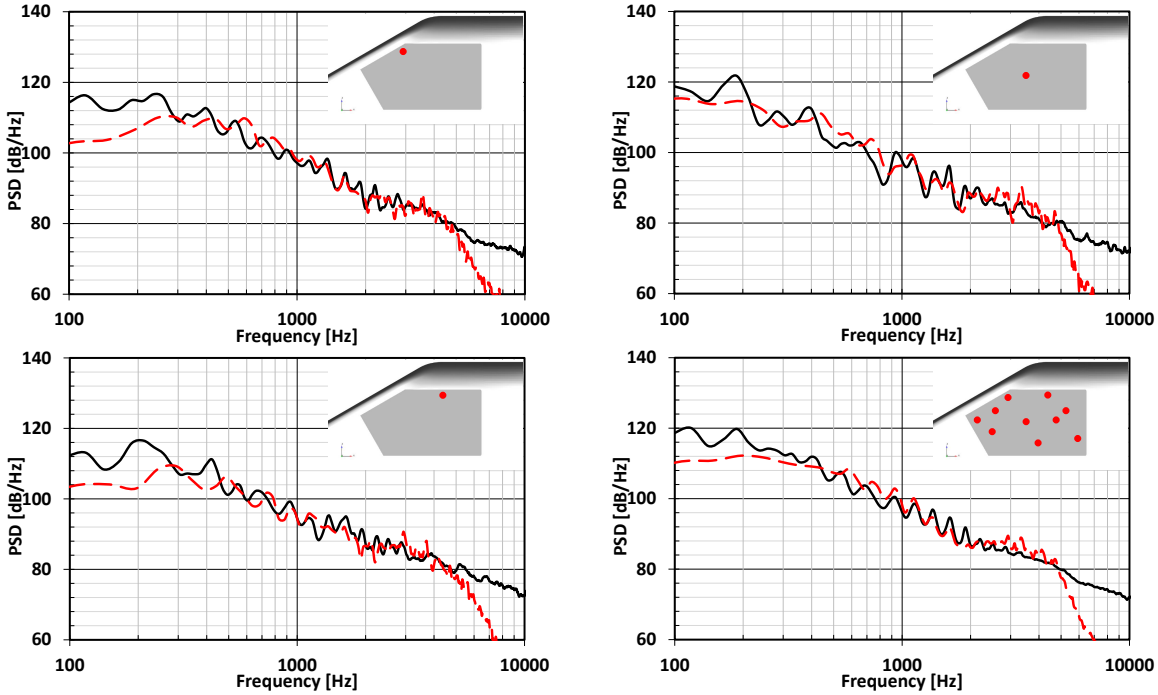

Figure 6.22: PSD spectra of the windows vibration for the case without side-mirror at different positions (red dots). Black solid lines correspond to wind tunnel measurements and red dashed lines to DNC results. The figure showing all accelerometer positions corresponds to the arithmetic mean of all positions.

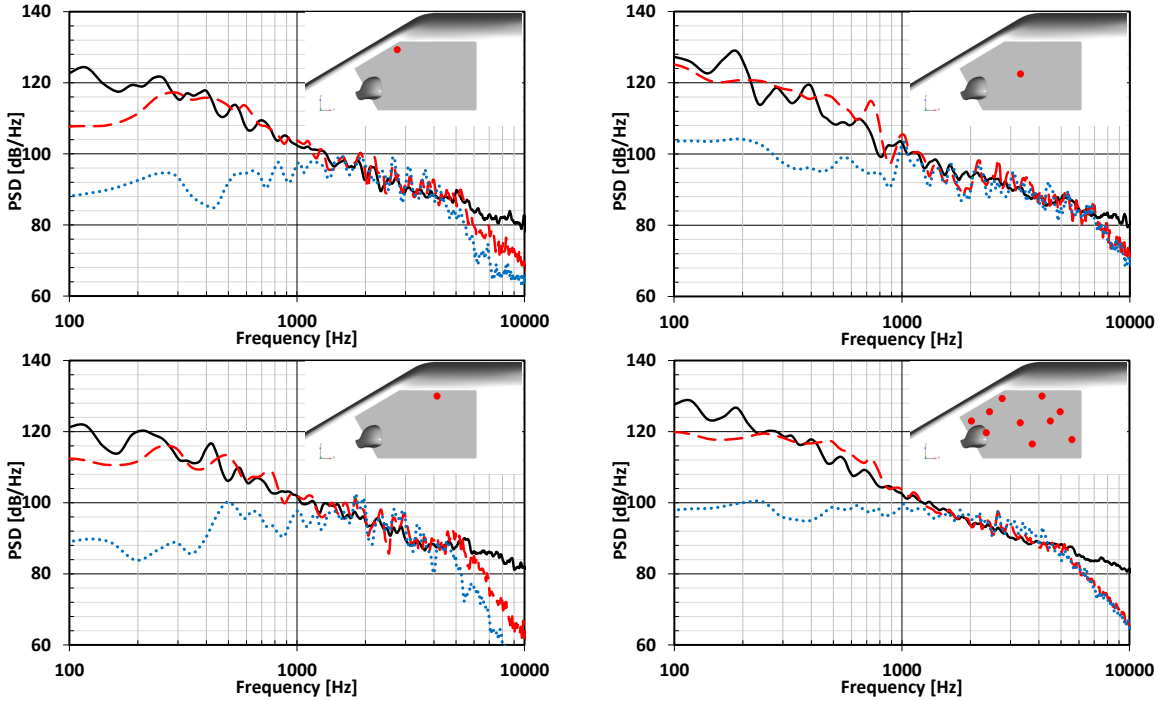

Figure 6.23: PSD spectra of the windows vibration for the case with side-mirror at different positions (red dots). Black solid lines correspond to wind tunnel measurements, red dashed lines to DNC, and blue dotted lines to FWH results. The figure showing all accelerometer positions corresponds to the arithmetic mean of all positions.

tunnels floor. Consequently, the good agreement between the results of both approaches shows the dominance of the side-mirror as an acoustic source in this case.

7 Conclusion

The purpose of this work was the development of a method for the direct computation of noise generated by the external flow past a vehicle was the purpose of this work. Due to the importance of hydrodynamic-acoustic interaction in certain flow configurations, the direct noise computation method is considered to be the most accurate approach for noise prediction. However, the direct approach can be challenging with respect to computational demands, numerical schemes, and grid topology. These aspects has been analysed in this work and the applicability and efficiency of the direct method have been studied and optimised.

For the simultaneous computation of acoustic and hydrodynamic pressure fluctuations, the compressible Navier-Stokes equations have to be solved. This includes solving the conservation equations for mass, momentum and energy. In this work, a new flow solver for low Mach number flows has been developed. The solver consists of the conservation equations for mass and momentum, without solving the energy equation. Instead, the temperature is algebraically calculated using the isentropic relation of ideal gases, which is valid for flow configurations with low Mach numbers. The omission of the energy equation results in a considerable reduction of the computational demand. Additionally, the flow solver was extended with a state of the art Rhie & Chow interpolation technique, which has been developed and extensively studied for aeroacoustic applications in [51]. Finally, a multi-purpose acoustic damping model has been introduced and implemented. The damping model is characterised by its selectivity regarding damping out acoustic waves without affecting the turbulence. In the course of this work, the damping model has been analytically studied and discussed in [20].

After introducing the numerical approach for the direct noise computation, it has been validated using the two-struts benchmark. The benchmark consists of two square cylinders placed in tandem arrangement and exhibiting a uniform flow of Mach number $Ma \approx 0.2$. Wind tunnel measurements were made available for a critical gap between the cylinders, at which two different and stable flow states can take place. The flow solver was able to capture both flow states, depending on the initial conditions of the flow upstream the configuration. The validation of flow solver has been performed based on comparing aerodynamic as well as aeroacoustic numerical results with wind tunnel measurements. For the aerodynamic validation, mean flow field variables, surface pressure spectra, and pressure coefficient distribution on the surfaces of the cylinders has been compared with experimental results. Numerical results showed good agreement with wind tunnel measurements for both flow states. However, numerical results of the full span case showed better agreement with experimental data for certain variables than the limited span case, which was related to the differences in the spanwise correlation and coherence between both cases. Afterwards, aeroacoustic results were validated by comparing numerical far-field spectra and directivity patterns with wind tunnel measurements. Herein, acoustic waves were calculated directly using the proposed solver as well as indirectly using a hybrid method based on a surface integral. For

the limited span case, far-field spectra could only be calculated using the hybrid method due to the spanwise periodic boundary conditions. For the full-span case, far-field spectra were calculated using both CAA methods, which showed good agreement with wind tunnel measurements. However, the direct method showed better agreement with experimental data regarding the directivity patterns in the high-frequency range, which was related to the absence of refraction effects as well as acoustic-hydrodynamic interaction in the hybrid method. Furthermore, the effect of the endplates has been presented and the simulation of the full span with short endplates showed better agreement with wind tunnel measurements, which were performed with perforated endplates.

The validation of the flow solver was followed by addressing spurious noise generation in the direct noise computation approach. For automotive applications, it has been shown that spurious noise could mask out physical sound waves and falsify the final acoustic solution. Hence, the mechanism of spurious noise generation and their potential sources has been examined. For this, a test case consisting of a convected isotropic turbulence package was considered. Different numerical setups consisting of various discretisation schemes and grid topologies have been analysed. Two main spurious noise sources have been identified: discretisation scheme related and grid related sources. The DES-hybrid scheme has shown continuous generation of spurious noise as the turbulence moves through the computational domain. The amplitude of spurious noise generated by the hybrid scheme did show a dependency on the blending degree of the corresponding schemes. Regarding grid induced spurious noise, it has been observed that refinement interfaces are the main source of numerical noise. Moreover, a dependency between the direction of refinement and spurious noise propagation has been indicated. Finally, two strategies for reducing spurious noise generated at grid interfaces have been developed and tested. The acoustic damping model has shown its potential in damping out high-frequency noise generated at refinement interfaces without affecting the turbulent structures in the package. Moreover, a grid stretching study has been performed and the effect of different expansion ratios on the amplitude of generated spurious noise has been studied.

The acoustic damping model as well as the grid stretching strategy were then applied to a single side-mirror test case. For the second strategy, a new grid stretching algorithm has been developed, which allows an automated stretching of the numerical grid in a user predefined region. Using a frequency-wavenumber analysis, it was possible to separate acoustic pressure fluctuations from hydrodynamic ones in the wake of the mirror. Due to the absence of any measurements for the side-mirror test case, a comparison between the results of the direct and hybrid methods was utilised in order to assess the effectiveness of the aforementioned strategies in reducing spurious noise generation in the vicinity of the mirrors surface. It has been shown that the acoustic damping model was able to reduce spurious noise generated at grid interfaces in the wake of the mirror, while the grid stretching method enabled the prevention of spurious noise generation near the surface of the mirror. Due to the low Mach number of the flow past the mirror, the surface of the mirror was considered to be the main noise source. Therefore, it was expected that the acoustic solutions in the wake of the mirror, calculated using the hybrid and direct methods, are equivalent. This was the case after utilising the strategies for spurious noise reduction. Furthermore, the test

case was used to validate the filtering approach, which has to be applied on the pressure fluctuations resulting from the compressible solver in order to avoid aliasing effects. The vibroacoustic results of both CAA-methods showed good agreement upto to a frequency $f \approx 6$ kHz. Finally, a grid study was performed in order to determine the necessary surface resolution of the side-mirror. The acoustic results in the wake of the mirror converged for a surface resolution equal to 0.25 mm. Moreover, a time-step size equivalent to $\Delta_t = 5 \cdot 10^{-6}$ s was necessary to resolve high frequency ($f > 6$ kHz) acoustic waves.

Finally, in order to examine the applicability of the proposed simulation method to production vehicles, noise generation caused by the flow past a generic vehicle model has been calculated. The flow past the SAE-body exhibits main flow features, that a typical production car has, such as an A-pillar vortex and a turbulent side-mirror wake. In order to reduce spurious noise, the aforementioned spurious noise reduction strategies have been applied. Two different variants have been calculated and compared to wind tunnel measurements. Simulated surface pressure spectra, which are mainly characterised by hydrodynamic pressure fluctuations, showed good agreement with wind tunnel measurements for both variants. It has been observed that the presence of the side-mirror affects the position of the A-pillar vortex. Furthermore, with the help of frequency-wavenumber analysis, the amount of spurious noise generated by the interaction between the wake of the mirror and refinement interface downstream the mirror could be quantified. The generated spurious noise has a substantially lower spectral level than the physical noise generated by the mirror. Hence, the final acoustic solution on the side-window was not masked out by spurious noise and the windows vibration was mainly caused by physical noise. It was also observed that acoustic waves on the side-window were mainly generated by the side-mirror. At the end, in order to validate the acoustic solution on the side-window, surface vibration including acceleration spectra have been calculated and compared to wind-tunnel measurements. For both variants, simulated data showed good agreement with experimental ones upto to $f \approx 5$ kHz. For $f > 5$ kHz, the damping loss factor of the side-window was not accurately modelled. Hence, no comparison was performed for the high frequency range.

Bibliography

[1] OpenFOAM User Guide, https://cfd.direct/openfoam/user-guide (March 2017).

[2] OpenFOAM Extended Code Guide, https://www.openfoam.com/documentation/cpp-guide/html/index.html (January 2018).

[3] I. Abalakin, P. Bakhvalov, T. Kozubskaya, Edge-based reconstruction schemes for prediction of near field flow region in complex aeroacoustics problems, International Journal of Aeroacoustics 13 (3-4) (2014) 207–233. doi:10.1260/1475-472X.13.3-4.207.

[4] H. Abe, H. Kawamura, Y. Matsuo, Direct numerical simulation of a fully developed turbulent channel flow with respect to the reynolds number dependence, Journal of fluids Engineering 123 (2) (2001) 382–393.

[5] R. Akkermans, P. Bernicke, R. Ewert, J. Dierke, Zonal overset-les with stochastic volume forcing, International Journal of Heat and Fluid Flow 70 (2018) 336 – 347. doi:https://doi.org/10.1016/j.ijheatfluidflow.2017.11.005.

[6] R. Amiet, Refraction of sound by a shear layer, Journal of Sound and Vibration 58 (4) (1978) 467–482.

[7] J. Benesty, J. Chen, Y. Huang, I. Cohen, Pearson correlation coefficient, in: Noise reduction in speech processing, Springer, 2009, pp. 1–4.

[8] J.-P. Berenger, A perfectly matched layer for the absorption of electromagnetic waves, Journal of computational physics 114 (2) (1994) 185–200.

[9] M. J. Berger, R. J. LeVeque, Adaptive mesh refinement using wave-propagation algorithms for hyperbolic systems, SIAM Journal on Numerical Analysis 35 (6) (1998) 2298–2316.

[10] L. C. Berselli, T. Iliescu, W. J. Layton, Mathematics of large eddy simulation of turbulent flows, Springer Science & Business Media, 2005.

[11] K. S. Brentner, Prediction of helicopter rotor discrete frequency noise: a computer program incorporating realistic blade motions and advanced acoustic formulation.

[12] K. S. Brentner, F. Farassat, An analytical comparison of the acoustic analogy and kirchhoff formulation for moving surfaces.

[13] G. A. Bres, D. Freed, M. Wessels, S. Noelting, F. Pérot, Flow and noise predictions for the tandem cylinder aeroacoustic benchmark, Physics of Fluids 24 (3) (2012) 036101.

[14] F. Brogi, O. Malaspinas, B. Chopard, C. Bonadonna, Hermite regularization of the lattice boltzmann method for open source computational aeroacoustics, The Journal of the Acoustical Society of America 142 (4) (2017) 2332–2345.

[15] J. Capon, High-resolution frequency-wavenumber spectrum analysis, Proceedings of the IEEE 57 (8) (1969) 1408–1418.

[16] B. Chaouat, The state of the art of hybrid rans/les modeling for the simulation of turbulent flows, Flow, Turbulence and Combustion 99 (2) (2017) 279–327.

[17] G. N. Coleman, R. D. Sandberg, A primer on direct numerical simulation of turbulence-methods, procedures and guidelines, Tech. rep., University of Southampton (2010).

[18] T. Colonius, S. K. Lele, P. Moin, Boundary conditions for direct computation of aerodynamic sound generation, AIAA journal 31 (9) (1993) 1574–1582.

[19] A. H. Dawi, R. A. D. Akkermans, Direct and Integral Noise Computation of Two Square Cylinders in Tandem Arrangement, Journal of Sound and Vibration.

[20] A. H. Dawi, R. A. D. Akkermans, Spurious noise in direct noise computation with a finite volume method for automotive applications, International Journal of Heat and Fluid Flow 72 (2018) 243–256.

[21] T. Deconinck, L. Temmerman, C. Hirsch, S. Oerlemans, T. Knacke, F. Thiele, A. Duben, A. Gorobets, T. Kozubskaya, J. Baiges, R. Codina, H. Espinoza, Final report on the assessment of the existing numerical approaches based on comparison of numerical predictions with each other and with experiments: two-struts test case, Tech. Rep. VALIANT project report D27, NUMECA (2011).

[22] P. di Francescantonio, A new kirchhoff formulation for transonic rotor noise, Tech. rep. (1996).

[23] P. Durbin, G. Iaccarino, An approach to local refinement of structured grids, Journal of Computational Physics 181 (2) (2002) 639–653.

[24] J. H. Ferziger, M. Peric, Computational methods for fluid dynamics, Springer Science & Business Media, 2012.

[25] J. Freund, Proposed inflow/outflow boundary condition for direct computation of aerodynamic sound, AIAA journal 35 (4) (1997) 740–742.

[26] J. Fröhlich, D. von Terzi, Hybrid LES/RANS methods for the simulation of turbulent flows, Progress in Aerospace Sciences 44 (5) (2008) 349–377.

[27] U. Gabbert, F. Duvigneau, J. Shan, Active and passive measures to reduce the noise pollution of combustion engines, in: Information and Automation (ICIA), 2014 IEEE International Conference on, IEEE, 2014, pp. 1072–1077.

[28] M. Germano, Differential filters for the large eddy numerical simulation of turbulent flows, The Physics of fluids 29 (1986) 1755–1757.

[29] B. Geurts, Elements of direct and large-eddy simulation, RT Edwards Philadelphia, 2004.

[30] S. Girimaji, K. Abdol-Hamid, Partially-averaged navier stokes model for turbulence: implementation and validation, in: 43rd AIAA Aerospace Sciences Meeting and Exhibit, 2005, p. 502.

[31] S. S. Girimaji, Partially-averaged navier-stokes model for turbulence: A reynolds-averaged navier-stokes to direct numerical simulation bridging method, Journal of Applied Mechanics 73 (3) (2006) 413–421.

[32] E. Goodfriend, F. Katopodes Chow, M. Vanella, E. Balaras, Large-Eddy Simulation of Flow Through an Array of Cubes with Local Grid Refinement, Boundary-Layer Meteorology 159 (2) (2016) 285–303. doi:10.1007/s10546-016-0128-y.

[33] L. Goodfriend, F. Chow, M. Vanella, E. Balaras, Large-eddy simulation of decaying isotropic turbulence across a grid refinement interface using explicit filtering and reconstruction, Journal of Turbulence 14 (12) (2013) 58–76. doi:10.1080/14685248.2013.867964.

[34] M. S. Gritskevich, A. V. Garbaruk, J. Schütze, F. R. Menter, Development of ddes and iddes formulations for the k-ω shear stress transport model, Flow, turbulence and combustion 88 (3) (2012) 431–449.

[35] G. Haller, An objective definition of a vortex, Journal of fluid mechanics 525 (2005) 1–26.

[36] M. Hartmann, J. Ocker, T. Lemke, A. Mutzke, V. Schwarz, H. Tokuno, R. Toppinga, P. Unterlechner, G. Wickern, Wind noise caused by the side-mirror and a-pillar of a generic vehicle model, in: 18th AIAA/CEAS Aeroacoustics Conference (33rd AIAA Aeroacoustics Conference), 2012, p. 2205.

[37] F. Hu, On constructing stable perfectly matched layers as an absorbing boundary condition for euler equations, in: 40th AIAA Aerospace Sciences Meeting & Exhibit, p. 227.

[38] F. Q. Hu, A stable, perfectly matched layer for linearized euler equations in unsplit physical variables, Journal of Computational Physics 173 (2) (2001) 455–480.

[39] F. Q. Hu, A perfectly matched layer absorbing boundary condition for linearized euler equations with a non-uniform mean flow, Journal of Computational Physics 208 (2) (2005) 469–492.

[40] X. Huang, Adaptive Mesh Refinement for Computational Aeroacoustics, Ph.D. thesis, University of Southampton (October 2006).

[41] O. Inoue, M. Mori, N. Hatakeyama, Aeolian tones radiated from flow past two square cylinders in tandem, Physics of Fluids 18 (4) (2006) 046101.

[42] M. Israeli, S. A. Orszag, Approximation of radiation boundary conditions, Journal of computational physics 41 (1) (1981) 115–135.

[43] R. I. Issa, Solution of the implicitly discretised fluid flow equations by operator-splitting, Journal of computational physics 62 (1) (1986) 40–65.

[44] M. C. Jacob, J. Boudet, D. Casalino, M. Michard, A rod-airfoil experiment as a benchmark for broadband noise modeling, Theoretical and Computational Fluid Dynamics 19 (3) (2005) 171–196.

[45] H. Jasak, Error analysis and estimation for finite volume method with applications to fluid flow, Ph.D. thesis, Imperial College London (University of London) (1996).

[46] H. Jasak, Numerical solution algorithms for compressible flows, Tech. rep., Faculty of Mechanical Engineering and Naval Architecture, University of Zagreb (2007).

[47] L. Jenkins, M. Khorrami, M. Choudhari, C. McGinley, Characterization of unsteady flow structures around tandem cylinders for component interaction studies in airframe noise, in: 11th AIAA/CEAS Aeroacoustics Conference, p. 2812.

[48] A. Kabat Vel Job, J. Sesterhenn, Prediction of the interior noise level for automotive applications based on time-domain methods, in: INTER-NOISE and NOISE-CON Congress and Conference Proceedings, Vol. 253, Institute of Noise Control Engineering, 2016, pp. 6000–6010.

[49] C. Kato, A. Iida, Y. Takano, H. Fujita, M. Ikegawa, Numerical prediction of aerodynamic noise radiated from low mach number turbulent wake, in: 31st Aerospace Sciences Meeting, 1993, p. 145.

[50] P. Khosla, S. Rubin, A diagonally dominant second-order accurate implicit scheme, Computers & Fluids 2 (2) (1974) 207–209.

[51] T. Knacke, Numerische Simulaton des Geräusches massiv abgelöster Strömung bei großer Reynoldszahl und kleiner Machzahl, Ph.D. thesis, TU-Berlin (2015).

[52] T. Knacke, F. Thiele, Prediction of Broadband Noise from Two Square Cylinders in Tandem Arrangement Using a Combined DDES/FWH Approach, Springer Berlin Heidelberg, Berlin, Heidelberg, 2014, pp. 123–131. doi:10.1007/978-3-662-43489-5_15.

[53] J. Kok, H. van der Ven, A High-Order Finite-Volume Method with Block-Structured Local Grid Refinement, in: IDIHOM: Industrialization of High-Order Methods - A Top-Down Approach: Results of a Collaborative Research Project Funded by the European Union, 2010 - 2014, Springer International Publishing, 2015, pp. 293–314. doi:10.1007/978-3-319-12886-3_14.

[54] J. Kok, A high-order low-dispersion symmetry-preserving finite-volume method for compressible flow on curvilinear grids, Journal of Computational Physics 228 (18) (2009) 6811–6832.

[55] K. Kucukcoskun, M. Eng, R. Boeykens, K. De Langhe, Prediction of exterior noise generated by a side-mirror of an suv, in: INTER-NOISE and NOISE-CON Congress and Conference Proceedings, Vol. 253, Institute of Noise Control Engineering, 2016, pp. 3306–3316.

[56] E. Labourasse, P. Sagaut, Reconstruction of turbulent fluctuations using a hybrid RANS/LES approach, Journal of Computational Physics 182 (1) (2002) 301–336.

[57] D. Lagrava, O. Malaspinas, J. Latt, B. Chopard, Advances in multi-domain lattice boltzmann grid refinement, Journal of Computational Physics 231 (14) (2012) 4808 – 4822. doi:https://doi.org/10.1016/j.jcp.2012.03.015.

[58] H. Le, P. Moin, J. Kim, Direct numerical simulation of turbulent flow over a backward-facing step, Journal of fluid mechanics 330 (1997) 349–374.

[59] S. Le Bras, H. Deniau, C. Bogey, A flux reconstruction technique for non-conforming grid interfaces in aeroacoustic simulations, in: 22nd AIAA/CEAS Aeroacoustics Conference, no. 2972, 2016.

[60] M. Lee, R. D. Moser, Direct numerical simulation of turbulent channel flow up to $Re_\tau \approx 5200$, Journal of Fluid Mechanics 774 (2015) 395–415. doi:10.1017/jfm.2015.268.

[61] S. K. Lele, Compact finite difference schemes with spectral-like resolution, Journal of computational physics 103 (1) (1992) 16–42.

[62] Y. Li, E. Perlman, M. Wan, Y. Yang, C. Meneveau, R. Burns, S. Chen, A. Szalay, G. Eyink, A public turbulence database cluster and applications to study lagrangian evolution of velocity increments in turbulence, Journal of Turbulence 9 (2008) N31.

[63] M. J. Lighthill, On sound generated aerodynamically i. general theory, Proc. R. Soc. Lond. A 211 (1107) (1952) 564–587.

[64] M. J. Lighthill, On sound generated aerodynamically ii. turbulence as a source of sound, Proc. R. Soc. Lond. A 222 (1148) (1954) 1–32.

[65] C.-H. Liu, J. M. Chen, Observations of hysteresis in flow around two square cylinders in a tandem arrangement, Journal of Wind Engineering and Industrial Aerodynamics 90 (9) (2002) 1019–1050.

[66] D. Lockard, Summary of the tandem cylinder solutions from the benchmark problems for airframe noise computations-i workshop, in: 49th AIAA Aerospace Sciences Meeting including the New Horizons Forum and Aerospace Exposition, p. 353.

[67] T. Lund, The use of explicit filters in large eddy simulation, Computers & Mathematics with Applications 46 (4) (2003) 603–616.

[68] S. Luo, T. Teng, Aerodynamic forces on a square section cylinder that is downstream to an identical cylinder, The Aeronautical Journal 94 (936) (1990) 203–212.

[69] A. S. Lyrintzis, Surface integral methods in computational aeroacoustics—from the (cfd) near-field to the (acoustic) far-field, International journal of aeroacoustics 2 (2) (2003) 95–128.

[70] S. Malekpour, J. A. Gubner, W. A. Sethares, Measures of generalized magnitude-squared coherence: Differences and similarities, Journal of the Franklin Institute 355 (5) (2018) 2932 – 2950. doi:https://doi.org/10.1016/j.jfranklin.2018.01.014.

[71] F. Menter, Y. Egorov, A scale adaptive simulation model using two-equation models, in: 43rd AIAA Aerospace Sciences Meeting and Exhibit, 2005, p. 1095.

[72] F. Menter, M. Kuntz, R. Bender, A scale-adaptive simulation model for turbulent flow predictions, in: 41st aerospace sciences meeting and exhibit, 2003, p. 767.

[73] F. R. Menter, M. Kuntz, R. Langtry, Ten years of industrial experience with the sst turbulence model, Turbulence, heat and mass transfer 4 (1) (2003) 625–632.

[74] F. Menter, Y. Egorov, The scale-adaptive simulation method for unsteady turbulent flow predictions. part 1: theory and model description, Flow, Turbulence and Combustion 85 (1) (2010) 113–138.

[75] U. Michel, D. Eschricht, B. Greschner, T. Knacke, C. Mockett, F. Thiele, Advanced des methods and their application to aeroacoustics, in: S.-H. Peng, P. Doerffer, W. Haase (Eds.), Progress in Hybrid RANS-LES Modelling, Springer Berlin Heidelberg, Berlin, Heidelberg, 2010, pp. 59–76.

[76] C. Mockett, A Comprehensive Study of Detached Eddy Simulation, Univerlag TU Berlin, 2009.

[77] R. D. Moser, J. Kim, N. N. Mansour, Direct numerical simulation of turbulent channel flow up to $Re_\tau = 590$, Physics of fluids 11 (4) (1999) 943–945.

[78] N.-A. Nilsson, O. Bennerhult, S. Soderqvist, External tire/road noise: its generation and reduction, in: Proceedings of the International Conference Noise Control Engineering, Noise Control for the 80's, Inter-Noise 80, Vol. 1, Miami, Florida, December 8-10, 1980., 1980.

[79] S. Oerlemans, Acoustic wind tunnel tests on two-struts configuration, Tech. rep., VALIANT project report D20, NLR (2011).

[80] S. Oerlemans, P. Sijtsma, Effects of wind tunnel side-plates on airframe noise measurments with phased arrays, AIAA Paper 2000-1938.

[81] S. V. Patankar, D. B. Spalding, A calculation procedure for heat, mass and momentum transfer in three-dimensional parabolic flows, in: Numerical Prediction of Flow, Heat Transfer, Turbulence and Combustion, Elsevier, 1983, pp. 54–73.

[82] S. B. Pope, Turbulent flows, Cambridge University Press, 2001.

[83] P. Quéméré, P. Sagaut, Zonal multi-domain rans/les simulations of turbulent flows, International journal for numerical methods in fluids 40 (7) (2002) 903–925.

[84] J. Ramshaw, P. O'Rourke, L. Stein, Pressure gradient scaling method for fluid flow with nearly uniform pressure, Journal of Computational Physics 58 (3) (1985) 361 – 376. doi:https://doi.org/10.1016/0021-9991(85)90168-8.

[85] J. D. Ramshaw, P. J. O'Rourke, A. A. Amsden, Acoustic damping for explicit calculations of fluid flow at low mach number, Tech. rep., Los Alamos National Lab. (1986).

[86] C. Rhie, W. L. Chow, Numerical study of the turbulent flow past an airfoil with trailing edge separation, AIAA journal 21 (11) (1983) 1525–1532.

[87] P. Sagaut, Large eddy simulation for incompressible flows: an introduction, Springer Science & Business Media, 2006.

[88] P. Sagaut, Multiscale and multiresolution approaches in turbulence: LES, DES and hybrid RANS/LES methods: applications and guidelines, World Scientific, 2013.

[89] H. Sakamoto, H. Hainu, Y. Obata, Fluctuating forces acting on two square prisms in a tandem arrangement, Journal of Wind Engineering and Industrial Aerodynamics 26 (1) (1987) 85–103.

[90] M. Schäfer, Computational engineering: Introduction to numerical methods, Springer, 2006.

[91] A. Schell, Entwicklung einer Berechnungsmethode zur Vorhersage der Schallausbreitung im Nahfeld eines umströmten Kraftfahrzeugs, Ph.D. thesis, Universität Stuttgart (2014).

[92] F. G. Schmitt, About boussinesq's turbulent viscosity hypothesis: historical remarks and a direct evaluation of its validity, Comptes Rendus Mécanique 335 (9-10) (2007) 617–627.

[93] M. Shoeybi, J. Templeton, Three-dimensional wall filtering formulation for large eddy simulation, in: Annual Research Briefs, Center of Turbulence, Livermore, CA, 2006.

[94] M. Shur, P. Spalart, M. Strelets, A. Travin, Detached-eddy simulation of an airfoil at high angle of attack, in: Engineering Turbulence Modelling and Experiments 4, Elsevier, 1999, pp. 669–678.

[95] M. L. Shur, P. R. Spalart, M. K. Strelets, A. K. Travin, A hybrid rans-les approach with delayed-des and wall-modelled les capabilities, International Journal of Heat and Fluid Flow 29 (6) (2008) 1638 – 1649. doi:https://doi.org/10.1016/j.ijheatfluidflow.2008.07.001.

[96] J. Smagorinsky, General circulation experiments with the primitive equations: I. the basic experiment, Monthly weather review 91 (3) (1963) 99–164.

[97] P. Spalart, M. Shur, M. Strelets, A. Travin, Sensitivity of landing-gear noise predictions by large-eddy simulation to numerics and resolution, in: 50th AIAA Aerospace Sciences Meeting including the New Horizons Forum and Aerospace Exposition, p. 1174.

[98] P. R. Spalart, Comments on the feasibility of les for wings, and on hybrid rans/les approach, in: Proceedings of First AFOSR International Conference on DNS/LES, 1997, 1997.

[99] P. R. Spalart, S. Deck, M. L. Shur, K. D. Squires, M. K. Strelets, A. Travin, A new version of detached-eddy simulation, resistant to ambiguous grid densities, Theoretical and computational fluid dynamics 20 (3) (2006) 181.

[100] J. Spurk, Strömungslehre: Einführung in die Theorie der Strömungen, Springer-Verlag, 2013.

[101] M. Strelets, Detached eddy simulation of massively separated flows, in: 39th Aerospace sciences meeting and exhibit, p. 879.

[102] W. Sutherland, LII. the viscosity of gases and molecular force, The London, Edinburgh, and Dublin Philosophical Magazine and Journal of Science 36 (223) (1893) 507–531. doi:10.1080/14786449308620508.

[103] F. Thiele, Simulation of Airframe Noise Using a two-step DES/FWH approach, TU-Berlin, MUSAF II colloquium, 2013.

[104] A. Travin, M. Shur, M. Strelets, P. R. Spalart, Physical and numerical upgrades in the detached-eddy simulation of complex turbulent flows, in: R. Friedrich, W. Rodi (Eds.), Advances in LES of Complex Flows, Springer Netherlands, Dordrecht, 2002, pp. 239–254.

[105] A. Travin, M. Shur, M. Strelets, P. Spalart, Detached-eddy simulations past a circular cylinder, Flow, Turbulence and Combustion 63 (1-4) (2000) 293–313.

[106] A. K. Travin, M. L. Shur, P. R. Spalart, M. K. Strelets, Improvement of delayed detached-eddy simulation for les with wall modelling, in: ECCOMAS CFD 2006: Proceedings of the European Conference on Computational Fluid Dynamics, Egmond aan Zee, The Netherlands, September 5-8, 2006, Citeseer, 2006.

[107] F. van Herpe, S. Vergne, E. Gaudard, Wavenumber-frequency analysis of the wall pressure fluctuations in the wake of a rear view mirror using a lattice boltzmann model, in: Proceedings of the Acoustics 2012 Nantes Conference.

[108] M. Vanella, U. Piomelli, E. Balaras, Effect of grid discontinuities on large-eddy simulation statistics and flow fields, Journal of Turbulence (9) (2008) N32.

[109] R. Vichnevetsky, Propagation through numerical mesh refinement for hyperbolic equations, Mathematics and Computers in Simulation 23 (4) (1981) 344–353.

[110] R. Vichnevetsky, Propagation and spurious reflection in finite-element approximations of hyperbolic equations, Computers & Mathematics with Applications 11 (7) (1985) 733–746, special Issue Computational Ocean Acoustics. doi:https://doi.org/10.1016/0898-1221(85)90168-3.

[111] R. Vichnevetsky, L. Turner, Spurious scattering from discontinuously stretching grids in computational fluid dynamics, Applied Numerical Mathematics 8 (3) (1991) 289 – 299. doi:https://doi.org/10.1016/0168-9274(91)90058-8.

[112] M. R. Visbal, D. V. Gaitonde, Very high-order spatially implicit schemes for computational acoustics on curvilinear meshes, Journal of Computational Acoustics 9 (04) (2001) 1259–1286.

[113] M. R. Visbal, D. V. Gaitonde, On the use of higher-order finite-difference schemes on curvilinear and deforming meshes, Journal of Computational Physics 181 (1) (2002) 155–185.

[114] C. Wagner, T. Hüttl, P. Sagaut, Large-eddy simulation for acoustics, Vol. 20, Cambridge University Press, 2007.

[115] R. Warming, R. M. Beam, Upwind second-order difference schemes and applications in aerodynamic flows, AIAA Journal 14 (9) (1976) 1241–1249.

[116] H. G. Weller, G. Tabor, H. Jasak, C. Fureby, A tensorial approach to computational continuum mechanics using object-oriented techniques, Computers in physics 12 (6) (1998) 620–631.

[117] J. F. Williams, D. L. Hawkings, Sound generation by turbulence and surfaces in arbitrary motion, Phil. Trans. R. Soc. Lond. A 264 (1151) (1969) 321–342.

[118] D. Wood, M. A. Passmore, A.-K. Perry, Experimental data for the validation of numerical methods - sae reference notchback model, SAE International Journal of Passenger Cars - Mechanical Systems 7 (1) (2014) 145–154. doi:https://doi.org/10.4271/2014-01-0590.

[119] X. Wu, P. Moin, Direct numerical simulation of turbulence in a nominally zero-pressure-gradient flat-plate boundary layer, Journal of Fluid Mechanics 630 (2009) 5–41. doi:10.1017/S0022112009006624.

[120] P. K. Yeung, D. A. Donzis, K. R. Sreenivasan, Dissipation, enstrophy and pressure statistics in turbulence simulations at high reynolds numbers, Journal of Fluid Mechanics 700 (2012) 5–15. doi:10.1017/jfm.2012.5.

[121] M. Yokokawa, K. Itakura, A. Uno, T. Ishihara, Y. Kaneda, 16.4-Tflops direct numerical simulation of turbulence by a Fourier spectral method on the Earth Simulator, in: Proceedings of the 2002 ACM/IEEE conference on Supercomputing, IEEE Computer Society Press, 2002, pp. 1–17.

[122] N. Yukawa, M. Nishikawa, T. Nakajima, C. Aoki, H. Sugihara, Tire noise reducing system, US Patent 6,726,289 (Apr. 27 2004).

[123] Q. Zhang, High-order, multidimensional, and conservative coarse-fine interpolation for adaptive mesh refinement, Computer Methods in Applied Mechanics and Engineering 200 (45) (2011) 3159 – 3168. doi:https://doi.org/10.1016/j.cma.2011.07.009.

[124] Y. Zhiyin, Large-eddy simulation: Past, present and the future, Chinese Journal of Aeronautics 28 (1) (2015) 11 – 24. doi:https://doi.org/10.1016/j.cja.2014.12.007.